The corrosion of Zn-4.8wt.%Al sacrificial coating used for the protection of steel

Callum Gallagher BEng

Submitted to Swansea University in fulfilment of the requirements for the Degree of Doctor of Engineering

Swansea University

2022

Summary

This work set out to elucidate the microstructural corrosion mechanisms of sacrificial corrosion coating, Galvalloy® (Zn-4.8wt.%Al), which is used extensively in the strip steel industry. Corrosion of Galvalloy® occurs at the surface, where only Galvalloy® is exposed, and the cut edge, where Galvalloy® and steel are coupled, which increases the corrosion rate of Galvalloy®.

Chapter 3 demonstrates the time-lapse microscopy (TLM) technique being used to analyse, in-situ, the microstructural mechanism of surface and cut-edge corrosion of Galvalloy® immersed in pH 7 1 wt.% NaCl. Rotating disk electrode (RDE) and potentiodynamic polarisation (PD) tests were performed on the individual phases of Galvalloy® to identify their anodic and cathodic activity in 1 wt.% NaCl. TLM showed that surface corrosion initiates and propagates through the binary eutectic Zn-Al phase, whereas cut-edge corrosion initiates within the primary zinc dendrite phase and proceeding through the entire microstructure. The electrochemical data validated this as the RDE showed that the Al containing phases could not support cathodic activity as well as the primary zinc phases and PD showed that the zinc phases are more susceptible to anodic dissolution when polarised.

Chapter 4 investigated, using TLM and PD, the corrosion rate and mechanism of the Galvalloy® surface across pH 3, 7, 10 and 13 in 1 wt. % NaCl. At pH 3 and 13, D showed a maxima of corrosion rate was seen and TLM illustrated no precipitation of corrosion product. PD showed pH 7 having the lowest i_{corr}, however, the precipitated corrosion product formed at a smaller radius relative to active anodes during TLM experiments of pH 10 compared to pH 7.

Chapter 5 utilized ZRA and TLM to investigate the rate and mechanism of the corrosion of Galvalloy® next to a steel 'cut-edge' across pH 3, 7, 10 and 13 in 1 wt. % NaCl. The corrosion rate of Galvalloy® was greater compared to the surface corrosion, due to the polarisation imposed by the connection to the steel substrate and the same corrosion rate to pH trend in Chapter 4 was see. At pH 7, 10 and 13, corrosion initiation occurs in the zinc dendrites, whereas at pH 3 the corrosion is generalised.

Chapter 6 investigated the effect of increasing steel to Galvalloy® on the corrosion rate of Galvalloy® at pH 7 in 1 wt.% NaCl using ZRA and TLM. ZRA demonstrated a linear trend, whereas TLM showed a non-linear trend which is suggested to be due to the increased ease of precipitation in the experimental set-up.

Chapter 7 is an example of a real-world corrosion problem involving organically coated Galvalloy®. 2 μL of HCl, $FeCl_2$, NaCl and Acetic acid (CH_3OOH) were administered to a scribed

region of PVB coated Galvalloy® and exposed to a high relative-humidity environment for a month to induce under-film corrosion in order to compare the results to deduce which salt was responsible for the real-world corrosion. NaCl was the salt that posed the greatest similarity and cathodic delamination is the postulated corrosion mechanism.

Declarations

I declare that this work has not previously been accepted in substance for any degree and is not being concurrently submitted in candidature for any degree.
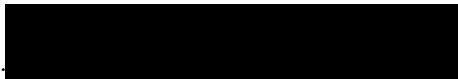
Signed █████████████████

Date...……16/02/2022...…..…

This thesis is the result of my own investigations, except where otherwise stated and that other sources are acknowledged by footnotes giving explicit references and that a bibliography is appended.

Signed…███████████████

Date...…… 16/02/2022...…..…

I give consent for the thesis, if accepted to be made available online in the University's Open Access Repository and for inter-library loan, and for the title and summary to be made available to outside organisations (unless a bar is in place).

Signed █████████████████

Date...…… 16/02/2022...…..…

The University's ethical procedures have been followed and, where appropriate, that ethical approval has been granted.

Signed…███████████████

Date...…… 16/02/2022...…..…

Contents

3   TIME-LAPSE MICROSCOPY INVESTIGATION INTO THE SURFACE AND CUT-EDGE CORROSION OF GALVALLOY® IN NEUTRAL PH NACL ELECTROLYTE ERROR! BOOKMARK NOT DEFINED.

4   TIME-LAPSE MICROSCOPY INVESTIGATION OF THE SURFACE CORROSION MECHANISM OF GALVALLOY® IN SALINE ELECTROLYTE AS A FUNCTION OF PH

Acknowledgements

Much like this thesis will seem long winded to a non-scientist/engineer, my acknowledgements will go on a bit. I'd like to take this time to acknowledge my time and the people I met whilst being at Swansea University. More specifically my doctorate, which I would not have done if it hadn't been for the support, encouragement and friendship from my undergraduate supervisor, James Sullivan. Also, my original lab PIC, Nathan Cooze, cheers fella.

TATA Steel and the Colors department were so generous with their time and wisdom, specifically Ann Brash, Peter Barker and Jon Elvins. Patrick Dodds also played a big role in this, providing help and assistance on a business trip to Ijuimden/Amsterdam, which was a very enjoyable visit. There I met Brian Cunnah, a very enthusiastic contracts manager, who was kind enough to invite on a roof inspection in Kettering, an experience I will never forget.

I have Pam Berry to thank for my exploration into the world of outreach, something I am still passionate about. I like to show my appreciation to Mrs. James at Gowerton school and Mr. Smallbones at Penllergaer primary for their teamwork in what turned out to be some great days.

Some of this outreach stretched further afield, to Cheltenham where I was joined by Carol Glover and Catherine Friar for a thrilling week of showing school kids how to put steel into copper sulphate. I am still surprised by how surprised those children were and for that I would like to pay them thanks.

Other adventures were less PG, one notable time was a lecture on Benjamin Franklin's acheivements at the Society for Chemical Industry, conveniently located by the Assange residents. Alex Neilsen, James Edy and myself decided that, after an evening of intellect, it would be rude to not continue with night at Ronnie Scott's.

The fun times continued into Japan where myself and the Hotel Niwa Crew bravely made our first international conference presentations. This was paired with a week of recovering from the jetlag and delving into Japanese culture. This included the Golden Gai, watching David Penney holding on for dear life on a high-altitude fun fare ride and the obligatory foot race in the street between myself and Sam Minshell. Thanks everyone for a great week!

Trips to the London at the Armourers guild hall were always treasured. The food, presentations, company, and setting were all to die for. Thanks to the Materials Processing Institute for putting on a good show every time and giving us a peek into how the other half live.

The experiences continued into Poland where as well as being given the opportunity to present my work to the European corrosion community, I was able to spend valuable time with Arnoud de Vooys, who is an intellect and a true character. I cannot go without mentioning the guided tour of Auschwitz from Neil McMurray, an afternoon of enlightenment nor myself or Geraint Williams could ever forget. Thank you both for your company.

Another hero I would like to recognize is Lee Bridgeman, pictured with myself and Sam Minshell at a steelmakers dinner in Newport. This photo was taken before one of many "Calm down Sam!"'s from Lee's mouth.

Visiting TATA's facility in Shotton gave Swansea's Colors EngD team the chance to engage with Britain's steel industry, where knowledge was imparted from both sides. These would then naturally lead to the annual trip to Teppan-Yaki in Cheshire. I managed to capture the group as we headed out on my final dinner.

Thanks everyone for a great time. A special thanks for Nat Wint for being incredibly supportive academically and a friend personally. To Phil Ansell and Tom Lewis, thanks for the many coffee discussions.

When I made it into the University from galivanting, I could not have done all the work I had if it wasn't for the diligent undergraduate students Dean Hardwicke, Rob Lunt and Matt Ritchie. Thank you for your help and allowing me to talk non-stop at you, you did a good job.

Thank you to the football and poker groups, and especially the organisation and patience from James Carlos, you are a saint. A shout out to Ben Morgan, Marcin Orzech, Alex Carr, Ben Smith and Luis Escott for the constant fits of laughter I was in whilst being in and out of the office.

The final presentation was a big moment. Catherine and Becky, you're both delightful and amazing to be around, thanks for making the TATA corrosion team of 2019 what is was.

I would also like to recognise the corroders of tomorrow, some of whom are pictured below. In the brief time we had together, I left very happy knowing that the reigns were being passed on to some great people. Keep up the good work and I look forward to my invite to the next Coating and Corrosion conference.

I took this last photo just before leaving Swansea for the last time. It's looking pretty tidy.

Lastly, I would like to thank my parents Cary and Carol for always being there and my incredible family for all of their support throughout the many years I have been away from home. To my wife Stephanie, thank you for putting up with me being non-existent for 3 months whilst I write up this beast.

Over and out.

List of Tables

List of Figures

13

is 100 minutes hours totalling 500 minutes. The red circles show the initial anode formation. The images also show a brightening in the regions of cathodic activity, due to the surface oxide layer being removed to allow for sufficient electron transfer. Meanwhile, the regions where anodes appear remain a darker shade. The regions in-between the notable cathodic and anodic activity areas is the location for corrosion product deposition. The outline of which is marked by a dotted white line in image F. These images depict Video 3.1. 102

Fig. 3.5 Time-lapse images specifically showing the anode growth on the Galvalloy® surface over a 100-minute period. The micrographs show the anodic growth in the binary eutectic Zn-Al phase leaving the primary Zinc dendritic phase intact. At 300 minutes it shows the anode engulfing the primary zinc dendrite, whilst also demonstrating a resistance from the dendrite. 103

Fig. 3.6 SEM images of Galvalloy® a) prior to and b) after 45 minutes of immersion within pH 7 1 wt.% NaCl. 103

Fig. 3.7 Images A-D: Time-lapse microscopy of Galvalloy® immersed in 1 wt.% NaCl electrolyte with 25% of the surface exposed to Steel. The time interval between the micrographs is 34 minutes, with a time of 36 minutes at the last micrograph. The images show anodes forming along the nodule boundary in the dendritic region almost immediately, indicated by red circles. These stills depict Video 3.2. 105

Fig. 3.8 SEM images of unetched Galvalloy® after immersion in 1 wt.% NaCl pH 7 for 30 minutes. Both images were taken on a Hitachi TM3000 with image A taken at 9000 x magnification, and image B taken at 1000 x magnification. Both images show the corrosion initiation in the binary eutectic region of the microstructure. In image A the corrosion is seen in on layer of the lamellar, and in image B the corrosion appears to have initiated in the eutectic and spread until it contacts several dendrites. 107

Fig. 3.9 Potentiodynamic anodic polarization curves of pure zinc, Zn0.7Al, Zn22Al and Zn68Al in aerated 1 wt.% NaCl at pH 7. 108

Fig. 3.10 Disc current density as a function of potential for a.) Zn (99.998%), b.) Zn0.7Al, c.) Zn22Al, d.) Zn68Al and e.) pure iron in aerated 0.5 M Na_2SO_4 buffered to pH 9.3. Potential sweet rate 3.3 x 10^{-4} $V.s^{-1}$. Angular velocity key: i) 55, ii) 108, iii) 163, iv) 217, v) 271, vi) 314 $rad.s.^{-1}$. 111

Fig. 3.11 Levich slope obtained from anodic going potentiodynamic experiments, alongside theoretical values for $4e^-$ and $2e^-$ oxygen reduction in 0.5 M Na_2SO_4 buffered to 9.3. 112

Fig. 3.12 Anodic going polarization curves obtained in aerated 0.5 M aqueous Na2SO4, borate buffered at pH 9.3. Potential sweep rate $3.3 \times 10{-4}V.s{-1}$. Angular velocity 271 rad.s−1. 113

Chapter One

Introduction

1   Literature Review

1.1   Introduction

Steel is an extremely widely used material and the world average steel use per capita was 208 kg in 2015 (1). Its wide usage is a consequence of the combination of strength, formability, abundancy, and versatility with which it is associated. It was used by the Romans and aided them when conquering other civilizations as the strength of steel could not be matched with brass in battle (2). This strength did not come without an Achilles' heel and after a period of exposure the steel would develop a red rust on the surface, compromising the structural integrity of the material. This rust formation was a consequence of corrosion, which results in an oxide layer on the surface, (in this case Fe_2O_3) The repair, replacement and downtime associated with corrosion contributes toward an estimated \$1372 billion cost to the oil and gas industry per year. In the UK an estimated 1 tonne of steel is converted into rust every 90 seconds (3). A variety of industries (for example aerospace and defence) are affected by corrosion and a drive exists to reduce corrosion as much as possible. Corrosion can also be detrimental to health and safety, for instance the corrosion of lead, which is commonly used for water supply piping, can lead to lead poisoning such as the case in Flint, Michigan (4).

Within nature, metals typically exist as metal ores or oxides, and a lot of energy is required to extract the metal. Corrosion takes place as a result of thermodynamic drive for metals to return to their lowest energy states (typically as a metal oxides). The difference between the energy state of a reactant and the product of a reaction is given by the Gibbs Free Energy change (ΔG) In the case that the value of ΔG is negative the reaction is thermodynamically feasible (5).

The are many ways by which steel is protected from corrosion. One method involves coating the steel with a metal that will corrode preferentially to the steel, protecting the steel and maintaining its structural strength. In 1742, Paul Malouin, a French chemist, presented findings to the French Royal Academy on the corrosion protection of steel by dipping it into molten zinc (6). This sacrificial protection was then demonstrated by Humphry Davy (7). And then in 1837, a French engineer, Stanislas Sorel, patented Hot Dip Galvanising (HDG) (6). This is because zinc, in relation to steel, has a more negative E^o/V on the electrochemical series, and in the galvanic series (8,9). The coating was applied via the hot dip process. To control the viscosity and to prevent brittle intermetallics from forming, as well as performance and economic benefits, a binary alloy with Al additions of 4.8wt% (Galvalloy®), 5wt% (Galfan) and 55wt% (Galvalume) have shown great developments in corrosion prevention in comparison to HDG coatings (10,11). The final microstructure due to the coating process conditions have shown to have an effect on the corrosion resistance of the binary alloy. The corrosion of these binary alloys was related to the volume fraction of the phases, size of the dendrites and the nucleation rate (12–14).

Once such alloy is Galvalloy® produced by and a registered trademark of Tata Steel, which is commonly used in conjunction with an organic overcoat to form their premium product, Colorcoat HPS200 Ultra® and Colorcoat Prisma®, which has a 40-year guarantee. Furthering our knowledge of the mechanism by which the coating corrodes will give a clearer indication of how to combat this corrosion, for example by the addition of inhibitors into the paint system (15). This thesis is an endeavour to continue to elucidate the corrosion mechanisms at work within the Galvalloy® microstructure during the corrosion reaction as it occurs within different industrially relevant environments.

1.2 Corrosion

The large majority of metals exist as ores. These ores are chemically stable states in which the metal exists, bound in an oxide, hydroxide, carbonate or sulphide-based compound. A substantial amount of energy input is required to extract the pure metal. One such iron ore, Hematite (Fe_2O_3), is heated with a reducing agent in a blast furnace (1600°C) to extract iron. This produces a pure metal which resides in a higher energy state and there exists a thermodynamic drive to reinstate this archetypal, lower energy state via reaction with the environment. Environments dictate the types of corrosion, e.g.:

- Dry Corrosion; dry, heated environments
- Mechanical; physical removal of the metal from a body, namely fretting and abrasion
- Wet or Aqueous Corrosion

1.2.1 Theory of Aqueous Corrosion

When this manner of corrosion occurs a wet corrosion cell is established. This cell consists of four components, without which corrosion cannot occur;

- An anode; this is site of anodic activity (also known as metal dissolution or loss), and provides electrons to the cathode and cations to the electrolyte
- A cathode; the site of cathodic activity (commonly the reduction of oxygen) uses the electrons from the anode and produces anions
- Electrolyte; this is where ion transport takes place between the anode and cathode, commonly resulting in the formation of corrosion product where the products are precipitated
- An electrical connection. This connection facilitates the transfer of electrons from the anode to the cathode, which can either be present on the same metal surface or different metal surfaces.

The reactions taking place make up a REDOX reaction, where there is REDuction at the cathode and OXidation at the anode. The oxidation reaction taking place at the anode is shown in Equation 1.1 where the metal atom losses an electron, becoming a positively charged cation.

$$M_{(s)} = M_{(aq)}^{n+} + ne^- \qquad 1.1$$

In the case of iron the principal oxidation reaction is:

$$Fe_{(s)} = Fe_{(aq)}^{2+} + 2e^- \qquad 1.2$$

The reduction reactions at the cathode can vary depending upon pH and aerated conditions. At a low pH, Equation 1.3 is relevant. When the pH is neutral and the environment is aerated Equation 1.4 is usual.

$$2H_{(aq)}^+ + 2e^- = H_{2(g)} \qquad 1.3$$

$$2H_2O_{(aq)} + O_{2(g)} + 4e^- = 4OH_{(aq)}^- \qquad 1.4$$

Many different electrolytes, for example seawater and rainwater, naturally occur within our environment. The ions contained in these salt electrolytes act as a charge transfer reducing the activation energy (*ΔG) required for the formation of the corrosion products from the pure metal. A schematic of the corrosion under a droplet of water is shown in Fig. 1.1, which illustrates how local differences in oxygen concentration effects the location of anodes and cathodes Local differences in pH and metal and passive film composition all play a role in determining where the anodes and cathodes exist.
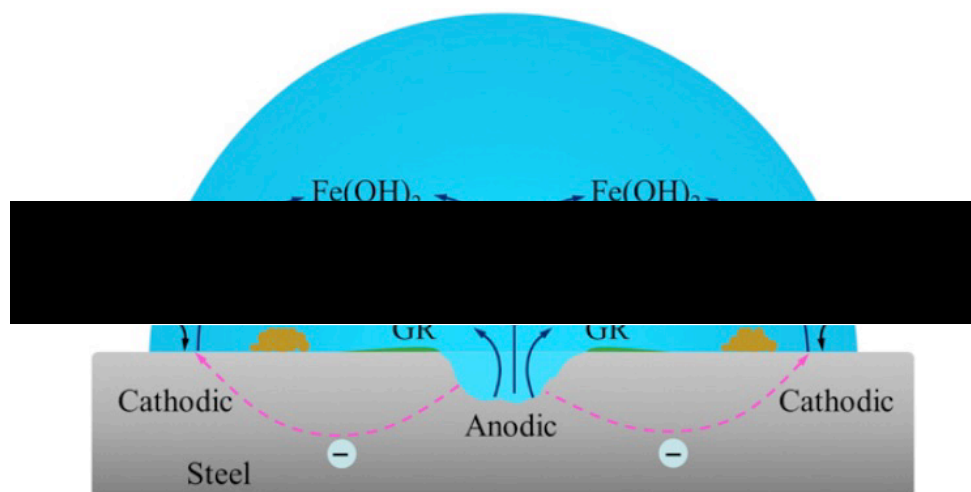
Fig. 1.1 Schematic representation of the Evans droplet corrosion cell (16).

1.2.2 Kinetics of Corrosion

The total current flowing into an external circuit is the sum of the currents of the individual couples present on the corroding surface. And under free corrosion:

$$\sum i_{anodic} = \sum i_{cathodic} = i_{corr} \qquad 1.5$$

Where i_{anodic} is the partial current density due to any anodic reaction, $i_{cathodic}$ is the partial current density due to any cathodic reactions and i_{corr} is the overall rate of corrosion. These electrochemical currents also depend upon potential and as such the corroding metal adopts a potential, called E_{corr} or the free corrosion potential.

Julius Tafel defined the mathematical relationship between current density, i, and potential, E (17):

$$i_{anodic} \propto \exp(E) \qquad 1.6$$

And

$$i_{cathodic} \propto \exp(-E) \qquad 1.7$$

Tafel plots show E against lg(i) (current density) and are used to plot electrode processes in a straight line. Different electrode processes generating a mixed potential are shown in Fig. 1.2. This plot is called an Evans diagram and demonstrates a simple corrosion process. During corrosion the metal loss that occurs at the anode results in ions entering solution and electrons flow to the cathodic site. This loss of electrons, results in a positive shift of potential by η_a, which is referred to as anodic polarisation. An opposing shift occurs at the cathodic region, where the potential is reduced by amount η_c, (cathodic shift). These shifts are illustrated in Fig. 1.2. The intersection of the Tafel slopes shows the point at which the cathodic and anodic currents are equal, therefore having a zero sum. This point is the free corrosion current, i_{corr} shown in Equation 1.5. The free corrosion potential, E_{corr} can also be obtained from this plot.
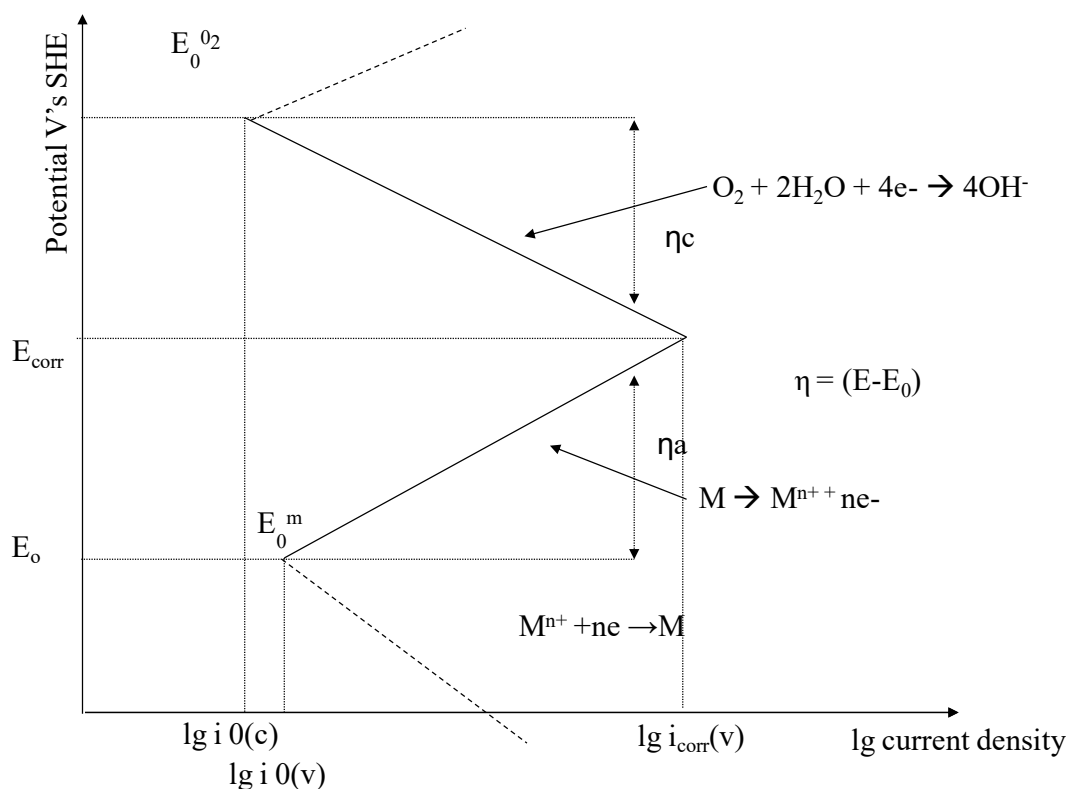
Fig. 1.2 Evans diagram of a metal immersed in aerated electrolyte.

1.2.3 Pourbaix Diagrams

Modern electrochemical studies have been heavily influenced by the works of Marcel Pourbaix and diagrams that he produced, allowing for easy understanding of the thermodynamic stability of species in combinations of pH and potential environments. When the concentration of a metals ions in solution $\geq 10^{-6}$ mol/L the metal is considered to be in a state of "corrosion". If the concentration of ions in solution is less than this then it is in a condition of "immunity". It has been assumed that all corrosion reactions involved the dissolution of metal ions, as seen in Equation 1.1. This is not always the case, some corrosion products are in fact insoluble and form films on the surface creating a barrier between it and the electrolyte. This barrier provides a great reduction in the corrosion rate leading to what is known as "passivity". One or more reactions can be involved in corrosion of metals, usually dependant on the pH of the electrolyte. These reactions and their predicted thermodynamic stabilities are represented in the Pourbaix diagrams as lines across a range of pHs and potentials.

Simplified Pourbaix diagrams for zinc and aluminium (metals of interest in this investigation) in water are shown in Fig. 1.3. It shows that at a pH below 8 and 4 for zinc and aluminium respectively, and with no impressed potential, both metals are in a state of corrosion. It can also be seen that for both metals, varying the pH of the metal of electrolyte or suppressing the potential, can change the state of the metal into that of passivity or immunity.

When a material has the ability to be active at both basic and acid pHs, it is called amphoteric.
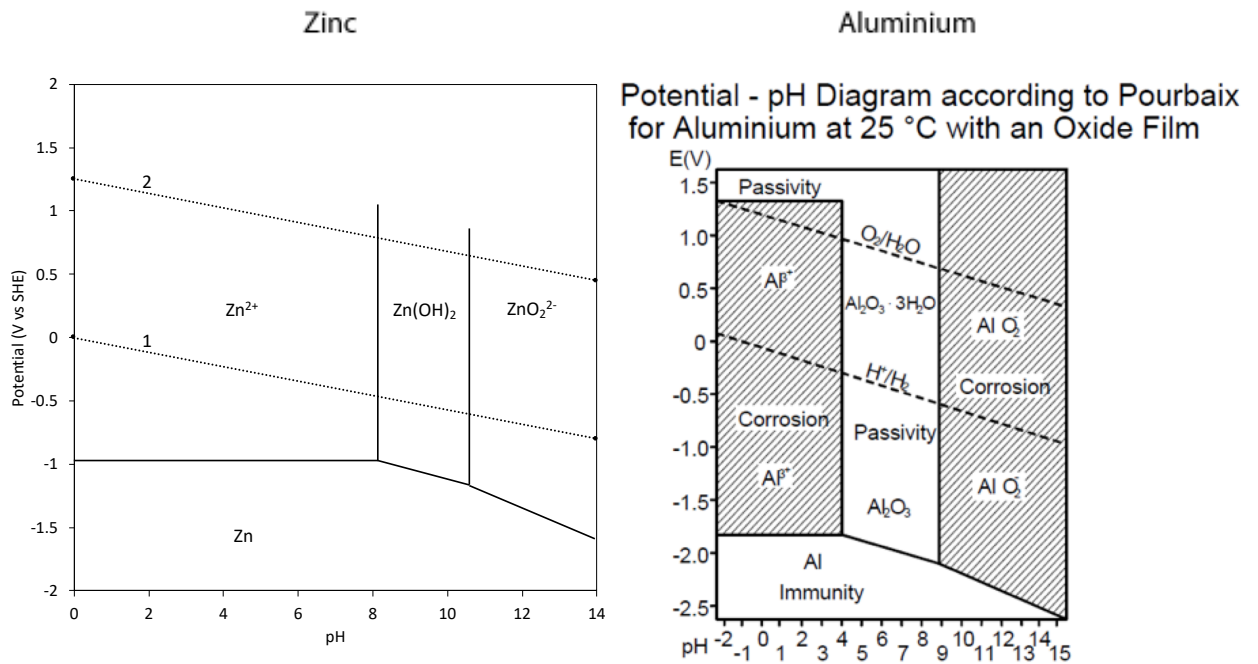
Fig. 1.3 The pH – potential diagrams (Pourbaix) for both Zinc and Aluminium, indicating the thermodynamic stability of the oxidation species of the respective metals.

In Fig. 1.4 it is clear to see that iron (the main constituent of steel) is not an amphoteric material, it has a region of passivity in alkaline water (> pH 8), unlike zinc and aluminium which are passive at a mid-range pH and are active at high and low pHs. This would lead us to believe that the steel and the Galvalloy® will both be active at low pH values, passive above pH 8 and both passive and active at high pH.
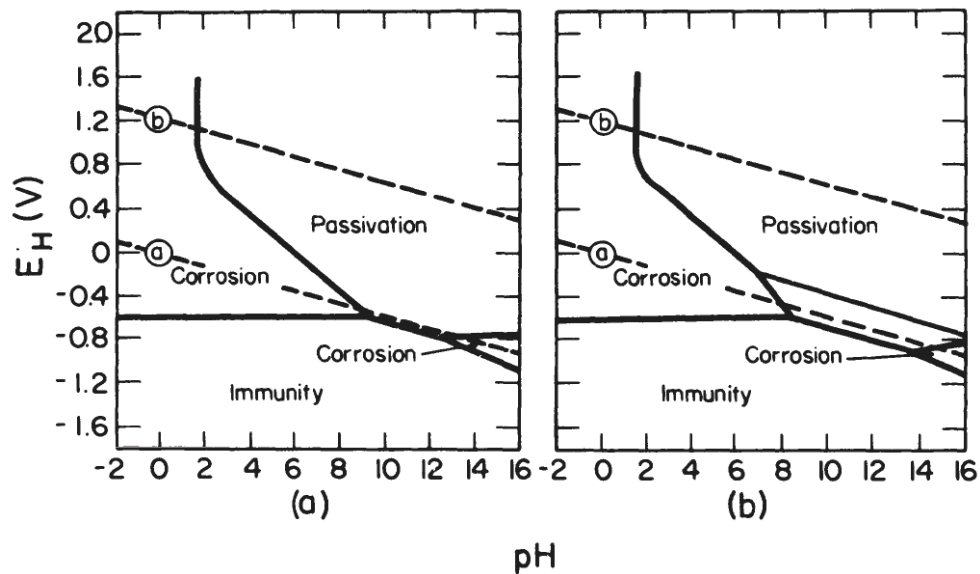
Fig. 1.4 Potential – pH (Pourbaix) Diagram of iron - water system (18). The graph shows the theoretical conditions of corrosion, immunity and passivation. (a) assuming passivation by a film of Fe_2O_3; and (b) assuming passivation by films of Fe_2O_3 and Fe_3O_4.

1.2.4 Localised Corrosion

The common forms of corrosion that zinc coated steels experience are localised. The major types of this corrosion will be outlined in this section.

1.2.4.1 Dissimilar Metal Corrosion (Galvanic)

This type of corrosion occurs when two metals of differing free corrosion potentials, E_{corr}, are in connection within bulk electrolyte forming a wet corrosion cell. The E_{corr} of these metals can be compared using the electrochemical series, shown in Fig. 1.5, which highlights their relative nobility or reactivity in a given electrolyte. The lower the value of the free corrosion potential the more reactive the metal. When in electrically connected in electrolyte, the metal with the lower E_{corr} will become the anode in preference to the metal with the higher E_{corr} which will become the cathode. The rate of this corrosion reaction is proportional to the magnitude difference between the E_{corr}. The type of corrosion can be exploited for benefit in some situations, such as zinc coatings on steel.

Fig. 1.5 The Galvanic Series of Metals and Alloys (8).

1.2.4.2 Differential Aeration and Crevice Corrosion

The cathodic oxygen reduction reaction (CORR), is a key driver in the anodic dissolution reaction and therefore the overall corrosion of a material. A differential aeration cell can develop when a difference in the rate of oxygen diffusion exists. As seen in Fig. 1.1 in section 1.2.1, this can occur in a system as simple as a droplet. The area with a higher oxygen concentration preferentially assumes the cathodic site while the oxygen depleted areas act as the anode. In real world scenarios, when two materials are fixed to one another, crevices form. Typically, these are areas $25 - 100$ μm wide, and occur often in fabrication. As shown in Fig. 1.6a, higher oxygen concentration occurs in the bulk compared to within the crevice (where oxygen diffusion is limited). As normal corrosion occurs on the metal, and with this oxygen differential in place, the inside of the crevice adopts the position of anode in the corrosion cell. Similarly to pitting corrosion, as the metal cations are released into solution due to dissolution, aggressive chloride ions torrent in to balance the charge causing the corrosion to progressive rapidly as shown in Fig. 1.6b.

(a)   (b)
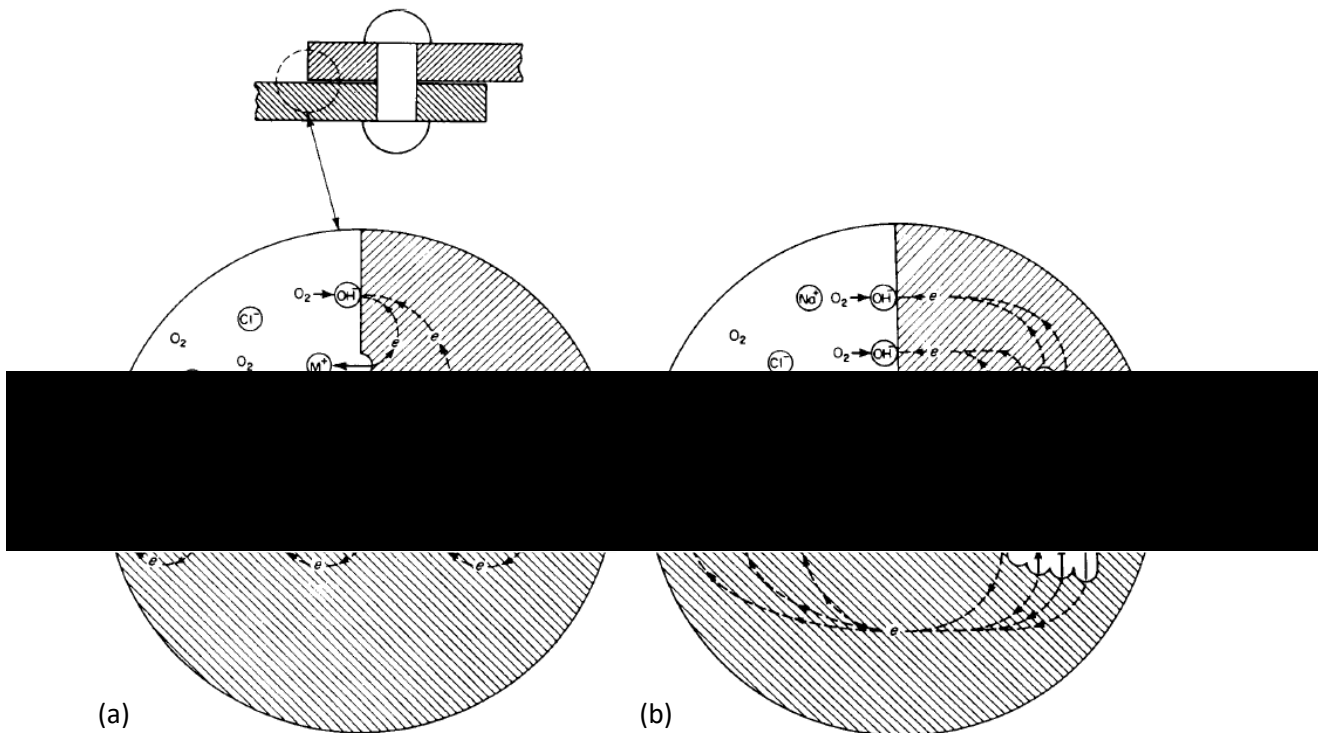
Fig. 1.6 Schematic diagram of crevice corrosion. (a) initial stage. (b) later stage (19).

1.2.5 Prevention of Corrosion with Coatings

1.2.5.1 Barrier Coatings

There are many engineering solutions that exist to protect underlying substrates from corrosive media. These can be:

- Organic (e.g., paints)

- Inorganic (e.g., sol-gel, titanate and zirconia pre-treatments, alumina, yttria-stabilized zirconia etc.)
- Metallic (e.g., Cr, Ni, Sn, Al, Zn etc.)

Painting metal objects with organic barriers has been a technique used for corrosion control for a long time (20). The mechanism works by providing the metal with a basic barrier from the corrosive environment (oxygen and electrolyte). However, water and oxygen can both penetrate paint sufficiently enough to initiate corrosion of the underlying metal. As well as paints, these organic coatings include enamels and plastic laminates. However, this coating must be unbroken to work properly as defects or scratches exposing the underlying metal will lead to corrosion. This form of corrosion can be particularly aggressive, and crevices can form as the paint becomes detached from the metal.

Inorganic coatings can be either fully inorganic or a combination of inorganic and organic. A benefit to combine is that platelets or flakes can be used as pigments within organic coatings. This is because water can pass through organic coatings with relative ease, but not through inorganics (21). Moreover, platelets present a tortuous meandering route through these platelets rather than a direct route. Other inorganic coating, such as alumina, are used against high temperature corrosive media, such as liquid metals and steam within the power generation industry and aerospace.

Metallic coatings such as Cr and Ni form surface oxides which are adherent and chemically inert, protecting the substrate as a barrier. This is a popular method of protection seen on cars and buildings as they are attractive to the consumer. Zinc and aluminium are used more broadly in construction, as well as being used for protection of cars beneath the paint coating.

1.2.5.2 Sacrificial Coating Protection

A metal may be protected from corrosion by being coated with a less noble metal. The principles of dissimilar metals corrosion are employed to our advantage with this cathodic protection technique, whereby the coating corrodes in favour of the metal substrate.

In the Evans diagram, shown on page 27, the equilibrium potential of oxygen (E_oO_2) is greater than the equilibrium potential of the metal (E_oM). If the oxygen reaction was the free corrosion potential of iron (substrate) and the M was the free corrosion potential of zinc (coating), and the cathodic overpotential (η_c) on the iron, due to the mix potential from the galvanic couple, is sufficient, then the iron dissolution reaction will negligible.

The most widely used sacrificial coatings for the protection of steel are based on zinc and its alloys. The free corrosion potentials of zinc and iron in seawater are -1.05 V and -0.65 V vs. SCE respectively, shown in Fig. 1.5. So, applying the knowledge we have learnt above, when coupled together the zinc will be polarised anodically, and the iron will be polarised cathodically, leading

to the dissolution of zinc and the oxygen reduction or hydrogen evolution reaction on iron, when the system is exposed to electrolyte. For example, a zinc coating which contains a surface defect, for example a scratch, exposes the underlying iron shown in Fig. 1.7. The small cathodic area of iron will drive the corrosion of the zinc coating. The zinc ions readily react with the hydroxide ions (produced by the cathodic reaction on the exposed steel) present in the electrolyte, forming insoluble zinc hydroxide which can fill the scratch, further reducing the corrosion rate.
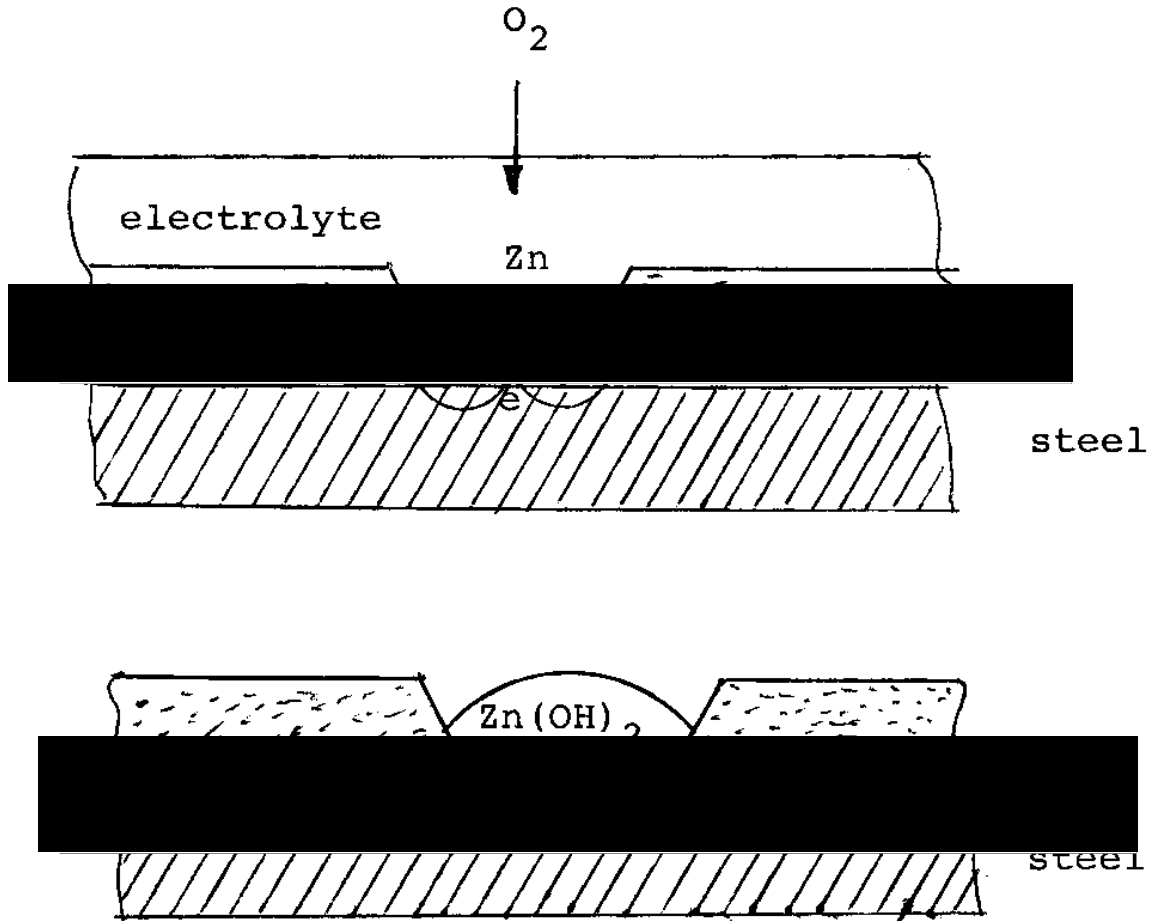
Fig. 1.7 Schematic diagram of zinc sacrificially protecting steel in the presence of electrolyte and insoluble zinc hydroxide filling in the gap made by the defect, further protecting the steel (22).

1.2.5.3 Organic Coatings (Colorcoat HPS200 Ultra®)

Organically coated galvanised steels (OCS) are a very popular product in the construction industry due to the low relative cost, flexibility and speed for the construction industry (23). Eurofer steel figures (24) show that 5 million tonnes of OCS steel is produced each year and that 35% of finished steel is used in the construction industry. With roughly a third of all flat products being coated, and the BEIS 2017 report (25) valuing the coated steel UK products market as the most valuable of all finished steels. Tata's commercial Colorcoat® system has been used for decades for cladding boasting a large number of Tier 1 projects. The Colorcoat® system is beneficial in

construction due to its improved lifetime over traditional galvanised products with guarantees reaching up to 40 years.

OCS are produced by continuous coil coating onto galvanised steel coils. The Colorcoat® material used in this investigation has been HPS200 Ultra®. This is made up of a steel substrate of 0.5-0.7 mm thickness and a Galvalloy® coating of 20 μm either side of the steel. The galvanised layer is pretreated followed by a primer and top coat.

The process comprised of these stages:

- Entry
- Process
- Exit (recoiled)

At the entry stage, much like the hot dipping process, the coil is joined to the previous coil and an accumulator is used to ensure the process is continuous.

The zinc coated steel is then pre-treated by cleaning with caustic spray, application of an inorganic conversion coating (10-60nm). The purpose of this is to prepare the surface physically and chemically for the subsequent organic coating.

Organic coatings are then applied to both sides of the strip. Firstly, a primer is applied by roller coating to one side, followed by curing. This primer is either polyurethane or polyester based and has a thickness of between 5 and 25 μm. The primer typically contains corrosion inhibitors, (normally based on sparingly soluble zinc salts). The next stage is the simultaneous coating of the top-coat on the front weather side and backing coat on the reverse side. The topcoat on the front consists of a 200 μm PVC coating and a 10 μm polyester coating is applied to the back via a roller coating process. The coating is then cured at temperatures of 220 °C for around 50 seconds.

As mentioned, the high durability of the organic coating is very desirable, providing an excellent ionic barrier to the metal beneath. The most common failure mechanism is at the cut edge where both steel and zinc are exposed to the environment (26).

1.2.6 Corrosion Under Organic Coatings

The role of organic coatings is to provide an ionic barrier between the metal surface and its surrounding environment. A number of corrosion mechanisms can occur at defects in the coating. The two that will be discussed are cathodic under-film delamination and anodically driven filiform corrosion (FFC), which both present aesthetic issues as well as structurally destructive damage, both undesirable in the steel industry.

In order for the coating to sufficiently fulfil requirements it is essential that the adhesion between itself and the metal it's protecting is maintained. Penetrative damage exposes the metal to

electrolyte, making it vulnerable to the establishment of an unwanted electrochemical corrosion cell.

1.2.6.1 Cathodic Delamination

The establishment of an electrochemical cell, within an under-film defect, could lead to two different types of failure mechanism, the first of which, cathodic delamination, which is shown schematically in Fig. 1.8. The other is anodic dissolution (Equation 1.1), which occurs at the original defect, is coupled to the cathodic reaction (in this case reduction of oxygen) at the delamination front, via an electrolyte layer which ingresses under the coating resulting in detachment. The oxygen reduction reaction (Equation 1.4) produces hydroxyl ions, raising the local pH and attacking the bonds between the metal and coating (27). The film is also attacked by intermediate reaction products that produces a hydrogel allowing for further ingress of electrolyte through this front. The diffusion through the hydrogel can be rapid, but is slower than aqueous diffusion (28). It was discovered that the formation of the galvanic cell was stimulated by the migration of cations from the defect site (29) and Auger analysis has been used to show the presence of anions (from the external electrolyte) within the defect zone (28).
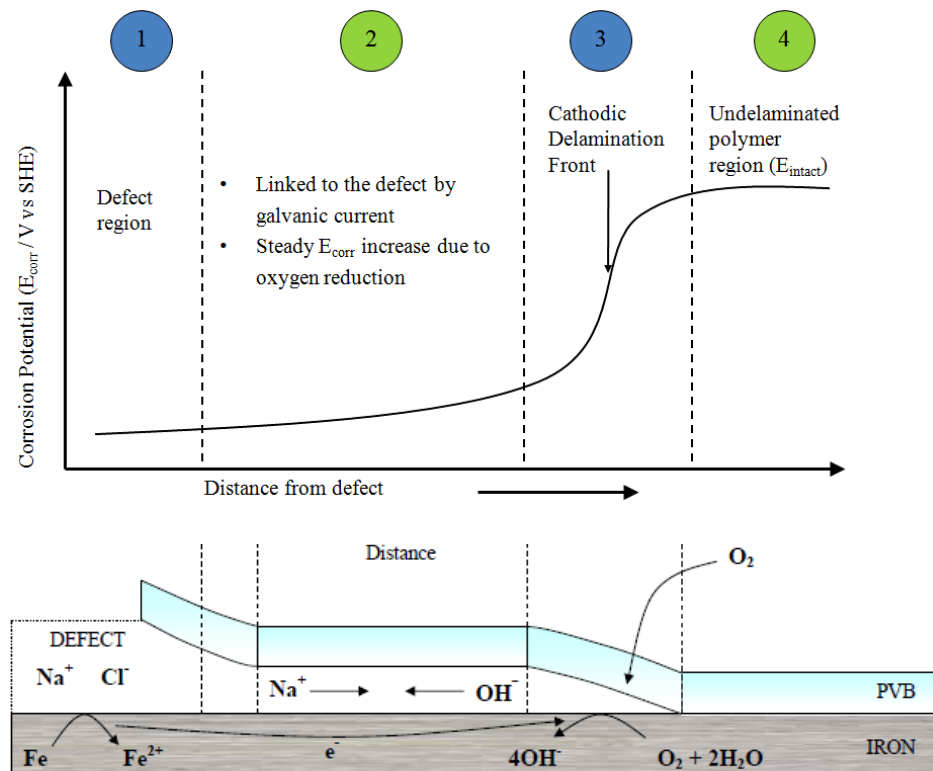
Fig. 1.8 Schematic diagram of E_{corr} measurements in the delamination cell.

A breakthrough method of studying the delamination of the polymer coating from the metal substrate is via the scanning kelvin probe (SKP). The SKP enables free corrosion potential at the metal surface to be measured through an intact paint film. Fig. 1.8 shows a typical E_{corr} profiles

obtained during the delamination process. Four distinguishable phases can be identified. They are:

1. The defect: where anodic metal dissolution occurs
2. Region of potential increase gradient which results from ohmic resistance to the galvanic current which flows through the under-film electrolyte to the delamination front
3. Delamination front: observed as a sudden jump in potential, and the location for the ORR which is responsible for the loss of coating adhesion
4. Intact interface which is defined by the potential plateau

1.2.6.2 Filiform Corrosion (FFC)

Filiform corrosion, a type of atmospheric corrosion, was first documented in scientific literature in 1944 by Sharman when fibrils were observed on lacquered tobacco cans (30). The thread-like corrosion product deposited under the organic films is mostly recognised for affecting organically coated aluminium and steel (iron) substrates. Filiform corrosion is mainly superficial with the main consequence being aesthetic, as shown in Fig. 1.9. This alone is unacceptable within the organic-coated metal industry product market, but nevertheless, this mode of corrosion can lead to more serious, structural issues. For instance, in the aeronautical industry, planes that operated in tropical atmospheres experienced corrosion on the rivet heads and at the edges of the aluminium sheets. This progressed to cracking in the paintwork due to flight vibrations resulting in the progression of FFC leading to corrosion in crevices surrounding the rivets. This resulted in crack development in highly stressed zones from FFC trails (31). Danger therefore can arise from FFC developing undetected underneath a lacquered coating. It is therefore of paramount importance that the substrates have resistance to this mode of corrosion if the product is used in environments where it can occur.
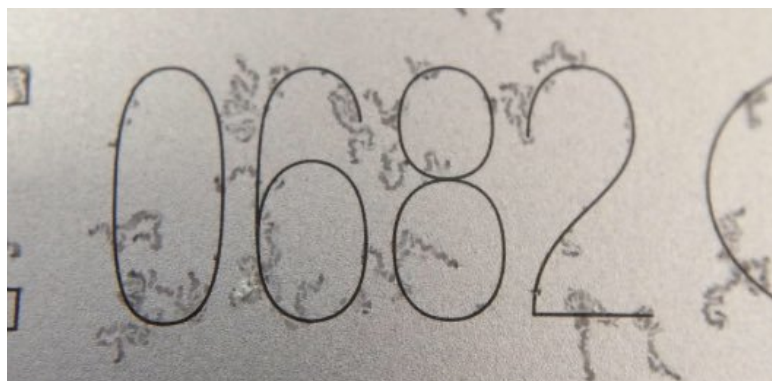
Fig. 1.9 Photography of filiform corrosion as seen on aluminium alloy iPhone 6S housing. Credit to Mike Rundle.

Initiation of FFC is caused by infiltration of soluble ionic species, such as chloride ions, at a defect which exposes the underlying substrate. A range of anions have been shown to initiate

FFC on iron. It is stipulated that a relative of humidity of 60-95 % is required for FFC to occur and where the RH is close to the saturation point (>95 %) leads to blistering instead of FFC (31). Table 1.1 shows the corrosion mechanisms expected at difference RH %. The availability of oxygen is also paramount for FFC as the corrosion process requires a redox reaction, therefore FFC does not occur in inert atmospheres (30). Temperature increases, to those above ambient, have been shown to increase the FFC growth rate (31). The phases and mechanisms of FFC will be discussed in the following sections.

Table 1.1 Under-film corrosion of steel at various relative humidities over H_2SO_4 solutions. Reproduced from (32).

Relative humidity (%)	Type of under-film corrosion	Width of filiform	Type of active head	Corrosion rate	Colour of final corrosion products
0 – 65	None	-	-	-	-
65 – 80	Filiform	Very thin	Very deep "V"	Low	Light yellow
80 – 90	Filiform	Wide	Shallow "V"	Medium to high	Rust colour
93	Filiform	Very wide	Flat or double "V"	High	Brown and black
95	Mostly blisters; scattered filiform	Very wide	Flat or double "V"	High	Yellow, brown
100	Blisters	-	-	Initially high, decreases rapidly	Rust and black

1.2.6.2.1 Filiform Corrosion Mechanism: Phase 1

It was shown by McMurray et al (33) that, on iron substrates, a phase of cathodic disbondment of coating precedes FFC, alongside ingress of group (I) Cl salt electrolytes to a penetrative defect. Fe^{2+} cations produced from the corrosion of iron migrate to the cathodic site, reducing their concentration around the defect. In comparison, the Cl⁻ anions which stay local to the defect

balancing the charge produced by the dissolution of iron to release Fe^{2+} cations. Naturally the group (I) cations at the cathodic delamination site are consumed and phase two of FFC begins due to the Fe^{2+} and Fe^{3+} chlorides at the defect.

Cathodic disbondment is not observed in the case that $FeCl_2$ is used to initiate. Instead, a layer of thick, dark brown precipitate was observed at the defect. It was suggested, through contact with atmospheric O_2, Fe^{2+} cations are oxidised to Fe^{3+}. It is known that the precipitation of an insoluble solid $Fe(OH)_3$ is the result of a tendency of Fe^{3+} aqua cations to undergo hydrolysis and produce a series of mono- and polynuclear hydroxyl-complexes. The absence of the cathodic delamination phase prior to the onset of FFC can be attributed to polyvalent Fe^{3+} aqua cation being unable to carry current through the alkaline under-film electrolyte layer. Nevertheless, after 40 h the initiation of FFC was observed and filament propagation rate was similar to those initiated by other group (I) chloride salts (33).

1.2.6.2.2 Filiform Corrosion Mechanism: Phase 2

The mechanism of the second phase was established by Kaesche (34) and further ratified by Ruggeri and Beck (35). The delamination of the coating during FFC is ascribed to an anodic mechanism. It is postulated that the filiform filament is made up of an active electrolyte-filled head composed of both aggressive Cl^- anions and metal cations. The tail is made up of an inert dry and porous corrosion product. A low pH (1-4) is present in the leading edge of the head due to the cation hydrolysis, whilst the back of the head has a much greater pH, with readings as high as pH 12 being recorded an iron substrate (30).

The initiation of FFC is likely caused by osmosis due to humidity restraints in which it operated, greater than 65% relative humidity (36). When the soluble salt ions contained within the electrolyte have a high affinity for water and electrolyte access in the defect forms a small liquid aggregate. As molecules build up under the film, liquid continues to form and further liquid is retained due to the vapour pressure of the concentrated electrolyte (37). Anodic dissolution then releases Fe^{2+} into solution along with a local decrease in oxygen concentration. This low oxygen concentration, as in a differential aeration cell, leads to oxygen depleted area assuming the anode and the surrounding area becoming cathodic. The tail allows oxygen to be passed to the head due to an O_2 concentration similar to air (210ml/L) (37), the front of the head becomes the anode and the tail the cathode, allowing the head to anodically undermine the coating and further spread the filaments via differential aeration

A gradient exists between the front and the back of the filament head due to anion migrate to the front and the cations migrate to the back (33). The Fe^{2+} formed in the oxidation of iron (Equation 1.18) at the front of the head then migrates to the back of the head. The higher concentration of oxygen at the back of the head causes the iron to be reduced further, via Equation 1.9.

$$Fe_{(s)} = Fe^{2+}_{(aq)} + 2e^-$$
<div align="right">1.8</div>

$$4Fe^{2+}_{(aq)} + O_2 + 2H_2O = 4Fe^{3+}_{(aq)} + 4OH^-$$
<div align="right">1.9</div>
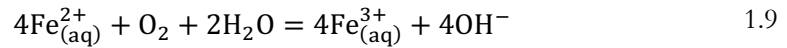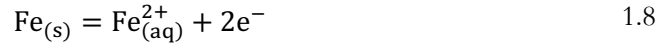
A 'V', shown in Fig. 1.10, exists between the boundary between the ferrous and ferric ions due to a characteristic colour change from anodic to cathodic regions.
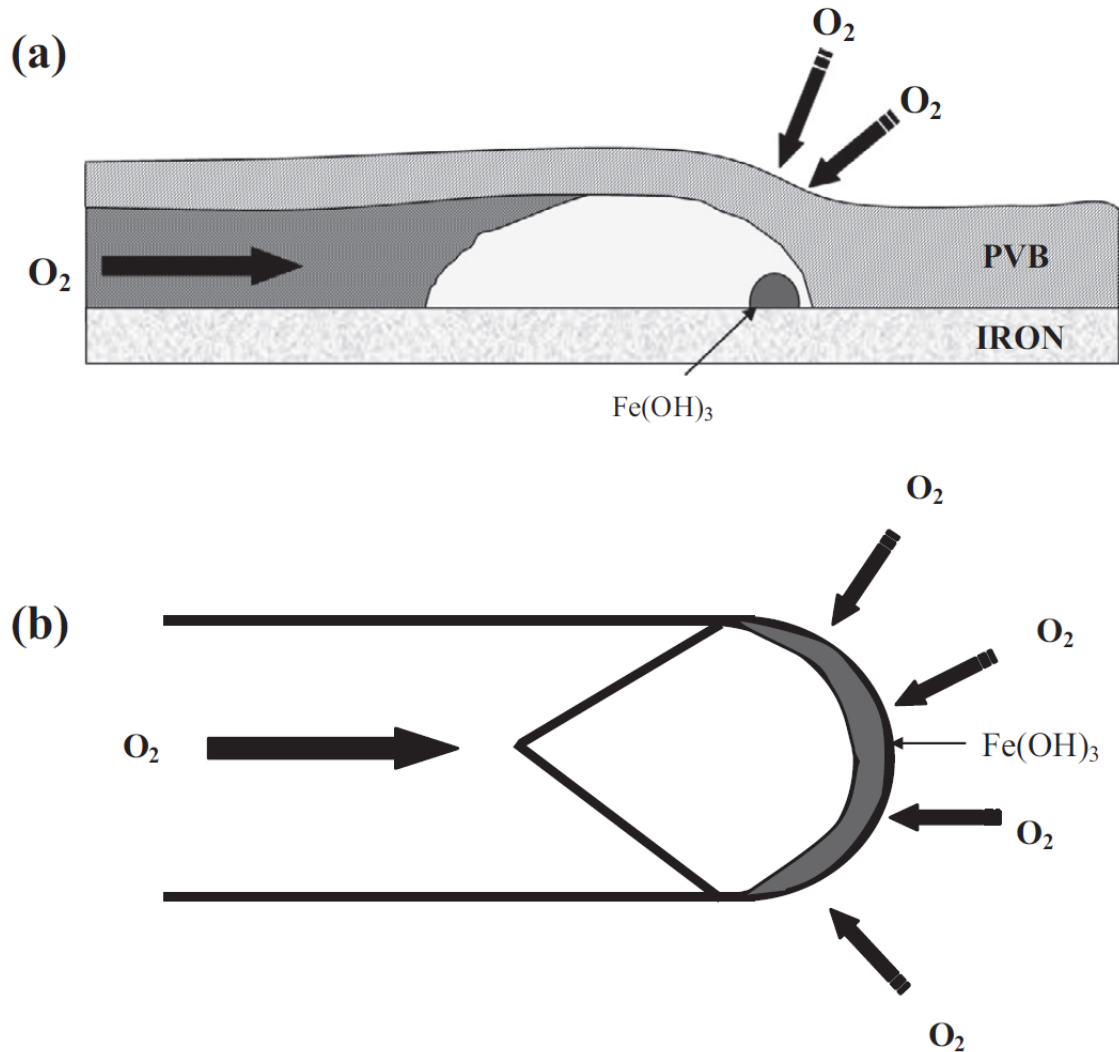
Fig. 1.10 Schematic diagram of (a) side-view and (b) top-view of a filament of FFC illustrating the mechanism of anterior ring formation. O2 diffuses through the PVB coating and the filament head droplet at the highest rate where the head droplet is thinnest; at the periphery of the droplet.

1.2.6.2.3 Alternative FFC Mechanism

As with everything in life, these postulated mechanisms have been disputed and this section will describe another mechanism. The opposing theory suggests cathodic activity at the area just before anterior edge (37,38) or even at a narrow region ahead of the filament head (35,36,39). Funke theorised that a cathodic region, lying ahead of the filament head, shown in Fig. 1.11,

allowed FF growth by the formation of under-film hydroxyl ions. once the cathodic region had become large enough, it would then merge with the filament head, leading to migration of hydroxyl ions to the anode while electrolyte cations from the anodic region migrate towards to cathodic head. This results in a polarity reversal due to the migration of anions and cations in opposing directions. This process is said to repeat itself in and incrementally grow.
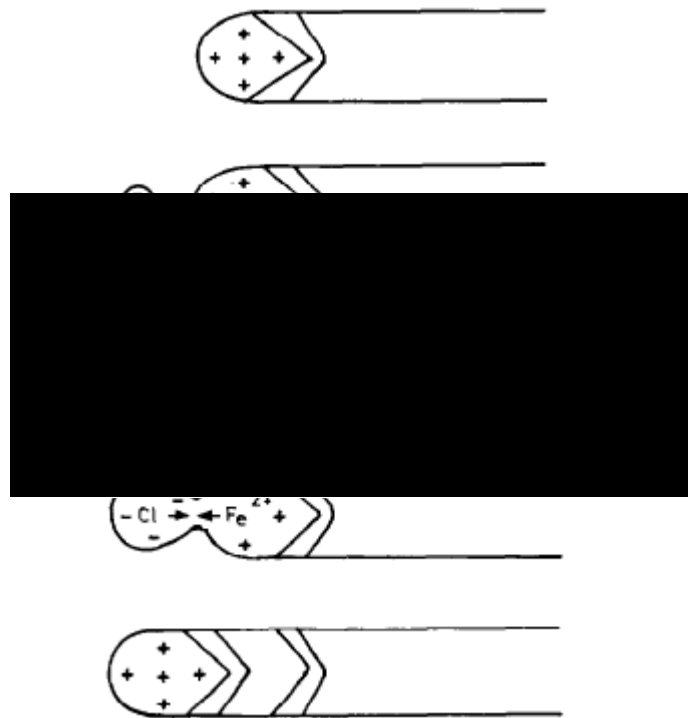
Fig. 1.11 Schematic diagram illustrating the cathodic mechanism of delamination at the filament head from proposed by Funke (37).

This hypothesis has various counter arguments that point to the inconsistencies in the model pertaining to the asymmetric separation observed between the corrosion cells anodic and cathodic regions. Ruggieri and Beck also illuminated that the mechanism requires that the ionic current must flow through the coating to get from the anode, to the anterior cathodic region (35). The resistance of the under laminated coating would thus limit the cathode size. The limited evidence of this preceding region also does not help to prove its existence. Williams et al. concluded that although the filament propagation rate is not the rate determining step in the FFC of iron, it should be considered as a major factor in the filament head electrolyte (33).

1.2.6.3 Accelerated Weathering

The steel industry utilises accelerated weathering to duplicate and investigate the long-term degradation effects on materials in different real-world environmental conditions, such as rainfall, temperature, humidity and exposure to ultraviolet (UV) radiation (40). The results of these tests are then used to estimate the service life of materials and to issue warranties for these products by the manufacturers. These methods include wet dry cycling (using ISO 9927 (41) and ASTM B117 (42) techniques) and cyclic immersion (mimicking rainfall and/or marine environments), amongst others (15,26).

1.3   Corrosion Testing

To study corrosion in the laboratory, equipment is used to measure the current and potential values associated with a corroding system. Other tests are also used, for instance time-lapse microscopy, which aid the quantitative evidence from electrochemical results, with qualitative images.

1.3.1   Time-Lapse Microscopy

Time-lapse Microscopy (TLM) is a technique whereby high-resolution microscopic images are acquired periodically allowing visualisation of the morphology of a reaction or event. TLM has been utilised in many fields, from studying embryo growth (43,44) to the progress of corrosion on a microstructural level (45–47). The images obtained allow us to visualise phases in which corrosion initiates, regions at which corrosion product is formed, if the corrosion continues under the product and even if the corrosion product dissolves and then precipitates again. The information we get from this can then be coupled with electrochemical experiments to provide a more complete picture of the mechanism. Sullivan et al. (46,47) demonstrated, using TLM, that zinc-magnesium-aluminium (ZMA) alloy coatings, when exposed to NaCl electrolyte, initially corrode preferentially in the eutectic phase, specifically the $MgZn_2$ lamellae. The dissolution of this phase leads to the de-alloying of both the binary and ternary eutectic phases. The images also demonstrate the build-up of corrosion product ring, and using phenolphthalein indicator showed the corrosion product forming on the interface between region of pHs below and above 8 (46).

1.3.2   Electrochemical testing

1.3.2.1 Open Circuit Potential (OCP)

The open circuit potential experiment allows the measurement of the free corrosion potential in a set environment. The setup is found in the experimental chapter and makes use of a working electrode and a reference electrode, in this case a KCl saturated calomel electrode (SCE). The time dependent potential is measured with respect to the reference electrode. These results can be used to provide information regarding the relative thermodynamic susceptibility of different

materials to corrosion. Similarly, the behaviour of the same material can be compared in a variety of electrolytes and under different conditions.

1.3.2.2 Zero-Resistance Ammeter (ZRA)

Zero-resistance ammetery (ZRA), is a method of gaining the currents that flow between two electrodes that are galvanically coupled with no impressed potential. This has been used previously to determine the current between Zn based alloys in electrical connection with carbon steel in an artificial rainwater electrolyte (48). It was found that most alloyed materials had a higher galvanic current compared to Zn, therefore providing greater protection to the steel. This current dropped by an order of magnitude over a period of 4 weeks, likely due to the passivation of the zinc alloy corrosion product. It also demonstrated that Al additions increased the galvanic current.

1.3.2.3 Potentiodynamic Polarisation

Potentiodynamic polarisation sweep utilises a three-electrode submerged in the electrolyte (23), as shown in the experimental chapter, in order to characterise the relative performance of metals or alloys in similar conditions. The initiation and propagation of the corrosion and the breakdown and reestablishment of passive films can also be ascertained. The working electrode is polarised from its free corrosion potential to cathodic or anodic over potentials and the current is measure. The results are then plotted on an Evans style axis of E vs $\log_i$. A materials ability to passivate and the extent to which it is able to passivate can be deduced from analysis of the anodic polarisation, also known are the anodic arm. The graph in Fig. 1.12 shows the $E/\log_i$ plot for a metal in a mild environment. The metal is not in a passive state at its free corrosion potential, labelled B, but does display passive behaviour at potentials greater than G. From potential B and higher, they are anodic, and below B, they are cathodic.

As the working electrode is swept positively away from the free corrosion potential (E_{corr}) the corrosion current rate increases, during the activity region (shown in Fig. 1.13), as the metal is oxidised, up until point G. This potential is noted as E_{pp}, the passivation potential. The formation of the protective film causes a sudden reduction in the corrosion current density from G to J. The low current is then maintained at this rate between potentials J and P. At P, sufficient energy is available to cause the protective film to breakdown, this is also known as the critical potential E_c, and can be especially parameter for assessing pitting properties of materials. When the potential is increased even further, the current becomes greater and greater as the corrosion begins to propagate, this is called the transpassive region.
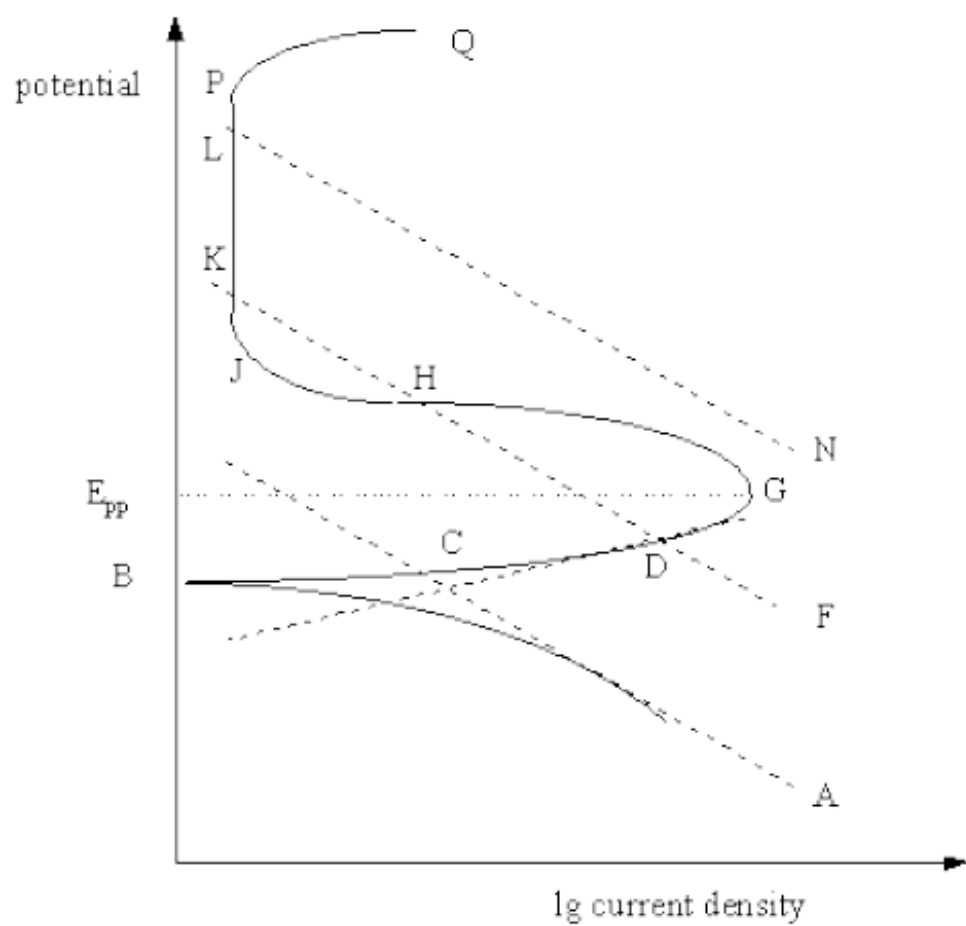
Fig. 1.12 Schematic potentiodynamic polarisation behaviour of some passivating metals. Demonstrating a general polarisation plot containing theoretical cathodic processes.
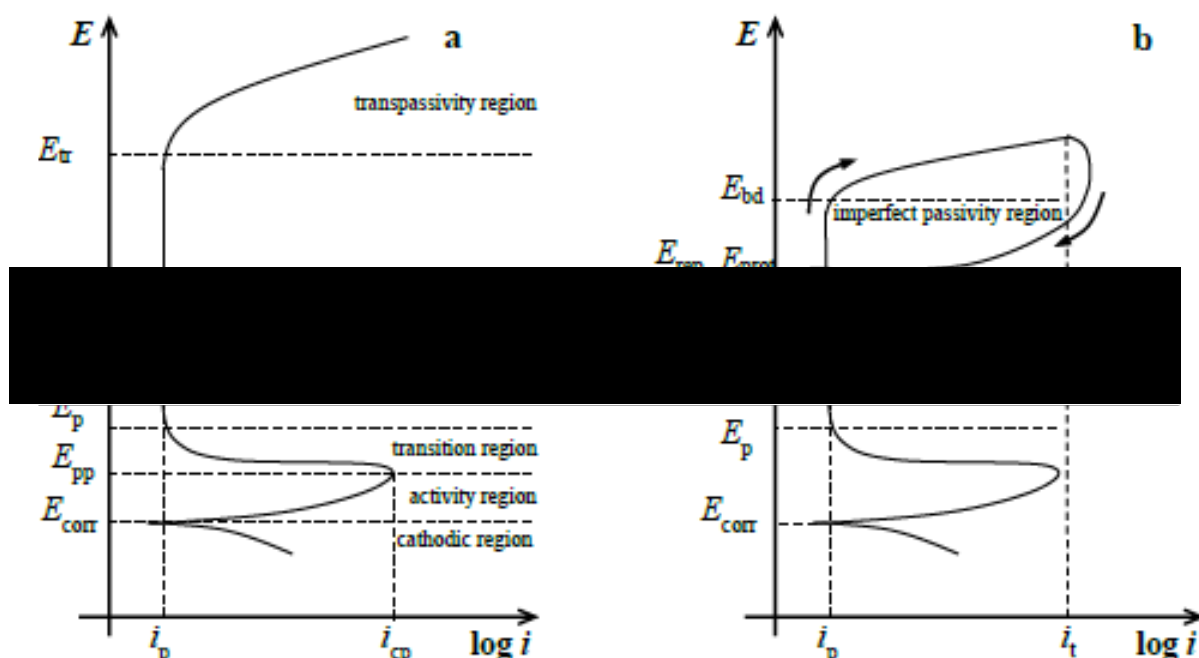
Fig. 1.13 Schematic representation of a generic anodic polarization curve (a) with the characteristic regions. Cyclic polarization curves (b) can also be recorded in the case of localised corrosion to assess pitting behaviour over a period of time (49).

Thomas et al. (50) performed potentiodynamic experiments on pure zinc in 0.1 M NaCl across a range of pHs (Fig. 1.14). They showed that the E_{corr} of zinc to be similar for pH 4, 7 and 10 (~ -1.05 V vs. SCE) and lower at pH 13 (-1.4 V vs. SCE), a trend that is consistent with the thermodynamically predictions from the Pourbaix diagram (Fig. 1.3). The i_{corr} is similar for both pH 7 and 10, at around 1.1×10^{-7} A.cm^{-1} but large increases in i_{corr} were observed at the extremes of pH investigated. Passivation was also observed in the sample at pH 13.
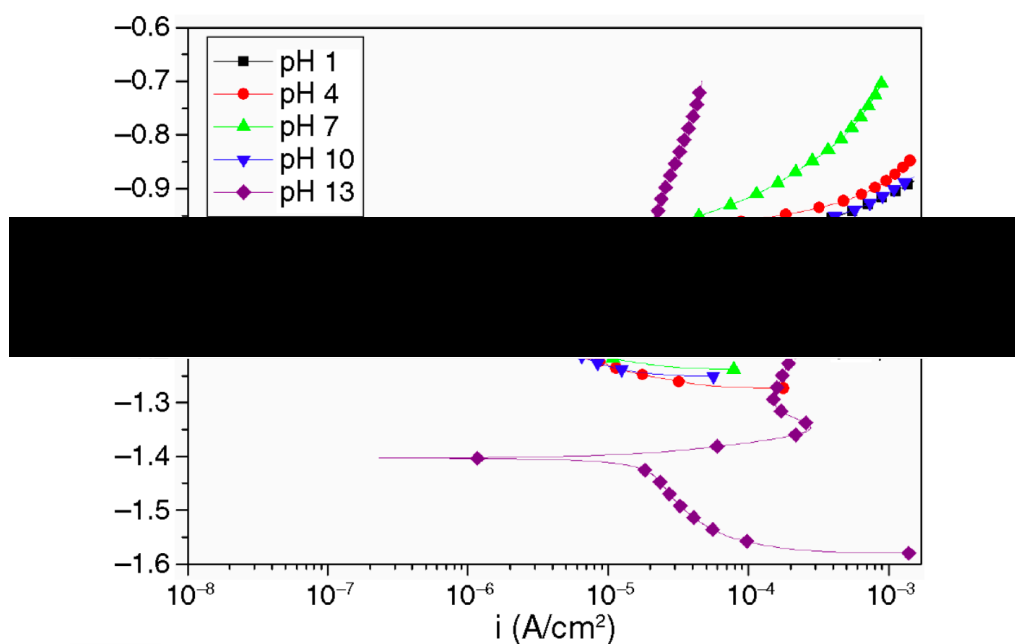
Fig. 1.14 Polarization curves of zinc in quiescent 0.1 M NaCl solution with pH 1, 4, 7, 10, and 13 (50).

1.3.2.4 Rotating-Disk Electrode (RDE)

The rotating disk electrode apparatus is utilised to control the movement of products away and reactants to the working electrode during the corrosion. The material of interest is designated as the working electrode and encased by an insulating material with a greater diameter (51). As the disk is rotated, forced convection occurs. The electrolyte accelerates towards to the surface of the disk, shown in Fig. 1.15a., and upon contact it is radially dissipated outward into the bulk solution. To simply the mass transport a 1D system is employed, with the direction of interest being normal to the electrode face.

The RDE allows both the control of migration and convection so the reaction at the electrode must be limited by mass transport and the rate of diffusion to the surface through the diffusion layer. The mass transport model is the Nernst diffusion model.

The Nernst diffusion layer model is used to define the mass transport of electroactive species, present in the electrolyte, to and from the electrode surface. Fig. 1.16 shows the solution is split into two regions. The first region is the bulk solution, which is strongly mixed, so maintains a constant concentration. The second is the stagnant boundary layer, of thickness δ, where diffusion is the only mode of transport. This second region is comparable to the solution being uniformly and sturdily pumped towards the disk and subsequently decelerating towards it eventually having a zero velocity at the surface (51).

The extent of the boundary layer is calculated using the following equation:

$$\delta = 1.61 v^{1/6} D^{1/3} \omega^{-1/2} \qquad\qquad 1.10$$

Where ν is the kinematic velocity, D is the diffusion coefficient and ω is the rotation velocity. Due to the inversely proportional relationship of the thickness to the rotation speed, the greater the speed, the less thick the Nernst diffusion layer is (51).

The electrode potential governs the surface concentration of the reactant. At the free corrosion potential, the concentration at the surface is equal to the bulk. At high cathodic overpotentials the rate of electron transfer must increase to a high rate. As the surface concentration decreases the current will increase until the surface concentration of R drops to 0. At this point the reactants are being used up faster than they can be supplied by diffusion and the reaction rate is no longer controlled by the rate of electron transfer. The current will then plateau, this is known as the limiting current density, i_L (51). At this point the current is generally unique of the electrode material.

The Levich equation is used to calculate i_L (52).

$$i_L = 0.62 n.F.D^{2/3} v^{-1/6}.c.\omega^{1/2} \qquad\qquad 1.11$$

Where n is the number of electrons that take place in the reaction, F is the Faraday's constant, D the diffusion coefficient, ν the kinematic viscosity, c the concentration of the active species and ω the angular velocity of the rotating disc.

Therefore Equation 1.11 can be expressed as

$$\frac{1}{j} = \frac{1}{j_d} + \frac{v^{1/6}}{0.62 n.F.D^{2/3}.c.\omega^{1/2}} \qquad\qquad 1.12$$

Equation 1.12 is the Koutecky-Levich Equation and can be used when both charge transfer and mass transport contribute to the overall reaction rate (52).
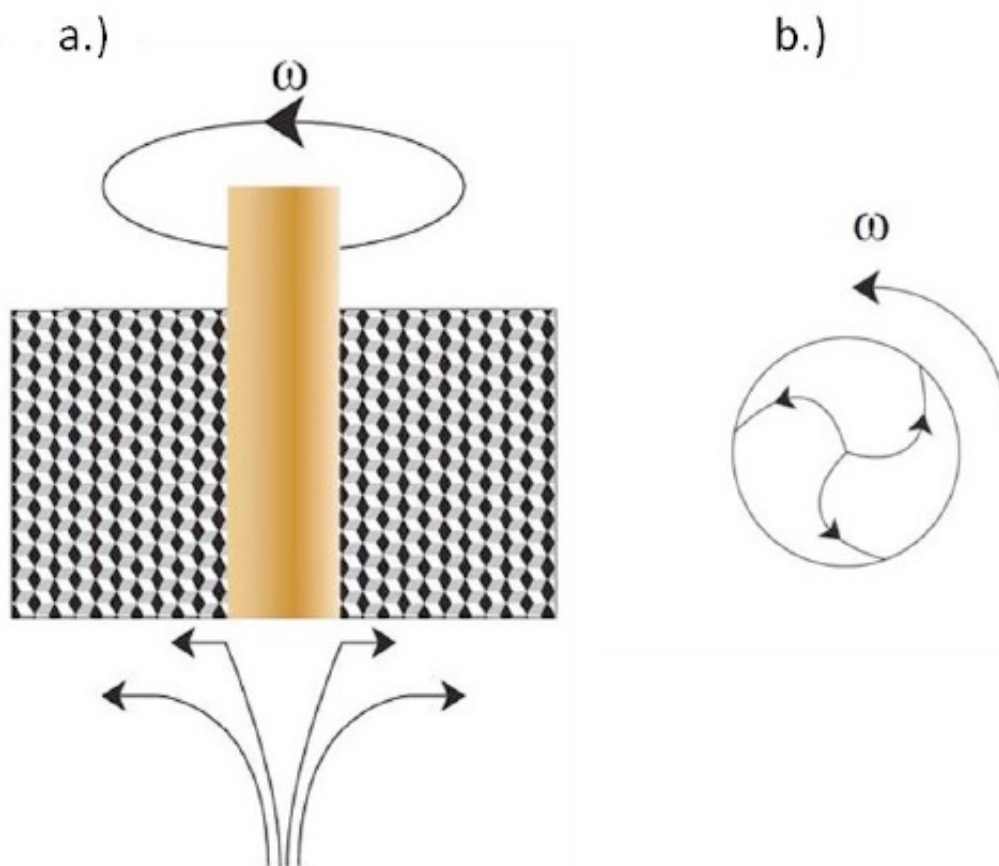
Fig. 1.15 Schematic diagram of flow patterns to the surface of the rotating disk (a) side view (b) top view.
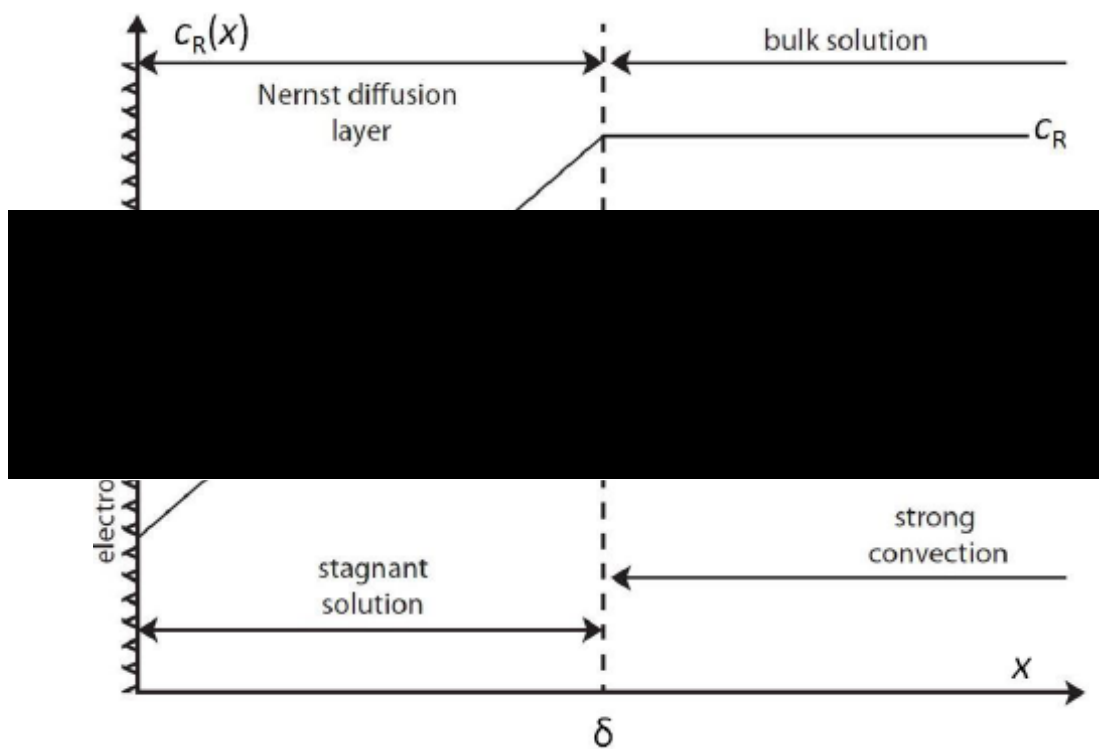
Fig. 1.16 Nernst diffusion layer model for the oxidation of R to O at the rotating disk electrode (51).

Dafydd et al. (27) employed RDE to determine the electrocatalytic activity of pure iron, pure zinc and the relevant zinc–aluminium intermetallics Zn22Al (β), Zn68Al (α) for the kinetics and mechanism of the ORR on zinc, Zn4.3Al and Zn55Al galvanized coatings in deaerated NaCl at pH 9.6. It was found that the Al content had little influence on the oxygen reduction kinectics and the lower reduction currents obtained in the case of pure zinc, compared to those observed in the case of Zn0.1Al and Zn55Al, was attributed to the electrocatalysis of trace iron present within the coating (27). Furthemore, the pure zinc samples exhibit current peaks at -0.91 V vs. SHE and -1.06 V vs. SHE during the anodic and cathodic wave respectively, behaviour consistent with an irreversible redox couple. Meanwhile, the aluminium sample showed no peaks in either wave, alluding to the currents coming solely from the oxidation and reduction reactions of zinc and no contribution from aluminium. This is due to the aluminium being covered with solid aluminium (hydr)oxide at potentials >ca. –2 V vs. SHE (53).

In other works, Zembura and Burzynska (54) performed RDE experiments on zinc in deaerated 0.1 M NaCl across a pH range. The results, shown in Fig. 1.17, demonstrate a $y=x^2$ shape in the rates of corrosion when the pH was taken from pH 1.6 to pH 13.3. Where the highest rate was seen at low pHs, the lowest rates were seen around pH 9 and with the rates increasing until pH 13.3, where they are an order of magnitude lower than pH 1.3. These results are agreement with the equilibrium thermodynamic predictions seen in the zinc Pourbaix diagram.
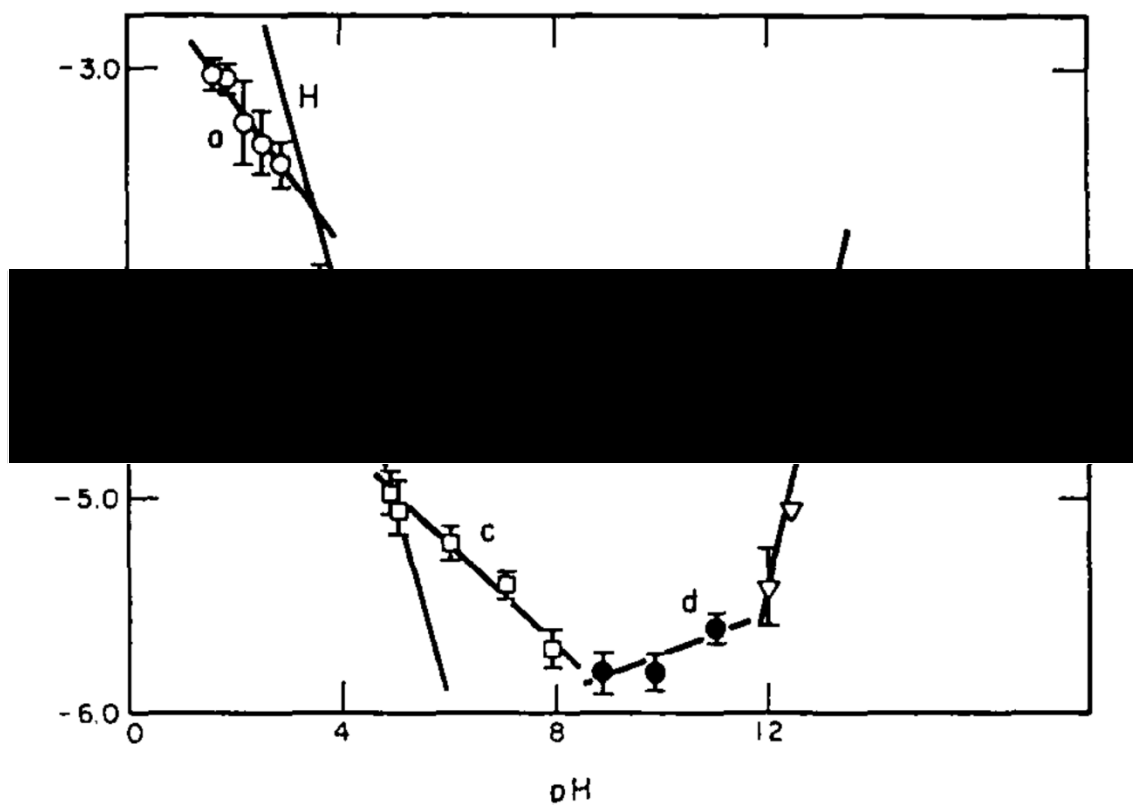
Fig. 1.17 The current density as a function of pH of the solution. Lines a, d - reaction control, b - intermediate control, c - two simultaneous reactions, e - diffusional control regime (54).

48

1.4 Hot Dip Galvanised Steel (HDG)

Hot dip galvanising (HDG) is the age-old process of zinc coating steel and the most widespread. This process involves the steel being fully immersed into a bath of molten zinc – 'dipping'. A rate of 200m/min can be achieved during large-scale production (55). The diffusion of both steel substrate and molten zinc results in the production of zinc and zinc-iron alloys on the surface of the iron or steel. It is the formation of the Fe-Zn intermetallic layer that creates the adhesion (55).

There are multiple reasons for zinc being used as a coating other than its obvious corrosion protection ability. It is soft and ductile so is easily formed when processed in industry (56). It can also be used in conjunction with other metals such as magnesium and aluminium to improve its corrosion resistance properties, much to the approval of industry.

The coating protects the steel in two ways: firstly, by physically barring the steel from the environment preventing water or oxygen contacting the steel, the second by cathodic protection. This is where, during corrosion, zinc preferentially corrodes with respect to the steel. This is due to where their nobilities lie in Fig. 1.5. The more noble a metal is, the increased likelihood it is to act cathodically (reduce oxygen), in a corrosion reaction. Conversely, the less noble a metal is, the increased likelihood it will act anodically (metal loss by dissolution). So, the steel will act as the cathodic site, reducing oxygen in solution, whilst the zinc will undergo metal loss. This metal ions that are lost into solution then react with hydroxide ions (produced by the cathodic reaction) to form metal hydroxide species that precipitate in the area of exposed steel, preventing the corrosion reaction from continuing.

Coating steel with zinc can be completed either by batch processing or continuous galvanising. For both processes the steel article needs to be correctly prepared for the galvanising process to be successful. This is done by three cleaning process shown below:

Degreasing → Pickling → Water Rinsing → Fluxing or Reducing → Hot-Dipping (55,57)

The resultant microstructures of the two different processing methods are shown in Fig. 1.18 and Fig. 1.19. The difference being in the size of the alloy region, with the batch method being far more visible as it has a greater thickness. The alloy region in the continuous casting can rarely be seen by optical microscopy.
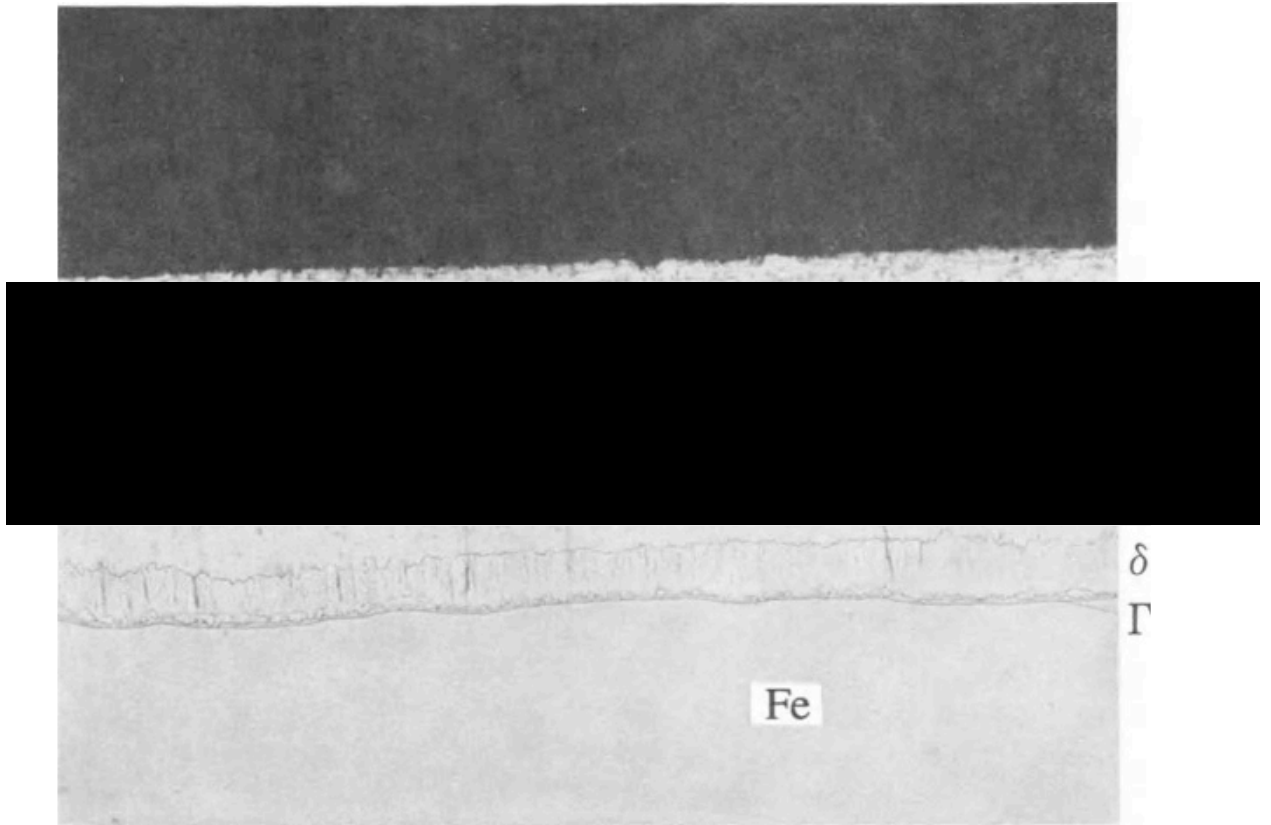
Fig. 1.18 Cross section of a batch-galvanised coating, illustrating the different layers of Zn, Zn-Fe and Fe (57). The phases labelled are outlined in Table 1.2.

Table 1.2 Characteristics of Fe-Zn Intermetallic Phases (58–62).

Phase	Formula	Iron Content (wt%)	Specific Gravity (g.cm^{-3})	Crystal Structure
αFe	Fe(Zn)	99.997		BCC
Γ	Fe$_3$Zn$_{10}$	21.0-28.0	7.36	BCC
Γ_1	Fe$_5$Zn$_{21}$	16.6-21.0		FCC
δ	FeZn$_{10}$	7.0-11.5		Hexagonal
ζ	FeZn$_{13}$	5.75-6.25	7.18	Monoclinic
ηZn	Zn(Fe)	Max 0.003	7.14	HCP
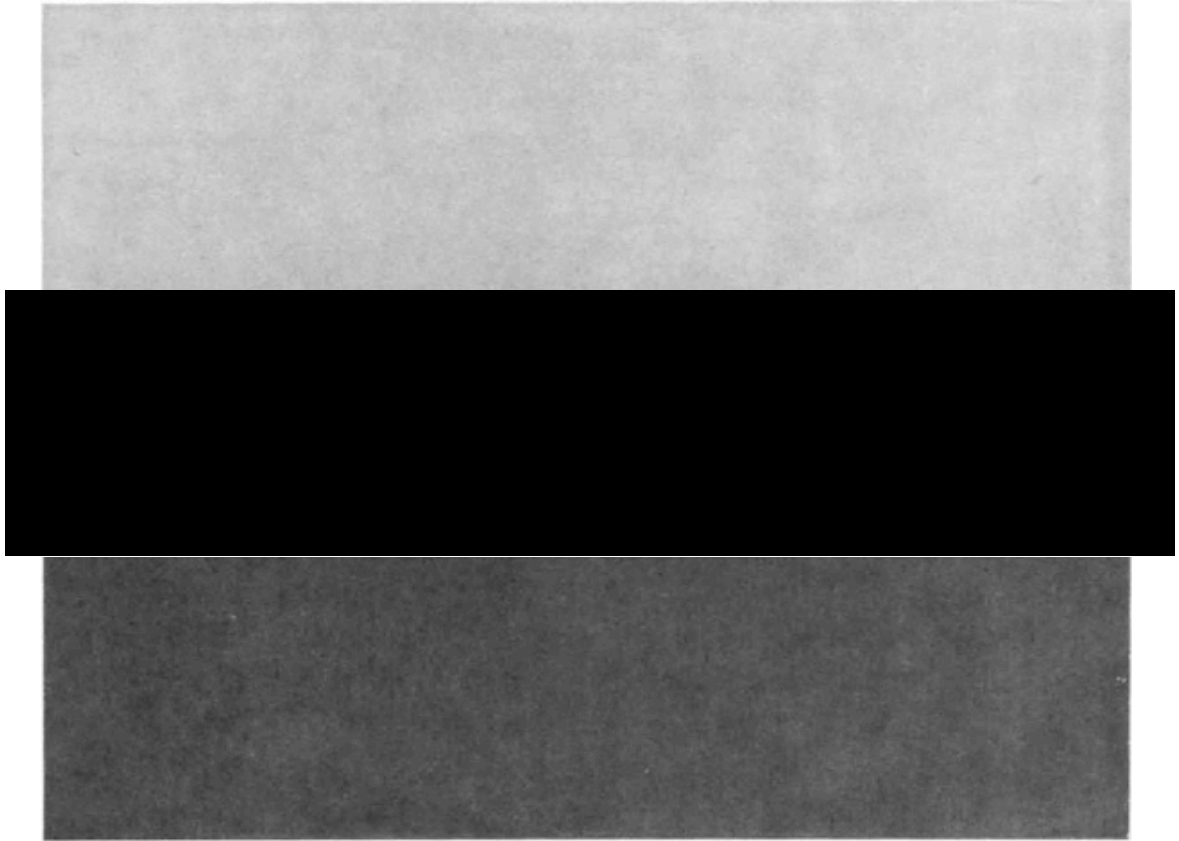
Fig. 1.19 Cross section of a continuous-galvanised coating (57).

1.5   HDG Process

There are several steps involved in the HDG process, (illustrated in Fig. 1.20). At the entry/front end of the process the joining steel coil is welded onto the tail end of the preceding coil and this is then fed into the accumulator. Accumulators, which are located at the entry end and exit end of the line, function to allow the continuous flow within the central process to operate at a continuous and high speed. For the ends of the coil to be welded, the accumulator will feed out the accumulated steel strip into the further stages of the process, allowing the strip at the start of the accumulator to be stationary for a period long enough to weld the next coil on. Once this process is completed the coil is then released into the line and the accumulator accumulates the steel strip in preparation for the next weld.
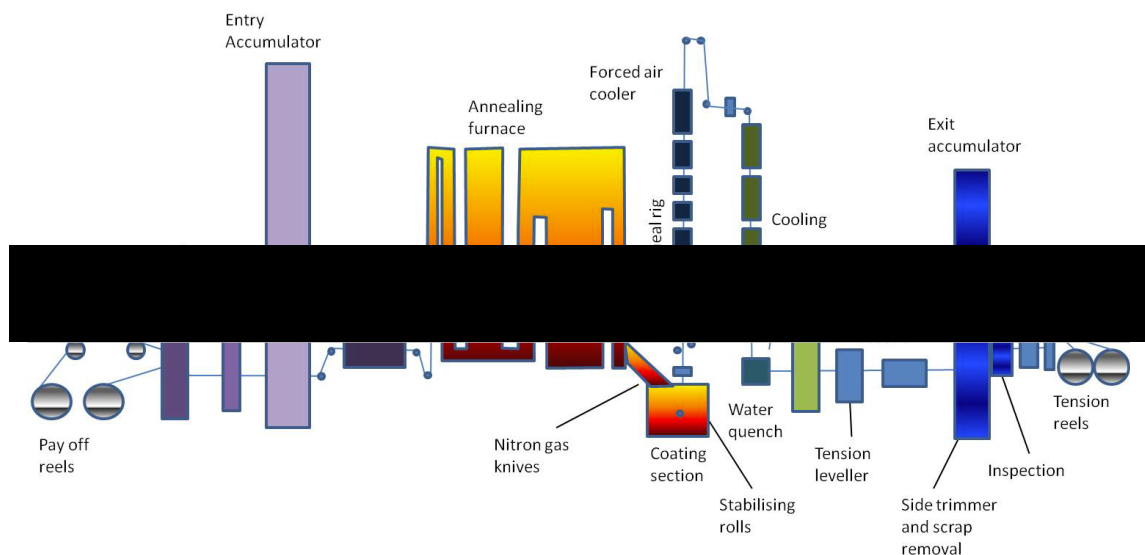
Fig. 1.20 Schematic of a continuous galvanising line (63).

For the zinc to adhere to the surface of the steel substrate, it needs to have a pristine chemically pure surface, free of dirt and surface oxides. Degreasing, which is the first cleaning step, involves removing the grease from the surface using an acid or alkali followed by a cold-water rinse. This is followed by pickling, where the steel is immersed in HCl at room temperature to remove rust and scale. This is performed to remove the surface oxides and to improve the surface wettability between the molten zinc and the steel. To activate the steel surface, the strip is passed through a reducing atmosphere of nitrogen and hydrogen. Once cleaned, the steel can be dipped into the molten zinc bath which is between 445-455°C (10). The immediate contact with the zinc promotes formation of an alloy layer which consists of an array of intermetallic phases (59,60). The steel exits the bath after 4-5 seconds where the air knives control the coating thickness. This is displayed in Fig. 1.21, which shows jets of air are aimed at the strip. This effectively removes excess zinc to give a uniform coating thickness and finish. The coating weight and spangle (Fig. 5) composition can be controlled by varying the distance and pressure (10,14). The strip is then fed into the temper mill, which controls shape, to remove yield point elongation and to impart a uniform surface on the sheet. It then enters the treatment section where, if desired, a passivation layer can be applied. The strip then enters into a cooling rig to solidify the coating at a controlled rate. This is followed by water quenching and then a bridle is used to maintain tension within the strip. To finish the process, the strip passes through the exit accumulator and is then inspected.

The finished product has a spangled look, each having a slightly different shade of grey, due to the differing orientations effecting the shade perceived Fig. 1.22. The samples studied in this thesis come out of a TATA continuous galvanising line. This process was patented in the 1920's by Sendzimir who used annealing instead of the pickling and fluxing processes, and this is still in use today (64).
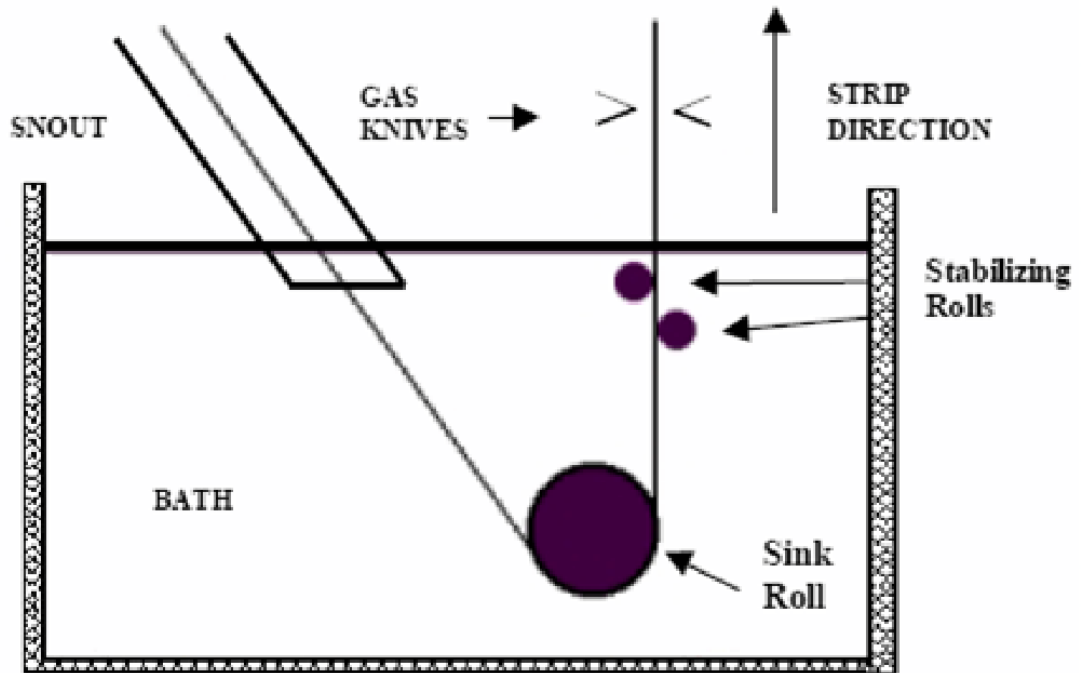
Fig. 1.21 Schematic of air knives.
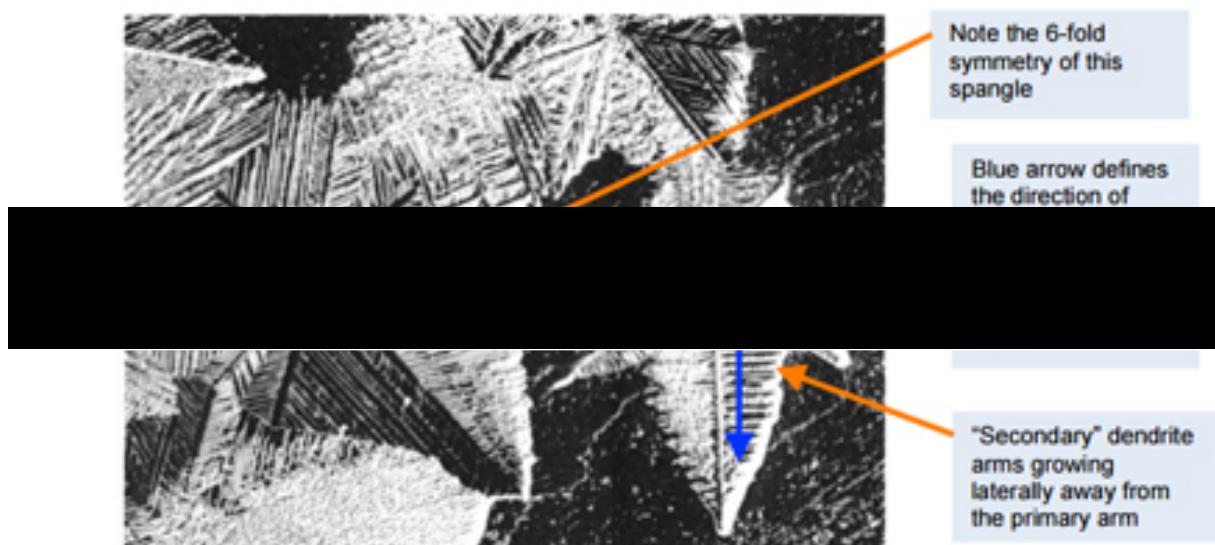
Fig. 1.22 Spangle Formation annotated image at 10x (65).

To further enhance the corrosion resistance and decrease the amount of raw materials (zinc) needed, Al has been added as an alloying element. Zn-Al coatings provide both sacrificial corrosion prevention afforded by zinc and the passive protective oxide of the aluminium. The aluminium additions spontaneously form an oxide layer when in contact with air which is a hard,

non-reactive surface film. The aluminium also improves the coating by forming an intermetallic layer which helps the adhesion of the coating to the substrate. The intermetallic layer formed between the coating and substrate is thinner than that on HDG,which increases formability and ductility. It is important that the melting point of the metal used as the coating is considerably less than that of the substrate, and if possible low enough to allow the substrate to retain characteristics from the work hardening procedure (66).

1.6   Solidification of Metals

Solidification is a process by which the metal transforms from a short-range order, non-crystallographic state to a long-range order, crystallographic one (67). There are two steps to the process; the first is nucleation during which ultra-fine crystallites,(nuclei of a solid phase) form from the liquid. The second step is growth, whereby where the solid nuclei grow due to atoms from the liquid attach themselves until no liquid remains (68).

1.6.1   Nucleation

This refers to the initial stage of formation of one phase from another phase. This can be from a liquid phase to a solid phase, or from an initial solid phase (α) to a second solid phase (β). The reason for this change in the former instance is due to the difference in energy state of the phases after reaching the transformation temperature (T_m – equilibrium melting temperature) This difference results in a driving force for this transformation (solidification) to take place (G_L-G_S)(67). and in the container and solid impurity particles act as catalyses for the nucleation reaction. This is known as heterogeneous nucleation. However, a liquid can be undercooled to a temperature below the T_m without any transformation when no solid particles are available for this nucleation and solid nuclei need to form from the liquid. This is called homogeneous nucleation

1.6.1.1 Homogeneous Nucleation
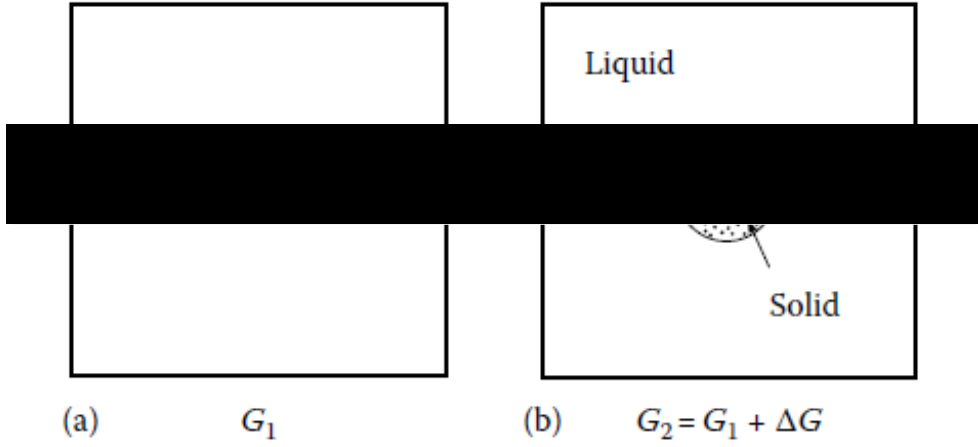
Fig. 1.23 Homogeneous Nucleation (67).

If a volume of liquid at a temperature $\varDelta T$ below T_m with a free energy G_1, Fig. 1.23a, and a collection of atoms form a small sphere of solid, Fig. 1.23b, the free energy of the system will change to G_2, denoted by equation:

$$G_2 = V_S G_v^S + V_L G_v^L + A_{SL}\gamma_{SL} \qquad 1.13$$

Where V_S is the volume of the solid sphere, V_L the volume of the liquid, A_{SL} is the solid/liquid interfacial area, G_v^S and G_v^L are the free energies pet unit volume of solid and liquid respectively, and the solid/liquid interfacial free energy is given by γ_{SL}. In the case that there is no solid present the free energy of the system is given by:

$$G_1 = (V_s + V_L)G_v^L \qquad 1.14$$

Using 1.13 and 1.14, the formation of a solid free energy change ($\varDelta G = G_2 - G_1$), can be written as

$$\varDelta G = -V_s \varDelta G_v + A_{SL}\gamma_{SL} \qquad 1.15$$

Where

$$\varDelta G_v = G_v^L - G_v^S \qquad 1.16$$

Due to undercooling $\varDelta T$, $\varDelta G_v$ is denoted as:

$$\varDelta G_v = \frac{L_v \varDelta T}{T_m} \qquad 1.17$$

where L_v is the latent heat of fusion per unit volume. This shows that below T_m, ΔG_v is a positive value so the free energy change due to the formation of this solid has a negative contribution as there is a lower free energy in the bulk solid. There is also a positive contribution as there is this creation of a solid/liquid interfacial free energy. This is all correct for sphere where γ_{SL} is isotropic. Equation 1.13 can now be denoted as

$$\Delta G = -\frac{4}{3}\pi r^3 \Delta G_v + 4\pi r^2 \gamma_{SL}$$

1.18

This free energy change is shown in Fig. 1.24. The interfacial term increases with rate r^2 whereas the volume free energy increases with rate r³. Initially the particle size is too small to reduce the overall free energy, meaning that a liquid state is conserved can to maintain a metastable state at temperatures below the melting point. The graph shows the maximum radius length for a liquid to maintain its metastable state, noted as r^*, the critical nucleus radius. If the $r < r^*$ then the free energy of the liquid can be reduced by dissolution of the solid. These nucleations are unstable solid particles and called embryos. If $r > r^*$, the free energy decreases if the solid continues to grow, these are known as nuclei. ΔG^* is the energy 'hump' that needs to be overcome.
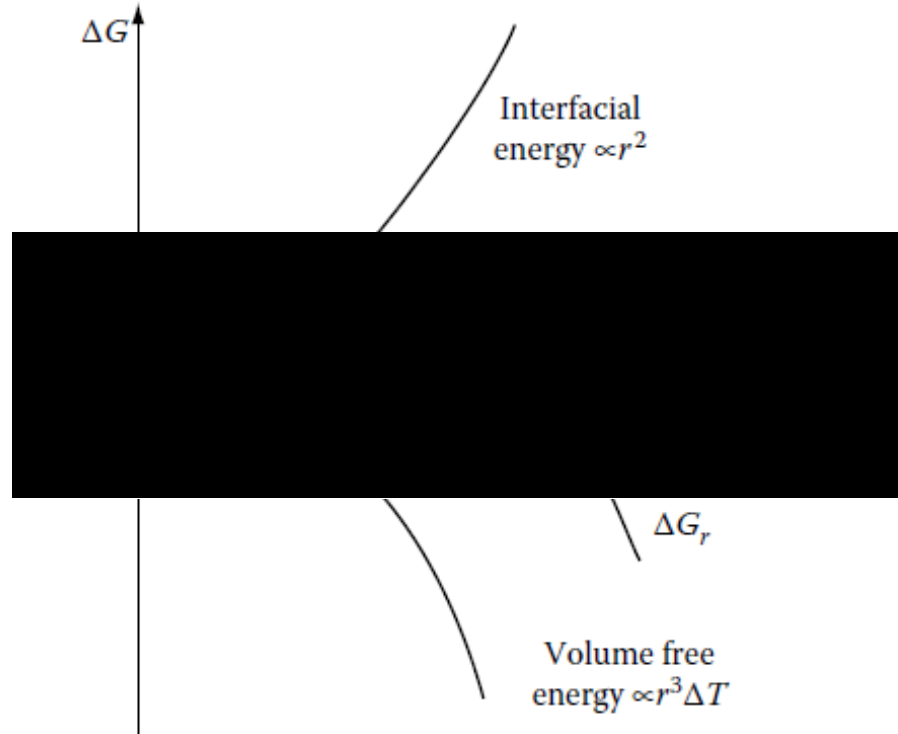
Fig. 1.24 The free energy change of a sphere of radius, r, during homogeneous nucleation (67).

56
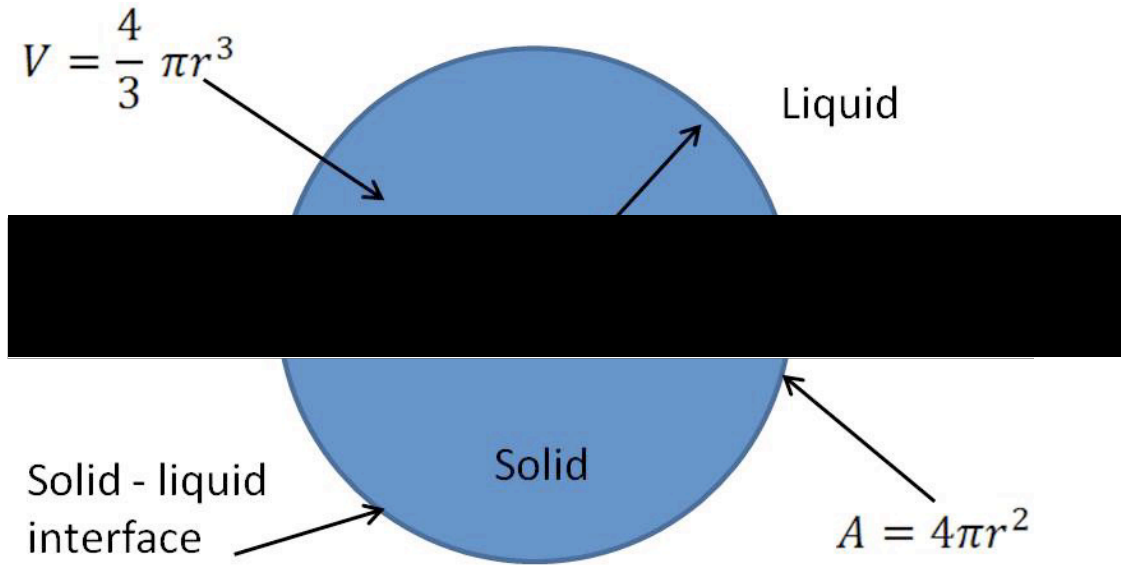
Fig. 1.25 Schematic of the interface between the solid particle in a liquid during homogeneous nucleation (63).

1.6.1.2 Heterogeneous Nucleation

The most common form of nucleation is heterogeneous nucleation (for example in a crevice or by contact with impurity particles), whereas homogenous nucleation is very uncommon. Consider an embryo forming in contact with a mould wall, or more topically on the steel substrate, such as depicted in Fig. 1.26. Assuming γ_{SL} is once again isotropic, it can be shown that the overall interfacial energy of the system is reduced if the embryo has the shape of a spherical cap with a 'wetting' angle θ (given by Equation 1.8 where, where γ_{ML} is the substrate/liquid interfacial free energy, γ_{SM} is the solid/substrate interfacial free energy and the values of the interfacial tensions γ_{ML}, γ_{SM} and γ_{SL} balance in the plane of the substrate)

$$\cos\theta = \frac{\gamma_{ML} - \gamma_{SM}}{\gamma_{SL}} \qquad 1.19$$

The γ_{SL} component remains unbalanced. This equation only provides the optimum embryo shape on the condition the mould wall is constantly planar. This is because over time the surface liquid

force would pull then mould surface upwards until all of the surface tension forces balance in every direction.
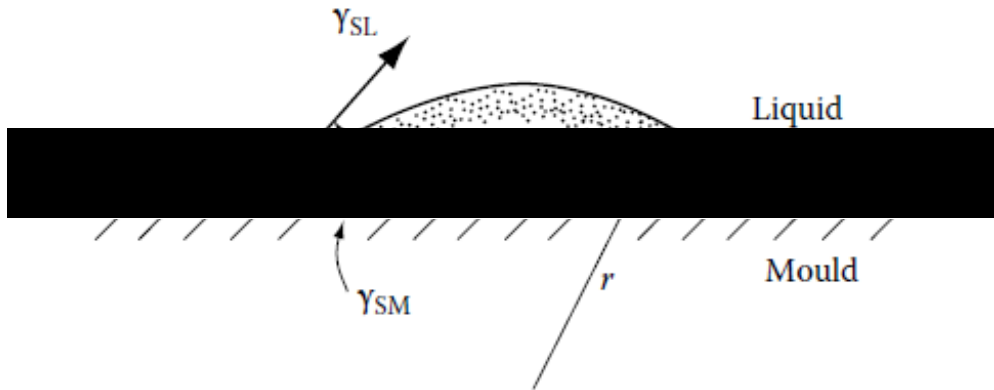
Fig. 1.26 Heterogeneous nucleation of an embryo cap on a flat substrate (67).

The radius has a curvature greater than the critical radius is formed with a small surface between the liquid and the solid. When sufficiently large numbers of atoms cluster on the surface producing a solid particle, they will not tend to re-join the melt. This is because the required radius of curvature has been formed, meaning less undercooling is required and that solidification is much easier (63).

1.6.2 Growth of a Dendrite

Dendritic, derived from the Greek word for tree, describes the shape of the microstructure. The growth is determined by the modes of transport for the heat that is generated during the solidification process and during the cooling of the liquid. Latent heat of fusion is generated locally during solidification and needs to be removed at the liquid solid interface before solidification can occur in the bulk. The heat during cooling is the specific heat and is the heat energy required to alter the temperature of a unit of mass of a material by a single unit degree.
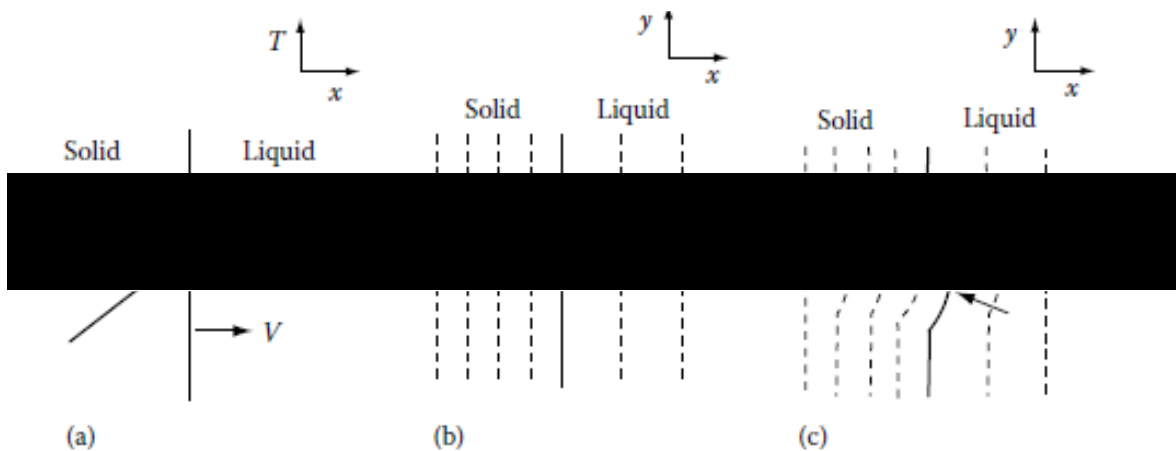
Fig. 1.27 (a) The temperature distribution during solidification when heat is extracted through the solid at the mould wall. Isotherms (b) for a planar solid liquid interface, and (c) for a protrusion (67).

In most cases the nucleation will occur on the wall of the mould wall as this is where the liquid will have cooled below the freezing temperature (T_m) as heat can be conducted away to the atmosphere. This is illustrated in Fig. 1.27. As the solid dendrite grows from the surface of the mould wall, the convection currents in the liquid can cause this primary dendrite arms to break off and float into the liquid, either re-melting or continuing to grow if the temperature of the liquid is low enough to permit further growth. Dendritic growth is made easier due to the heat conduction being possible in all 3 axes from the tip of the protuberance/the direction in which the dendrite is growing. The dendrite will also grow secondary and tertiary arms due to the ease of head conduction/growth, shown in Fig. 1.28. These dendritic arms always grow in certain crystallographic directions: e.g. ⟨100⟩ in cubic metals, and ⟨1100⟩ in HCP metals (67).
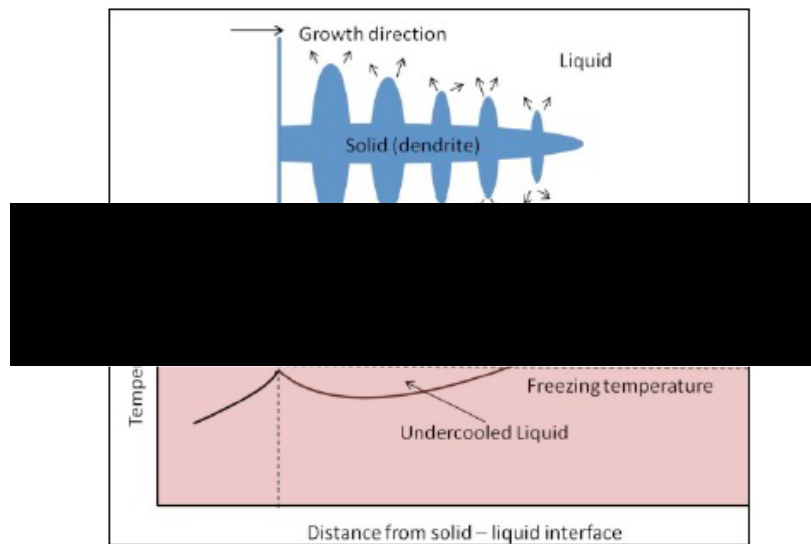
Fig. 1.28 The growth of a dendrite in an undercooled liquid via a protuberance on the solid liquid interface (63).

This growth is called thermal dendritic growth in a pure metal and dendritic growth when found in alloys. This is because not only does the conduction of latent heat need to be considered, so does the diffusion of solute from the dendrite during the solidification of the pure metal. This change is shown in Fig. 1.29.
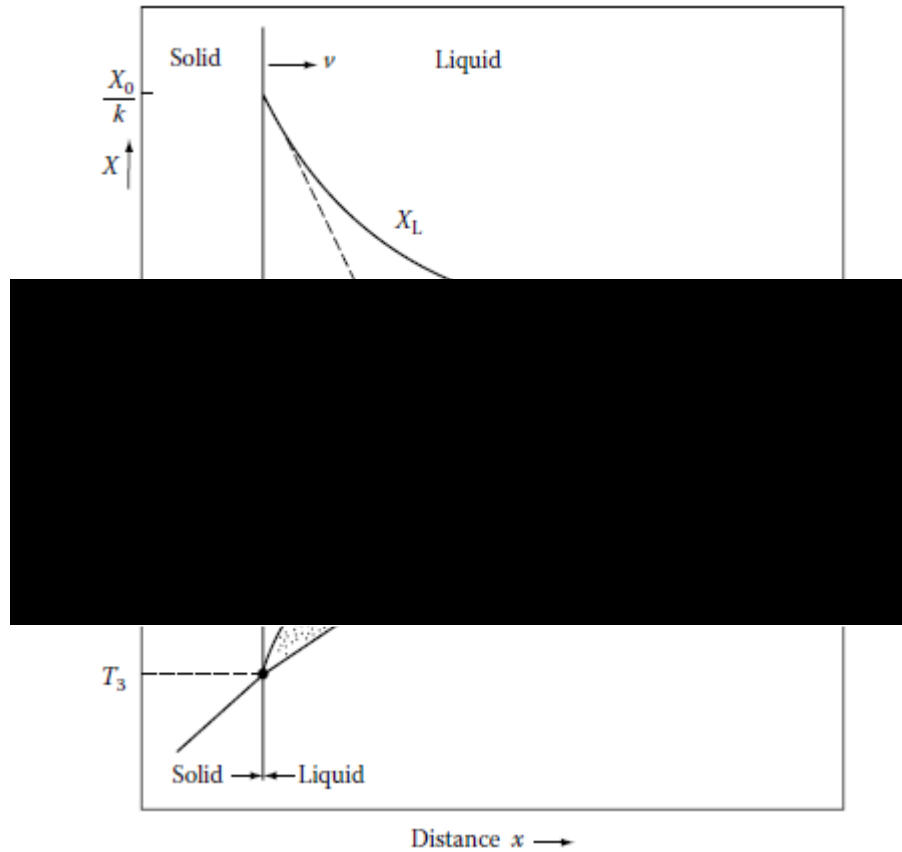
Fig. 1.29 The origin of constitutional supercooling ahead of a planar solidification front, (a) Composition profile across the solid-liquid interface during steady-state solidification. The dashed line shows $\frac{dX_1}{dx}$ at the solid-liquid interface, (b) The temperature of the liquid ahead of the solidification front follows line T_L. The equilibrium liquidus temperature for the liquid adjacent to the interface varies as T_e. Constitutional supercooling arises when T_L lies under the critical gradient (67).

1.7   Galvalloy®

Galvalloy® is an alloy development of HDG, with a composition of 95-96.4 wt% Zn and 5-4.6 wt% Al. This was developed with the aim of improving the galvanized steel corrosion resistance. In the 60s, ILZRO (the International Lead Zinc Research Organization) asked CRM (Centre for Metallurgical Research in Liège, Belgium) to produce a zinc based alloy with an Al content below 15 %, with a primary use of continuous casting for steel (69). Studies had shown that a maximum resistance to corrosion occurred with an Al composition of 5 %, which is the eutectic composition (associated   with   a   minimum   melting   point)   of   the   alloy,   as   shown   in
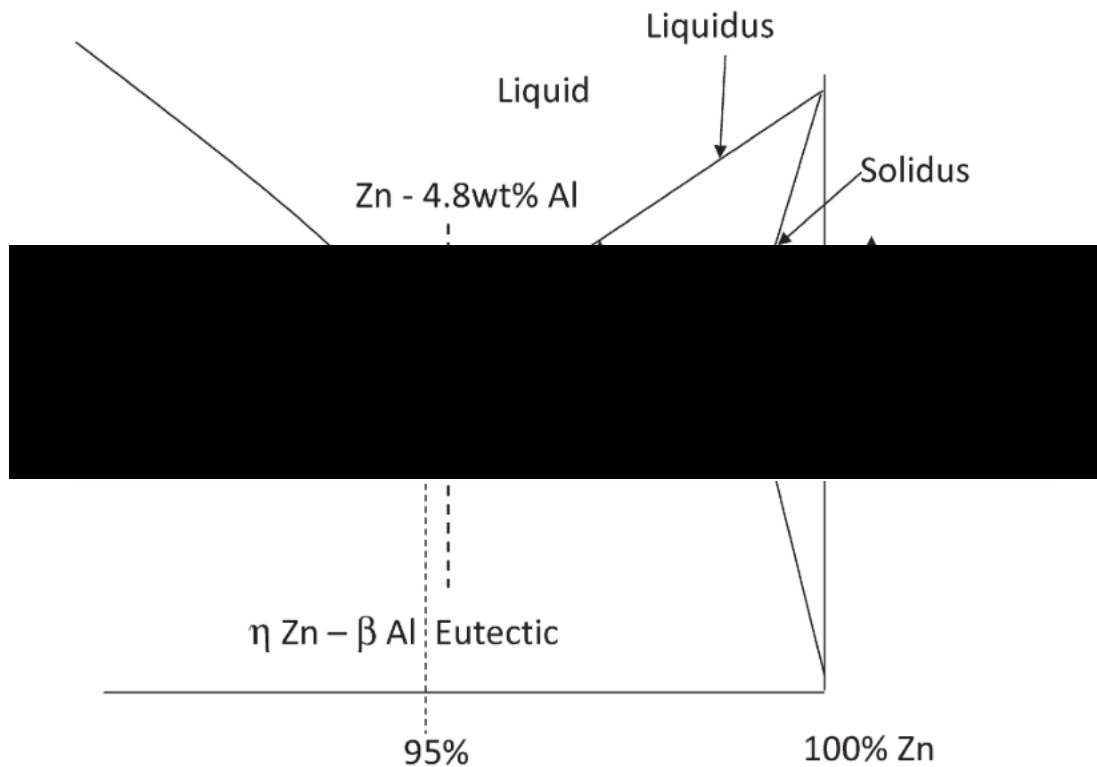
Fig. 1.30. A misch metal consisting of Cerium and Yttrium are included to improve wettability and fluidity within the molten bath which reduces uncoated portions of the substrate whilst not affecting the corrosion resistance. The name Galfan is a sobriquet come tradename coming from a portmanteau of GALvanized and FANtastic (69). The preliminary trials were conducted by CRM in 1978, with industrial developments starting in 1981 and have continued ever since especially in Europe and Japan.
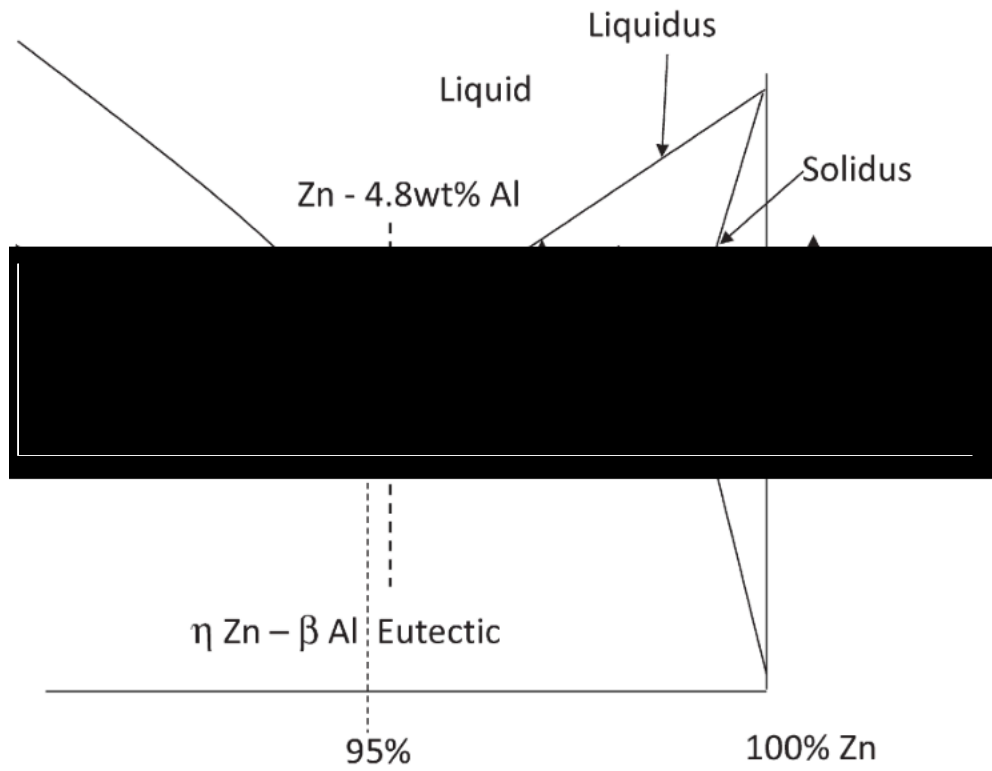
Fig. 1.30 Schematic portion of Zn–Al equilibrium phase diagram showing the freezing characteristics of the Zn–4.8 wt.% Al alloy (70).

1.7.1 Solidification and Microstructure of Galvalloy®

The microstructure of Galvalloy® consists of two phases, a Zn-rich η proeuctectoid phase encircled by a eutectic phase made up of β Al and η Zn binary lamellae.

During solidification, the pro eutectic Zn particles are the first to heterogeneously nucleate on the surface of the steel substrate. The solidification of the eutectic Zn & Al matrix follows and grows from the dendrites heterogeneously. It is calculated that the amount of the proeuctectic dendrite phase is 18 %, which indicates that this primary phase acts as a heterogeneous nucleation site for the eutectic phase to grow. These are nonreciprocal nucleating characteristics. This growth is detailed in a schematic Fig. 1.31 (10).

The surface structure is made up of nodules which have a diameter of around 4mm. These can be differentiated further into grains, which are either Zn rich dendrites or colonies of lamellae of alternating layers of β Al and η Zn Fig. 1.32. As opposed to the microstructure associated with a HDG cross section, (formed in a molten bath temperature of 420-440CC), the intermetallic layer is only 5µm thick and hard to detect by eye. This suggest the Fe-Zn alloy formation is inhibited(10).

The surface nodules have solidification defects at their boundaries. These dips surface are exacerbated at triple points and are usually around 10-15µm in depth. These defects are attributed to interactions with the steel substrate, as the same phenomena occurred on an inert substrate. Impurities such as Pb strongly segregate to the eutectic nodules and triple points so effort should be made to avoid contamination. Solidification cracking is another issue which appears to be associated with the dents and the segregated impurities (10).

During the solidification of the alloy on the substrate, the liquid metal is consumed very fast by the relatively sizable volume changes that occur during the solidification of Al and Zn. The reduction in liquid on the surface due to solidification of the nodules grow leave an impingement on the surface because of the volume change during the liquidus to solidus transformation. Cracks can then occur at both the weakened boundaries (caused by solidification stresses) and the precipitation of the Pb impurity particles. Reducing the Pb impurities has improved the surface finish (10).
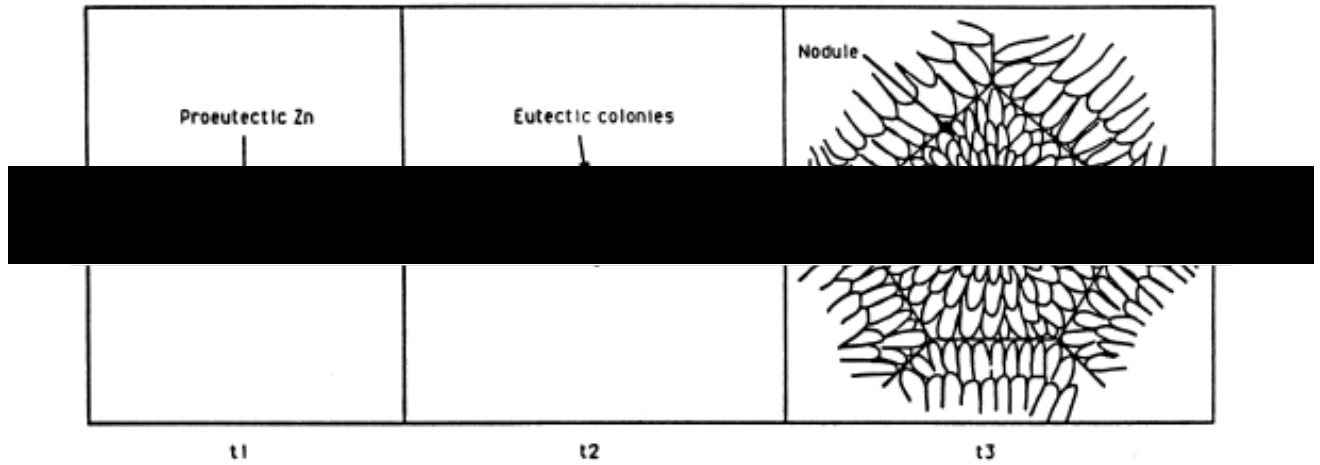
Fig. 1.31 Schematic of the nucleation and growth of the oroeutectic Zn and the eutectic lamellae colonies of Zn-Al in Galfan/Galvalloy® (10).
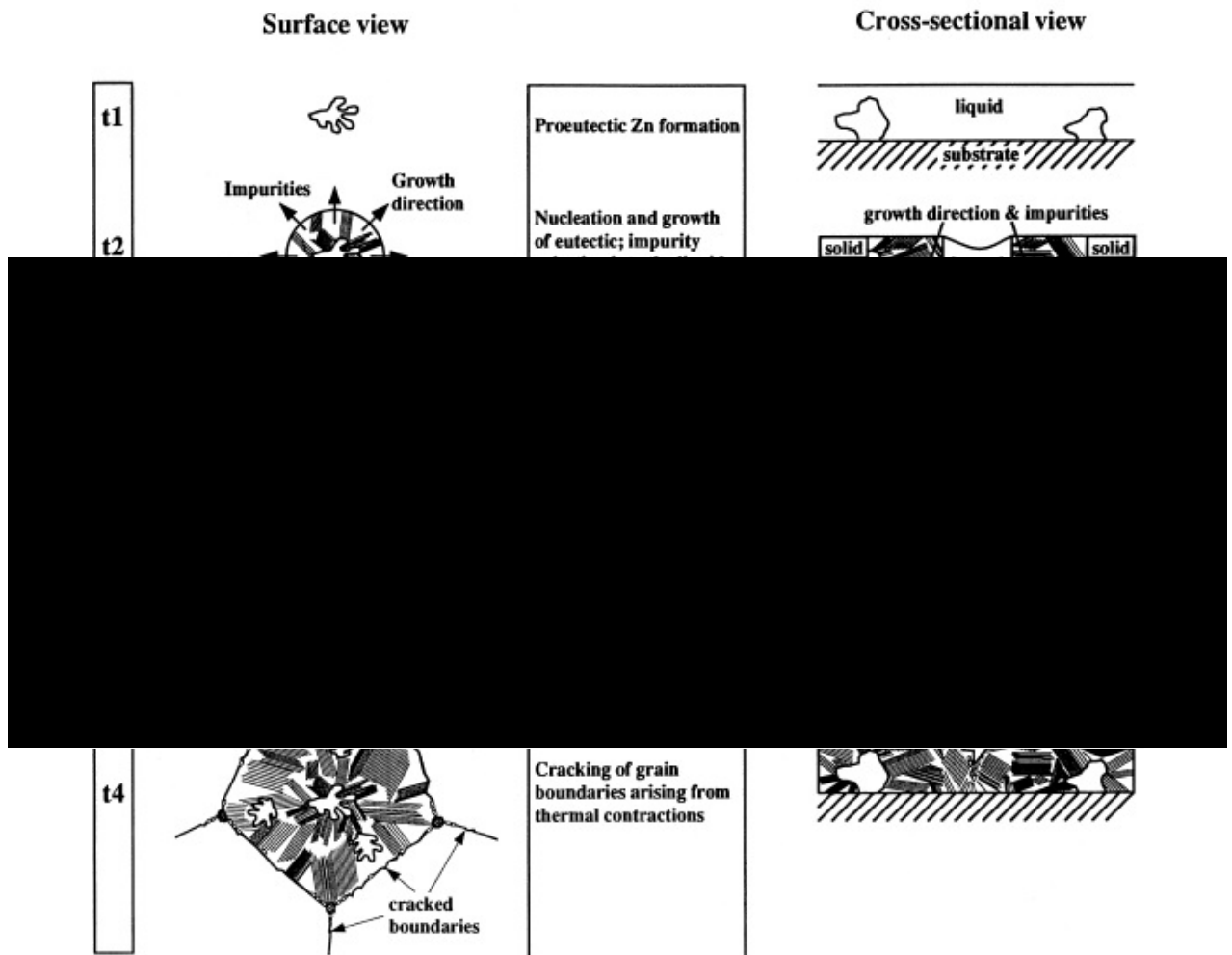
Fig. 1.32 Schematic detailing the formation of the nodules: how the dents form and why the cracking occurs (10).

1.7.2 Advantages Over Conventional HDG

- **Corrosion resistance**

The corrosion resistance seen in Galvalloy® compared to HDG is reported to be around twice as effective(10,22,55,71). This is seen in tests such as time require for 5 % red rust in a salt spray test (69). In the Kesternich test, the loss of coating thickness for samples exposed to a SO_2 rich environment is about 1/3 with Galvalloy® in comparison to HDG (69), even with test across 10 years (10).

- **Forming and shaping**

Galvalloy® has much improved forming capability compared to HDG. This is a consequence of ductility which arises from its fine lamellar eutectic structure that makes up a bulk of the microstructure, and enhanced adhesion as there is little or no intermetallic layer seen (11,69,72,73).

Galvalloy® also demonstrates a grand resistance to galling, this is due to the coefficient of friction remaining constant in Galvalloy® compared to it increasing strongly in hot-dipped galvanized samples (69).

- **Assembling**

The presence of aluminium in Galvalloy® means that special care is required for electrical spot welding, however, the presence of aluminium in the alloy results in of a better adhesive bonding surface when glues such as polyurethane or epoxies are used (69). Galvalloy® is also perfect for mechanical assembly due to its ductility and adhesion to the substrate as noted above.

- **Practical application**

The increased corrosion performance leads to lower coating thickness for instance a 10µm/side (125g/m²) has the same performance as a HDG coating of thickness 20µm/side (275g/m²)(69). This smaller thickness allowance means it is less expensive, as less material is used, also meaning the overall weight is reduced.

1.7.3 Literature on Corrosion Performance

The corrosion will occur in two locations on the sample, on the surface or at the cut edge. Within the cut edge it has been postulated that the Zinc rich areas corrode preferentially to the eutectic matrix (72).

The surface corrosion of the coating occurs within three notable points. The defects presence due to the formation of the nodules are notable sites of corrosion (58,74) as well as the interarm spacing of the Zn rich dendrites (72). The cracks that appear, again due to the solidification of the nodules also behave as a differential aeration cells.

1.7.4 Corrosion of Galvalloy®

Due to its use in sheet steel the surface corrosion (that is the corrosion of the Zn-Al) and the cut-edge corrosion (that is the corrosion of the Zn-Al coupled to the steel substrate) will be explored separately. As Galvalloy® is an alloy composed of two metals zinc and aluminium, with two different chemical behaviours it is prudent to look at the corrosion behaviours of them separately to appreciate them when they are alloyed together.

In previous works (57), the rate of corrosion of Zn5Al, an alloy very similar to the Zn4.8Al composition of Galvalloy®, was examined in different environments, seen in

Table 1.3. The rates are shown to increase from a rural, to urban, to marine, to severe marine. When compared to traditional galvanised (~ 100 wt.% Zn) coatings, Zn5Al had a better performance, however, it did not perform as well as Zn55Al.

Table 1.3 Corrosion Losses for Galvanized Steel, Zn5Al, and Galvalume (Zn55Al) after One-Year Exposure in Four Different Atmospheric Environments (57).

	Corrosion rate (µm in first year)			
		Zn5Al		Galvalume
Environment	Galvanized	Max.	Min.	(Zn55Al)
Rural	1.0	1.0	0.3	0.3
Urban	3.0	1.4	0.7	0.6
Marine	2.4	2.8	1.4	1.1
Severe Marine	5.4	3.8	2.8	2.6

1.7.4.1 Corrosion Products of Galvalloy®

The corrosion products that form during exposure to marine environments have been investigated over a series of years (40,75–77). Fig. 1.33 shows the corrosion products which form on zinc, aluminium and Galvalloy®. The zinc, aluminium and zinc-aluminium oxides/hydroxides form instantaneously in moist atmospheres on all materials. High chloride environments result in the formation of hydroxychlorides, Simonkolleite ($Zn_5(OH)_8Cl_2.H_2O$) on bare zinc and $Zn_2Al(OH)_6.Cl.2H_2O$ and/or $Zn_5(OH)_8Cl_2.H_2O$ on Zn-Al coatings such as Galvalloy®. Sulfate (derived from sea spray and gaseous sulphur dioxide) also exists in marine environments, and it

is important to recognise that over long exposure periods, Zn and Galvalloy® can form a layer structure of $Na_4Zn_4SO_4(OH)_6Cl_2.6H_2O$. The understanding of these corrosion products is essential for the understanding of the performance of these coatings, especially when comparing them. They can act as diffusion barriers, such as in new alloy systems such as Zn-Al-Mg (78–81). It is then the stability of these products, and the bare metal, in different conditions that dictates the overall corrosion performance.
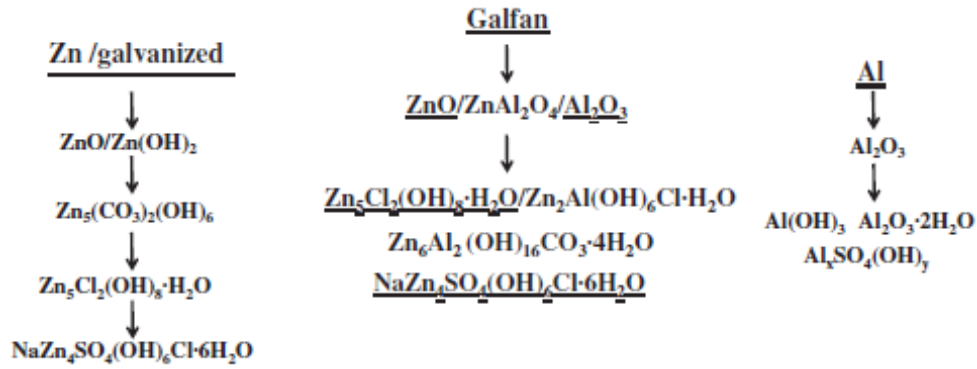
Fig. 1.33 Sequences of phases observed in corrosion products that form on Zn, Galvalloy®, and Al upon long-term exposure to marine environments. Vertical arrows indicate the morphology of the phases. Phases without arrows can exists simultaneously. Underlined phases are also observed in corresponding sequences for bare Zn and bare Al metals (40).

1.7.4.2 Corrosion of Galvalloy® on the Surface

It has been long accepted that corrosion will occur in defects in the coating surface (23). In Galvalloy® these are the depressed grain boundaries, and Zn dendrites arms which form as a result of solidification shrinkage (72). Triple points shown in Fig. 1.32 lead to the formation of cracks in the surface, and these can also behave as initiation site for differential aeration cells. The rest of this section will provide an overview of the current works on the corrosion of the surface of Galvalloy®.

1.7.4.2.1 Corrosion of Galvalloy® on the Surface in NaCl

X. Zhang et al. have shown that during atmospheric corrosion, corrosion products containing carbonates ($Zn_6Al_2(OH)_{16}CO_3.4H_2O$) formed, and more interestingly it formed over the Zn-richer η-Zn phase (40). It was thus assumed that the corrosion initiated in the η-Zn phase of the eutectic lamellar rather than the Al-richer β-Al as *due to it's slightly higher Al-content the β-Al could be expected to be the anode, but the oxide formation seems to reverse the conditions so that the β-Al phase acts more noble than the η-Zn phase.*

1.7.4.2.2 Corrosion of Galvalloy® on the Surface as a Function of pH

It has been shown that the corrosion rate of pure zinc (54,82) and pure aluminium (53,83) follow a $y=x^2$ shape with respect to pH with significant rates being observed in both basic and acidic solutions and a minima seen between pH 7 - 10.

Vu et al. (84) performed atomic emission spectroelectrochemical (AESEC) experiments on Zn5Al in saline solution as a function of pH. The technique identifies the species (Zn or Al) that are in dissolution as a function of time, and in this case was utilized to ascertain which phases of the microstructure were preferentially attacked at a range of pH values, demonstrating similar trends to the work carried out by Zembura and Burzynska.
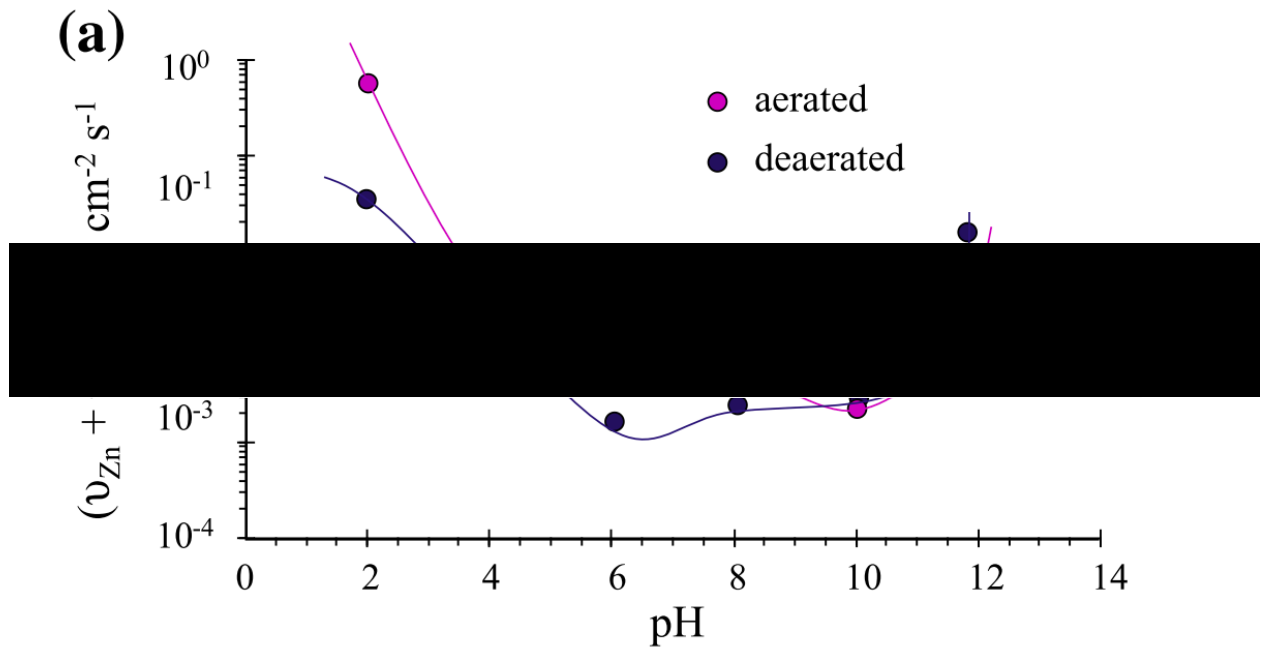
Fig. 1.34 Total dissolution rate (vZn + vAl) of 5 wt.% Al–Zn in aerated and deaerated 30 mM NaCl solutions as a function of pH (84).

Work was also performed to attempt to identify the phases undergoing dissolution, which is found in Fig. 1.35. This graph details, in relative proportions, the quantity of Zn and Al in solution. Fig. 1.35a, shows that in aerated conditions, between pH 2 -12, Zn undergoes more metal loss than Al, however, at pH 10, this difference is at its lowest, as well as the corrosion rate being the lowest. Moreover, when the corrosion takes place in a deaerated system, the same trend exists between pH 2 – 4, and conversely at pH 6 – 8, the rate of dissolution of Zn and Al are identical, until it reaches pH 10 – 12, where the Al dissolution overtakes that of Zn.

(a) aerated

DL of Al

pH

(b) deaerated

pH
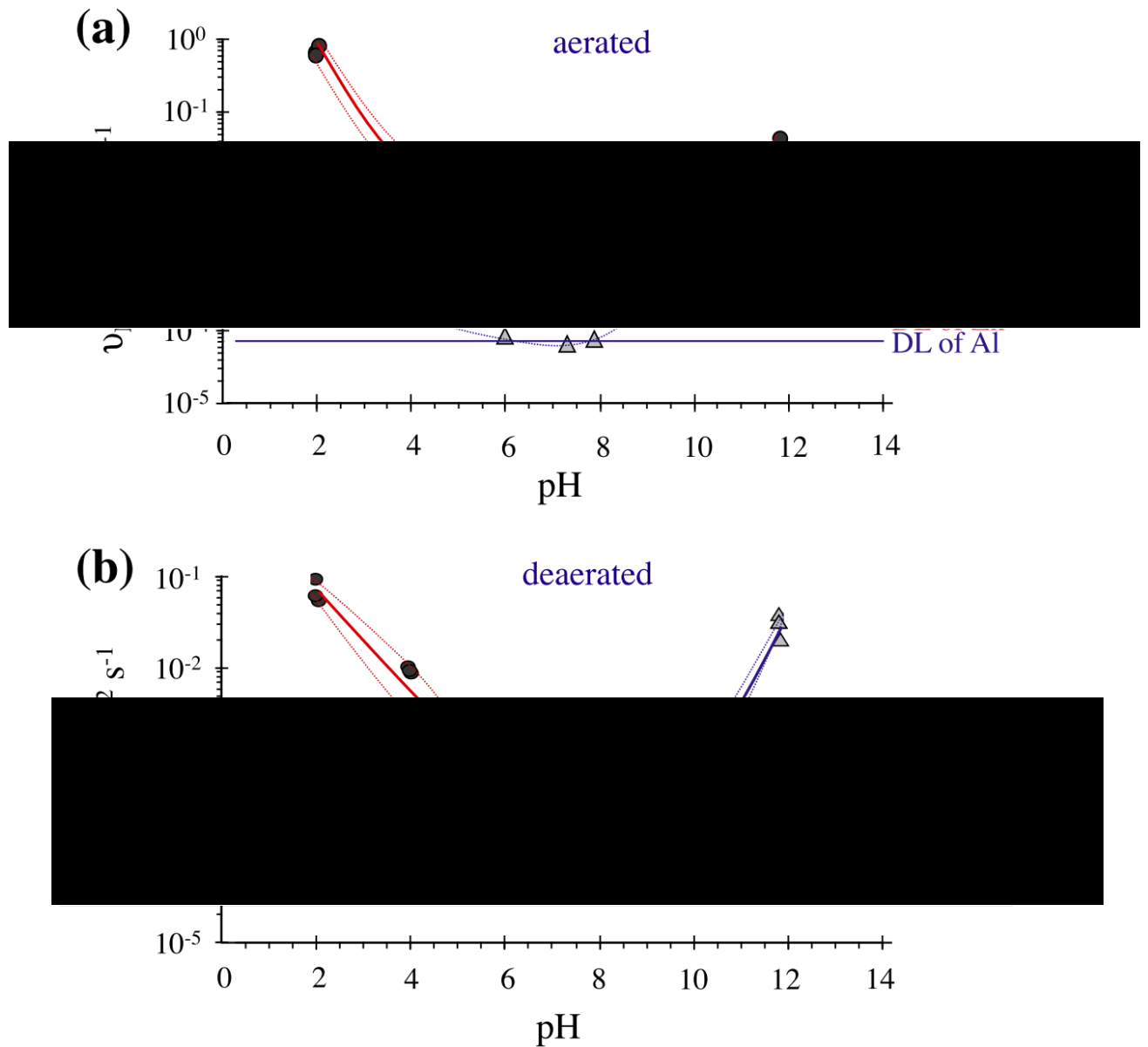
Fig. 1.35 Average dissolution rates of Zn and Al (v_{Zn} (circles) and v_{Al} (triangles)) for 5 wt.% Al–Zn as a function of pH (pH did not change significantly after measurement) in (a) aerated 30 mM NaCl and (b) deaerated 30 mM NaCl. The dashed lines indicate the dispersion of the data set. Detection limit lines of Zn and Al are also given (84).

Selective dissolution of zinc is seen at low pH (2-4) during surface corrosion and Al is seen to selectively dissolve at higher pHs (84), shown in Fig. 1.35. As mentioned in the section above, the corrosion products that form play an important role in the overall corrosion behaviour of the material. The corrosion products that form across a range of pHs are shown in Fig. 1.36, courtesy of J. Han et al. (85), and allow us to identify the products present with Zn, Al and Mg.
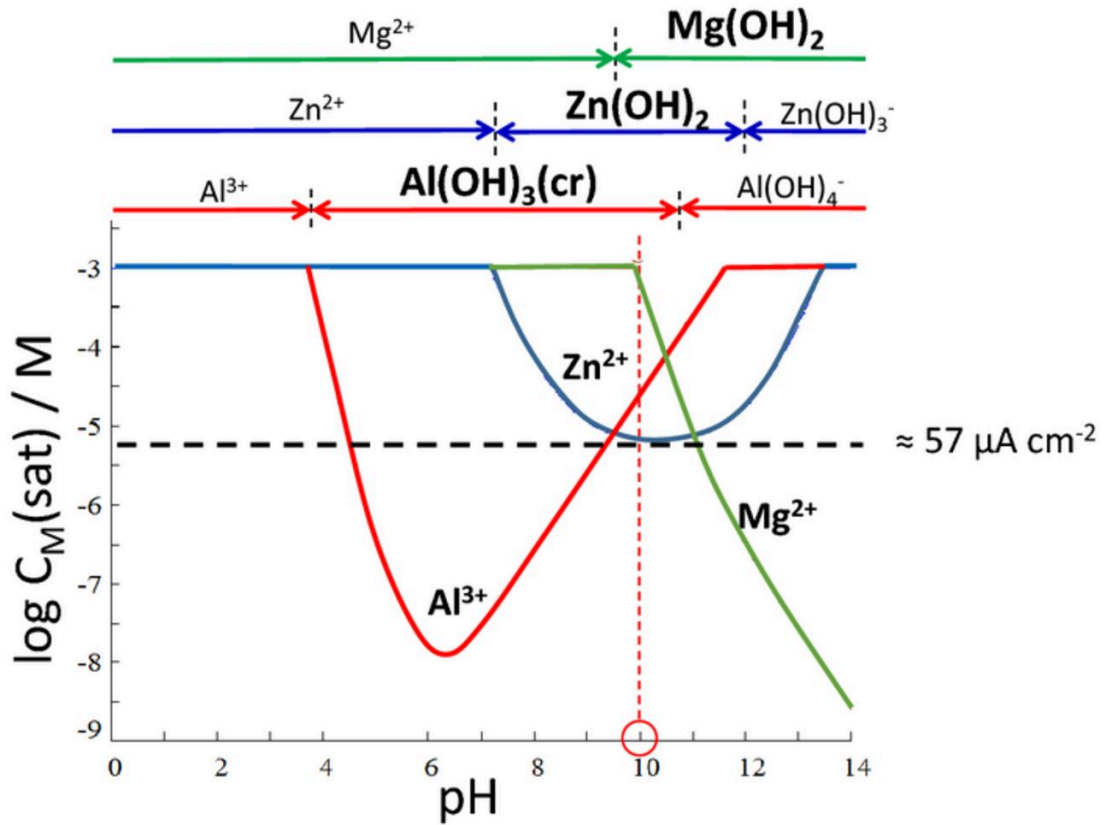
Fig. 1.36 $C_M(sat)$ of Zn^{2+}, Al^{3+} and Mg^{2+} in pure water calculated by Hydra-Medusa software and default database. The arrows above the curve indicate the predominant species in the pH ranges. The precipitated solid phase is indicated in bold. The metal ions complexes considered included: $Al(OH)_2^+$, $Al(OH)_3$, $Al(OH)_4^-$, $Al_{13}O_4(OH)_{24}^{7+}$, $Al_2(OH)_2^{4+}$, $Al_3(OH)_4^{5+}$, $AlOH_2^+$, $Mg_4(OH)_4^{4+}$, $MgOH^+$, OH^-, $Zn(OH)_2$, $Zn(OH)_3^-$, $Zn(OH)_4^{2-}$, $Zn_2(OH)_6^{2-}$, Zn_2OH^{3+}, $Zn_4(OH)_4^{4+}$, $ZnOH^+$; and insoluble species: $Al(OH)_3(am)$, $Al(OH)_3(cr)$, $AlOOH(cr)$, $Mg(OH)_2(s)$, $MgAl_2O_4(cr)$, $MgO(cr)$, $Zn(OH)_2(s)$, $ZnO(cr)$ (85).

1.7.4.3 Corrosion of Galvalloy® on the Cut-edge

The corrosion of Galvalloy® on the cut-edge is a mechanism that may very well seem obvious. The steel, a metal which is noble to Galvalloy®, cathodically drives the anodic dissolution of the sacrificial coatings, and of course, this is the intention. The regions of the microstructure that are attacked first are of great interest as the microstructure can be manipulated by composition changes and adjustments to the cooling rates.

Elvins et al. (86) discovered that cooling rate has an effect on the microstructure and the cut-edge corrosion properties of Zn4.5Al coatings. Coatings of identical thicknesses cooled at different relative rates of 55, 80 and 100%. The fastest cooling rate (100 %) produced a microstructure containing over 5 times the number of zinc dendrites compared to the slowest cooling rate of 55 %, however, the volume fraction of zinc dendrites remained consistent at 14%. The cut-edge of the different samples were exposed to aerated, 5 % NaCl solution for 24 hours. The presence of fewer, larger dendrites, formed at slower cooling rate, resulted in decreased corrosion performance compared to more, smaller dendrites, formed at faster cooling rate. An increase in relative cooling rates to 55 % and 100 %, the metal loss after 24 hours was 2500 µg and 250 µg respectively, a reduction of one order of magnitude. Another finding, shown in Fig. 1.37, demonstrates the preferential corrosion of the η zinc dendrites during the cut-edge corrosion of the zinc aluminium coating.
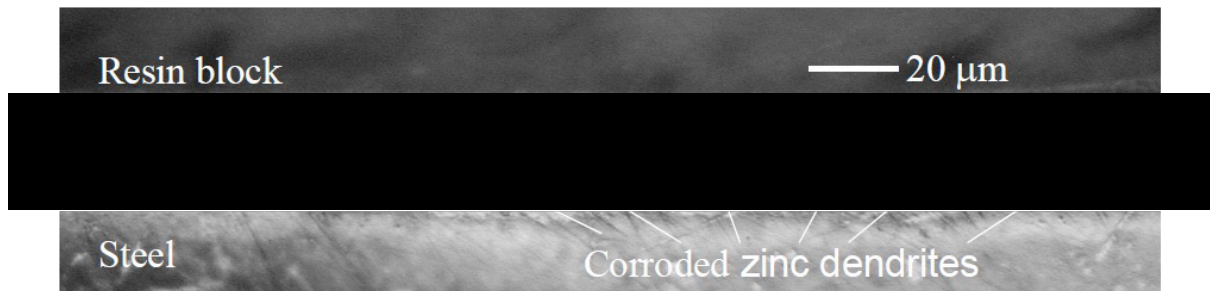
Fig. 1.37 Micrograph showing preferential corrosion of primary η zinc dendrites during cut-edge corrosion (14).
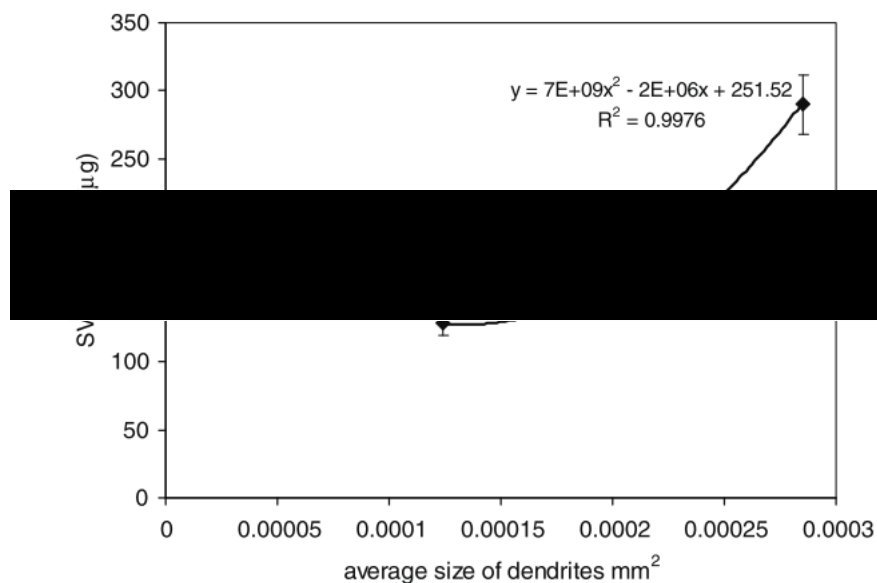
Fig. 1.38 Comparison of the average size of primary zinc dendrite observed for the steel gauges against SVET measured zinc loss (lg) for Zn4.8Al coated steels (13).

Similar work from J. Sullivan et al. (13) showed again that manipulating the microstructure of the coating by cooling rates effects the rate of corrosion. The cooling rate of the Zn4.8Al was controlled by increasing the steel gauge thickness (0.39, 0.55, 0.68 and 0.85 mm) which possessed the necessary residual heat to control the cooling of the coating, where thicker gauges produced increased cooling times. (in the previous study the cooing rate was controlled by a high-powered air cooler). Once again, slower cooling rates produced fewer, larger dendrites compared to faster cooling rates. The samples were exposed to 0.1 % NaCl electrolyte for a 24-hour period. As demonstrated previously, the η zinc dendrites are preferentially attacked and undergo a higher rate of anodic dissolution. The relationship of dendrite size and zinc loss is shown in Fig. 1.38 to be polynomial.

Elvins et al. (87) further investigated the effect of microstructure of Zn4.5Al by trialling low levels (0.1 – 0.5 wt.%) of Mg additions. The experiment showed that increasing the Mg concentration increased the zinc dendrite volume fraction. During cut-edge corrosion SVET tests in 5 % NaCl solution, the coatings with greater Mg contents and therefore greater zinc dendrite volume fraction had greater corrosion rates. This is again attributed to the increased anode lifetimes of larger dendrites.
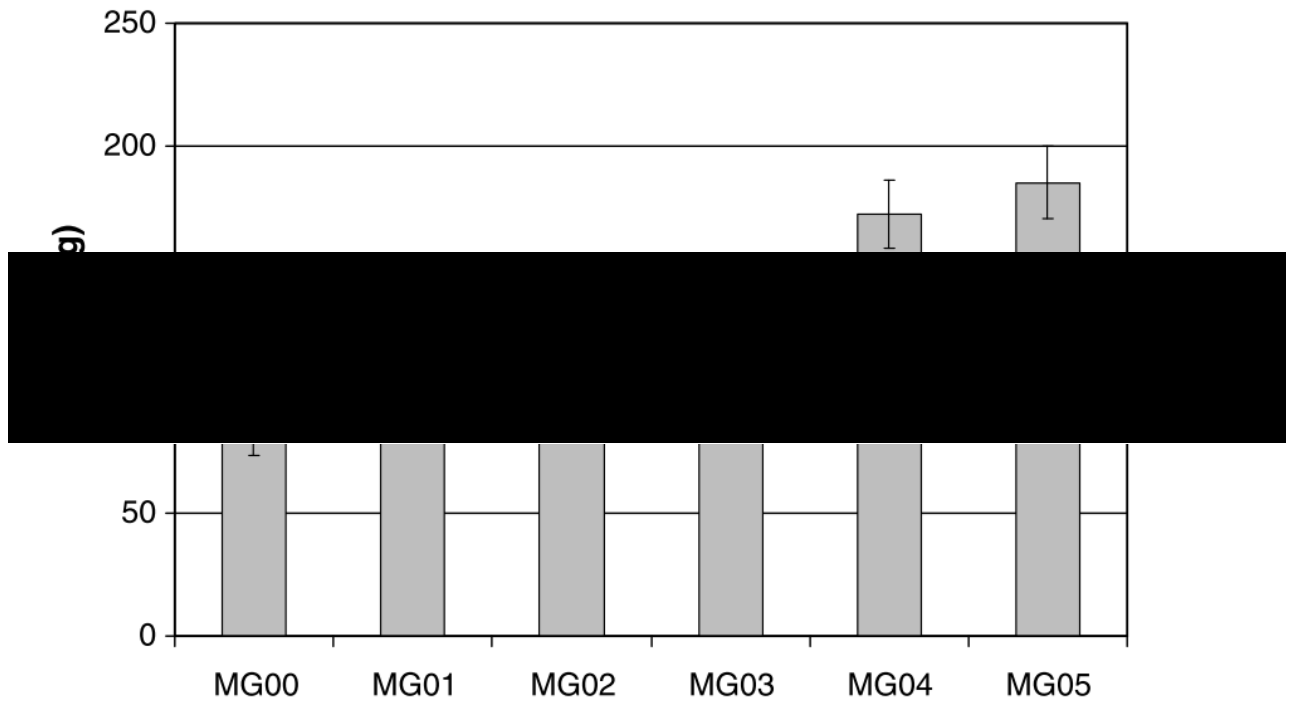
Fig. 1.39 SVET measured total zinc loss from 2 x 20 mm cut edges zinc aluminium alloy galvanised steel samples embedded in a resin block after 24 h immersion in 5% aerated NaCl as a function of the magnesium level. Data presented as an average of five 24 h experiments and error bars are shown to indicate the scatter (twice standard deviation) (87).

Sullivan et al. (70) studied the effect of ultrasonic irradiation during solidification of model Zn4.8Al coatings and the subsequent cut-edge corrosion performance in 0.1 % NaCl solution. Ultrasonic irradiation caused an increase in the number of η phase zinc dendrites and a decrease in their resultant size. Steel was introduced in electrical contact with the model coating during immersion to replicate a cut-edge. The ultrasonic irradiation improved the cut-edge corrosion performance. This was postulated to be due to the reduction of crevice-like corrosion phenomena that may be associated with larger dendrites.

1.8   Aims and Objectives

The work that makes up the results body of this thesis aims to:

- Investigate, using Time-lapse microscopy, the microstructural corrosion mechanism of Galvalloy® in saline media. To understand how the coating behaves in different environments, the pH will be adjusted from low, to neutral, to alkali pHs as the Pourbaix diagrams and previous literature indicate a change in corrosion behaviour. The variation of the rate of the corrosion at different pHs will also be deduced.

- Learn if there is a change can be seen, using TLM, between the mechanism of corrosion during cut-edge and surface corrosion modes. As if there is a difference in behaviour and sites of preferential attack, better informed placement of inhibitors can be performed in future. For instance, a different inhibitor can be used near the cut-edge compared to the surface areas and a gradient between the two can lead to enhanced corrosion performance and lifetime of the products. As well as this, more accurate lifetimes and therefore guarantees can be issued with products.

- Use an array of electrochemical and analytical techniques to better understand and support the visual results from TLM. This will allow quantitative and qualitative data to complement one another.

- Reproduce a real-world corrosion environment to expand the current knowledge of the under-film corrosion mechanisms of Galvalloy®.

Chapter Two

Experimental Methods

2 Experimental Methods

The work carried out during this research programme involves the assessment of the corrosion performance of industrial coatings in an variety of environmental condition using novel techniques. This section outlines the materials and chemicals used, alongside the experimental procedures followed.

2.1 Materials

2.2 Metals

Novel techniques have been employed to understand the mechanistic aspect of aqueous and atmospheric corrosion of Galvalloy® alloy coating, namely microstructural and filiform corrosion (FFC) respectively.

Metals used during this research programme are;

- **Iron**. Iron (Fe) circular disk, purity 99.5 % obtained from Goodfellows Cambridge Limited.

- **Zinc**. Zinc (Zn) circular disk, purity 99.998 % obtained from Goodfellows Cambridge Limited.

- **Galvalloy®**. Galvalloy® (Zn-4.8wt.%Al) coated steel, A4 sheets, 0.6 mm gauge thickness, 255 g/m^2 equivalent to 20 μm thick coating, supplied by TATA Steel, Shotton production line.

- **Zn0.7Al (η)**. Zn-0.7wt.%Al (η) phase, 50 mm diameter, were produced by heating pure metals in a ceramic crucible within a muffle furnace. at 350°C for 30 minutes before water quenching. The mixture was filtered through a frit prior to casting.

- **Zn22Al (β)**. Zn-22wt.%Al (β) phase, 50 mm diameter, were produced using method for Zn-0.7wt.%Al (η) phase.

- **Zn68Al (α)**. Zn-68wt.%Al (α) phase, 50 mm diameter, were produced using method for Zn-0.7wt.%Al (η) phase.

This technique for producing these model phases has been used previously (27,88) therefore comparisons can be easily drawn between the two findings.

2.2.1 Organic Coatings

Polyvinyl butyral (PVB), molecular weight 70,000 – 100,000 g.mol^{-1}, was employed as an organic coating. PVB is easily dissolved in ethanol and is safe in liquid form. It also displays very good adhesion to metal as it possesses both hydrophilic and hydrophobic monomers. A model coating was used instead of a commercial coating as it is free of stabilisers, and pigments, which could affect the corrosion performance of the metallic substrate.

2.2.2 Solution Preparation

Solutions were prepared by dissolving the relevant salt in water and from more concentrated solutions in molar concentration.

From solid stock

$$n = \frac{M}{M_r}$$
<div align="right">2.1</div>

where

n = number of moles (mol)

M = Mass (g)

M_r = Molar mass (g.mol^{-1})

From more concentrated solutions

$$M_c V_c = M_D V_D$$
<div align="right">2.2</div>

where

M_C = Molarity of more concentrated solution

V_C = Volume of more concentrated solution

M_D = Molarity of dilute solution

V_D = Volume of dilute solution

2.2.2.1 Solution in Weight Percentage Concentration

From solid stock

$$weight\ \% = \frac{weight\ of\ solute}{weight\ of\ solution} \times 100$$
<div align="right">2.3</div>

where all weights are in (g).

2.3   Filiform Preparation

The investigation of filiform corrosion (FFC) involved 50 x 50 mm coupons of Galvalloy® cut from A4 sheets. They were washed with distilled water and degreased with acetone. To ensure a uniform and more reproducible experiments, the surface was polished using 5 μm aluminium oxide powder then cleaned with Isopropanol (IPA) to remove excess residue.

This technique was used to determine whether FFC corrosion would initiate on the materials. This involved scribing a coated substrate to observe initiation. If FFC did not initiate it may be shown that the metallic coating does not support FFC under these conditions.

Parallel strips of insulating tape (thickness 25 μm), were placed on the sides of the coupons. This left an exposed area of Galvalloy® coated steel in the centre A small amount of 15.5 wt.% ethanolic solution of PVB was applied to the coupon then drawn across the exposed area using a glass rod. The polymer coating was left for dry over a 24 hour period. The PVB coating was then scribed thrice, with a length of 10 mm, using a scalpel blade. 2 μL of 2 M $FeCl_2$, NaCl, HCl, CH_3OOH was applied to initiate FFC, shown in Fig. 2.1. The electrolytes were chosen for the following reasons;

- **NaCl**. Sodium Chloride electrolyte's existence is widespread, so it's testing could be considered a benchmark (89).

- **FeCl₂**. Iron Chloride is used because unlike NaCl, it does not radially form cathodic delamination from the scribe area then initiate FFC corrosion. $FeCl_2$ initiates FFC first (89).

- **CH₃OOH**. Acetic Acid is the most common electrolyte to form FFC. Initially it was discovered on tobacco cans. As it comes from wood and trees exist near where the alloy is used, this will yield valuable results. Acetic acid is also the only electrolyte that initiates FFC on MagiZinc (89).

- **HCl**. Hydrochloric acid has been employed due to its highly acid properties creating an environment that stimulates acid filiform head formation (89).

The solution was left to dry on the defect and then the samples were left at a constant temperature and humidity. A constant RH was maintained throughout experiments by storing the samples in an atmosphere containing a pool of 5 wt.% NaCl (96%) and a pool of saturated salt solution KCl (84%), acting as a reference. The samples were removed from the chamber at regular intervals to photograph. Image analysis software Sigma Scan Pro ® was used to determine the FFC corroded area. The software can quantify the area considered to be corroded by differentiating the background colour, shown in Fig. 2.2. The software was first calibrated using the 10 mm scribe.
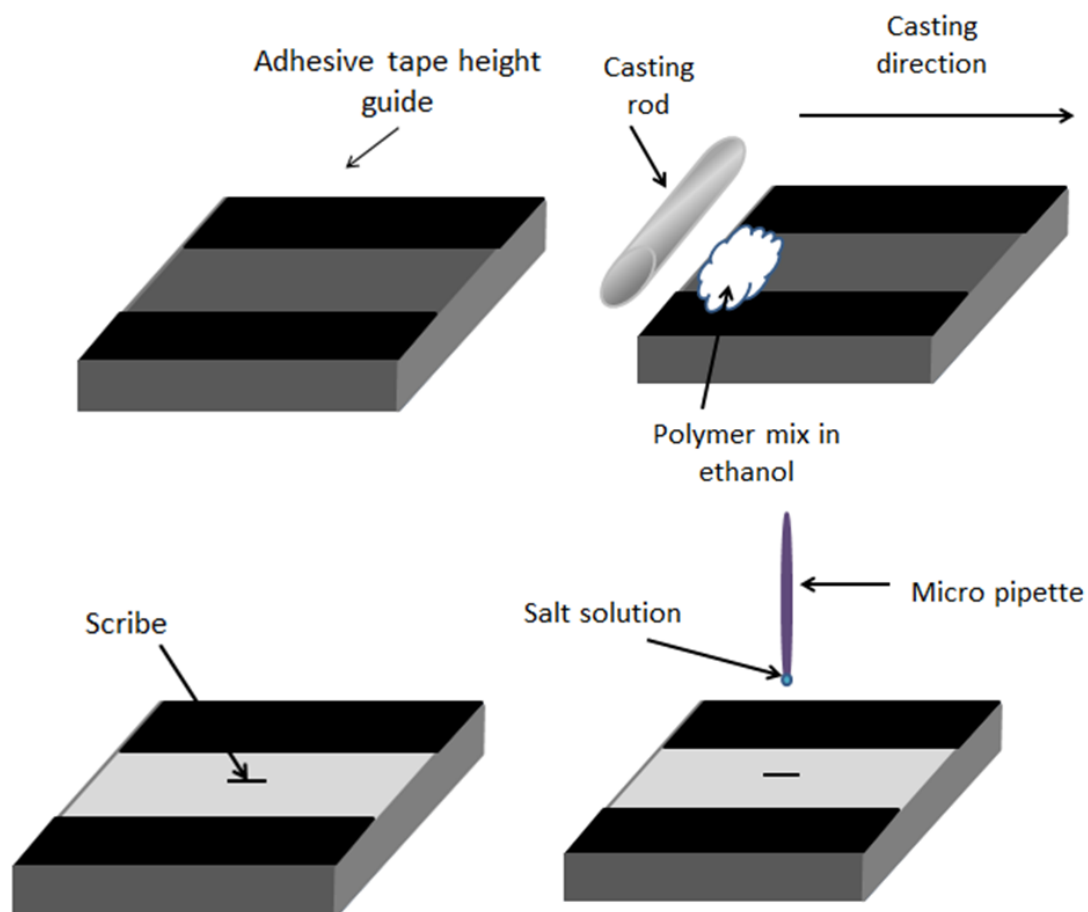
Fig. 2.1 Schematic of FFC sample coated with PVB
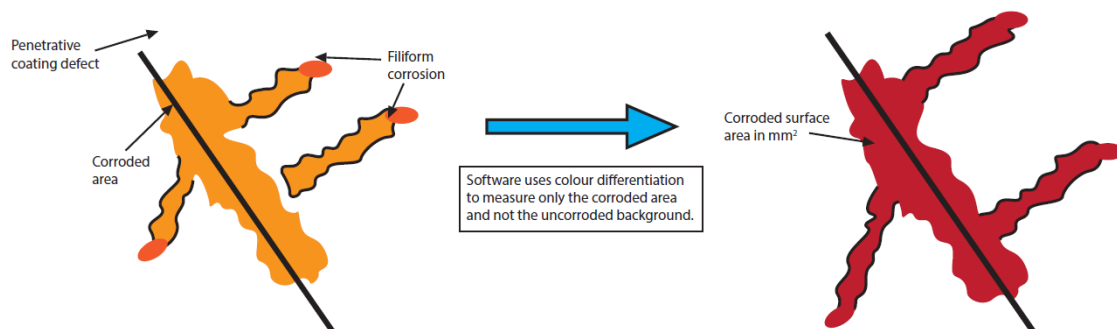
Fig. 2.2 Schematic of image analysis process

2.4 Cut-edge Microscopy Imaging

Galvalloy® coated steel was imaged using microscopy to measure the ascertain the thickness and quality of the coating. The images were captured using a Meiji Techno 7100 optical microscope with an Infinity 2-5C microscope mounted digital camera connected to a computer with Infinity Imaging Software.

2.4.1   Cut-edge Metallographic Preparation

The samples were hot mounted in non-conductive resin using instructions provided by Buehler. Grinding and polishing required trial and error, due to issues arising. One of the issues was that the steel substrate, which is a lot harder than the metallic or organic coatings, grinds down at a much slower rate than the coatings. The differentiation in height meant that the focal length varied across the sample. In order to prevent the coatings to grind down at such a fast rate, the sample was held at the same orientation on the grinding wheel, perpendicular to the direction of spin (Fig. 2.3C) following a methodology described elsewhere (90,91). This however led to uneven grinding of the resin mount, So, as shown in Fig. 2.3A and Fig. 2.3B, metal stabilizers were added to give support to the mount, in the form of metal screws. Additional pieces of scrap sheet steel were added either side of the samples to give more support closer to the sample. The order shown in Table 2.1 was used.

Table 2.1. The conditions used for polishing cut-edge samples.

Order	Grit (p)	Time (mins)	Revolutions (rpm)
1st	120	5	175
2nd	320	5	175
3rd	700	7	175
4th	1200	10	175
5th	2500	10	175
6th	4000	15	175

.
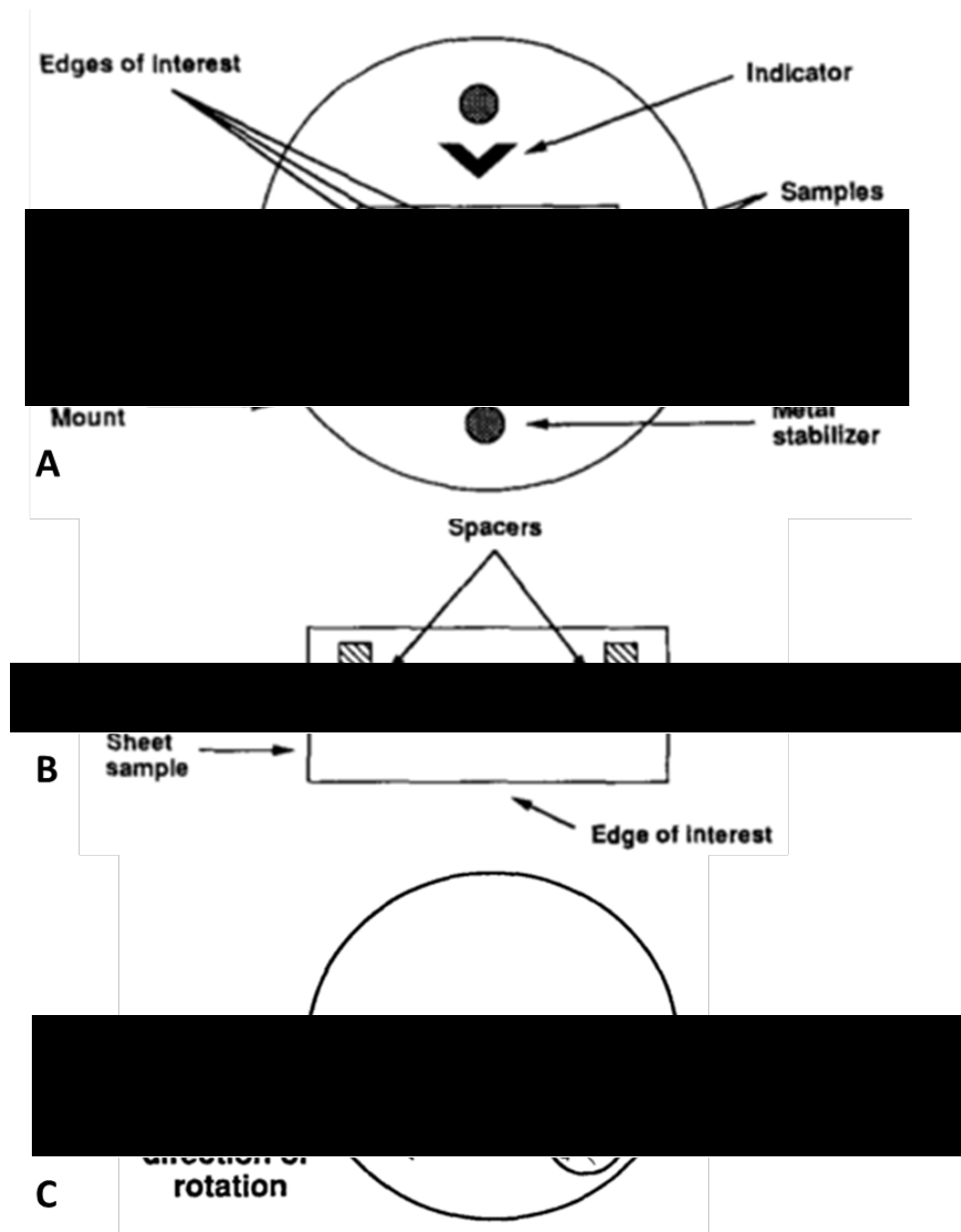
Fig. 2.3 Schematic of mounting and grinding process for coated steel substrates (90,91).

2.5   Scanning Electron Microscope (SEM)

The scanning electron microscope (SEM), shown in Fig. 2.4, is an electron microscope which utilizes a high energy beam of electrons to image. The narrow beam ensures details in the nanometre range (~ 1-5 nm) can be resolved, whilst retaining depth of field, thus overcoming the major downfalls of light microscopy. Images are therefore presented in a 3D view. The beam and the surface of the sample interacts and signals are detected by a detector which give information on the composition, surface properties and topography.

The most common signals are back scattered electrons (BSE) and secondary electrons (SE).

- BSE are produced during elastic collisions. The materials atomic number is proportional to the production efficiency of the BSE. The detector converts the received signal and maps out the surface; heavier elemental compositions appear brighter in the image.

- Secondary electrons are created during inelastic collisions between incident electrons and sample electrons, providing information on morphology and topography.

The SEM used during this thesis is the Hitachi TM3000 desktop microscope.
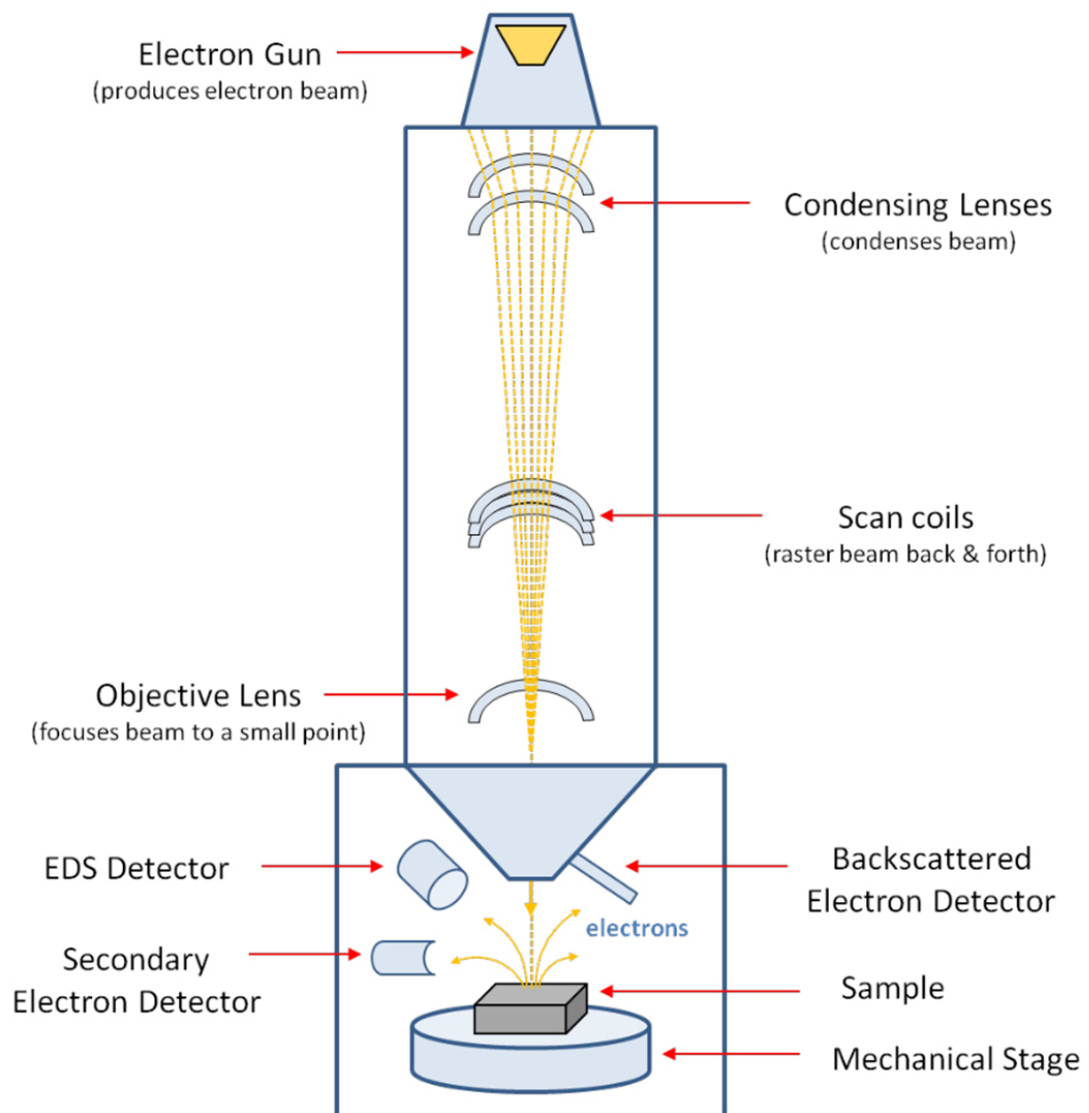
Fig. 2.4 Schematic of a typical Scanning Electron Microscope (SEM) with Energy Dispersive X-Ray Spectroscopy (EDX).

2.5.1 SEM Sample Preparation and Experiment Method

The SEM was used to characterise the surface of the sample before and after immersion in electrolyte. Areas of anodic attack were imaged at high magnification to ascertain if phases were

preferentially attacked upon immersion in 1 wt.% NaCl. The samples surface was cleaned with ethanol and dried before being inserted into the SEM chamber.

2.6   Energy Dispersive X-Ray Spectroscopy (EDS)

Energy dispersive x-ray spectroscopy is a technique which can be used in conjuction with SEM, allows the identification of the elemental composition of the sample. Again, an electron beam is utilised. The sample emits x-rays which was be used to identify the atomic composition of a sample as each atomic structure has a unique set of peaks in its x-ray spectrum.

A high energy electron beam is first focussed on the sample. The beam then excites an electron from the inner shell, which is ejected, and a hole remains in its place. A higher energy electron fills the hole and an x-ray, of corresponding energy to the difference between the higher energy shell and low energy shell, is emitted. Due to these characteristic x-ray energies relating to the atomic element, the composition can be determined. It is possible for elements to have multiple peaks and for peaks of different elements to overlap.

2.7   Time-lapse Microscopy (TLM) Technique and its Progression

The time-lapse microscopy technique has been developed through a number of iterations since its invention. The current design, detailed in section 2.7.4, comprises of a microscope with a waterproof shroud on the objective lens, a digital camera attachment connected to a computer with software to take images over regular intervals of a polished metal surface submerged in electrolyte.

2.7.1   Sample and Experimental Preparation

The samples were prepared as 20 x 20 mm coupons, mounted in non-conductive resin and polished with 1 μm diamond polish to achieve a comparable surface finish, free from production line oils, oxides and scratches. The surface was then etched with 2% Nital to reveal the grain structure, rinsed with water and dried. A sample area of 0.7855 mm^2 was masked off using a 1mm diameter biopsy pen and 3M non-conductive PTFE tape. This sample area was chosen as it fills the field of view that the microscope can image under 100X magnification and was found to give a representative area of the microstructure for the samples used in this study. The prepared sample was secured to the base of a beaker or petri dish first using double-sided tape and then 3M non-conductive PTFE tape.

The electrolyte used was 1 wt.% NaCl, as this provided a significant corrosion rate within the experimental period for the samples chosen in this study. After the electrolyte was poured into the beaker (250ml), any air trapped between the bottom of the shroud and the surface of the sample was removed using a pipette. The imaging software was set to take an image every 2 minutes for up to 36 hours and a time-lapse video was created from these image sets using

Windows Movie Maker. Each image became a frame of the video lasting 0.05s, giving a run speed for each time-lapse video of 2400 x real-time.

2.7.2 Mk. 1 Design

The initial design shows a flowcell with an inert adhesive to seal the electrolyte in the cell, see Fig. 2.5. The experiments were not conducted with continuous flow, but rather a pump was used to introduce electrolyte into the cell to cover the sample. There were a number of limitations with this design. Firstly, the flow-cell was unstable on the microscope stage and as the technique images on a microstructural level, any small jolt dramatically affected the quality of the final image which in turn resulted in an unstable time-lapse video. Another limitation of this technique was the introduction of air bubbles into the system, caused by a poor seal from the inert adhesive. Creating this seal was a laborious task as the adhesive had to be manually shaped and prepared with the glass slide sitting on top being manually positioned. The process was prone to process and human errors and an insufficient seal meant that the corrosion of the sample would be affected by the presence of air bubbles on the surface and because of the nature of the sealed flowcell these air bubbles were very difficult to remove. The technique was also limited by magnification as for anything higher than 100X magnification the working distance from the microscope objective lens to the metal surface was too small to physically achieve, i.e. because of the flowcell-type design it was not possible to get the sample close enough to focus.
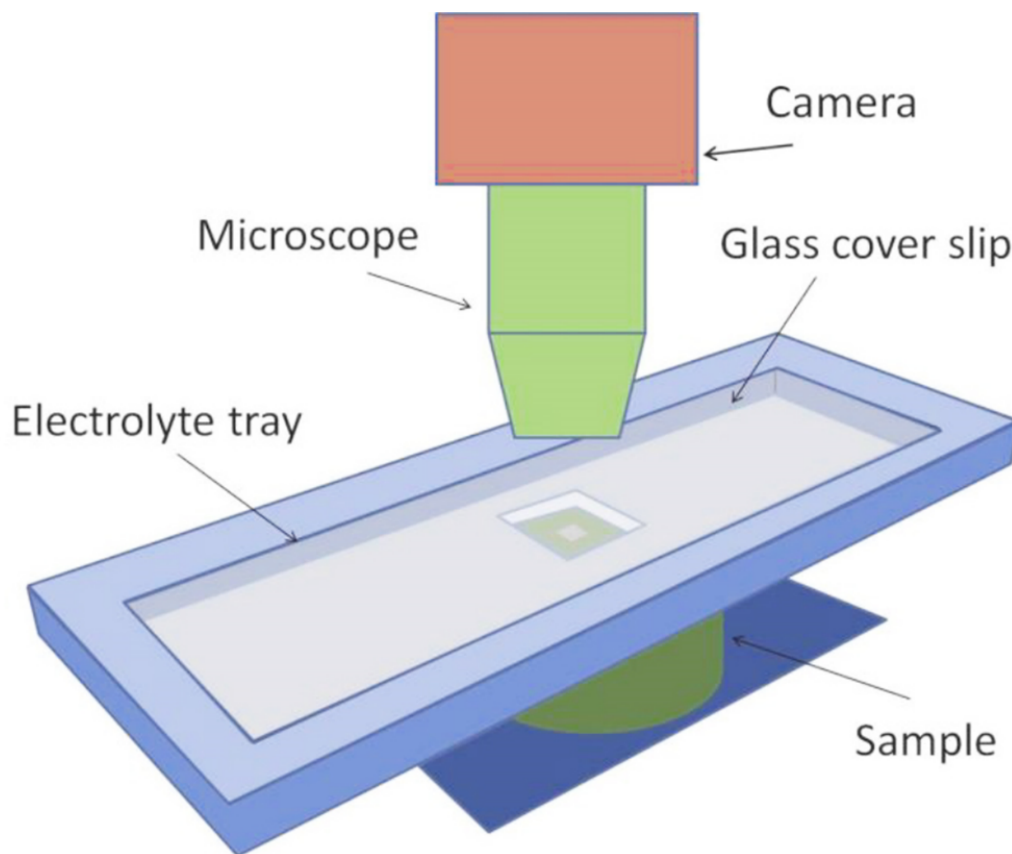
Fig. 2.5 Schematic Diagram of Mk.1 Design, with a glass cover slip and a manually applied inert adhesive seal.

2.7.3 Mk. 2 Design

In order to resolve the problems with Mk. 1 Design, initial improvements were made to the flowcell design as part of this study. The flowcell was re-designed with CAD using Autodesk Inventor to include a rubber seal and base plate which was screwed in using 4 bolts to create a less labour intensive, more robust seal, see Fig. 2.6 and Fig. 2.7. A jig was also manufactured so the flowcell could sit inside and this allowed a more stable base to minimise image movement. A thinner glass slide (No.1=0.16mm thick) was used to allow higher magnifications of up to 200X to be achieved. Overall, Mk. 2 was a considerable improvement on its predecessor, however it did have a number of drawbacks of its own. Firstly, achieving a good seal was problematic and although the use of a silicon sealant in addition to the rubber seal did help, it was still not an ideal solution and removing air bubbles from the flowcell remained an issue. Although higher magnifications could be achieved, the thinness of the glass slide caused it to be very brittle and it would occasionally crack by surges of electrolyte entering the cell during the start of the experiment. Contamination also occurred when inhibitors were used.
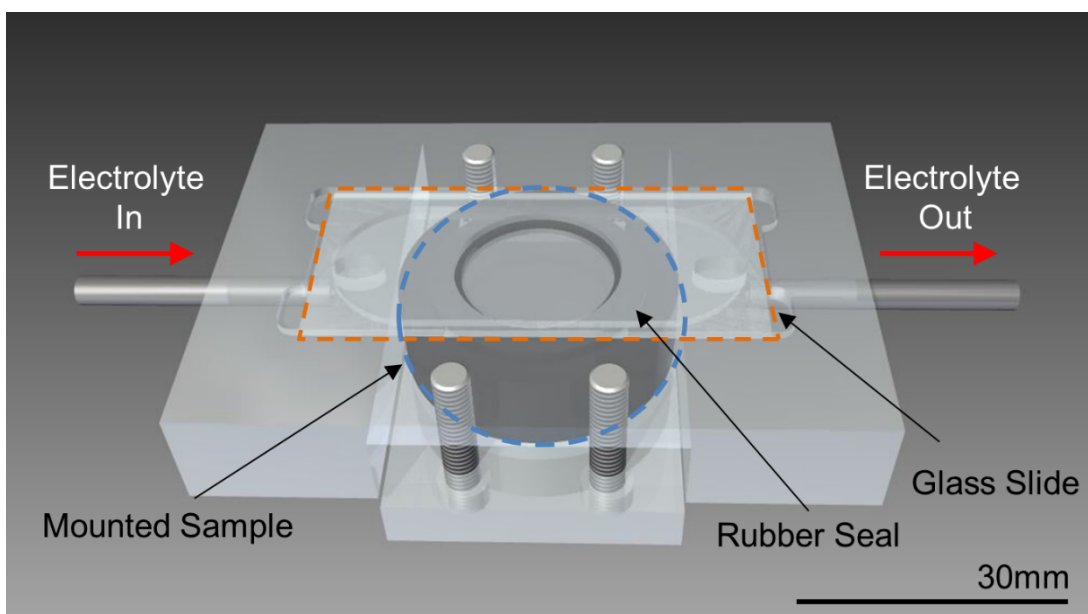
Fig. 2.6 CAD render of Mk. 2 with a more robust flowcell design with rubber seal and thinner glass slide to allow higher magnifications to be achieved.
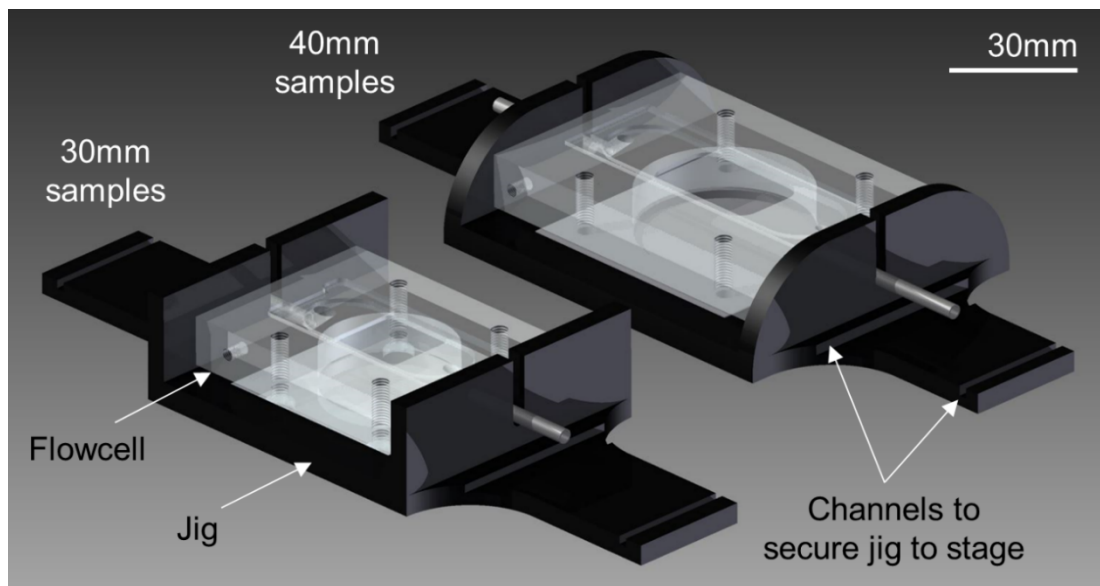
Fig. 2.7 CAD render of Mk. 2 with jig attachment to minimise image movement.

2.7.4 Mk. 3 Design

The current design used predominantly in this study no longer resembles the flowcell type setup. The process has been simplified to identify the key components required, namely a polished sample submerged in electrolyte and an optical microscope with camera and imaging software, see the schematic in Fig. 2.8.

The problem area is the microscope objective lens and electrolyte interface. The lens is designed to image through the medium of air and therefore has a refractive index, n, of 1. However, the refractive index of the electrolyte will be different to air and will be closer to that of water, approximately n=1.34287(92). This difference in n means that the image will become more distorted the more the light has to travel through the electrolyte. To minimise image distortion, the lens needed to be as close to the sample surface as possible whilst also leaving a thin layer of electrolyte over the sample to not limit oxygen diffusion to surface. To achieve this, a protective, waterproof shroud was designed and fitted onto the lens so that it could be submerged into the electrolyte to the required depth, see Fig. 2.9. The cylindrical PET shroud had a glass window (No.1=0.16mm thick) on the bottom, sealed with inert resin, to allow close imaging of the sample with minimum distortion. The new setup enabled the objective lens to be positioned much closer to the sample than previous designs, allowing for higher magnification and better quality images to be taken.
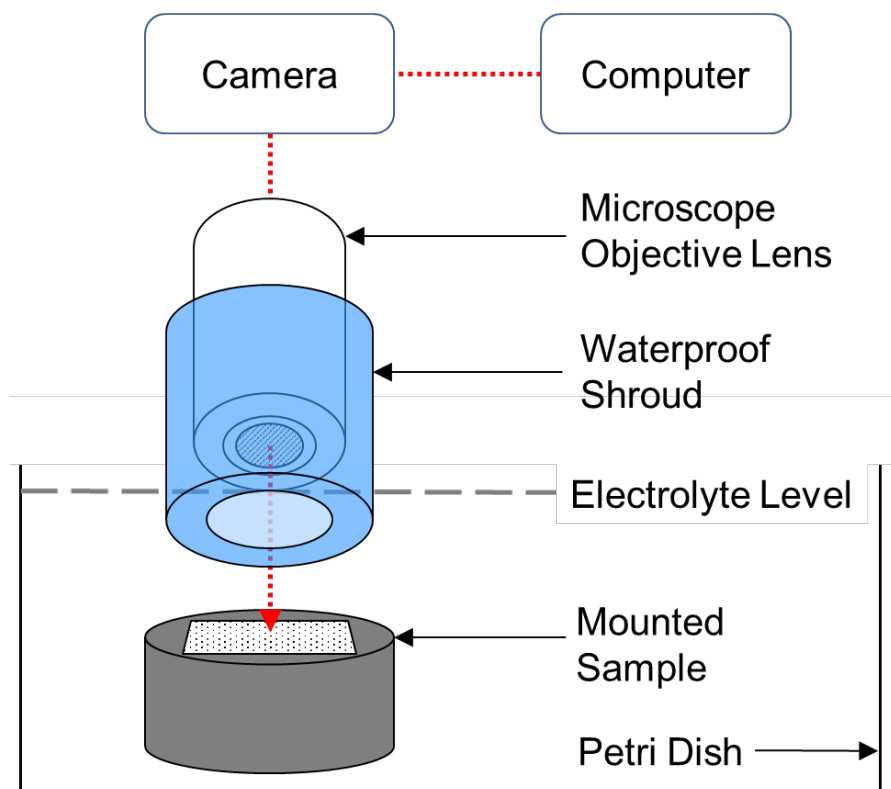
Fig. 2.8 Process schematic of key time-lapse components. Time-lapse software is programmed to take an image using the microscope-mounted digital camera at set intervals over the duration of the experiment. The microscope objective lens is protected by a waterproof, PET shroud allowing it to be submerged into the electrolyte in order to focus the image. The mounted sample is secured to the bottom of the electrolyte bath to prevent image movement.
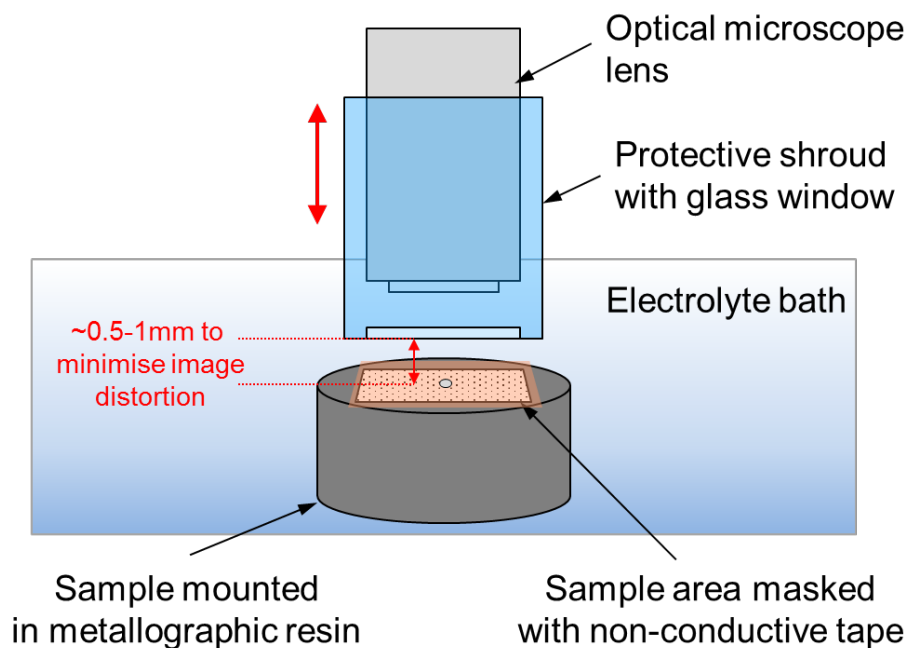
Fig. 2.9 Schematic of Current Design showing waterproof shroud to protect objective lens from electrolyte and allow it to be submerged into the electrolyte in order to focus the image and minimize image distortion.

The current design has dramatically simplified the technique, allowing experiments to be carried out in an open beaker, negating the need for an air-tight cell and therefore solving previous problems with air bubbles. The mounted sample is secured to the bottom of the beaker using first 3M double-sided mounting tape and then 3M PTFE non-conductive tape (see Fig. 2.10 for the current setup). The new design has provided greater image stabilisation than the previous designs and has also opened up a large amount of scope for additional experimentation, including the simplicity of adding inhibitors into solution, as well as various probes in order to perform electrochemical measurements in-situ. The additional access between the glass slide and the sample surface allows for removal of bubbles from the sample which 1) prevents the capture of a clear image and 2) prevents the contact of the sample and the electrolyte thus preventing the intended corrosion.
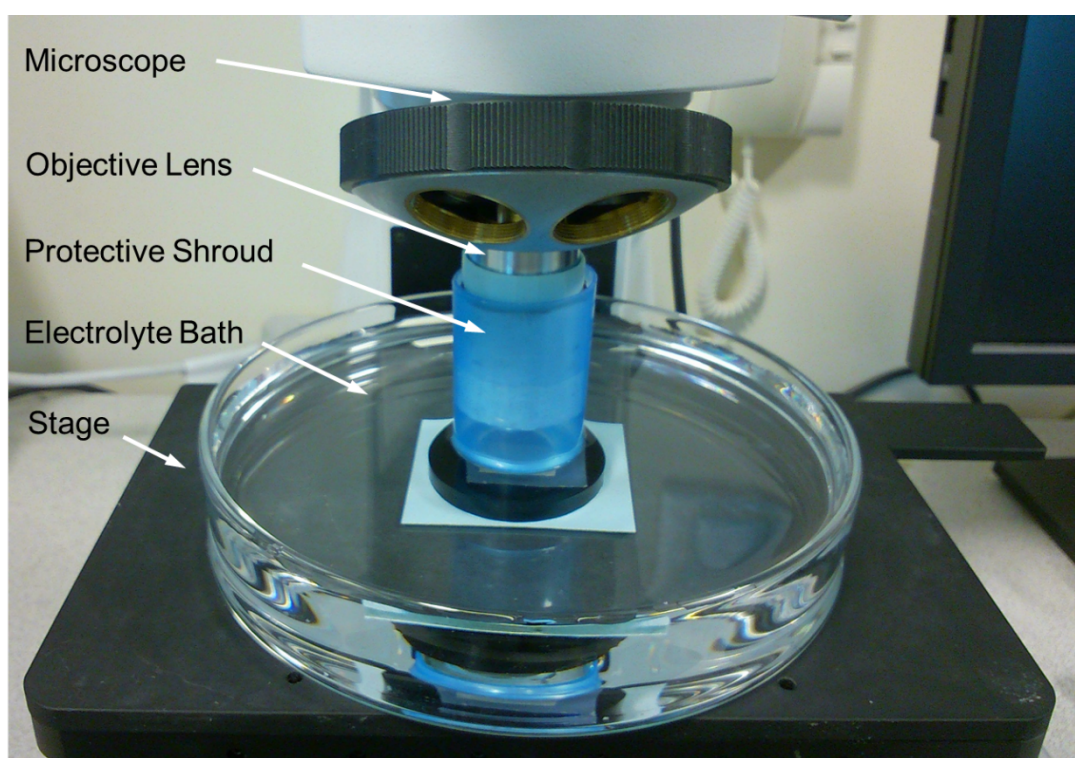
Fig. 2.10 Photograph of current time-lapse setup using protective shroud in an open beaker.

2.8   Artefact Assessment

In order to establish whether the corrosion seen during Time-Lapse Microscopy were not an artefact of the etching process, etched and unetched samples were imaged. An area of 0.3 mm diameter was exposed, and the entire area was imaged. The sample was then immersed in 1 wt.% NaCl pH 7 for 30 minutes before being imaged again.

2.9   Sample Preparation to Simulate Cut-Edge Corrosion

The Galvalloy® coated steel sheets were cut into approximately 20 x 20 mm coupons using a guillotine before being mounted in non-conductive resin. The samples were then polished to a 1μm finish and etched using a 2% Nital solution to reveal the microstructure. For cut-edge experiments areas of the coating were removed from the substrate. To remove the coating, half of the sample were suspended in 2 M HCl for ~20 minutes until the coating was visibly removed leaving bare steel. This allowed the 3M PTFE tape to be placed accordingly on the surface of the sample, to leave a total area of 0.7855 mm² exposed, containing varying amounts of bare steel and Galvalloy® coating.

2.10   DC Electrochemical Measurements
2.10.1   Sample Preparation

The Galvalloy® coating samples that are prepared follow the same procedure as for TLM experiments. To produce a steel sample the coated steel substrate, in 20 x 20 mm coupons, was subjected to P120 grit until the coating was removed, then P320, P600 and P1200 were used. For the pure phases (Zinc, Zn-0.7wt.%Al (η), Zn-22wt.%Al (β)and Zn-68wt.%Al (α)) P1200 SiC grit paper was used. The samples were then mounted into an Acetal sample holder.

2.10.2   Potentiostat Equipment

A Solartron SI 1280 Electrochemical workstation potentiostat was used alongside a personal computer installed with the CorrWare2 and CorrView2 software (Scribner Associates). For all experiments, a Sentek saturated calomel reference (SCE) electrode (Hg/Cl electrode enclosed in glass with a ceramic frit) was used. A platinum gauze counter electrode was used in the case of the potentiodynamic experiments. The setup of this three-electrode cell can be seen in Fig. 2.11.
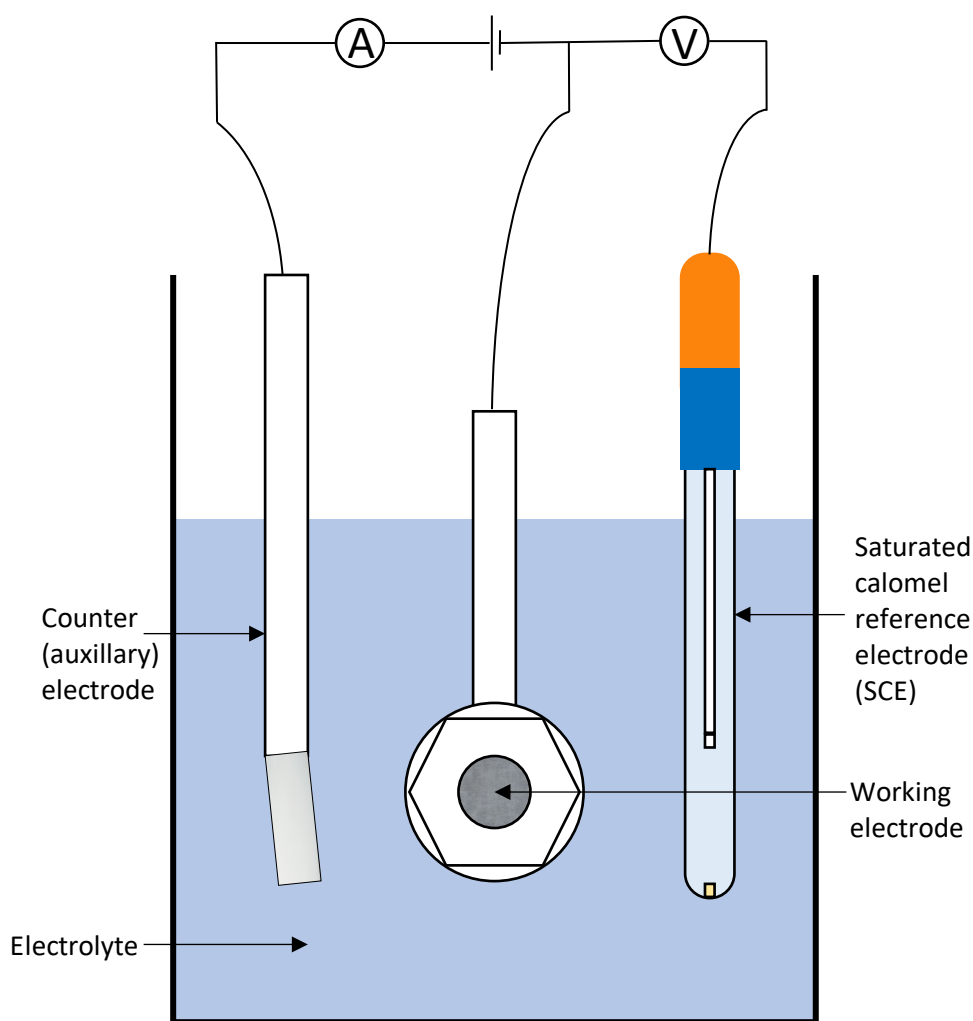
Fig. 2.11 Schematic of three electrode cell for electrochemical measurements.

2.10.3 Open Circuit Potential

No current is applied during open circuit potential measurements meaning that the sample is undriven. The potential of the sample (working electrode) is measured against the SCE reference electrode. In all cases the OCP experiments were conducted at 20°C for 24 hours, after which the current had plateaued.

2.10.4 Potentiodynamic Polarisation

Potentiodynamic curves are used during corrosion investigations to examine a wide range of substrates and corrosion media. A semi-log plot of log [i] against potentials (vs. SCE) allows for a large range of current densities to be compared.

A voltage is applied to displace the system from its equilibrium potential. The voltage is then changed at a constant rate, moving away from that potential. A positive or negative net current will flow dependent on the displacement. The overpotential η defines the movement from the equilibrium, where E_p is the polarised potential and E_{eq} the equilibrium potential

$$\eta = E_p - E_{eq} \qquad\qquad 2.4$$

An anodic current flows and oxidation reactions occur for positive overpotentials, whereas cathodic current flows and reduction reactions occur at negative overpotentials.

A Tafel extrapolation can be used to calculate the free corrosion potential. The linear parts of the anodic and cathodic arms of the produced curve are extrapolated and the intercept is the point of free corrosion potential.

2.10.5 Zero-Resistance Ammeter (ZRA)

For the evaluation of galvanic corrosion, zero-resistance ammeter (ZRA) is used to measure the current which flows between two connected metals (93), shown in Fig. 2.12. When the potentiostat is in ZRA mode, 0V is imposed between the working electrode (Galvalloy®) and the counter electrode/reference electrode (steel) and the net current versus time is measured. If the net current is positive this means that the anodic current flows from the working electrode to the counter electrode where the cathodic current flows. Therefore, the working electrode will be experiencing oxidation and the counter electrode will be experiencing reduction.

The ZRA was used to analyse the variation corrosion rate of Galvalloy® when galvanically coupled with steel.

- The first variable were the ratio of steel to Galvalloy®, increasing the amount of steel exposed in ratios (steel:Galvalloy®) 1:1, 2:1, 3:1, 5:1, 10:1 whilst maintaining a constant area of Galvalloy® (3 mm diameter). These were carried out in 1 wt.% NaCl at pH 7.

- The second variable was to measure the steel and Galvalloy® at a 1:1 (1 cm diameter) with varying pHs, pH 2, pH 3, pH 7, pH 10 and pH 13. The solution was 1 wt.% NaCl, adjusting the pH with NaOH and HCl.
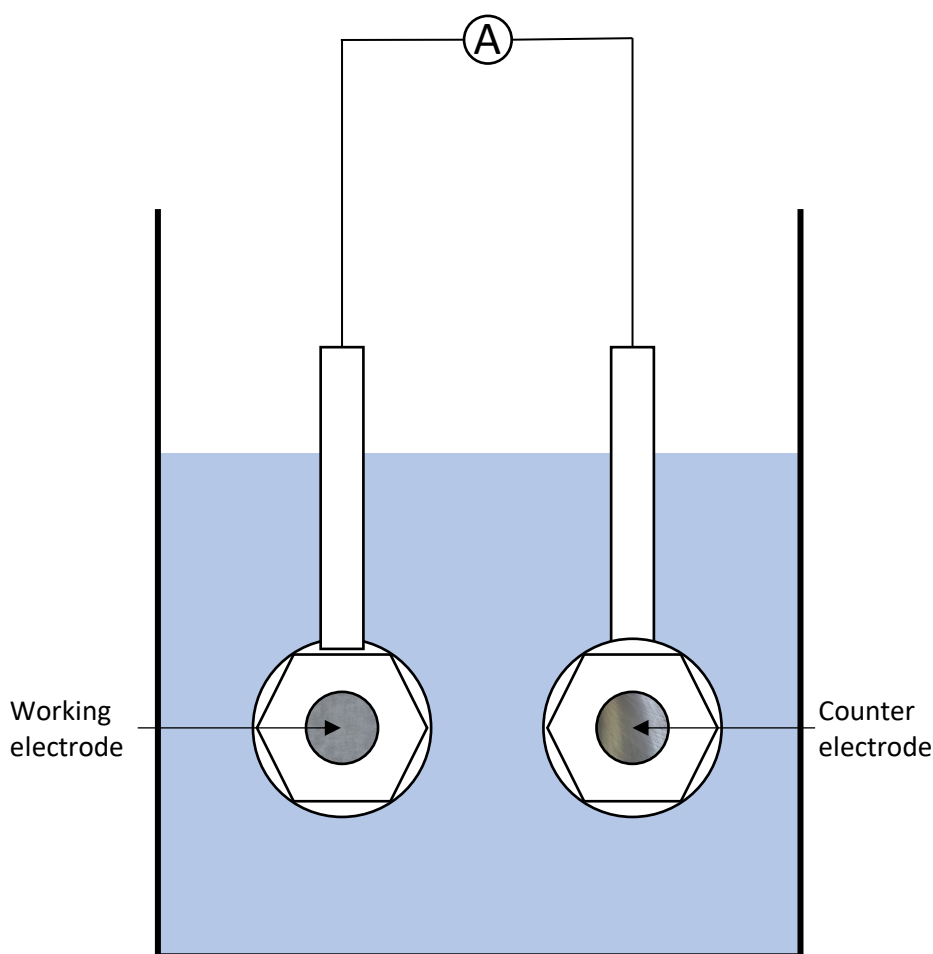
Fig. 2.12 Schematic of the two-electrode cell for zero-resistance ammeter electrochemical measurements.

2.11 Rotating Disk Electrode Measurements

A rotating disk electrode (RDE) was used to investigate the kinetics and mechanism of oxygen reduction as it occurs on the surface of pure iron, pure zinc, Zn-0.7wt.%Al (η), Zn-22wt.%Al (β) and Zn-68wt.%Al (α).

Circular samples were obtained of pure iron and pure zinc. The pure phases that were manufactured were punched into 22 mm diameter disks to fit the rotating disk electrode apparatus. The samples were abraded using European P grade P1200 silicon carbide paper to remove surface oxides. The samples were degreased and rinsed using ethanol and distilled water.

A 0.5 M sodium sulphate electrolyte buffered to pH 9.3 using 0.1 M sodium hydroxide (NaOH) and 0.05 M sodium tetraborate ($Na_2B_4O_7$) was used for the measurements. Neither pure zinc or iron are active at this pH, as their oxidation products are insoluble, avoiding high dissolution rates (27,53).

The rotating disk electrode apparatus was supplied by Sycopel Scientific and is shown in Fig. 2.13. A motor was mounted on two rails and controlled by a MC989 OE controller which allowed rotations of up to 50 hertz (3000 RPM).

The rotating electrode could be detached from the motor and is shown in Fig. 2.14. The metal disk that constituted the working electrode was held against a brass back plate. A rubber gasket was used to provide a seal between the disk and the closing nut. An area of 1.13 cm^2 was exposed. When rotating, an electrical connection was created using a mercury reservoir. The heat generated limited the time of experiments to avoid mercury spillage. All experiments were conducted at room temperature. Rotation speed was varied between 55 and 314 rads^{-1} as shown in

Table 2.2 RDE measured rotation speeds.

rads^{-1}	Hertz	RPM
55	8.75	525
108	17.19	1031
163	25.94	1557
217	34.54	2072
271	43.13	2588
314	49.97	2999

When immersing the electrode into the electrolyte an air bubble was often created, so the electrode was rotated to remove the bubble prior to measurement. E against current density *(i)* polarization curves were gained by means of a quasi potentiostatic technique, for which the potential did not change with scan rate (27). The disk potential was swept from above the onset of hydrogen evolution to E_{corr} and back to the starting point. The electrode was cathodically pretreated by holding potentiostatically. The sweep was automatically sweep was automatically reversed once an anodic current of +1 pA was detected. A sweep rate of 3.3 x 10^{-4} V.s^{-1} was used. A Gamry mercury/mercurous sulphate reference electrode was used over the more common calomel electrode to avoid production of chlorine ions (94).

Cyclic voltammograms with sweep rates of both 0.1667 mV.s^{-1} and 50 mV.s^{-1} were produced. Measurements were taken after sparging the cell compartment with nitrogen for 30 minutes to produce deaeration.
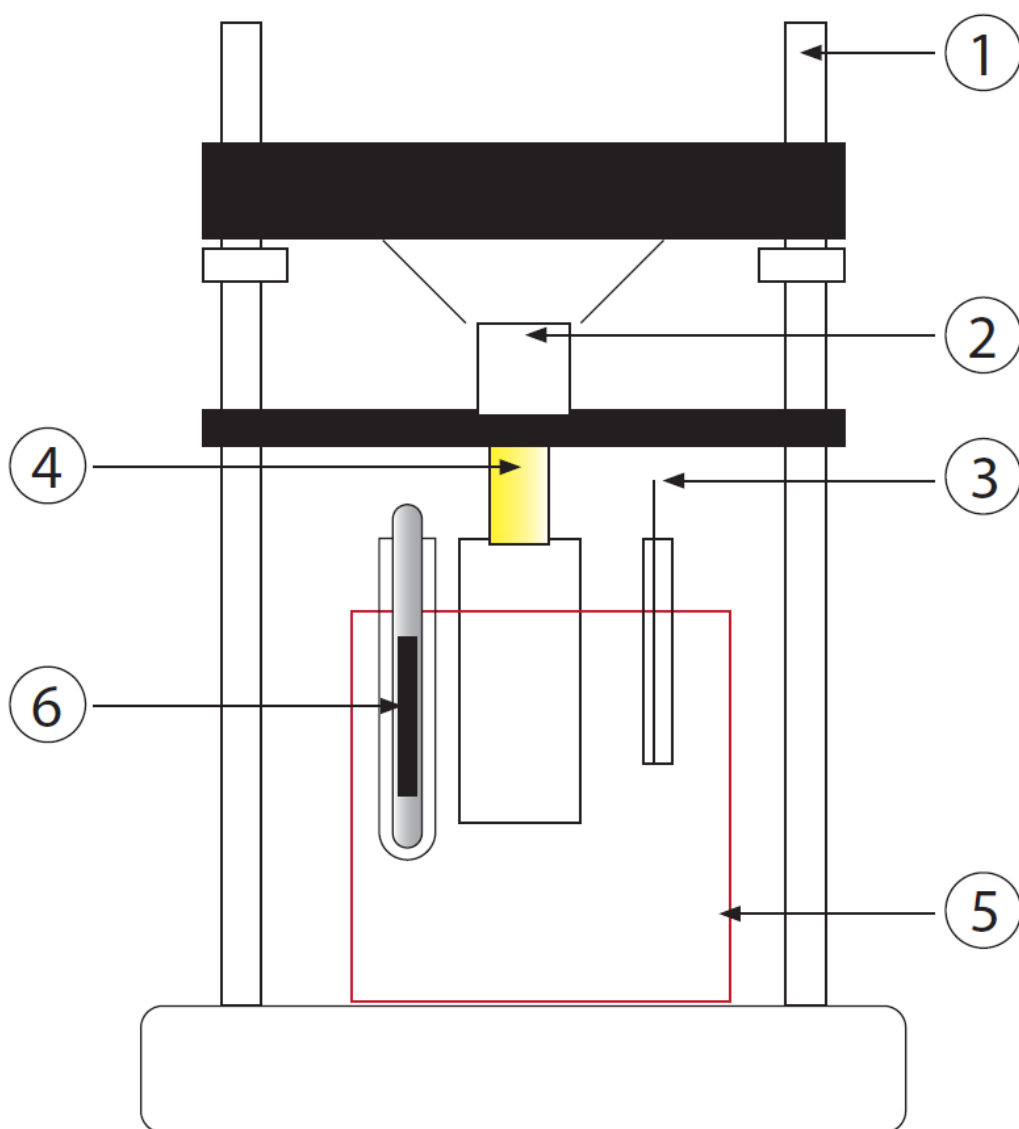
Fig. 2.13 RDE-2 Oxford Rotating Disk System 1) guide rail 2) motor 3) counter electrode 4) rotating (working) electrode 5) beaker (cell) 6) reference electrode.
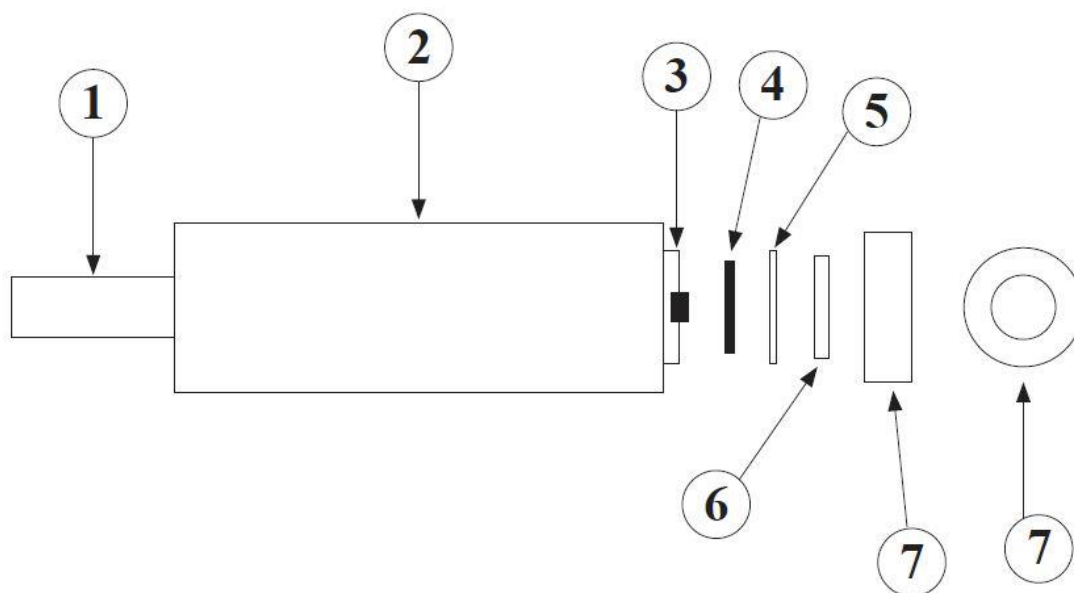
Fig. 2.14 The rotating disk electrode 1) connections point to motor 2) shaft 3) thread 4) brass back plate 5) sample 6) rubber gasket 7) closing nut.

2.12   Materials, Reagents and Chemicals Used

The experiments were performed in 1 wt.% NaCl of varying pH. pH 2, pH 3, pH 7, pH 10 and pH 13 were achieved with small additions of NaOH and NaCl.

The electrolyte was deaerated using nitrogen gas for 1 hour before experiments for deaerated electrochemical experiments.

Table 2.3 Table of materials, reagents and chemicals used.

Material	Supplier	Purity/Grade
Galvalloy®	TATA Steel	Production Line
NaCl	Sigma Aldrich	ACS Reagent ≥99.0 %
Acetone	Sigma Aldrich	Analar
Ethanol	Sigma Aldrich	Analar
HCl	Sigma Aldrich	12M 37.5%
KCl	Sigma Aldrich	ACS Reagent 99.0-100.5%
NaOH	Sigma Aldrich	Puriss 98-100.5 %

PVB	Sigma Aldrich	
PTFE tape	3M	1
Acetic Acid	Sigma Aldrich	
$FeCl_2$	Sigma Aldrich	98 %
Zinc	Goodfellows Cambridge Ltd.	99.998 %
Iron	Goodfellows Cambridge Ltd.	99.5 %
Aluminium	Goodfellows Cambridge Ltd.	
1μm MetaDi Supreme Polycrystalline Diamond Suspension	Buehler	
Non-conductive hot mount resin	Buehler	
MicroCloth	Buehler	
CarbiMet SiC P180	Buehler	
CarbiMet SiC P320	Buehler	
CarbiMet SiC P600	Buehler	
CarbiMet SiC P1200	Buehler	
CarbiMet SiC P2500	Buehler	
CarbiMet SiC P4000	Buehler	
Oxygen free Nitrogen	BOC	

Chapter Three

Surface and false cut-edge corrosion mechanisms of Galvalloy® in neutral pH NaCl electrolyte

3 Surface and false cut-edge corrosion mechanisms of Galvalloy® in neutral pH NaCl electrolyte

3.1 Introduction

As mentioned in the literature review of this thesis, steel is coated with zinc alloys, to improve the lifetime of the steel product, in a variety of industries, by sacrificial protection. The morphology of corrosion observed on Zn-Al coatings has previously been shown to depend upon the microstructure, which is in turn related to the process parameters employed during production (12–14,40,47,63,80,86,95–98). However, these findings were obtained using spectroscopy or physical weight loss and, as such, were limited by the assumptions made about which phases had been anodically attacked. Microscopy, which allows for in-situ observation of the phases being attacked, was not performed in either the case of surface or cut edge corrosion (13,99–101).

The sub-micron sized microstructure of Galvalloy® has limited the amount of research which focuses on its initial corrosion behaviour (40).

This chapter aims to determine the mechanism by which Galvalloy® coatings corrode both in isolation (surface) and coupled to the steel substrate (cut-edge) immersed in 1 wt.% NaCl. As such, the in-situ time-lapse microscopy technique is used to provide mechanistic information regarding the corrosion of individual phases within the alloy. The technique has previously been used to provide mechanistic information regarding the corrosion of ZMA alloy coatings (46,47). A rotating disk electrode (RDE) technique has subsequently been employed to explain these results in terms of the electrocatalytic activity of the constituent phases of Galvalloy® for the CORR. These have then been supported by potentiodynamic polarisation (PD) experiments of the same phases in order to inform on the anodic behaviours.

3.2 Experimental

The Sample and Experimental Preparation (2.7.1), Potentiodynamic Polarisation (2.10.4) and Rotating-Disk Electrode (RDE) (2.11) sections in the methods chapter detail the experimental procedure carried out for this chapter.

3.3 Results

3.3.1 Microstructure of Galvalloy®

3.3.1.1 Optical Light Microscopy of Galvalloy®

Optical light microscopes images were taken of the Galvalloy® coating and are shown in Fig. 3.1. The micrographs show the zinc-rich eta (η) proeutectic primary dendritic phase (Zn0.7Al), which appears as the lighter regions, surrounded by a lamellar of the Zn-Al eutectic phase darker region, which is predicted from the phase diagram to be made up of zinc-rich eta (η) and Zn22Al (β).
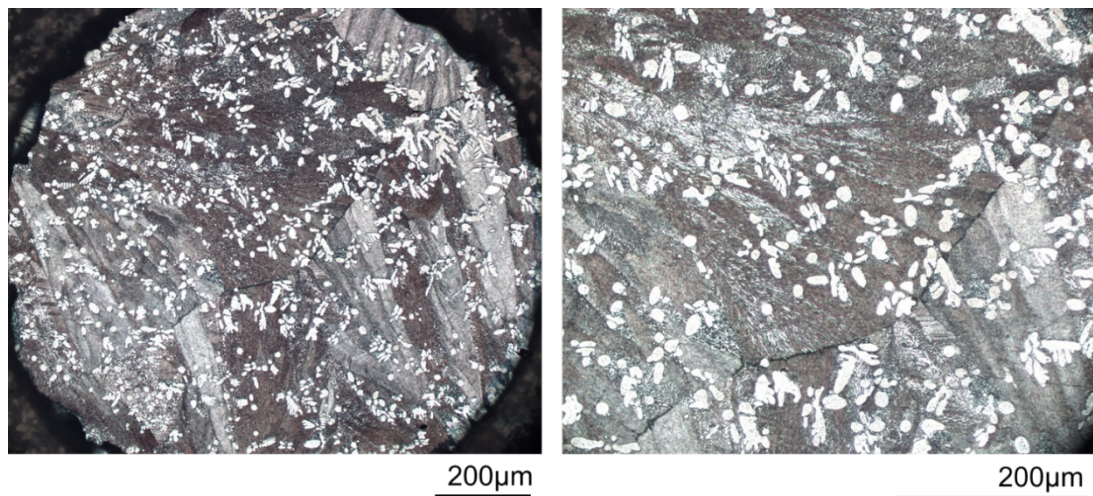
Fig. 3.1 These Optical Light Microscope images of the microstructure of Galvalloy®. The lighter region of the microstructure are the primary zinc dendrites, whilst the darker regions are the Zn-Al lamellar eutectic phase.

3.4 Scanning Electron Microscope (SEM) Images of Galvalloy®

High magnification and resolution images of Galvalloy® were captured using a Hitachi TM3000 desktop SEM, and are shown below in Fig. 3.2. The images clearly show, once again, the primary Zn dendrites at 1000 x zoom. This higher magnification lends itself to a more detailed image of the fine dendritic microstructure. Another notable feature of the Galvalloy® coating seen are the solidification defects at the boundary between the nodules (10). Additionally, the higher magnification image of the eutectic shown in Fig. 3.2b) shows that the dark Zn22Al (β) lamellae predicted from the phase diagram were actually composed of a two-phase structure themselves, namely Zn (η) and Zn68Al (α). The presence of only two phases in the microstructure as a whole was confirmed by X-ray diffraction (XRD) analysis as shown in Fig. 3.3 where Zn (η) and Zn68Al (α) were the two phases detected.
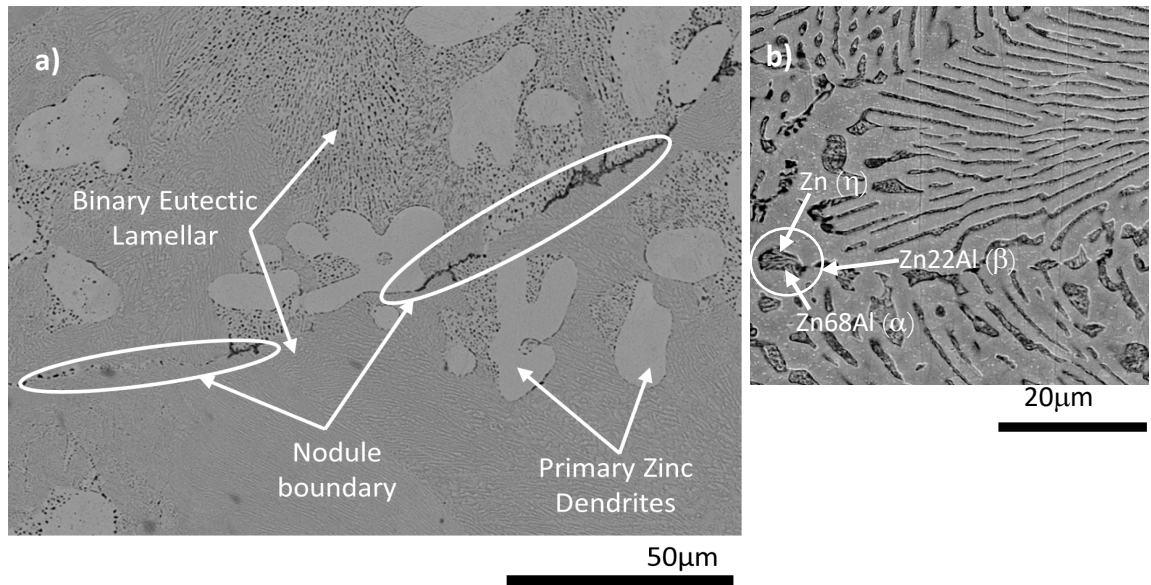
Fig. 3.2 a) Scanning Electron Microscope Image of the microstructure of Galvalloy® at 1000x zoom. Shows the Zn primary dendrites surrounded by the binary eutectic lamellar phase of Zn-Al. b) Magnified image of eutectic phase showing Zn (η) (light) and Zn22Al (β) (darker) lamellar. The Zn22Al (β) has a sub-microstructure within its lamellae composed of Zn (η) and Zn68Al (α).
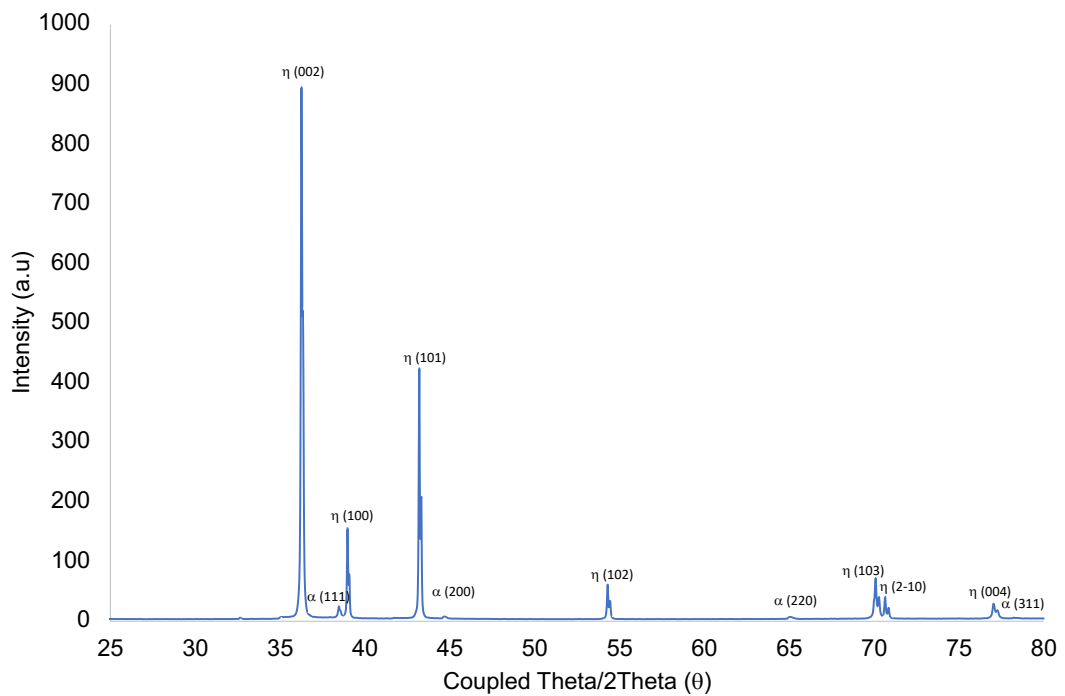
Fig. 3.3 XRD pattern of Galvalloy® surface, demonstrating the existence of the Zn (η) and Zn68Al (α) phases.

3.5 Galvalloy® in pH 7 1 wt.% NaCl: surface

Video 3.1, depicted as stills in Fig. 3.4, shows the Galvalloy® when immersed in pH 7 1 wt.% NaCl electrolyte. After 100 minutes, anodic features (indicated by the circles) are present within the binary eutectic Zn-Al lamellar phase. The anodes continue to grow in size and at 300 minutes a prominent corrosion product ring can be observed. The formation of this corrosion product ring has been observed previously and was suggested to form at the boundary of ionic counter currents from the anode and cathode (47). The surface of the coating appears to optically brighten both from the bottom right quadrant, and in a horizontal line halfway up the top section. This brightening seems to expand and be coincident with developing cathodic regions of the electrochemical reaction. Concurrently, the anodic regions optically darken which can be attributed to 1) small undulations, due to metal dissolution, cause reduced reflectance, 2) corrosion products on the surface and 3) it is comparatively dark compared to the brightened cathodic region.
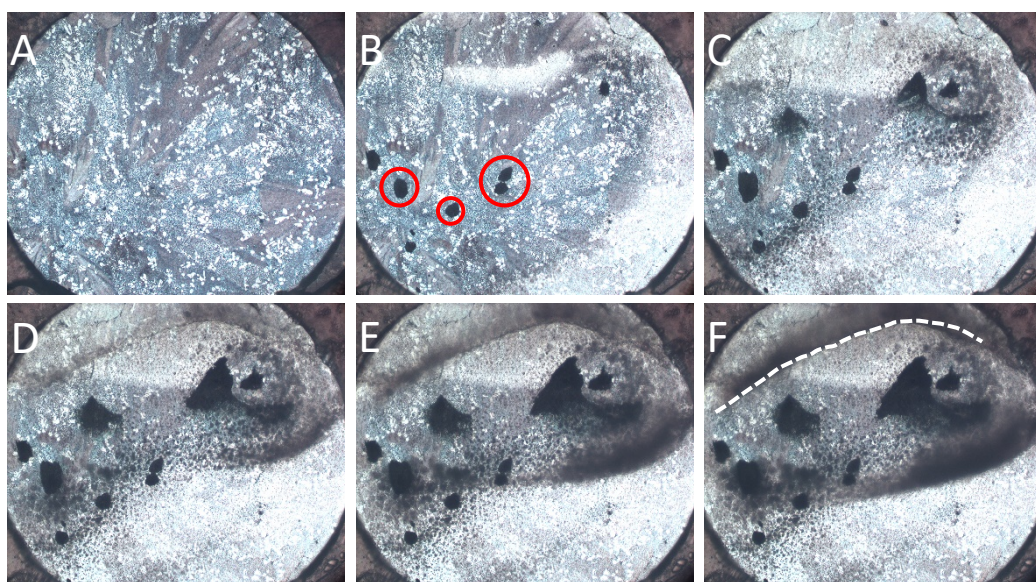
Fig. 3.4 Images A-L: Time-lapse microscopy images of Galvalloy® surface corrosion when immersed in 1 wt.% NaCl electrolyte solution. The time interval between each of the micrographs is 100 minutes hours totalling 500 minutes. The red circles show the initial anode formation. The images also show a brightening in the regions of cathodic activity, due to the surface oxide layer being removed to allow for sufficient electron transfer. Meanwhile, the regions where anodes appear remain a darker shade. The regions in-between the notable cathodic and anodic activity areas is the location for corrosion product deposition. The outline of which is marked by a dotted white line in image F. These images depict Video 3.1.

Fig. 3.5 Time-lapse images specifically showing the anode growth on the Galvalloy® surface over a 100-minute period. The micrographs show the anodic growth in the binary eutectic Zn-Al phase leaving the primary Zinc dendritic phase intact. At 300 minutes it shows the anode engulfing the primary zinc dendrite, whilst also demonstrating a resistance from the dendrite.
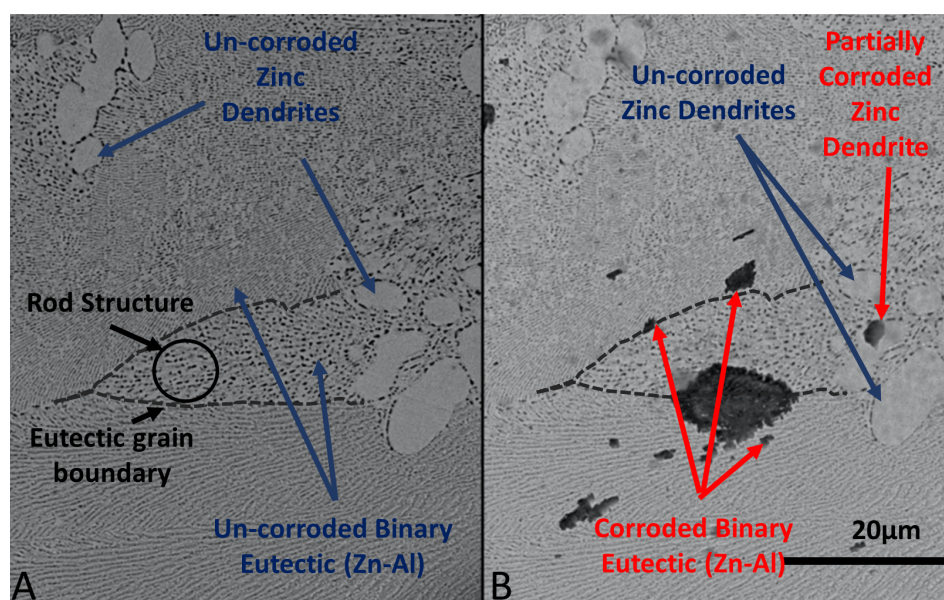
Fig. 3.6 SEM images of Galvalloy® a) prior to and b) after 45 minutes of immersion within pH 7 1 wt.% NaCl.

The technique allows for the acquisition of high-quality images on a microstructural level allowing the identification of phases in which initial attack occurs. Fig. 3.5 shows images from Fig. 3.4 at various immersion times and illustrate that the anodes initiate and propagates in the eutectic region and at 300 minutes will not propagate into the adjacent zinc dendrite. Fig. 3.6 shows SEM images of the Galvalloy® surface prior to, and post 45 minutes, immersion in pH 7 1 wt.% NaCl. The black regions in Fig. 3.6B correspond to anodic areas where metal dissolution has occurred. The largest site in Fig. 3.6B appears to have initiated in the binary eutectic region, and more specifically, on the boundary between two binary eutectic grains. This anode appears to have grown into both grains at a similar rate. The region at the top of the boundary appears to have a rod structure suggesting that the orientation of the growth is roughly perpendicular to that of the neighbouring grain colony (70).

In comparison, the initial stages of metal dissolution in the lamellar occurs along the lengths of the lamellar instead of forming a circular anode that grows radially as seen in Video 3.1.

3.6   Galvalloy® in pH 7 1 wt.% NaCl: cut-edge

For the cut-edge experiments, the Galvalloy® sample was prepared the same way as the surface experiment. The sample is not a true cut-edge, but is a flat specimen where some of the underlying steel has been exposed in an area immediately adjacent to the Galvalloy® region which is visualised in the figure below. In order to expose the steel, the sample was taped with PTFE tape across leaving an area exposed. The sample was then held, using a stand apparatus, in a solution of 2M HCl. It was held in this position for roughly 20 mins, long enough for the Galvalloy® coating to be removed from the steel substrate. This process left an area of 25% steel exposed. This is not completely representative of the real cut-edge as the gauge of the steel would be around 0.7 mm vs. the 0.02 mm used here. The reduced amount of steel here is expected to produce a reduced rate of cathodic activity on the steel and therefore reduced anodic activity on the Galvalloy® which allows for slower-motion detail to be captured. Advancements in polishing techniques will allow for a real cut-edge to be captured using a light microscopy. Video 3.2, shown in Fig. 3.7, shows Galvalloy® when immersed in 1 wt.% NaCl. The corrosion initiated after 24 minutes, shown in image Fig. 3.7A, at which point an anode is observed in the primary zinc dendrite phase adjacent to a nodule boundary. 6 minutes later (Fig. 3.7B), another anode forms in a primary zinc dendrite located on the same nodule boundary. When comparing images, A and C from Fig. 3.7, it is very apparent that the only regions that have undergone metal dissolution, during the 68-minute time-period, are the zinc-rich dendrites (η).
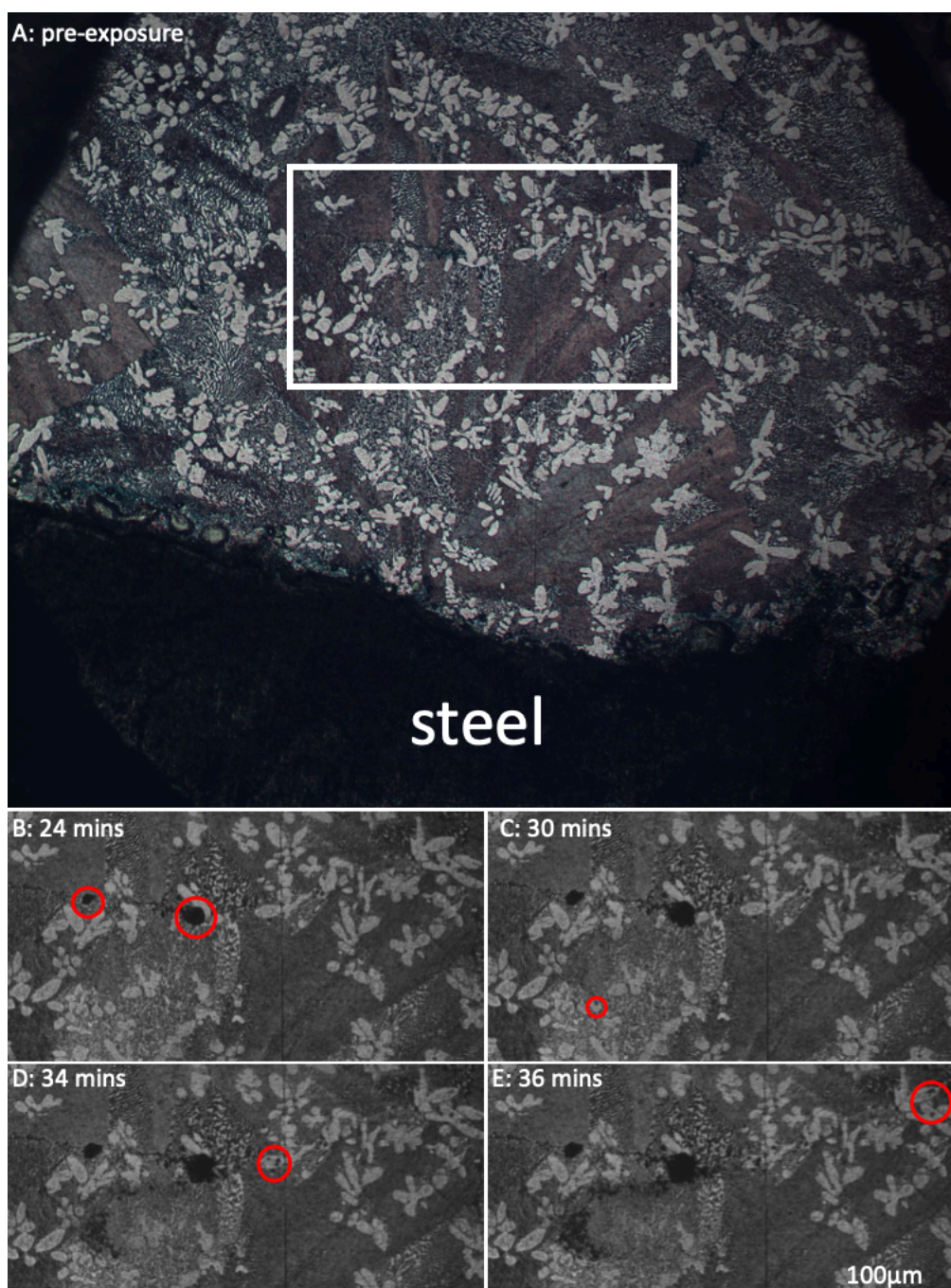
Fig. 3.7 Image A: Galvalloy® and exposed steel (labelled) prior to immersion in electrolyte. Images B-E: Time-lapse microscopy of Galvalloy® immersed in 1 wt.% NaCl electrolyte with 25% of the surface exposed to Steel. The time interval between the micrographs is 34 minutes, with a time of 36 minutes at the last micrograph. The images show anodes forming along the nodule boundary in the dendritic region almost immediately, indicated by red circles. These stills depict Video 3.2.

3.6.1 SEM Images of Unetched Galvalloy® After Immersion in 1 wt.% NaCl

The Galvalloy® sample preparation was the same as the rest of the samples tested, however, the etching process was not performed. An exposed area of roughly 0.2 mm² was exposed to pH 7 1 wt.% NaCl electrolyte for 30 mins to allow for corrosion to initiate. This allowed the investigation to eliminate the corrosion mechanism being attributed to artefacts of the etching process.

Fig. 3.8 shows the surface after this exposure. The corrosion has initiated in a small section of the lamellar and is still in its infancy. The anode has grown to a length of around 2 μm, along the direction of the lamellar, which is consistent with previous results. In Fig. 3.8B, the corrosion has initiated in the binary eutectic lamellar and grown radially until the anode reaches the periphery of the surrounding dendrites which appear to have developed partial anodes growing along the interface between the dendrite and the eutectic rather than directly into the microstructure.
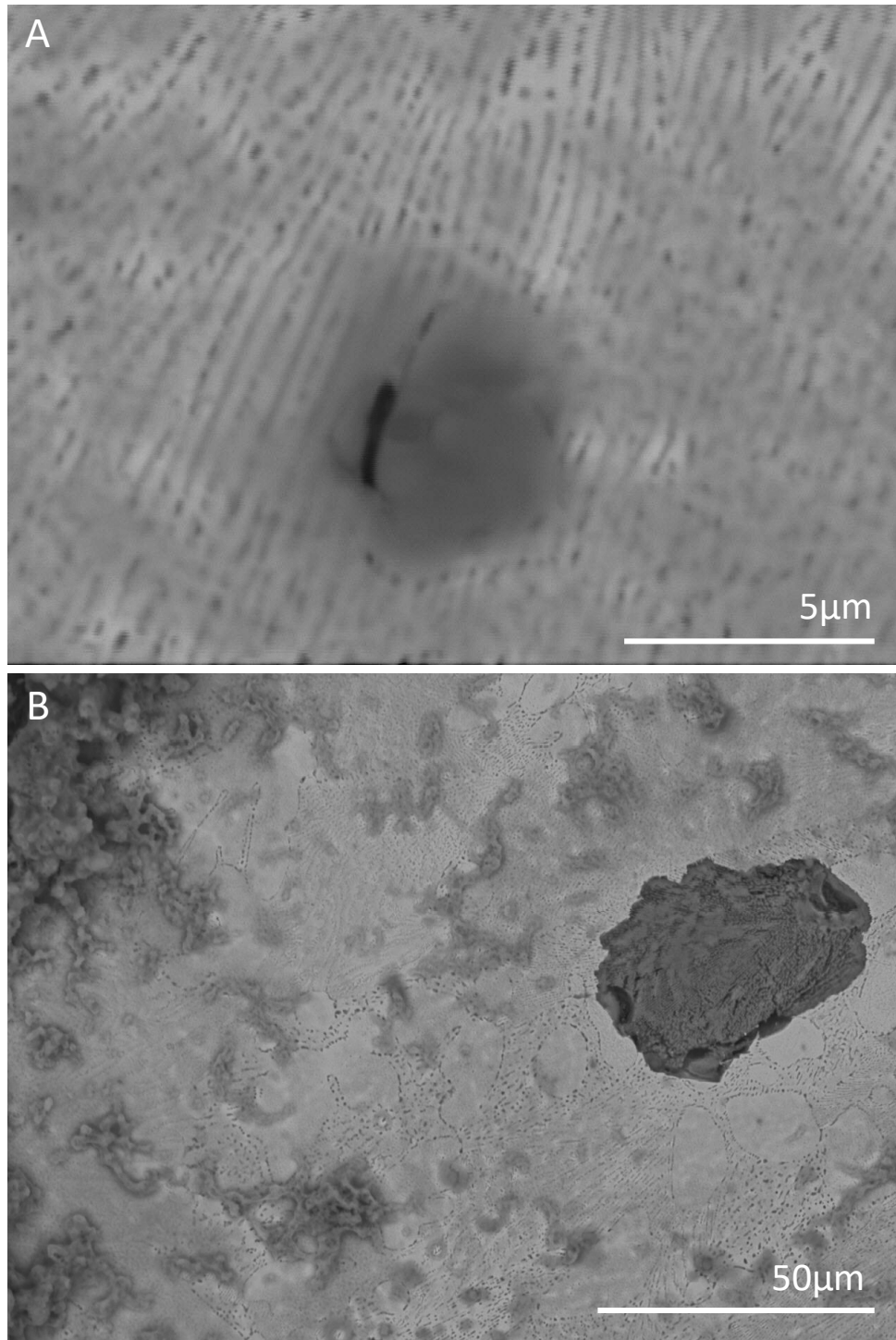
Fig. 3.8 SEM images of unetched Galvalloy® after immersion in 1 wt.% NaCl pH 7 for 30 minutes. Both images were taken on a Hitachi TM3000 with image A taken at 9000 x magnification, and image B taken at 1000 x magnification. Both images show the corrosion initiation in the binary eutectic region of the microstructure. In image A the corrosion is seen in on layer of the lamellar, and in image B the corrosion appears to have initiated in the eutectic and spread until it contacts several dendrites.

3.7   Potentiodynamic polarisation of pure phases in Galvalloy®

Anodic going polarisation curves for pure zinc, Zn0.7Al, Zn22Al and Zn68Al are shown in Fig. 3.9. The E_{corr} (Table 3.1) is shown to increase with increasing Al content in the phases, from ~ -0.79 V vs. SHE for pure zinc to ~ -0.72 V vs. SHE for Zn68Al. The i_{corr}, from the polarisation curves, is almost identical for pure zinc and Zn68Al, the icorr increases 10-fold from the pure zinc and Zn0.7Al to the Zn22Al.
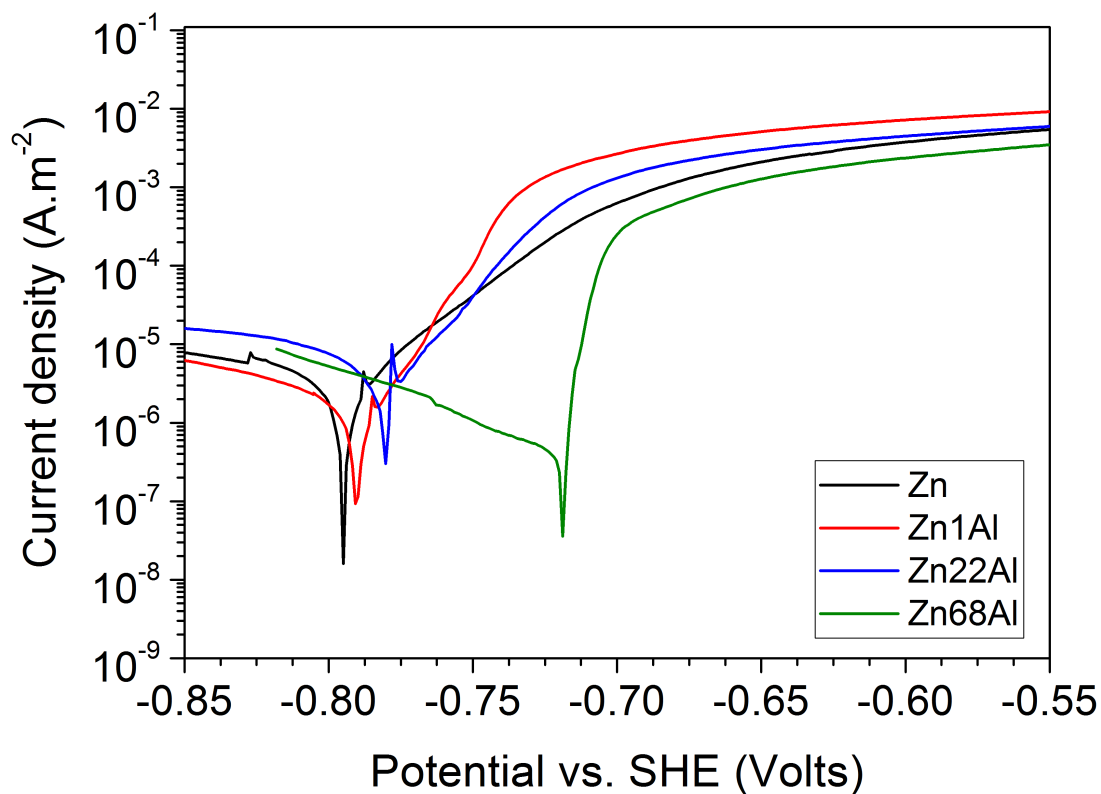
Fig. 3.9 Potentiodynamic anodic polarization curves of pure zinc, Zn0.7Al, Zn22Al and Zn68Al in aerated 1 wt.% NaCl at pH 7.

Table 3.1 E_{corr}, i_{corr}, as extracted from Fig. 3.9.

Phase	E_{corr} vs. SHE	i_{corr} (A.cm^{-2})
Zn	-0.795	8.0 x 10^{-7}
Zn0.7Al	-0.79	5.2 x 10^{-7}
Zn22Al	-0.78	1.7 x 10^{-6}
Zn68Al	-0.72	2.8 x 10^{-7}

3.8   Rotating Disk Electrode (RDE) of pure phases in Galvalloy®

In order to characterize the various surfaces in terms of their relative ability to electrocatalyze the cathodic oxygen reduction reaction (CORR), a series of polarization experiments were carried out using a RDE using the method found in the Rotating Disk Electrode Measurements section in chapter 2.

Anodic going polarisations were performed in order to observe the cathodic current of the samples at cathodic potentials, minimalizing the amount of anodic currents detected. The curves obtained at different rotation speeds for a.) pure zinc, b.) Zn0.7Al, c.) Zn22Al, d.) Zn68Al and e.) pure iron are shown in Fig. 3.10. Well-developed rotation speed dependent current plateaus are developed < -0.95 V vs. SHE for pure zinc and Zn0.7Al, and < -0.4 V vs. SHE in the case of pure iron. In the case of Zn68Al the current plateaus values appear to be independent of the rotation speed. The divergence in behaviour in the case of both Zn22Al, and to a greater extent ZnAl68, is as yet undetermined, but may be a result of the higher Al content.

The dependence of current density on rotation speed is indicative of diffusion control and the Levich equation (Equation 3.1) can therefore be used to predict the limiting current

$$i_L = 0.62nFD^{\frac{2}{3}}v^{-\frac{1}{6}}c\omega^{\frac{1}{2}} \qquad 3.1$$

where i_L is the limiting current, n is the number of electrons transferred per molecule of oxygen reduced, F is the Faraday constant (96485 C.mol^{-1}), c the bulk concentration of dissolved oxygen (mol.cm^{-3}), D is the oxygen diffusion coefficient (cm^2.s^{-1}), v is the kinematic viscosity (cm^2.s^{-1}) and ω is the angular velocity (rad.s^{-1}) (52). Values of D and c were taken from published data (D=1.74 x 10^{-5} cm^2.s^{-1}, v=10^{-2}cm^2.s^{-1}) (102).

The Levich plots shown in Fig. 3.11 are constructed using i vs. $\omega^{1/2}$ values obtained from Fig. 3.10. The i values used in each case were taken at the greatest cathodic overpotential possible whilst minimising the contribution of cathodic current from competing reactions, for example hydrogen evolution. Fig. 3.12 also includes the theoretical Levich slopes for 4 (69.3 x 10^{-6} A.cm^{-2}.s$^{-1/2}$) and 2 (34.7 x 10^{-6} A.cm^{-2}.s$^{-1/2}$) electron pathways of the CORR (given by Equations 3.2 and 3.3 respectively). Oxidation of H_2O_2 can also occur via reaction in Equation 3.3 and it is therefore possible to observe 4e$^-$ and 2e$^-$ pathways both alone and in parallel.

$$O_2 + H_2O + 4e^- \rightarrow 4OH^- \qquad\qquad 3.2$$

$$HO_2^- + H_2O + 2e^- \rightarrow 3OH^- \qquad\qquad 3.3$$
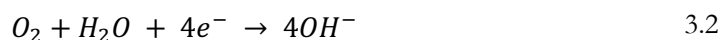
The currents used are not purely diffusion controlled and the experimental slopes obtained are consequently offset from the theoretical slopes. This offset value corresponds to the kinetic current term i_k. Linear regression analysis of each data set was completed to calculate the experimental Levich slope values, which are shown in Table 3.2, along with corresponding values for ne^-. With the exception of ZnAl68 the values obtained are consistent with diffusion controlled 4 electron CORR via Equation 3.2. Rotating ring disk electrode (RRDE) studies on iron at near neutral and alkaline conditions have previously shown that O_2 is reduced to hydroxyl ions (OH$^-$) via reaction (1) at potentials values for which the metal surface was bare. (103–105). Conversely, when the surface was oxide covered, the reaction shown in Equation 3.2 became the dominant pathway. In the case of Zn and Al alloy galvanized coatings (27) the dominant reduction pathway and the electrocataytic behaviour of the alloy was found to be determined by the Zn component of the coating. The Al constituents of ZnAl coatings remained hydr(oxide) and changing the Al content had little effect on the behaviour observed (27).

Table 3.2 Experimental Levich slope values calculated by linear regression analysis of each phase data set.

Electrode	Levich Slope (x 10^{-6} A.cm^{-2}.s$^{-1/2}$)	Value of ne$^-$
Iron (Fe)	68.8	3.97
Zinc (Zn)	93.6	5.41
Zn0.7Al	67.5	3.90
Zn22Al	71.2	4.11
Zn68Al	40.7	2.35

The value of n obtained for Zn68Al is 2.3, this being similar to that obtained previously in the case of Zn55Al coatings. (27) During this work the deviation from $n = 4$ was attributed to the aluminium rich areas of the coating remaining inert and 4 electron CORR only occurring on the zinc rich portion of the microstructure. (27).
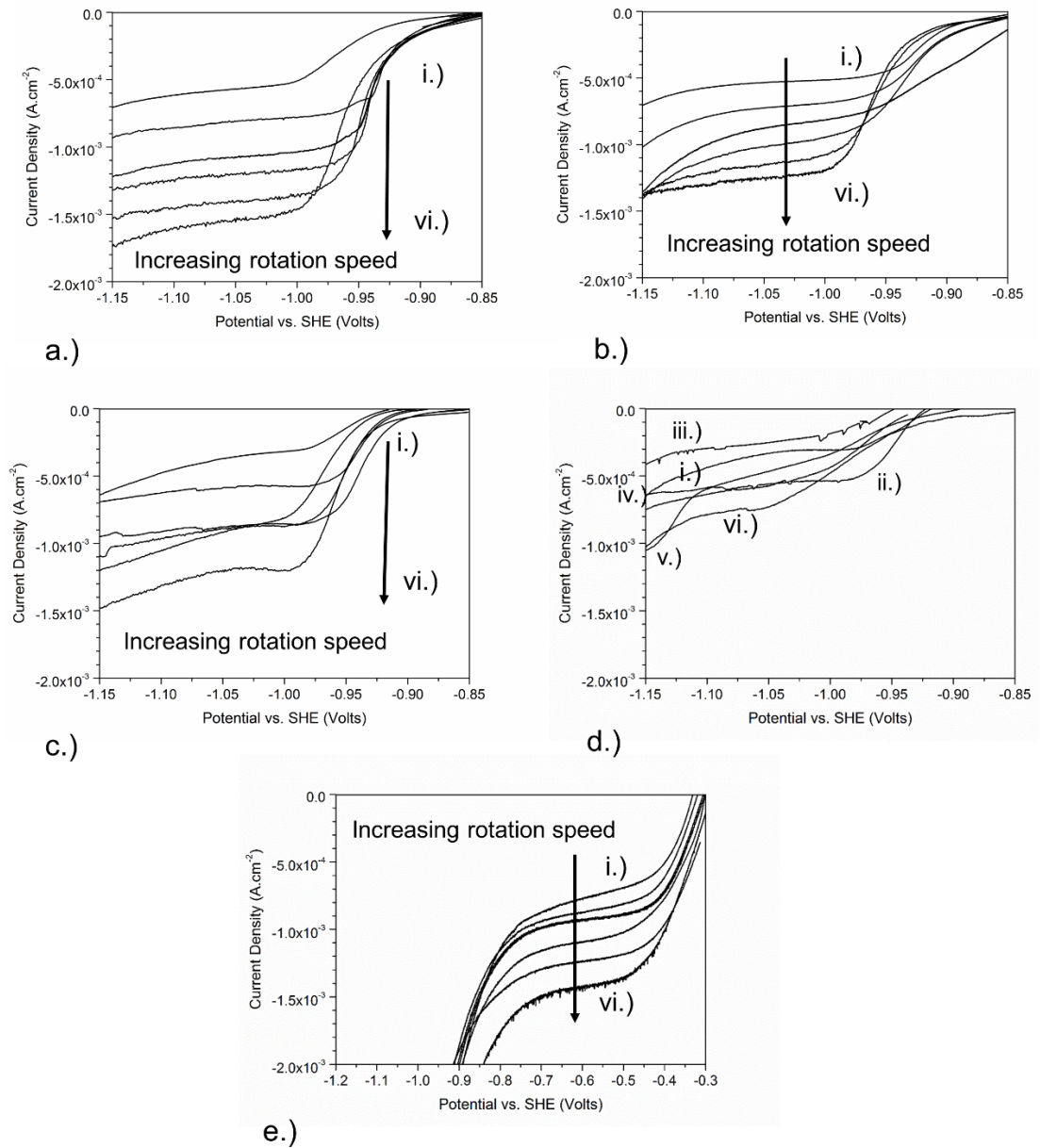
Fig. 3.10 Disc current density as a function of potential for a.) Zn (99.998%), b.) Zn0.7Al, c.) Zn22Al, d.) Zn68Al and e.) pure iron in aerated 0.5 M Na₂SO₄ buffered to pH 9.3. Potential sweet rate 3.3 x 10⁴ V.s⁻¹. Angular velocity key: i) 55, ii) 108, iii) 163, iv) 217, v) 271, vi) 314 rad.s⁻¹.
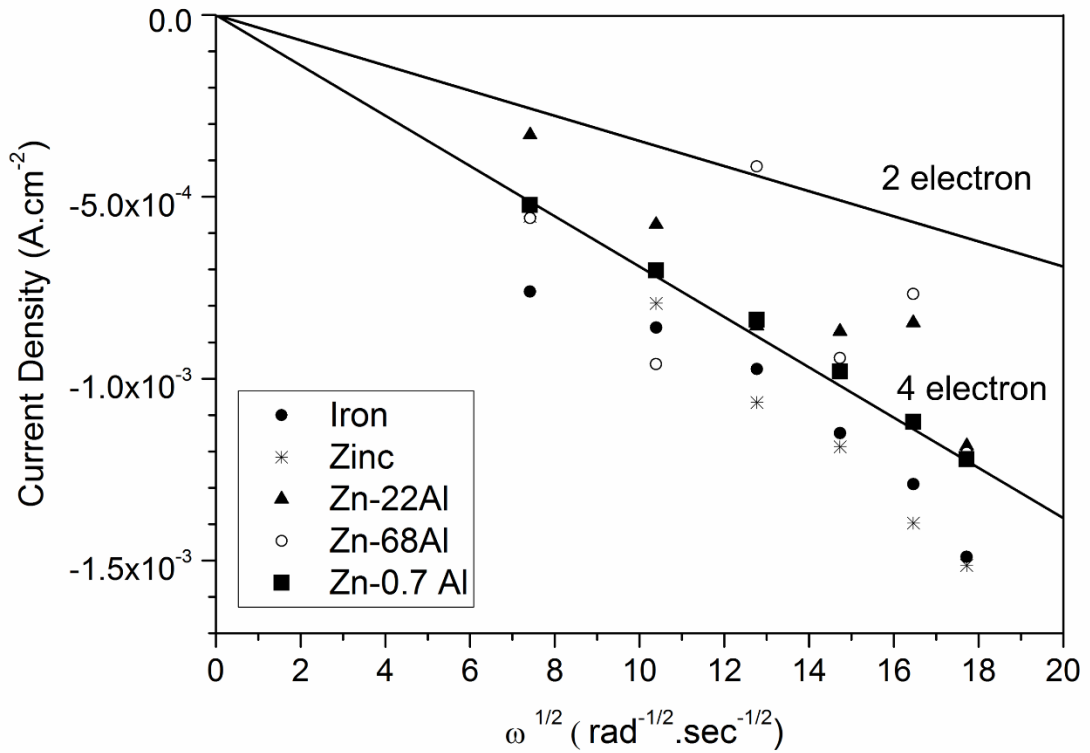
Fig. 3.11 Levich slope obtained from anodic going potentiodynamic experiments, alongside theoretical values for 4e⁻ and 2e⁻ oxygen reduction in 0.5 M Na₂SO₄ buffered to 9.3.

The CORR overpotential can be used as an electrochemical parameter by which to determine the relative electrolycatalytic activity of materials to the CORR. The CORR, as it occurs on iron, has previously been shown to be first order with respect to O_2 (104). In this instance the Levich-Koutecky equation, given by Equation (3.4), can be used to determine a value for the kinetic current density (i_k).

$$\frac{1}{i} = \frac{1}{i_k} + \frac{1}{i_L}$$

3.4

Values of the overpotential for oxygen reduction (η_{OR}) were calculated using Equation 3.5 and Equation 3.6, assuming the partial pressure of oxygen to be 0.2 atm.

Values of E were obtained from the quasi potentiostatic curves recorded at rotation speed $\omega=271$ rad.s⁻¹ (shown in Fig. 3.13) as this was considered a compromise between maximising i_L and therefore the useable region of i_k, whilst preventing error introduced by the decreased signal to noise ratio observed at higher speeds . The value was taken from a region where the overpotential value obtained was, as much as possible, a kinetic overpotential (with minimum diffusion contribution), but at which the contribution of anodic current was believed to be limited.

$$\eta_{OR} = E - E_{eq} \tag{3.5}$$

$$E_{eq} = 1.228 - 0.0591\,pH + 0.0147\log pO_2 \tag{3.6}$$

Fig. 3.13 shows that pure zinc, Zn0.7Al, and Zn22Al are all associated with a similar η_{OR} of 1.62 V vs. SHE. The η_{OR} value associated with Zn68Al is ~0.05 V greater, suggesting that it is a poorer electroctalyst for CORR. In comparison, iron is the best electrocatalyst of CORR coatings and is associated with a significantly lower η_{OR} value of ~1 V vs. SHE.

It should at this point be considered that the η_{OR} values displayed in Fig. 3.13 are given for current density values calculated based on the geometric surface area and as such does not account for variation in true surface area (for example due to porosity) from material to material.
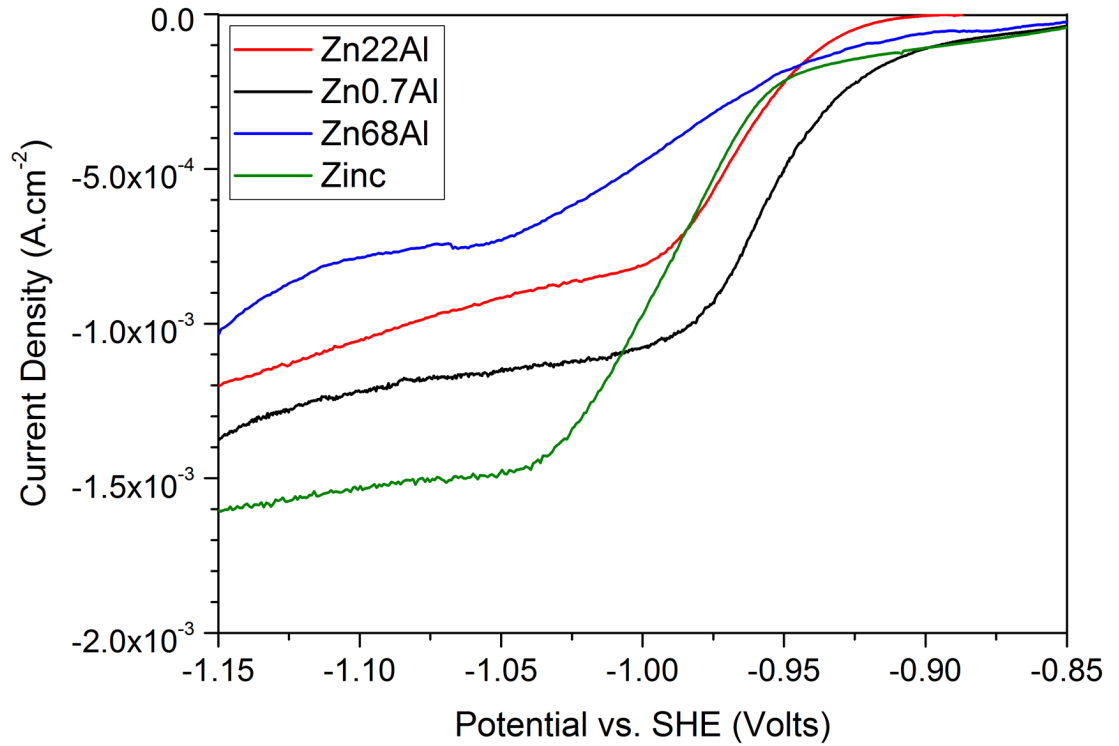
Fig. 3.12 Anodic going polarization curves obtained in aerated 0.5 M aqueous Na2SO4, borate buffered at pH 9.3. Potential sweep rate 3.3 × 10−4V.s−1. Angular velocity 271 rad.s−1.
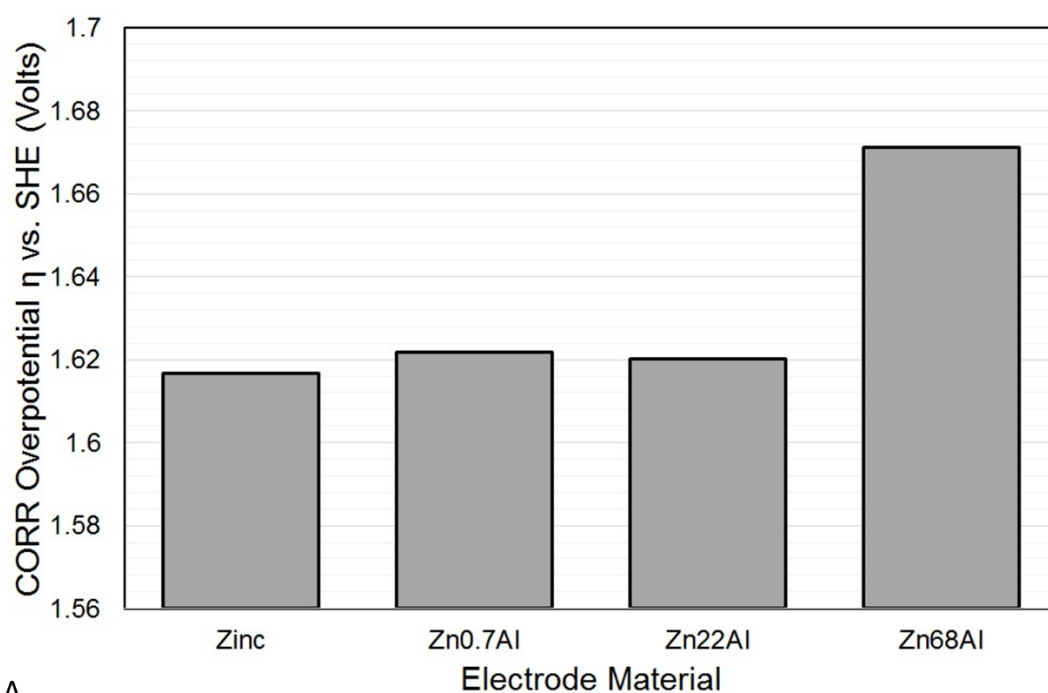
A
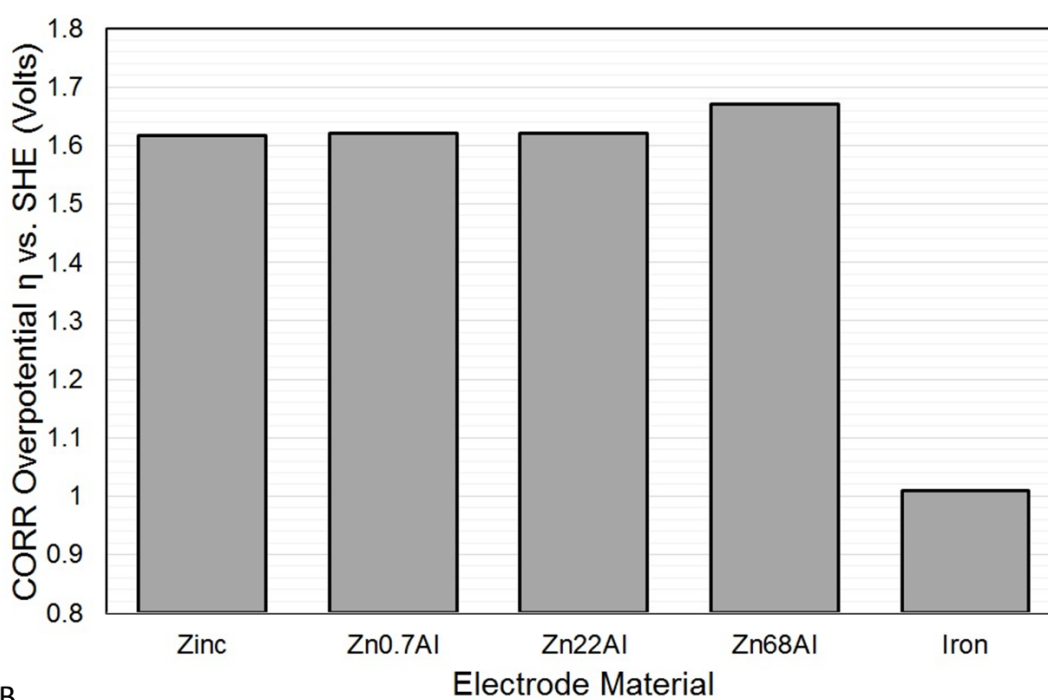
B

Fig. 3.13 Overpotential for oxygen reduction acquired from anodic polarization curves obtained for pure Zn, Zn0.7Al, Zn22Al, Zn68Al and pure iron tested in aerated 0.5 M Na_2SO_4 buffered to pH 9.3. Potential sweep rate $3.3 \times 10^{-4} V.s^{-1}$. Rotation rate 271 $rad.s^{-1}$.

3.9   Discussion

There is a distinct difference in the mechanism of Galvalloy® surface corrosion compared to that which occurs at the cut edge in the case that the steel substrate is exposed. In the former case, corrosion initiates within the binary eutectic ZnAl region and propagates until dissolution of the zinc dendrites also occurs as seen in Fig. 3.5. It is proposed that surface corrosion is cathodically controlled. Zn dendrites, which are associated with the lowest relative overpotential for the ORR, will thus become the sites of cathodic activity (Fig. 3.5) and anodic attack will occur within the eutectic region. Despite the Zn22Al phase having a similar overpotential to the zinc-rich phases, at room temperature the Zn22Al is unstable as a pure phase and transforms to a eutectoid structure composed of Zn (η) and Zn68Al (α) as shown in section 1.2.2. Zn68Al (α) has a greater overpotential for CORR than Zn (η) and hence the presence of Zn68Al (α) within the eutectic especially in a lamellar morphology may render this phase somewhat discontinuous in terms of its ability to support CORR in comparison to the larger and uniform Zn (η) dendrites. This will result in a reduced ability to support ORR in the eutectic region, which will favour the cathodic activity at the Zn dendrites and anodic attack in the eutectic regions.

Visible corrosion products observed by means of SEM seem to start forming in the slightly Zn-richer Zn (η) phase adjacent to the Al containing phase as shown in Fig. 3.6. This would again support the notion that the Zn (η) phase is more anodically susceptible than the Al containing regions due to the presence of Alumina at the Al rich areas (40).

In comparison, in the case of cut-edge corrosion, steel is exposed to electrolyte and becomes galvanically coupled with the overlying Galvalloy® coating. The relative nobility of the steel (106), compared to Galvalloy® means that it becomes cathodic, the alloy becoming a net anode. The preferential site of anodic attack within the coating will then be determined by the relative susceptibility of the phases present. As shown in Fig. 3.7 corrosion initiates within the zinc rich dendrite phase, which is consistent with previous studies (13,14,70,86). This observation is consistent with Fig. 3.9, which shows the increased anodic current associated with zinc rich phases compared to the Zn22Al and Zn68Al as they are covered in a protective alumina film.

It is worth considering the mechanisms of corrosion discussed within this paper may change at extended time periods as a result of the progressive dezincification and increasing O_2 reduction overpotentials on the cathodically inert aluminium (107). The relative stability of Al-rich phases present within Zn-5Al are strongly dependent upon pH (95) and are likely to activate upon alkalization which occurs as a result of the ORR (97,98).

3.10 Conclusions

An investigation into the mechanism of surface and cut edge corrosion of Galvalloy® was completed using time-lapse microscopy and electrochemical techniques. The results showed that;

- The coating consists of Zn-rich primary dendrites and a lamellar ZnAl binary eutectic phase.

- Surface corrosion of Galvalloy® is initiated and propagates through the binary eutectic region.

- Corrosion on the 'cut-edge' of Galvalloy® initiates in the primary zinc dendrites and propagates through the microstructure.

- The relative electrolytic activity for the CORR was found to decrease in the order Fe≫Zn,Zn0.7Al,Zn22Al>Zn68Al

- Potentiodynamic results showed that, if polarised by a more noble metal such as steel, the zinc-rich phases were least stable thermodynamically and would exhibit the highest anodic currents.

- In the case of surface corrosion, anodic attack is cathodically controlled. The phase which exhibits the highest relative electrolytic activity for the CORR is Zn0.7Al and the zinc dendrites become cathodically polarized. Corrosion is subsequently initiated within the eutectic phase.

- In the case of cut edge corrosion, the exposed steel substrate acts as the cathode. The initial site of corrosive attack is therefore determined by the relative susceptibility of the phases present within the Galvalloy® coating, to anodic attack. Zn0.7Al and Zn are associated with the highest anodic currents and therefore the site of initial attack when iron acts as the cathode.

Chapter Four

Surface corrosion mechanism of Galvalloy® in saline electrolyte as a function of pH

4 Surface corrosion mechanism of Galvalloy® in saline electrolyte as a function of pH

4.1 Introduction

This chapter is a direct continuation from the previous chapter, as the experimental techniques utilised are the same, expanding on the pH of the electrolyte. The Galvalloy® (Zn4.8Al) corrosion resistant coating is used in many products and those products are used in different industries such as marine (chloride rich), civil, industrial (sulfur rich) and agricultural (ammonia rich). A specific case study is the Colorfarm® product that was used as cladding in a foie gras farm building where the ducks were being held. The coatings are all designed and guaranteed to perform in these environments. Therefore, it is prudent to understand how the Galvalloy® coating performs.

The thermodynamic predictions of the oxidation states of zinc and aluminium across a range of pHs are discussed fully in the Pourbaix Diagrams section of the literature review. It shows that at low pH values (< pH 10 for Zn and < pH 5 for Al) and high pH values (> pH 11 for Zn and > pH 9 Al), Zn and Al have high solubilities, forming the oxidation species that are present in the red areas of the graph. This causes the elements to leave the alloy. The areas in the graph where it is green are where the oxidation species is insoluble, causing passivation of the corrosion, showing pH 10 to be an optimum pH for Galvalloy®.

To compliment the already existing literature, qualitative, time-lapse microscopy (TLM) experiments were performed across this range of pHs (pH 3, 7, 10, and 13) in 1 wt.% NaCl. The samples were polished to a mirror finished and etched to reveal the microstructure under the light microscope. The procedure can be found in the Experimental Methods chapter.

Imaging and quantitative, potentiodynamic polarisation electrochemical experiments, described in the Experimental Procedure chapter, were performed on Galvalloy®. The samples were polished and etched to replicate the conditions of the TLM experiments. Cathodic going and anodic going sweeps were performed independently in electrolyte purged of oxygen by nitrogen gas. This was done to reveal more of the anodic curve for a better understanding of the anodic dissolution kinetics.

The results of the TLM experiments were then analysed and compared to the results of the kinetics results obtained from the potentiodynamic experiments and those available in literature of zinc and similar Zn-Al alloys. These were also compared to the thermodynamic values available in the form of the Pourbaix diagrams. Conclusions were drawn about the electrochemical processes that are responsible for the activity seen in the TLM images.

4.2   Experimental

The Sample and Experimental Preparation (2.7.1) and Potentiodynamic Polarisation (2.10.4) sections in the methods chapter detail the experimental procedure carried out for this chapter.

4.3   Results

4.3.1   Galvalloy® in pH 3 1 wt.% NaCl

Video 4.1 (depicted as stills in Fig. 4.1) shows the surface corrosion of Galvalloy® in aerated 1 wt.% NaCl adjusted to pH 3. Generalised corrosion is seen as widespread darkening of the surface after a 3-hour period (Fig. 4.1B). The darkening can be interpreted as anodic attack on the surface. The corrosion appears to be within both the eutectic and dendritic regions, and to the same extent. Some dendrite regions, such as at the bottom left rim (labelled 1), are completely blackened, suggesting severe dissolution. This also occurs in eutectic regions, such as in the middle of the sample area. This is in alignment with the thermodynamic predictions in the Pourbaix diagram (Fig. 1.3) and also kinetic results found by Vu et al. (Fig. 1.35), where at pH 3, both Zn and Al experience dissolution. The aggression of corrosion is also in agreement, where pH 3 has a higher corrosion rate compared to the other pH levels tested within this experiment.
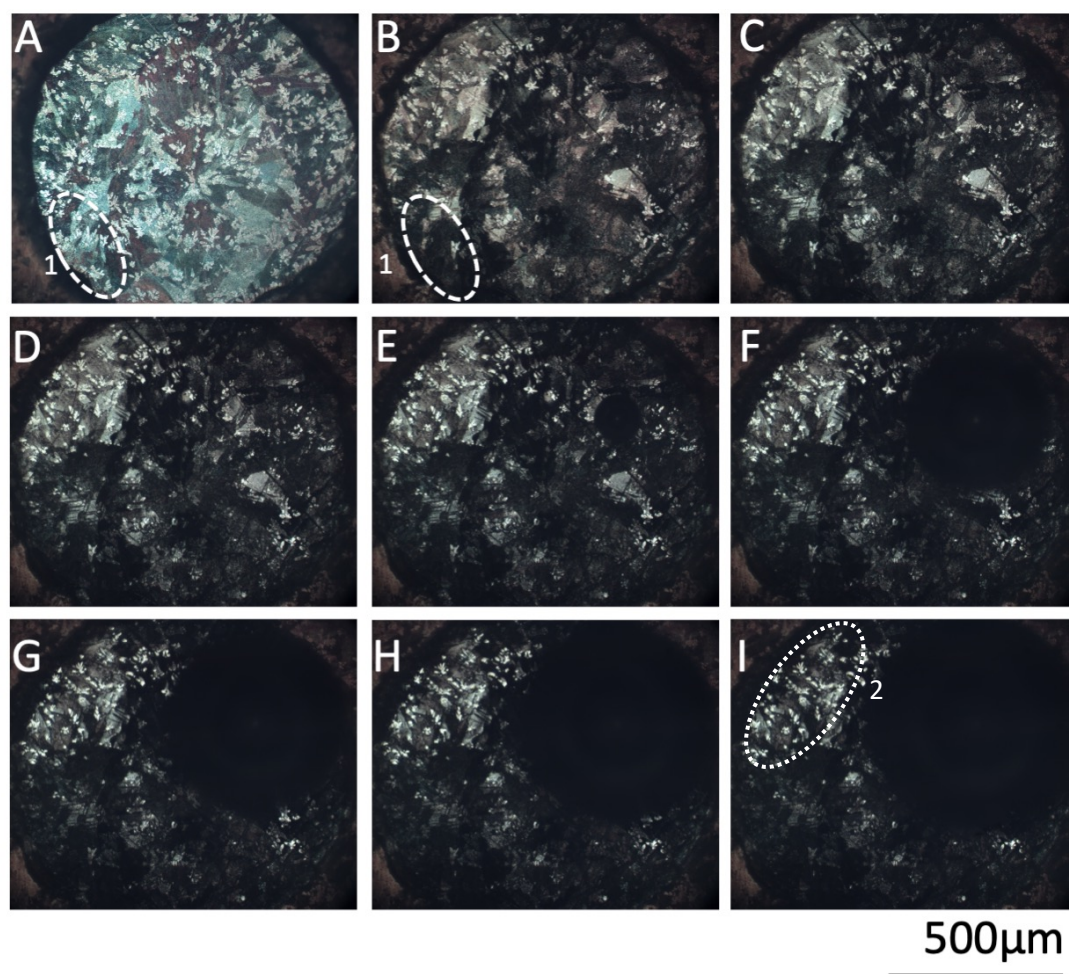
Fig. 4.1 Images A-I: Time-lapse microscopy images of Galvalloy® immersed in aerated pH 3 1 wt.% NaCl. These have been captured every 3 hours and the total time of 24 hours. The label 1 in images A and B is indicating an area of dendrites attacked in the initial stages of corrosion. Label 2 identifies an uncorroded region. These stills represent Video 4.1.

The corrosion in the top left quadrant (labelled 2) of the exposed region seems to be significantly slower than the rest of the area, it also has a high population of zinc dendrites which could possibly be acting as a cathode. The potentiodynamic results, found in Fig. 4.5, show a high cathodic current, which suggests reduction of oxygen or evolution of hydrogen. Then, in Fig. 4.1E the formation of a bubble in the top right quadrant of the exposed area. The formation of this bubble is an indicator that hydrogen gas is being evolved which is a process that is a result of cathodic activity. This is likely due to the initial oxide being removed by the pH 3 electrolyte revealing bare metal of a significantly higher cathodic activity, allowing the hydrogen evolution (HE) reaction. The region in which this bubble formed seems to be at the interface of a dendrite and a eutectic region, making the site of this cathodic activity difficult to pin-point.

4.3.2 Galvalloy® in pH 7 1 wt.% NaCl

Video 4.2, depicted by stills in Fig. 4.2, shows the surface corrosion of Galvalloy® when immersed in 1 wt.% NaCl adjusted to pH 7. Initially, anodic attack occurs in the eutectic phase (Zn-Al lamella) as opposed to the primary zinc dendrites, shown in Fig. 4.2B and video 4.2. The corrosion proceeds in the eutectic phase until around 12 hours where, in the top right quadrant (labelled 3), the corrosion engulfs the zinc dendrites. However, it is noted, that before 12 hours the corrosion seems to be resisted by the zinc dendrites. The corrosion product forms in between the anodic and cathodic region. The anodic region, where the dissolution is occurring, develops a decreased local pH, in the region of pH 4 – 6, where the cathodic region has an increased local pH, in the region of pH 8 – 10 (46).
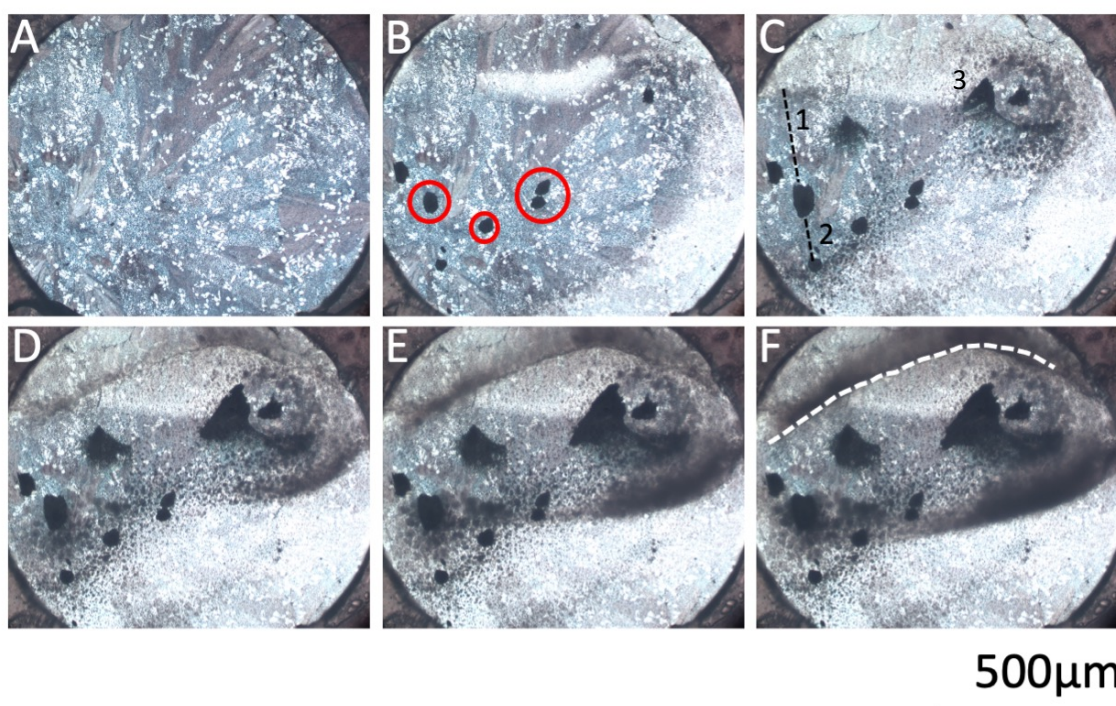
Fig. 4.2 Images A-F: Time-lapse microscopy images of Galvalloy® immersed in aerated pH 7 1 wt.% NaCl. These have been captured every 3 hours and the total time of 15 hours. In image B red circles indicate the initiation of corrosion, showing anodic regions. In image C, the lines labelled 1 and 2 are 275 and 154 μm in length, respectively. These are is the distances from the anode to the corrosion product ring. Label 3 identifies the region where the dendrites become engulf by metal dissolution. In image F, the white dotted line shows the distinction between the anodic region and the cathodic region by corrosion product. These stills represent Video 4.2.

Comparing the images at pH 3 and 7 after 3 hours of exposure, it is apparent that the lower pH has a greater anodic area. This matches the rates found in work performed by Vu et al. (Fig. 1.34) and Zembura and Burzynska (Fig. 1.17).

4.3.3   Galvalloy® in pH 10 1 wt.% NaCl

Video 4.3, depicted by stills in Fig. 4.3, shows the surface corrosion of Galvalloy® when immersed in 1 wt.% NaCl adjusted to pH 10. At pH 10, the anode, which appears after 3 hours (Fig. 4.3B), is small compared to pH 7, and the corrosion product ring which forms around the anode is constrained with respect to distance from the anode to the corrosion product ring (38-102 μm at pH 10 compared to (154-275 μm at pH 7). This would indicate a large cathodic region as there is no other anode formation or formation of corrosion product anywhere else until 15 hours (Fig. 4.3F) where a darkening to the left of the anode is seen. The increased cathodic activity compared to pH 7, is also seen in the potentiodynamic (Fig. 4.5), where the cathodic arm current is ~ 8 times greater at a E - 0.9 vs. SHE.
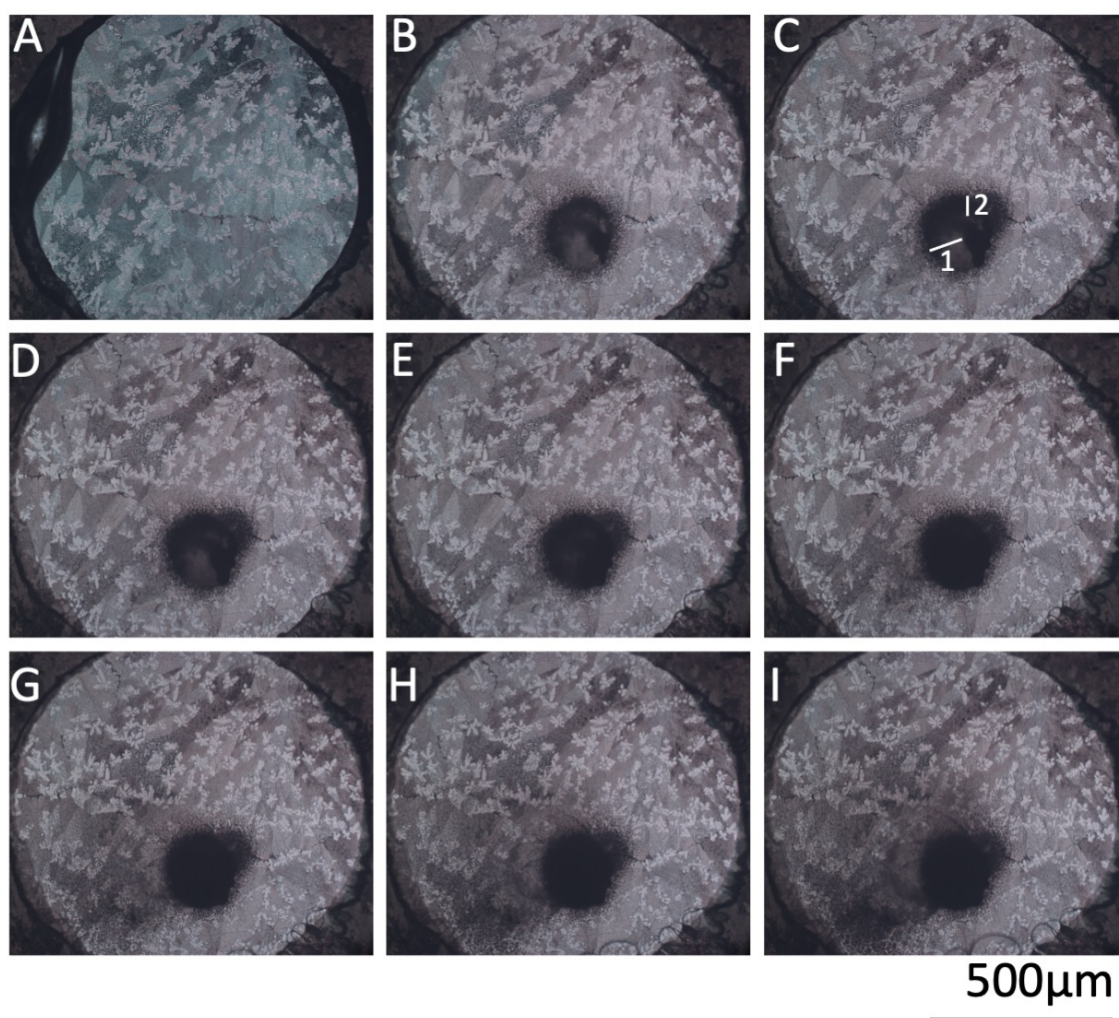
Fig. 4.3 Images A-I: Time-lapse microscopy images of Galvalloy® immersed in aerated pH 10 1 wt.% NaCl. These have been captured every 3 hours and the total time of 24 hours. In image B after a period of 3 hours an anode has formed in a small region just below centre. This anode has very little growth and appears to be constrained. The lines 1 and 2 are 102 and 38 μm in length, respectively. These are is the distances from the anode to the corrosion product ring. These stills represent Video 4.3.

After 6 hours, shown in Fig. 4.3C, the corrosion appears to spread to a region outside of the corrosion product ring. This can be explained by a local pH increase caused by cathodic activity, to a pH greater than pH 10. The Pourbaix diagram shows that corrosion activity will occur at a pH greater than 13 for both Al and Zn, as they are no longer in a passive region, which possibly explains this anodic activity. What further supports this, is the suppression of this anodic activity near enough immediately, as the pH is reduced to one where Al and Zn are in the passive region (< pH 13).

The decrease of the overall corrosion rate is in agreement with the literature (108).

4.3.4   Galvalloy® in pH 13 1 wt.% NaCl

Video 4.4, depicted by stills in Fig. 4.4, shows the surface corrosion of Galvalloy® when immersed in 1 wt.% NaCl adjusted to pH 13. After initial immersion (Fig. 4.4B), hydrogen evolution (HE) is apparent, suggesting HE is the dominant cathodic reaction at pH 13. The corrosion activity, after 12 hours, (Fig. 4.4E), shows a uniform darkening all phases of the sample surface, suggesting uniform corrosion, which is found in the work performed by Vu et al. (84). However, as corrosion continues the dendrites seem more robust, evidenced by the region labelled 1, in the still at 5 hours. An increased rate of corrosion of Al, compared to Zn, at higher pHs has been seen previously   in   literature   (75,109).
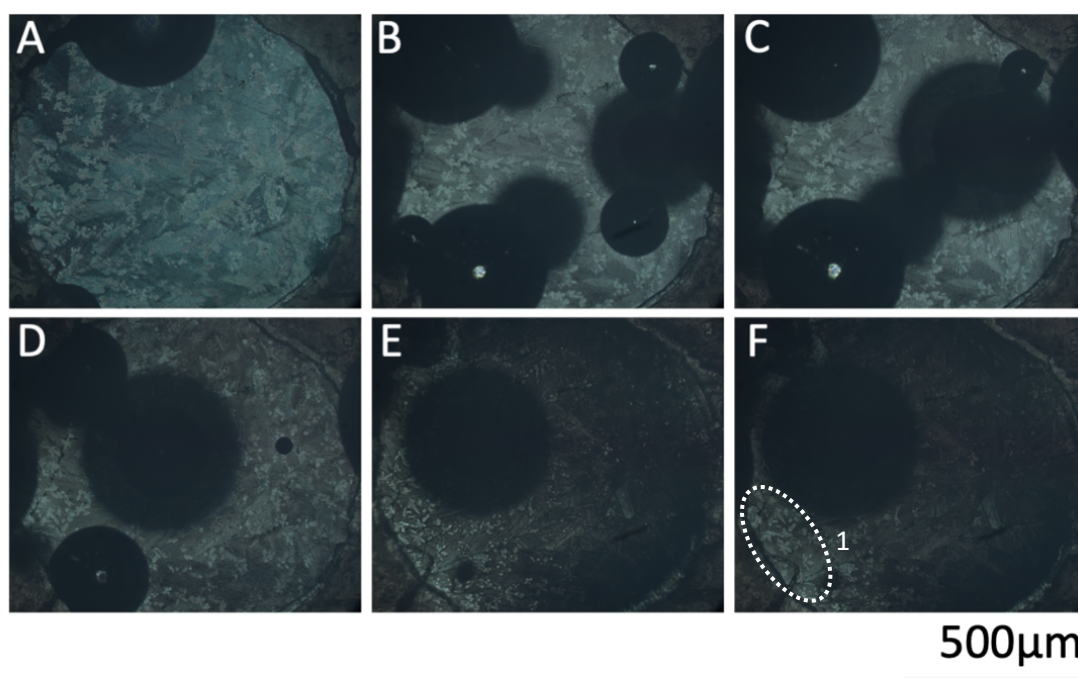
Fig. 4.4 Images A-F: Time-lapse microscopy images of Galvalloy® when immersed in aerated pH 13 1 wt.% NaCl. Image A shows the surface immediately after immersion and the images thereafter are captured every hour. Label 1 shows an area of un-attacked dendrites. These stills represent Video 4.4.

4.3.5 Galvalloy® Potentiodynamic Polarisation as a function of pH

The Galvalloy® samples were polished to the same finish as for the TLM experiments in order to have as accurate representations of the conditions as possible for a fair comparison. The samples were immersed in 1 wt.% NaCl that had been adjusted to the respective pHs. The solution had been deaerated for a period of 1 hour prior to the experiments taking place. During the test the nitrogen was fed above the solution to provide a blanket to prevent oxygen ingress. The tests were performed in deaerated conditions to extrapolate the anodic arm to better understand the anodic behaviour at the different pH values.

The samples were left to settle at OCP for 10 minutes before the experiment proceeded. For an anodic sweep the starting voltage was - 50 mV from this OCP, and for a cathodic sweep the starting voltage was + 50 mV.

The potentiodynamic results shown in Fig. 4.5, which describe the cathodic and anodic activity of the samples at pH3, 7, 10 and 13, agree with the thermodynamic predictions (53) and kinetics results from literature. Thomas et al. study on zinc (50) showed a similar shift in E_{corr} at pH 13, so the difference in polarisation curves here is not purely down to the presence of Al.
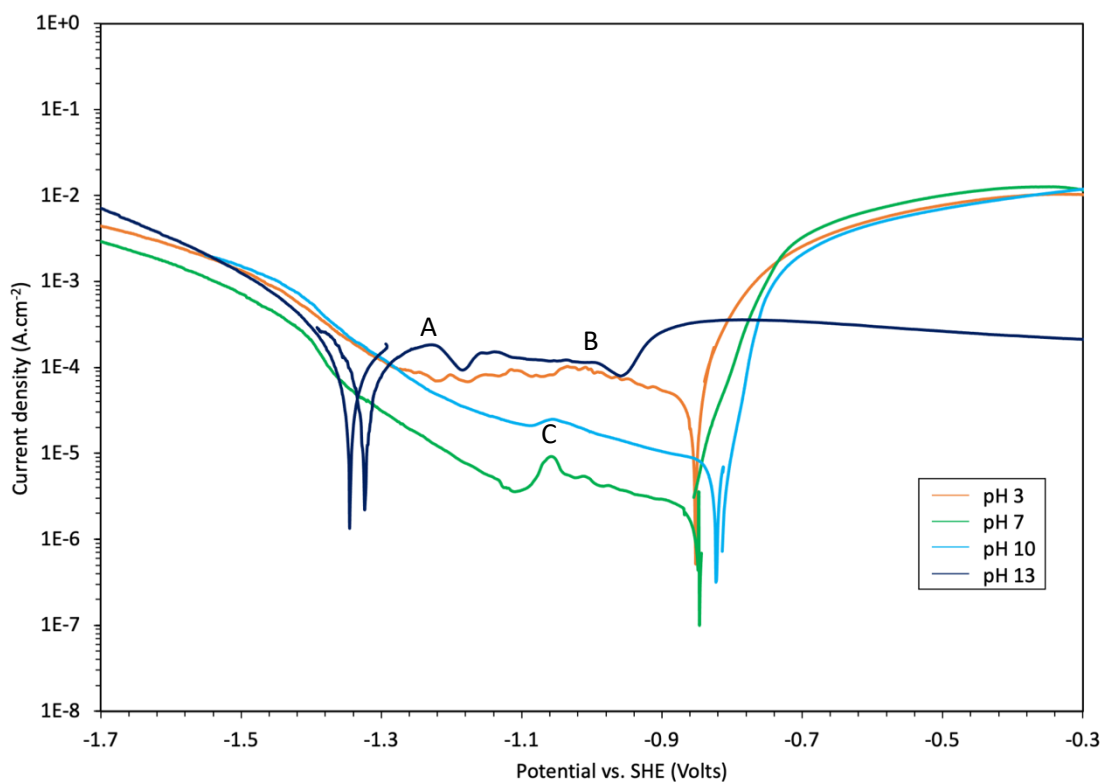
Fig. 4.5 Potentiodynamic polarisation of the surface of Galvalloy® immersed in deaerated 1 wt.% NaCl at pHs a) 3, b) 7, c) 10 and d) 13. The anodic and cathodic sweeps were conducted separately, with the linear potential sweep starting from 50 mV either side of the measured E_{corr} (vs. SHE) prior to the experiment starting. Labels A, B and C indicate the reduction potentials of the oxides present.

The key data in terms of E_{corr}, i_{corr} and Tafel constants can be found in

Table 4.1. The trend of the corrosion rate, which can be represented from i_{corr}, vs. pH is that the corrosion rate follows a U shape (shown in Fig. 4.6), where the rate is highest for pH 3 and 13 and lowest around pH 7 a with a slight rise at pH 10. In fact, the i_{corr} is approximately 2 orders of magnitude greater at pH3 than 7 and one order of magnitude greater at pH 13 than 7. This is in agreement with the thermodynamic predictions from the Pourbaix diagram where Al and Zn are active at pH 3 and 13. It is also in agreement rates found with the ICP-AES work on de-aerated Zn5Al performed by Vu et al., as shown in Fig. 1.34 where a minima of Zn and Al ion flux was observed around pH 7 again showing a $y=x^2$ shape around this minima.

Table 4.1 E_corr, i_corr and Tafel constants (β_c and β_a), as extracted from Fig. 4.5.

pH	E_corr vs. SHE	i_{corr} (A.cm^{-2})	$β_c$ (mV.dec^{-1})	$β_a$ (mV.dec^{-1})
3	-0.87	1.3×10^{-4}	-109	67
7	-0.87	2.5×10^{-6}	-141	39
10	-0.82	5.3×10^{-6}	-68	34
13	-1.32	1.3×10^{-5}	-111	101
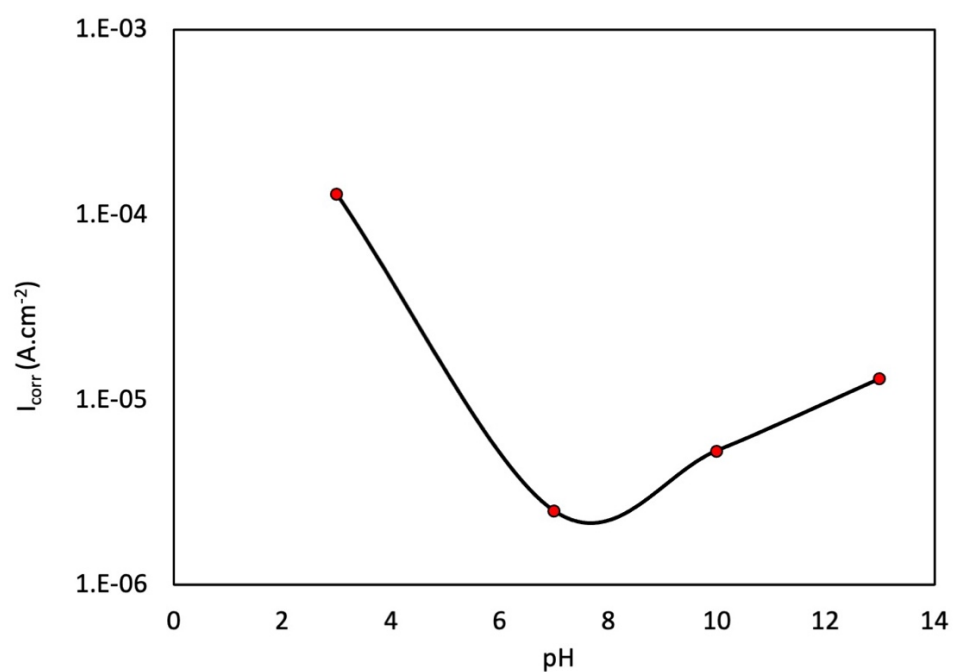
Fig. 4.6 A plot of pH vs. i_corr for pHs 3, 7, 10 and 13, illustrating the $y=x^2$ shape.

4.4   Discussion

The TLM technique has enabled, for the first time, the mechanisms of corrosion of Galvalloy®
to be visually assessed with respect to pH. These mechanisms are discussed here.

pH 3

The TLM experiments show generalised corrosion and an absence of corrosion product rings.
Under aerated, free-corrosion conditions the cathodic reaction, in this region being dominated by
the hydrogen evolution reaction, $H^+(aq) + 2e^- = H_2 (g)$ (HER) (50,54), is demonstrated by the
appearance of bubbles in the experiments. The low pH prevents the precipitation of corrosion
products and hence any passivation and as both Zn and Al are, thermodynamically, in the active
dissolution region of their Pourbaix diagrams, generalised attack all over the surface tends to
occur. The potentiodynamic scans showed that pH 3 had the highest i_{corr} of all the tested pH
values with no evidence of passivation in the anodic curve and increased cathodic kinetics
compared to pH 7 and 10, probably due to the rapid solubilisation of the natural Zn/Al oxide
surface layers at this pH.

pH 7 and 10

The TLM experiments show anodic attack initiate and progress from the Zn/Al lamellar eutectic
phase with respect to time. Precipitation of the corrosion product occurs at a distance from the
anodic features where the counter flux of metal cations from the anode and hydroxide anions
from the cathode meet and the solubility product of the corrosion product is exceeded. The
mechanism observed at pH 7 and 10 is thus a localised corrosion mechanism with distinct
separation of anodes and cathodes in comparison to the general attack observed at pH 3. The
TLM technique has enabled the effect of pH on the precipitation of corrosion products to be
assessed. The corrosion product ring boundary areas and mean diameters are, 346,073 and 35,560
μm^2, and 152 and 47 μm, after 6 hours, at pHs 7 and 10, respectively. This constraining effect in
terms of distance of precipitation of corrosion products from the anode is a result of increasing
the OH⁻ ion content by 1000 times from pH 7 to pH 10 in the experimental electrolyte. This
means the local concentration of metal cations and hydroxide anions required to exceed the
solubility limit of the corrosion products will be achieved at a shorter distance from the site of
the anode; i.e. it is easier to achieve precipitation of corrosion products at pH 10 and hence
precipitation of the corrosion product occurs closer to the anodic site.

TLM also shows that the progression of anodic features is retarded at pH 10 compared to 7. After
6 hours pH 7 and 10 have anodic areas of 20189 and 10053 μm^2 (calculated from image analysis
in imageJ), respectively, which shows the kinetics from the TLM indicate an approximate
doubling of metal dissolution rate from pH 7 to 10. This was also observed in the AES work
performed by Vu et al. (84), shown in Fig. 1.34, where in aerated 30mM NaCl the dissolution rate

of a Zn5Al alloy at pH 7 is double that of pH 10, and in fact at pH 10 the dissolution is at a minima. A caveat must be made however that the TLM technique is a two-dimensional measurement of corroded area and the depth of corrosion is not able to be measured.

In the deaerated potentiodynamic scans a different order of performance was observed with Galvalloy® at pH 10 having a higher i_{corr} compared with pH 7. However, this increased kinetics is consistent with other metal loss data in deaerated conditions (84), shown in Fig. 1.34. In the anodic curve of pH 7 there is an inflexion (labelled C) of pseudo passivity (circa -0.8 V vs. SHE) indicative of film formation, consistent with work performed on pure zinc (50). This is also seen at pH 10 but to a much lesser extent indicating that any film formation is not as robust or stable. It has been shown previously that in open circuit potential (83,84) and polarisation (84) conditions, the release of Al dramatically increases at pH 10 whilst the rate of Zn loss tends to decrease (84) as would be predicted thermodynamically by the phase diagrams in figure 1. Accordingly, the increased anodic kinetics observed at pH 10 in the polarisation data could be a reflection of this higher Al loss. The difference in apparent performance between the aerated TLM and de-aerated potentiodynamic scans may reflect the ability to reform and stabilise surface oxides/hydroxides that form under these different conditions of oxygen concentration at the different pH levels.

Additionally, a change in cathodic kinetics will contribute to the increase in i_{corr} observed at pH 10. The cathodic curve for pH 10 shows an increased cathodic current and a reduction in the peak heights at -1.06 V (vs. SHE), which is attributed to the "formation and reduction of a $Zn(OH)_2$ film of intermediate stability" (110). As this peak is less prominent at pH 10 vs. 7 it implies the pH effects the stability of this hydroxide. A reason could be that as the cathodic process proceeds (i.e. water reduction in deaerated conditions) the pH increases and reaches levels where it destabilises and breaks down due to the amphoteric nature of both Zn and Al oxide/hydroxide. This is breakdown will occur more readily at pH 10 compared to 7 both the Al and Zn oxides will break down if the pH rises above approximately pH 10.5 – 11 whereas at pH 7 initial rises in pH associated with cathodic activity are more likely to stabilise both the Zn and Al oxides.

pH 13

The TLM shows an anodic attack primarily in the eutectic phases, whilst the zinc dendrites undergo a lesser attack. This behaviour is different from the generalised corrosion at pH 3 where Zn and Al are actively dissolving. The attack of the eutectic region is consistent with aerated dissolution rates of a Zn5Al alloy in 30mM NaCl at pH 11.8 (84), where Zn and Al have identical steady state metal loss, despite Zn making up 95wt.% of the alloy, also shown in Fig. 1.35. Nevertheless, the attack stabilises at the 5 hour mark.

At pH 13 the alloy had an i_{corr} value and order of magnitude greater than that observed for pH 7 - 10. The potentiodynamic results shows the highest cathodic kinetics of the pHs tested, which is due to the low E_{corr} of the system. This increased corrosion rate was also seen in other investigations as shown in Fig. 1.34, in deaerated conditions there is an increase in the release of Al, which would also contribute to the increased i_{corr} at pH 13. At pH 13 is predicted from the Pourbaix diagrams in figure1 that both metals in the alloy will again become active due to their amphotericity.

The anodic curve follows the dual passivation mechanism, labelled A and B, where there is a marked drop in current densities. Peak A, found at -1.23V, would indicate from the Pourbaix diagram that zinc is in the active, $Zn(OH)_3^-$ zone (53). The local super saturation of $Zn(OH)_3^-$ at the surface limits the transport of OH^- ions to the metal surface, allowing the build up of $Zn(OH)_2$ (ZnO is also able to form), consequently giving rise to peak A. This resistant oxide is referred to as a Type II oxide (111). Peak B is attributed to the formation of ZnO, which if only Zn was present would lead to full passivation (50). Therefore, the increase in current density is attributed to the dissolution of Al, which is expected at high pH levels (83,84).

Even though there is passivation seen in the anodic arm of the pH 13 potentiodynamic data, the current density is still considerably higher than pH 7 and 10, demonstrating a decrease in corrosion performance at this pH, which is also supported by literature (84).

4.5   Conclusions

- TLM and electrochemical techniques were used to deduce the rate and microstructural mechanism of the surface corrosion of Galvalloy® in a range of pHs.

- General corrosion of the microstructure was observed at pH 3 and pH 13 with no apparent precipitation of corrosion products.

- Localised corrosion was observed at pH 7 and pH 10 with anodic attack initiating on the Zn/Al eutectic with the formation of corrosion products rings between anodic and cathodic sites. The distance to the corrosion product rings from the anodes were constrained at pH 10 due to the higher initial concentration of OH- in the electrolyte.

- In open circuit and polarised conditions, the best corrosion performance of Galvalloy® is seen in the pH 7 -10 range for the pHs tested. pH 3 and 13 give increased corrosion.

- Polarisation indicates cathodic control is important for Galvalloy® at pHs 3, 7 and 10 as the cathodic current density varies significantly, but elements of the anodic differences occur due to the differing dissolution rates of Zn and Al as pH increases. At pH 13, anodic control seems to dominate.

Chapter Five

False cut-edge corrosion mechanism of Galvalloy® in saline electrolyte as a function of pH

5 False cut-edge corrosion mechanism of Galvalloy® in saline electrolyte as a function of pH

5.1 Introduction

Galvalloy® is a strip steel product that is manufactured in a method that carriers its namesake – strips, and the coating of the strip does not extend to the edge, leaving an area of exposed steel which is coupled to the galvanised coating and the organic paint system. As the strips are designed so that the widths can be cut down to the desired measurements, and as the strip is cut in appropriate lengths, the amount of these edges increases and brings with it a corrosion challenge. This is because when the steel and Galvalloy® are exposed together in an aqueous environment they form a couple and the steel rapidly drives the dissolution of the zinc alloy coating which leads to undermining of the organic coating followed by the formation of blisters at the cut-edge (112). It has been seen in the chapter 3, that the microstructural mechanism of corrosion initiation is in the eutectic and the zinc dendrites when the coating is undergoing surface and cut-edge corrosion, respectively.

Previous work from J. Sullivan et al. (13) showed that manipulating the microstructure of the coating, such as, increasing the size of the dendrites in the Zn4.8Al coating, by decreasing the cooling rate, leads to an increased loss of zinc, as they are the site of preferential attack during cut-edge corrosion. This work does not focus on how the corrosion at the cut edge is influenced by pH.

As we see in the previous chapter, pH has a great effect on the corrosion rate and mechanism of Galvalloy®, and this chapter sets out to expand on that horizon of knowledge by investigating how Galvalloy® behaves whilst coupled to steel across a range of pHs (3, 7, 10, and 13).

To carry out this investigation, time-lapse microscopy (TLM) was employed to capture the corrosion of the Galvalloy® when steel is exposed. The rate of the corrosion can be observed from the progression of the anodic region in the Galvalloy®. To assist the quantification of the corrosion rate, zero resistance ammetery (ZRA) was used. This electrochemical experiment measures the current, the rate of electrons, passing from the anode (Galvalloy®) to the cathode (steel) whilst they are immersed in identical electrolytes to those used in the TLM experiments.

5.2 Experimental

The Sample Preparation to Simulate Cut-Edge Corrosion (2.9) and Zero-Resistance Ammeter (ZRA) (2.10.5) sections in the methods chapter detail the experimental procedure carried out for this chapter.

5.3 Results

5.3.1 Galvalloy® in pH 3 1 wt.% NaCl

Video 5.1, illustrated as stills in Fig. 5.1, shows the cut-edge corrosion of Galvalloy® immersed in aerated 1 wt.% NaCl, adjusted to pH 3. The area of steel exposed is between 20-25%. After 3 hours (Fig. 5.1B), the Galvalloy® samples underwent immediate darkening in a specific 'line', which appears to be a nodule boundary (Fig. 5.2).
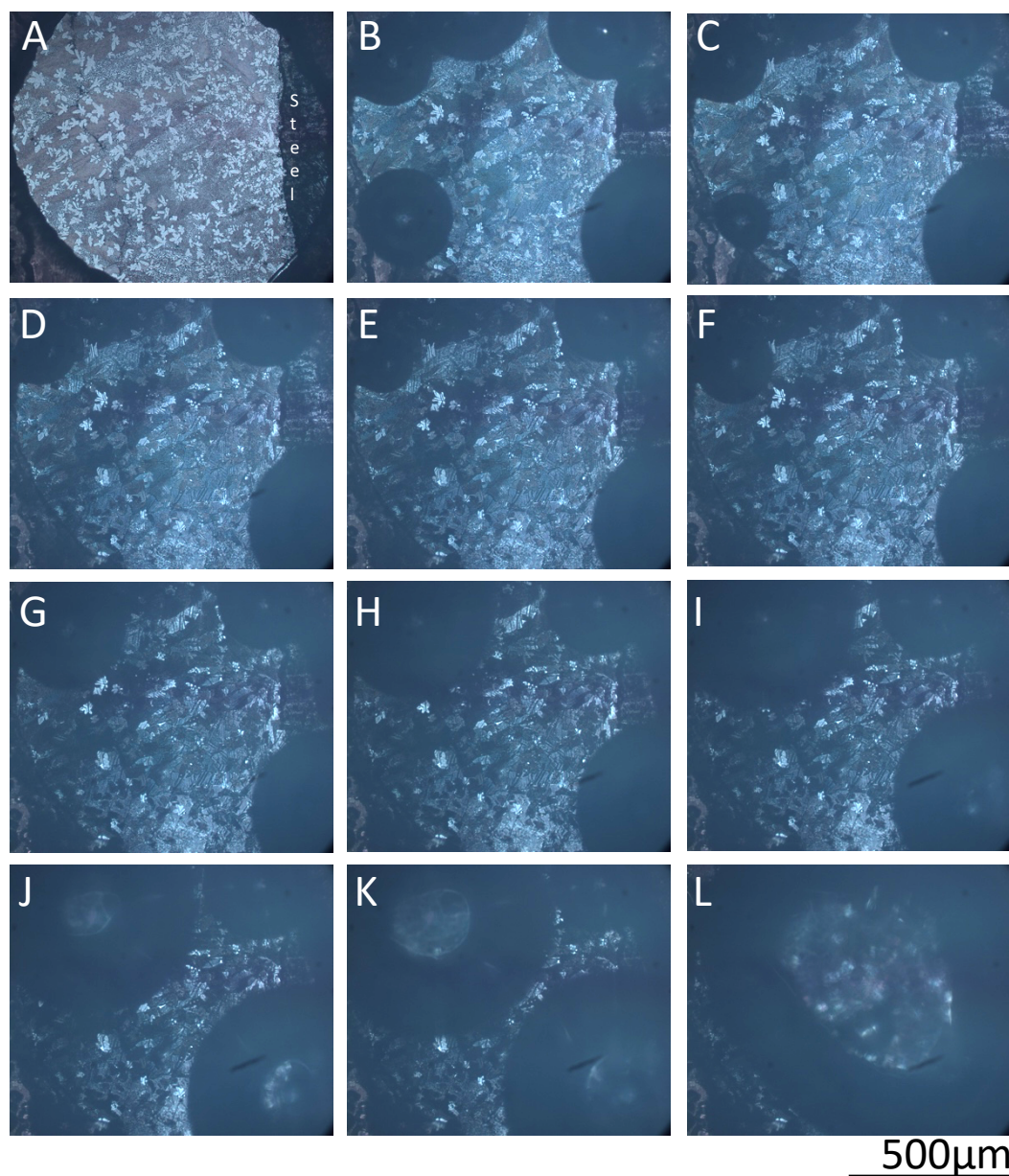
Fig. 5.1 Images A-L: Time-lapse microscopy images of Galvalloy® with exposed cut-edge (~20 %) immersed in pH 3 1 wt.% NaCl. These have been captured every 3 hours and the total time of 33 hours. These stills represent Video 5.1.
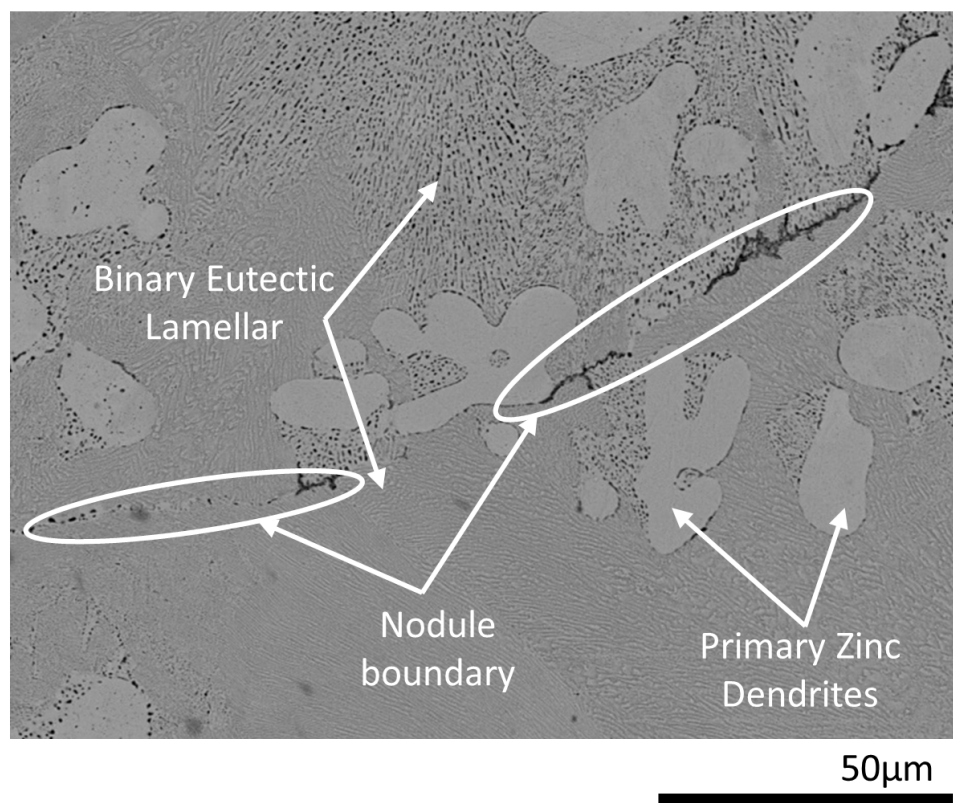
Fig. 5.2 SEM micrograph of Galvalloy® with annotations of the microstructural features.

In the initial stages of corrosion it is clear that the zinc dendrites are the site of preferential attack, and this has been annotated in Fig. 5.3. This phenomenon was seen in chapter 3 when the saline solution was adjusted to pH 7.

Fig. 5.3 Close-up image of the Galvalloy® after 3 hours immersion in pH 3 1 wt.% NaCl. The circles show the dendrites that have been attacked in the initial stages of corrosion.

The cathode appears to be located on the steel, as there is little discolouration on the surface. However, it is known from previous studies that steel will act as a net cathode when paired with zinc or aluminium. There is considerable bubble formation associated with the exposed steel. The outer limits of the Galvalloy® that are furthest from the steel, as well as the steel, show bubble formation. This points toward hydrogen evolution reaction (HER), which is a process which occurs at the cathode, suggesting that despite the Galvalloy® being a net anode, is also can act as a cathode locally. The HER is expected to occur more readily at pH 3 when steel is exposed due to the increase in potential (E_{corr}) associated with the polarisation of the Galvalloy® surface when in contact with the more noble steel.

As the corrosion progresses, dark lines on the surface of the microstructure become more apparent. They occur in both the dendritic and eutectic region indicating the 'attack' is independent of phase. This effect could be due to the residual scratches from polishing acting as the size of corrosion initiation.

5.3.2 Galvalloy® in pH 7 1 wt.% NaCl

Video 5.2, shown as stills in Fig. 5.4, shows the TLM experiment of Galvalloy® immersed in 1 wt.% NaCl adjusted to pH 7. After 3 hours (Fig. 5.4B), an anode has initiated at the interface between the Galvalloy® and the exposed steel. There is rapid initial attack of the Zn dendrites as demonstrated in the annotated close-up images in Fig. 5.5 but rapidly, the attack becomes indiscriminate of phase with both dendrites and eutectic becoming consumed. Within 6 hours a clear corrosion product ring has formed, and corrosion progresses across the Galvalloy® surface until 21 hours where rapid, anodic growth is seen on the cathodic side of the corrosion product, as annotated in Fig. 5.4H. After 6 hours the anode area was calculated using image analysis to be 33558 μm².
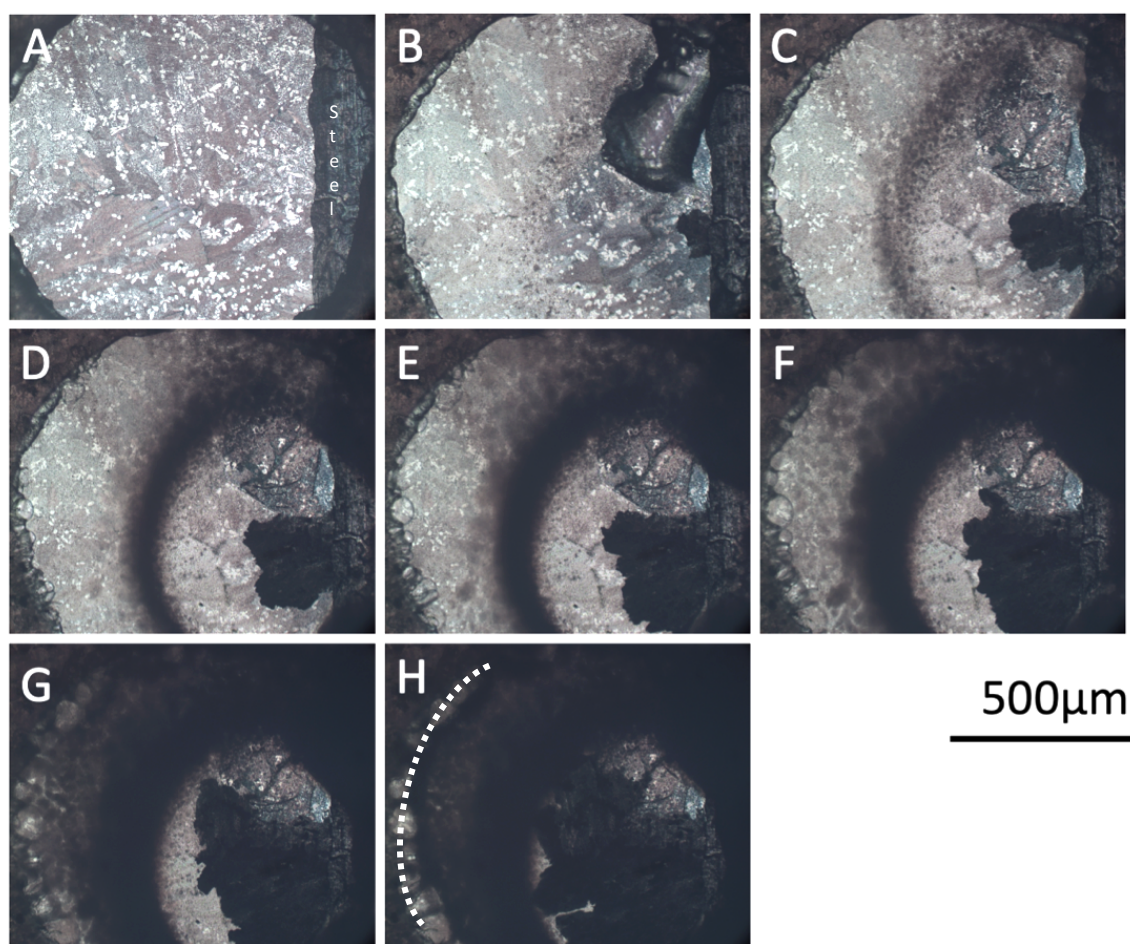
Fig. 5.4 Images A-H: Time-lapse microscopy images of Galvalloy® with exposed cut-edge (~20 %) immersed in pH 7 1 wt.% NaCl. These have been captured every 3 hours and the total time of 21 hours. The anodic area after 6 hours, image C, has been measured to be 33558 μm2. These stills represent Video 5.2.
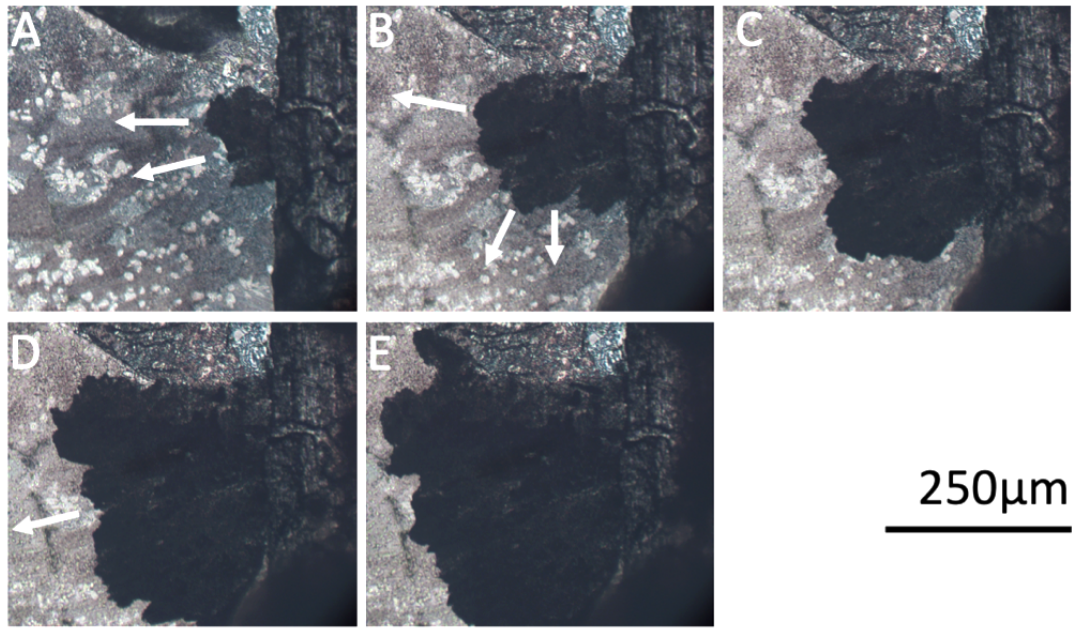
Fig. 5.5 Images A-E: Close-up time-lapse microscopy images of Galvalloy® with exposed cut-edge (~20 %) immersed in pH 7 1 wt.% NaCl, taken from Fig. 5.4. The arrows represent the anodic growth following the location of the zinc dendrites, demonstrating preferential attack of this phase during cut-edge corrosion.

5.3.3 Galvalloy® in pH 10 1 wt.% NaCl

Video 5.3 (stills found in Fig. 5.6), shows the cut-edge corrosion Galvalloy® when immersed in aerated 1 wt.% NaCl, adjusted to pH 10. Firstly, an anode is formed on the interface between the Galvalloy® and the steel with a clear anode and product ring seen within 3 hours, shown in Fig. 5.6B. The anodes that form are in the locations of dendrites, and close-up images are shown in Fig. 5.5. This demonstrates preferential attack of the zinc dendrites during cut-edge corrosion, as seen at pH 7 and in work performed by J. Sullivan et al. (13).
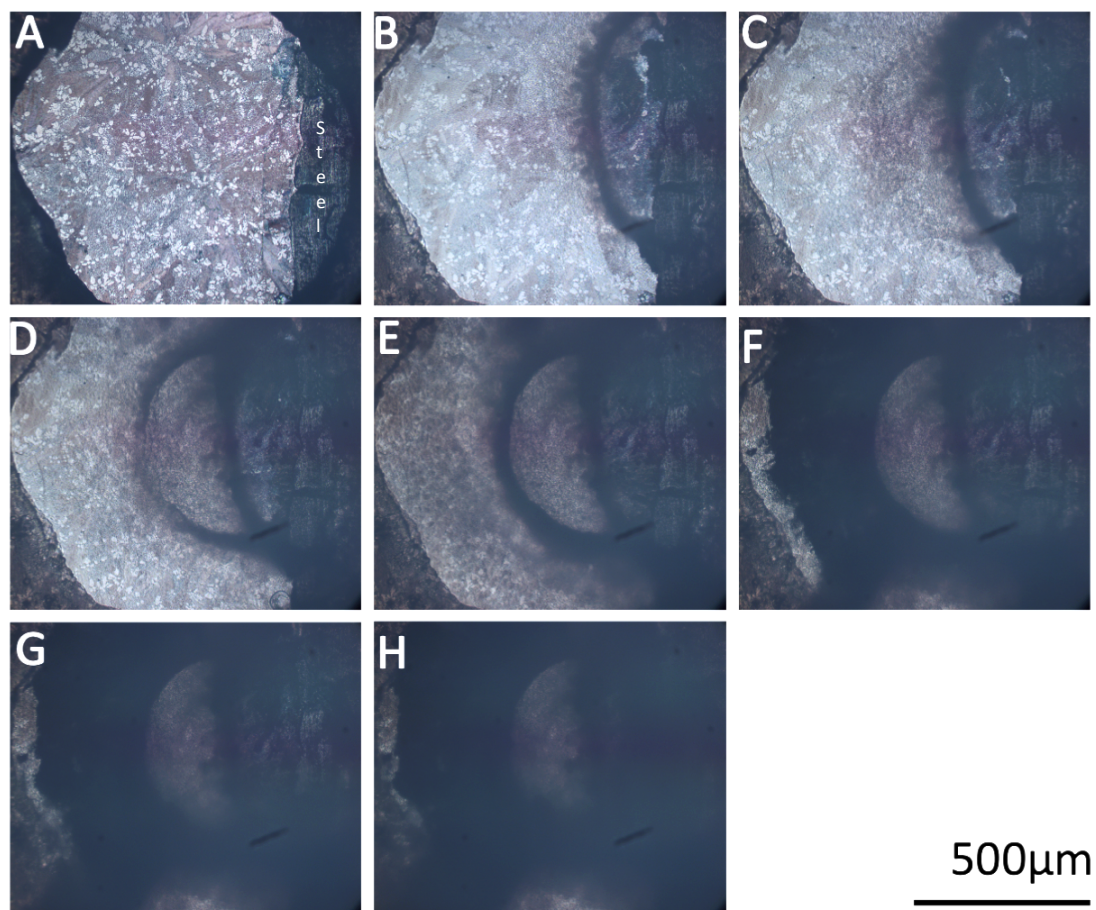
Fig. 5.6 Images A-H: Time-lapse microscopy images of Galvalloy® with exposed cut-edge immersed in pH 10 1 wt.% NaCl. These have been captured every 3 hours and the total time of 21 hours. The anodic area after 6 hours, image C, has been measured to be 31076 μm². These stills represent Video 5.3.
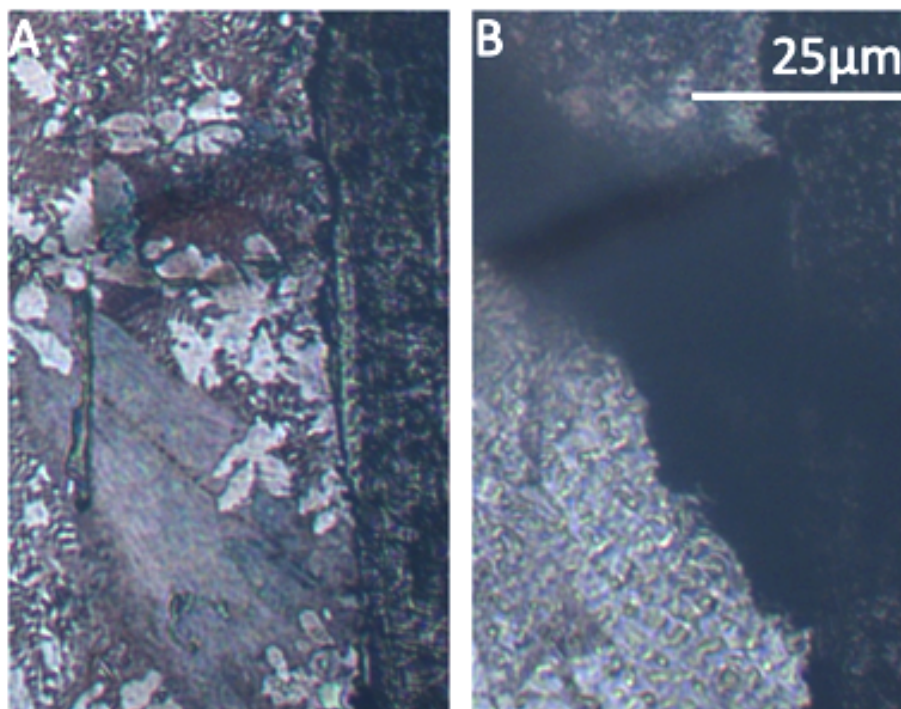
Fig. 5.7 Close up time-lapse microscopy images of the pH 10 experiment from showing the initial micrograph and the preferential anodic attack of the zinc dendrites after 3 hours immersion in 1 wt.% NaCl.

In Fig. 5.8, the micrographs show the corrosion at intervals of 30 minutes. After 30 minutes a product ring is beginning to form at the top of the interface between the Galvalloy® and the steel, as well as an initial darkening of the surface, most evident in the eutectic regions. 30 minutes later, there is a lightening of the surface from areas away from the anode, except the area to the top of the micrograph. Within another 30 minutes most of the Galvalloy® surface, that is not obviously an anode, sees a brightening of the surface.

Over time, the anode and the product ring move left across the Galvalloy® at a steady rate until 15 hours (Fig. 5.6F), when an extremely large anode appears to have formed on the far left of the corrosion product ring. Fig. 5.9 shows close-up images of the anodes that initiate and rapidly grow in this region. This is where a cathode could have been located on the Galvalloy®. The surface continues to get darker until there it is completely black at the end of the 21-hour period.
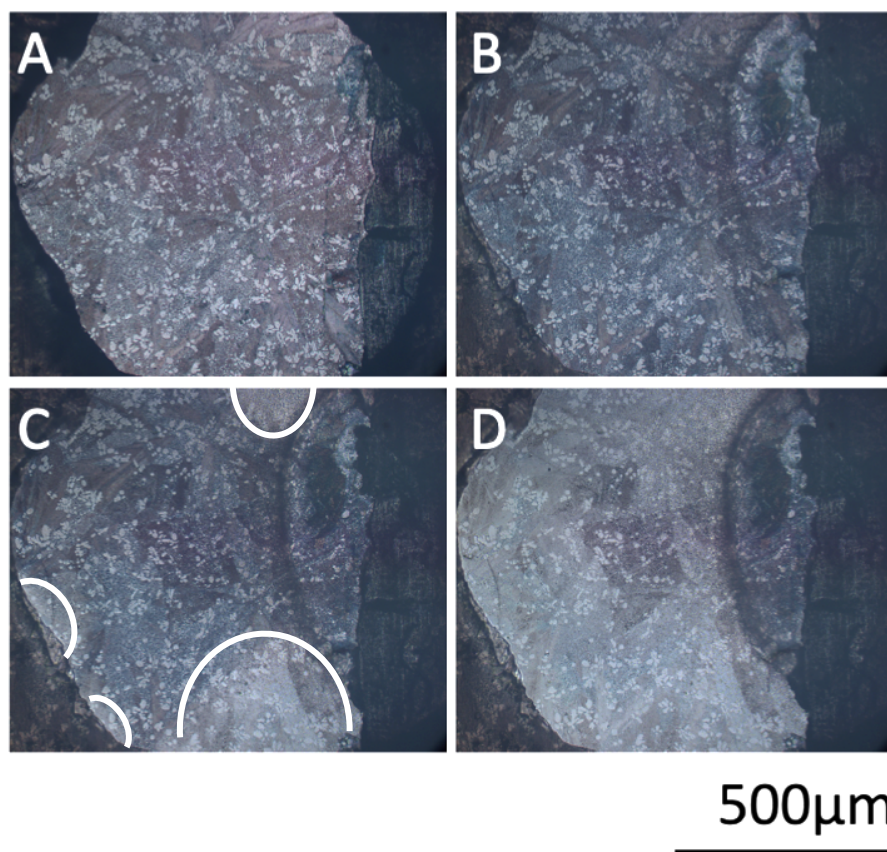
Fig. 5.8 Images A-D: Time-lapse microscopy images of Galvalloy® with exposed cut-edge immersed in pH 10 1 wt.% NaCl. These have been captured every 30 minutes and the total time of 1.5 hours. The initial stages of corrosion demonstrating the change in precipitation of corrosion products. These stills represent Video 5.3.
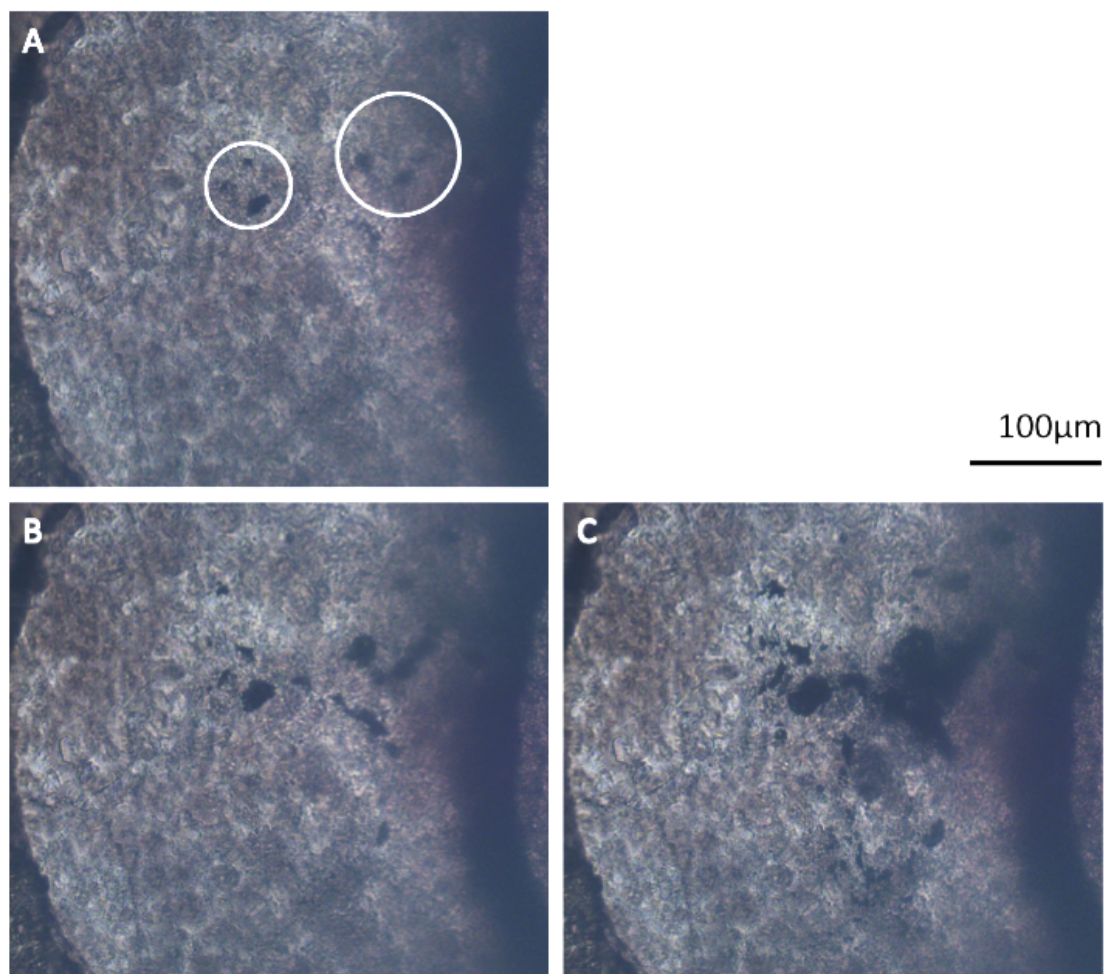
Fig. 5.9 Images A-C: Time-lapse microscopy images of Galvalloy® with exposed cut-edge immersed in pH 10 1 wt.% NaCl. Image A was captured after 12 hours and 12 mins, and the other images are at 6 minute intervals. The images take place in between E and F from Fig. 5.6. The images show the initiation of corrosion on the Galvalloy® on the cathodic side of the corrosion product ring. The anodic areas in images A, B and C are 672, 4421 and 8574 μm², respectively.

5.3.4 Galvalloy® in pH 13 1 wt.% NaCl

Video 5.4, shown as stills in Fig. 5.10, shows the cut-edge corrosion of Galvalloy® when immersed in 1 wt.% NaCl adjusted to pH 13. After 3 hours (Fig. 5.10B), the area on the Galvalloy® near the interface with the steel substrate shows some activity under a bubble that has formed. After 6 hours (Fig. 5.10C), a distinct dark region has formed under the bubble, which can be assumed to be anode. To note, the region where this anode forms is the location and shape of two groups of dendrites. This demonstrates preferential attack of zinc dendrites at pH 13, as well as pH 7 and 10, as well as literature (13).

By 9 hours (Fig. 5.10D), this anode is very clear and has grown about 6 times. This growth does not continue at a noticeable rate, until 30 hours (Fig. 5.10R), when the bubble moves, showing the anode underneath, resembling the same shape and size as it did through the bubble, demonstrating that the bubble did not affect the ability to see the rough shape of the anode. Another noteworthy observation is that the anode does not extend to the interface of the steel and Galvalloy®, and that the anode is large and runs parallel to the interface.

At 33 hours (Fig. 5.10S), another anode is shown to form to the right of previous anode. Similarly, to the previously anodes, the nucleation is at the interface between the zinc dendrite and eutectic phase.
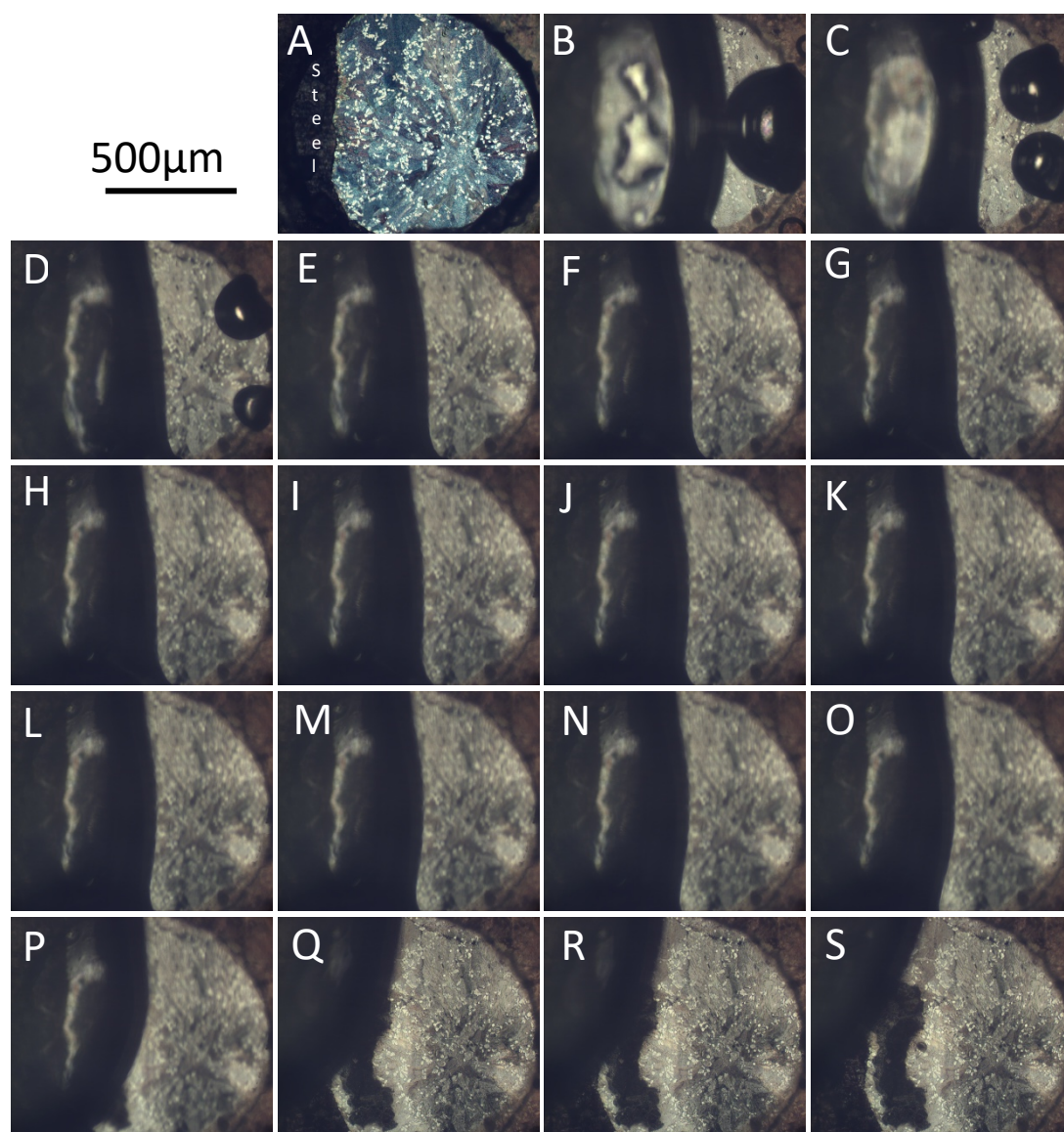
Fig. 5.10 Images A-L: Time-lapse microscopy images of Galvalloy® with exposed cut-edge immersed in pH 13 1 wt.% NaCl. These have been captured every 3 hours and the total time of 48 hours. These stills represent Video 5.4

5.3.5   Zero Resistance Ammetery

The Galvalloy® and steel, of equal areas (1 cm diameter, 0.785 cm²) were immersed in 1 wt.% NaCl at pHs 2, 3, 7, 10, and 13.

The cumulative charge passed from the Galvalloy® to the steel after a period of 3 and 12 hours can be found in Fig. 5.11a) and b) respectively. The charge, in coulombs (C) is a positive value, demonstrating that the electrons have passed from the Galvalloy® to the steel, which confirms what we see in the TLM images: that the Galvalloy® acts as the anode and the steel acts as the cathode. This has also been demonstrated in literature (13).

The trend that is seen in Fig. 5.11, of metal loss to pH, is similar to the $y=x^2$ shape seen when the steel is not coupled to the Galvalloy® in the potentiodynamic and literature of the previous chapter (54,84). However, unlike the previous chapter, the metal loss at pH 13 is higher than that of 3.

Comparing the average charge dissipated over 12 hours with that of the rate from 3 hours extrapolated (multiplied by 4), it is clear that over time the rates of metal loss go down for pH 2, 3, 7 and 13, but not 10. This is seen clearly in Fig. 5.12 for pHs 2, 3, 7 and 13 where the starting current density linearly reduces over the 12 hour period. This decrease in kinetics suggests passivation of the Galvalloy® coating. Notably, the delta between the metal loss of pH 7 and 10 decreases over time.
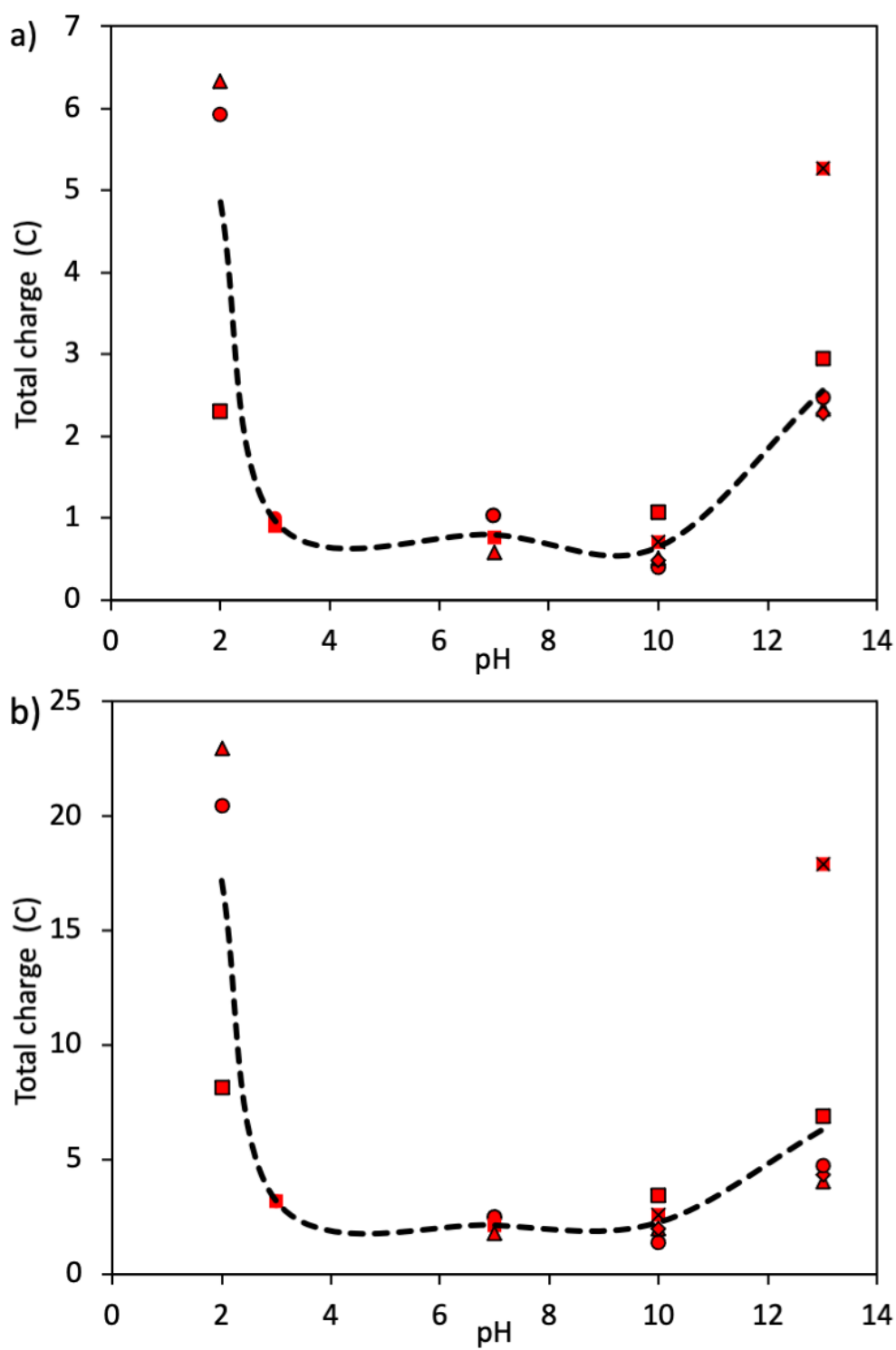
Fig. 5.11 The cumulative charge (C) measured passing from the Galvalloy® net-anode to the steel net-cathode after a period of a), 3 hours and b), 12 hours. The black dotted line represents the average of multiple results from the test performed at that pH. The other markers represent the different results measured at that pH.

Fig. 5.12 shows the rate of pH 13 very noticeably decreases over time, with a 10-fold decrease in current density (0.45 to 0.036 mA.cm^{-2} from 0 to 12 hours). At the 6 hour mark, the pH 13 plot also shows oscillations which have been seen previously in zinc in alkaline medium (113,114). The oscillations can be attributed to metal loss increasing the rate, followed by passivation due to corrosion product decreasing the corrosion rate once again. It is not clear if this passivation is occurring on the Galvalloy® or the steel. Another phenomena that could be causing these oscillations is formation and desorption of H$_2$ bubbles on the surface.

The pH 2 results in Fig. 5.12 show a large variance in the current density, whilst keeping a high average of around 3 order of magnitude greater than pH 13 and 6 orders of magnitude greater than pH 10, which is also seen in Fig. 5.11. The sharp peaks, and subsequent troughs, could be attributed to hydrogen bubbles forming and then dispersing, briefly occluding the surface of electrolyte and hence the area available to pass current so the current density decreases.
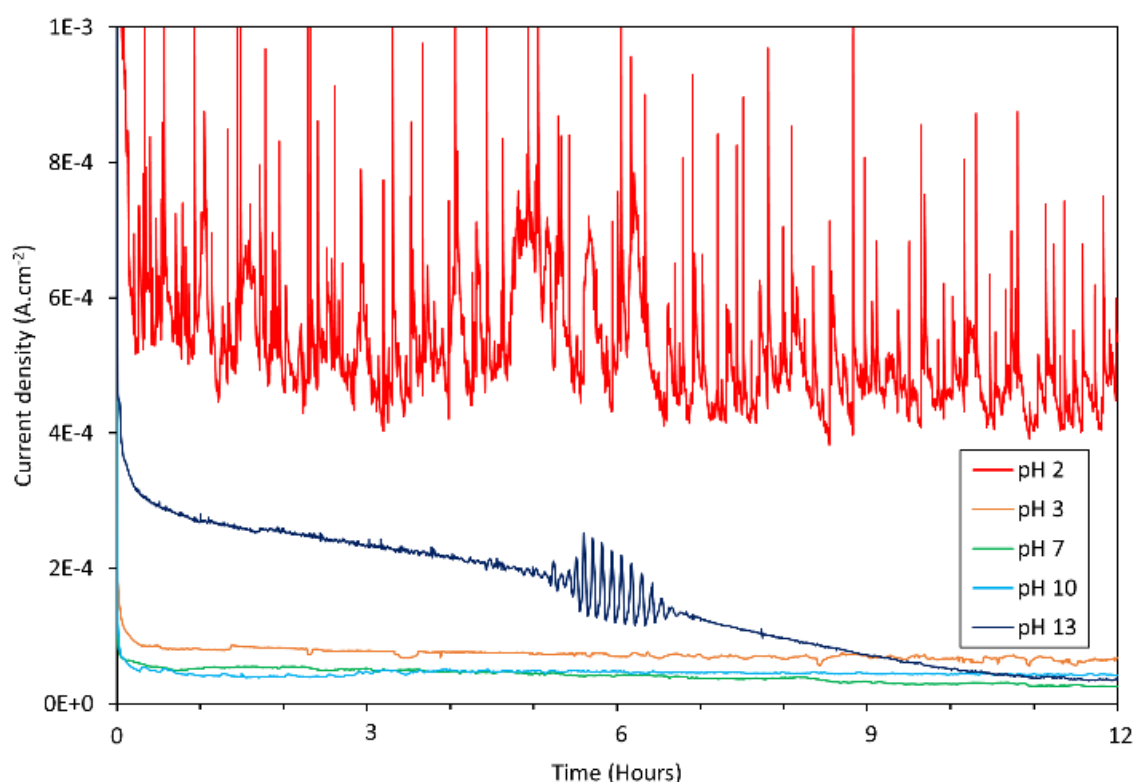
Fig. 5.12 Representative ZRA plots displaying the current density against time for a range of pH levels (pH 2, 3, 7, 10, 13). The total test time being 12 hours.

Table 5.1 shows the comparison of the i$_{corr}$ values from the deaerated potentiodynamic polarisation tests from chapter 4 and the aerated ZRA results, after 3 hours, from this chapter. It shows that across all pH values, the i$_{corr}$ is increased when the cut-edge is introduced into the system. The introduction of oxygen to the system is also expected to increase the the i$_{corr}$ at pH 7, 10 and 13 as the oxygen reduction reaction controls the corrosion rate at this pH range.

Table 5.1 A comparison of the i_{corr} (A.cm^{-2}) measured by potentiodynamic polarisation of the surface of Galvalloy® versus the ZRA experiment of Galvalloy® coupled to the steel substrate, as a function of pH in 1 wt.% NaCl solution.

pH	i_{corr} Surface (PD) A	i_{corr} Cut-edge (ZRA at 1 hours) B	i_{corr} δ (B - A)
3	1.3 x 10^{-4}	1.6 x 10^{-4}	3 x 10^{-5}
7	2.5 x 10^{-6}	1.5 x 10^{-4}	1.5 x 10^{-4}
10	5.3 x 10^{-6}	1.5 x 10^{-4}	1.4 x 10^{-4}
13	1.3 x 10^{-5}	2.3 x 10^{-4}	2.2 x 10^{-4}

Fig. 5.13 Graphical representative comparison of the i_{corr} of the Galvalloy® surface (PD) and cut-edge (after one hour) corrosion, as a function of pH.

5.4   Discussion

pH 3

TLM showed that when coupling Galvalloy® to steel, it was found that the zinc dendrites became the site of initial anodic attack, which is a change in mechanism compared to surface corrosion shown in chapter 4, where generalised corrosion occurs.

Comparing the i_{corr} of Galvalloy® coupled with steel (ZRA) and that from surface corrosion from chapter 4 (potentiodynamic), it was shown that of the corrosion rates of all pHs tested, at pH 3, the rate was least affected by coupling to steel as shown in Fig 14. As the PD were performed in deaerated conditions and the ZRA experiments were performed in aerated conditions, this difference can be attributed to the ORR having little influence on the corrosion of surface corrosion of zinc at pH 3 compared to pH 7, 10 and 13. This is because the HER influences the kinetics of zinc corrosion at pH 3 (50).

pH 7 and 10

TLM shows the corrosion of Galvalloy® coupled to steel at pH 7 and 10 follow a similar behaviour to that of surface corrosion. At pH 10 the corrosion product is noticeable at an earlier stage and is more constrained, due to the increase (x1000) in initial concentration of OH- ions to allow for the easier formation of $Zn(OH)_2$.

TLM shows the corrosion at both pHs initiates at the Galvalloy®-steel interface. Yet again, the corrosion at pH 7 proceeds at a higher rate. Table 2 provides a comparison of the corroded areas measured for surface corrosion from chapter 4 and cut edge corrosion at pH 7 and 10 for samples immersed for 6 hours. Table 2 shows that although an increased anodic area is again seen at pH 7 compared to pH 10, the difference between the two, when the steel is exposed, is decreased.

Table 5.2 Comparison of surface and cut edge corroded areas at different pH for Galvalloy® samples immersed in 1wt% NaCl for 6 hours

Conc. [H⁺]	Surface corroded area after 6 hours (μm^2)	Cut edge corroded area after 6 hours (μm^2)
pH 7	20189	33558
pH 10	10053	31076

This image analysis also demonstrates that the corrosion rate is increased for both the pH 7 and 10 experiments when the steel is exposed. It needs to be considered this is purely a surface, 2D, assessment of the corrosion and does not indicate more penetrative corrosion. Nevertheless, the same trend is seen in the ZRA data, when comparing the i_{corr} with the surface polarisation data as shown in Fig 14. Although, the ZRA and PD experiments were performed in aerated and deaerated conditions, respectively, so the additional oxygen in the ZRA experiments would increase the cathodic reaction and therefore the overall corrosion rate. This means it is difficult to determine how much of the current density (i_{corr}) increase is caused by the introduced oxygen and the introduced steel.

TLM shows that at pH 10 there is anodic initiation in the cathodic region. Due to the production of OH$^-$ ions, the pH in this region would have increased and may have increased to the point that both the zinc and the aluminium were in the active region on the Pourbaix diagram leading the rapid corrosion. Also, the current density of pH 10 during the ZRA test remains constant, where at other pHs it slowly reduced, and passivated. Polarisation experiments in the previous chapter showed a small inflection of pseudo-passivity in the anodic arm at pH 10, which does not seem to occur when coupled with steel. Whereas in the case of pH 7 and 13, this passivity is seen in the ZRA results. This demonstrates that at pH 10 there is a tipping point where the corrosion is able to be reinitiated on the Galvalloy®. This is possible due to zincate and aluminate species that have been produced whose alkalinity is encouraging further corrosion, as seen in the TLM experiments.

pH 13

TLM shows prolonged bubble formation over the Galvalloy®-steel interface, which can be explained by a cathodic reaction of water splitting to produce hydrogen gas, as evidenced in the images and happens by the following equation: OH$^-$ ($2H_2O + 2e^- = H_2 + 2OH^-$). This reaction was seen in the surface corrosion videos at pH 13. The presence of iron has led to an increase in hydrogen formation as the reaction is more facile on iron.

ZRA showed that coupling Galvalloy® to steel at pH 13 leads to the highest increase in initial corrosion rate (i_{corr}) out of all pHs tested. This can be attributed to the large E_{corr} shift from free corrosion to the couple. As pH 13 has an E_{corr} of roughly 0.4 V lower than the other pHs during free corrosion, this would mean there is a larger overpotential compared to the other pHs.

As this corrosion is allowed to continue passivation is seen in the ZRA results in the form of oscillations of current density, attributed to the passivation mechanisms of zinc at high pHs (50).

5.5   Conclusion

- ZRA and TLM experiments were performed on Galvalloy® coupled to steel to determine the effect of the steel cathode on the corrosion rate and how this is influenced by the pH.

- Both ZRA and TLM data showed an increase in the rate of corrosion of the Galvalloy® when compared to the surface corrosion across all pHs tested.

- The initiation of corrosion of the Galvalloy® occurs in the primary zinc dendrites at pH 7, 10 and 13, whereas generalised corrosion occurs at pH 3.

- When comparing the i_{corr} from ZRA (aerated) with the PD of the surface corrosion (deareated), the rate of corrosion at pH 3 was least affected by the coupling, whereas pH 7 – 13 all increased markedly. This could also be attributed to the increase in cathodic current as during the aerated ZRA experiments, there is more oxygen for the oxygen reduction reaction.

Chapter Six

Corrosion rate of Galvalloy® false cut-edge as a function of the ratio of exposed steel in neutral pH NaCl electrolyte

6 Corrosion rate of Galvalloy® false cut-edge as a function of the ratio of exposed steel in neutral pH NaCl electrolyte

6.1 Introduction

This chapter is a continuation from the previous chapter, investigating the implications of the manufacturing design fault; the cut-edge. It is known that the corrosion of Galvalloy® is cathodically controlled (110), which would suggest that an increase in cathode area, in this case the steel, would lead to an increased rate of corrosion.

J. Sullivan et al. (13) performed work in order to establish how an increase in gauge thickness, so cathodic area would affect the microstructure and therefore corrosion rate of a Zn4.8Al galvanised coating in 0.1 wt.% NaCl solution. It was shown that an increase in gauge thickness led to a smaller number of larger dendrites due to the decreased cooling time associated with the heat retained in the steel. Weight loss measurements showed a polynomial trend between the gauge thickness and the zinc loss over the same period of time, a linear relationship was seen was standard HDG (55). Scanning vibrating electrode technique (SVET) experiments showed that with an increase in steel gauge thickness, there was an increase in cathodic area and an increase in the intensity of the anodic events.

As well as this trend of thicker gauge – higher rate, the fewer, larger zinc dendrites demonstrated "more intense, long lived anodes" versus the more plenty, smaller dendrites found in the thinner gauge samples.

To reaffirm these results and to verify the worth of the novel time-lapse microscopy, the cut edge experiments performed in the previous chapter were expanded. The ratio of exposed steel to Galvalloy® was altered, with experiments performed with increasing ratios of steel exposed (1, 2 and 3:1). And just as before, ZRA measurements have been performed to compliment the qualitative results provided by TLM, however, higher ratios (1, 2, 3, 5, 10:1) of exposed steel have been used as well to investigate if the effect is finite or not. The solution had a concentration of 1 wt.% NaCl and the pH has been adjusted to pH 7 by using NaOH. Another difference between these experiments and that performed by J. Sullivan et al. (13) is that the microstructure attacked is the surface of the Galvalloy®. This is because when preparing the 'cut-edge' samples, the polished Galvalloy® was taped with PTFE tape, to produce a straight line, and then immersed in 2 mol HCl for 20 minutes to remove the Galvalloy® and expose the steel substrate. This is because imaging the cut-edge produced during manufacturing requires a much greater magnification to resolve the microstructural features on the 20 µm cross-section of the Galvalloy® coatings, and this is not achievable with the current TLM set-up.

6.2   Experimental

The Sample Preparation to Simulate Cut-Edge Corrosion (2.9) and Zero-Resistance Ammeter (ZRA) (2.10.5) sections in the methods chapter detail the experimental procedure carried out for this chapter.

6.3   Results

6.3.1   Steel to Galvalloy® ratio 1:1

Video 6.1, shown as stills in Fig. 6.1, shows the cut-edge corrosion of Galvalloy® when the ratio of steel to Galvalloy® is 1:1. After 1 hour of immersion in the saline electrolyte anodic dissolution of the coating has occurred at a zinc dendrite (indicated by a circle), located at the interface of the coating and the steel substrate. The anodic dissolution continues to initiate at zinc dendrites, annotated by a circle in Fig. 6.1C. The anodic front continues its growth perpendicular from the interface in a uniform front.
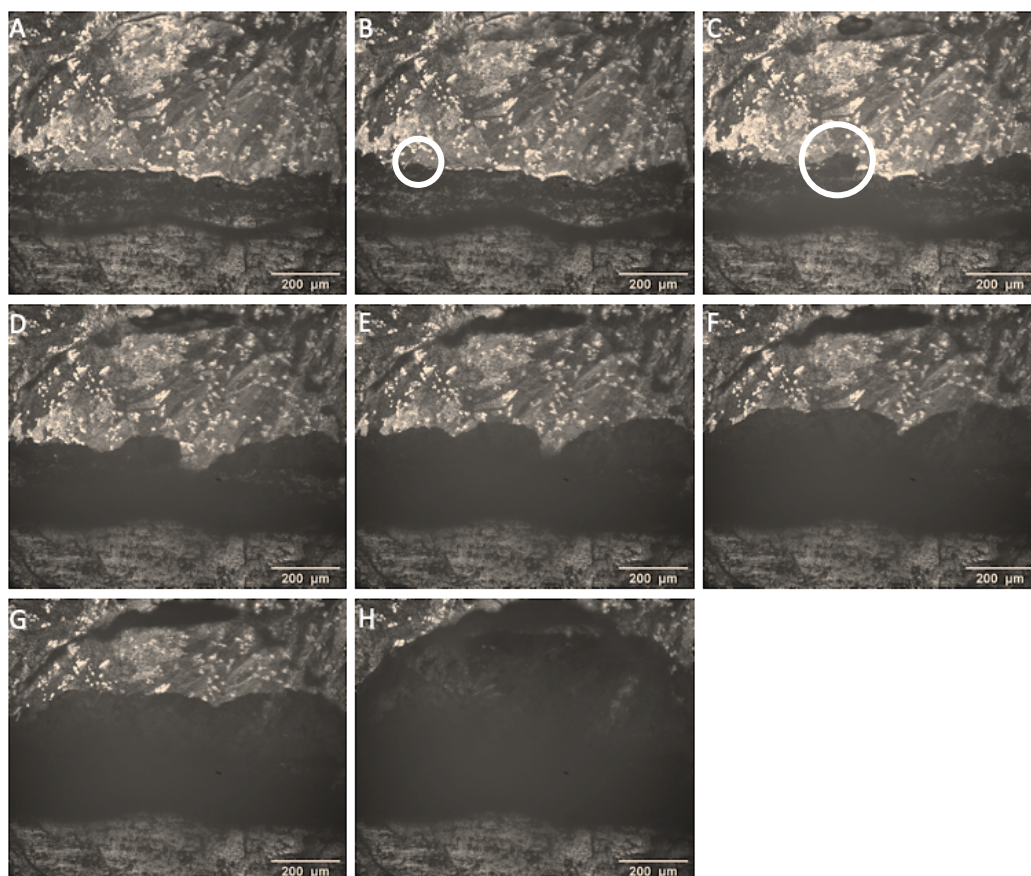
Fig. 6.1 Images A-H: Time-lapse microscopy images of Galvalloy® with exposed steel at a ratio of 1:1 in pH 7 1 wt.% NaCl. The images are taken every hour from 0 - 6 hours (A - G). Image H is taken at 10 hours and 40 minutes (640 mins), where complete anodic spread has occurred. These stills depict Video 6.1.

The corrosion continues across the entire exposed Galvalloy® where, at 10 hours and 40 minutes, the entire surface has undergone visible anodic dissolution.

6.3.2 Steel to Galvalloy® ratio 2:1

Video 6.2, shown as TLM stills in Fig. 6.2, shows the cut-edge corrosion of Galvalloy® when the ratio of steel to Galvalloy® is 2:1. The initial still shows the corrosion initiating in the zinc dendrite regions, as indicated by circles. Within one hour (Fig. 6.2B), the corrosion product is forming a ring on the steel substrate, similarly to the 1:1 experiment. However, the location of product ring is further onto the steel, with a gap between the steel and the coating-steel interface, annotated by a white arrow in Fig. 6.2C. The corrosion of the Galvalloy® continues to grow the initial initiation sites until they engulf the whole Galvalloy® area after 6 hours and 30 mins. The corrosion product continues to grow and become more dense over the course of the experiment.
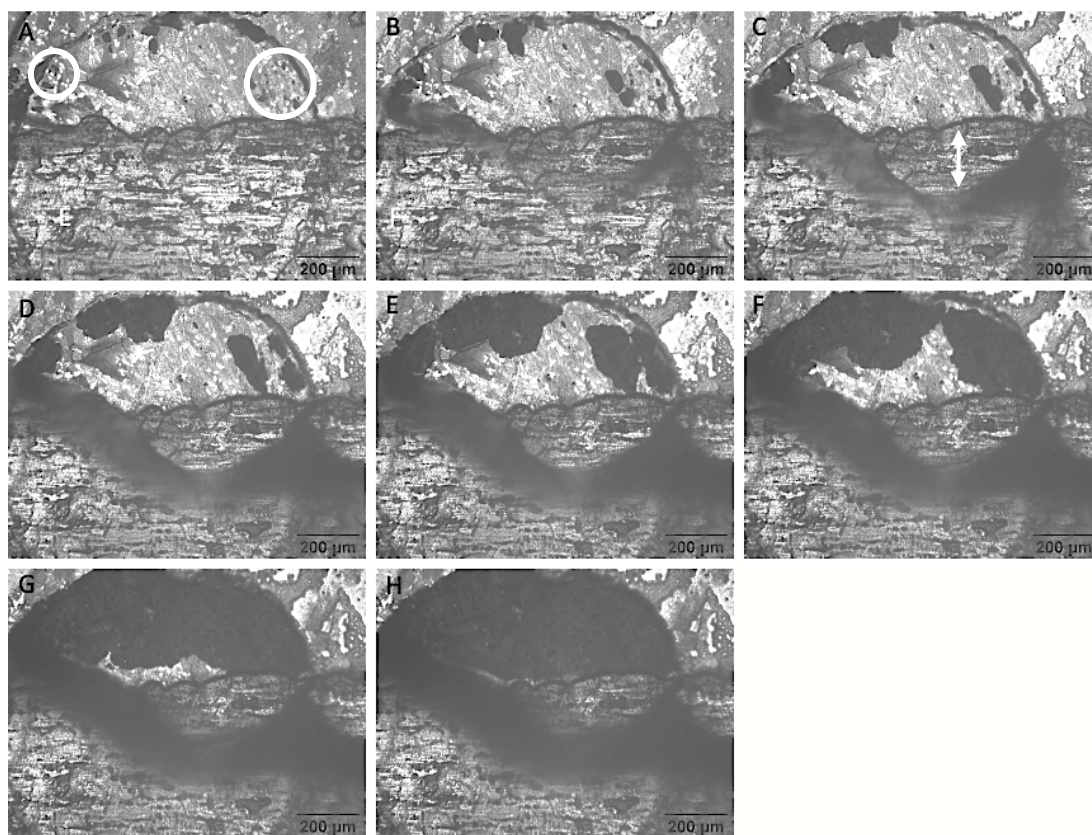
Fig. 6.2 Images A-H: Time-lapse microscopy images of Galvalloy® with exposed steel at a ratio of 1:1. The images are taken every hour from 0 - 6 hours (A - G). Image H is taken at 6 hours and 30 minutes (390 mins), where complete anodic spread has occurred. These stills depict video 6.2.

6.3.3   Steel to Galvalloy® ratio 3:1

Video 6.3, shown as TLM stills in Fig. 6.3, shows the cut-edge corrosion of Galvalloy® when the ratio of steel to Galvalloy® is 3:1. Anodes appear immediately on the Galvalloy® when immersed in the electrolyte, whilst in electrical contact with the steel substrate. Within an hour (Fig. 6.3B), a clear corrosion product ring appears equidistant between the coating-substrate and substrate-tape interface of the steel at the furthest point from the coating. The corrosion product forms a semi-circle shape surrounding the anodic area on the left-side Galvalloy®. As the anode continues to grow, moving across to the right-side of the Galvalloy®, as does the corrosion product, forming along a line parallel to the coating-substrate interface. After 5 hours, Fig. 6.3F, the corrosion product has formed over a large area on the steel. The entire Galvalloy® area is then completely corroded by 5 hours and 40 mins.
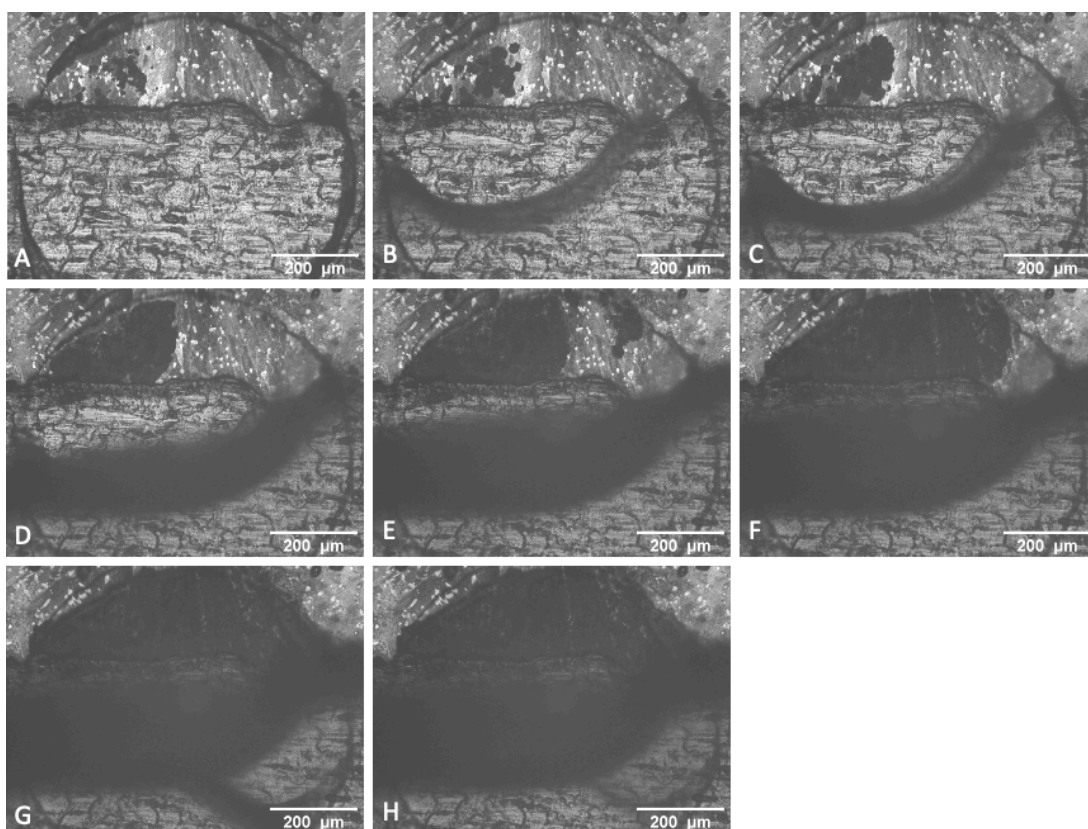
Fig. 6.3 Images A-H: Time-lapse microscopy images of Galvalloy® with exposed steel at a ratio of 1:1. The images are taken every hour from 0 - 6 hours (A - G). Image H is taken at 5 hours and 40 minutes (340 mins), where complete anodic spread has occurred. These stills depict video 6.3.

6.3.4   Image analysis of time-lapse microscopy

ImageJ software was used to measure the anodic area on the Galvalloy® at time intervals to quantify the growth seen in the TLM. Fig. 6.4a) shows the anodic area increasing over the duration of the test as a percentage of the Galvalloy® surface exposed. It shows that with increasing ratio of steel to Galvalloy®, the rate of corrosion of the Galvalloy® as a percentage of the area is also increased. The overall rate trend is shown in Fig. 6.4b) displays this trend to be fairly linearly between the Galvalloy® samples with steel exposed. It shows that when no steel exposed, this trend is not fitting and that the rate of corrosion is dramatically decreased, which clearly demonstrates how the steel cathodes effects the corrosion rate of the Galvalloy®.
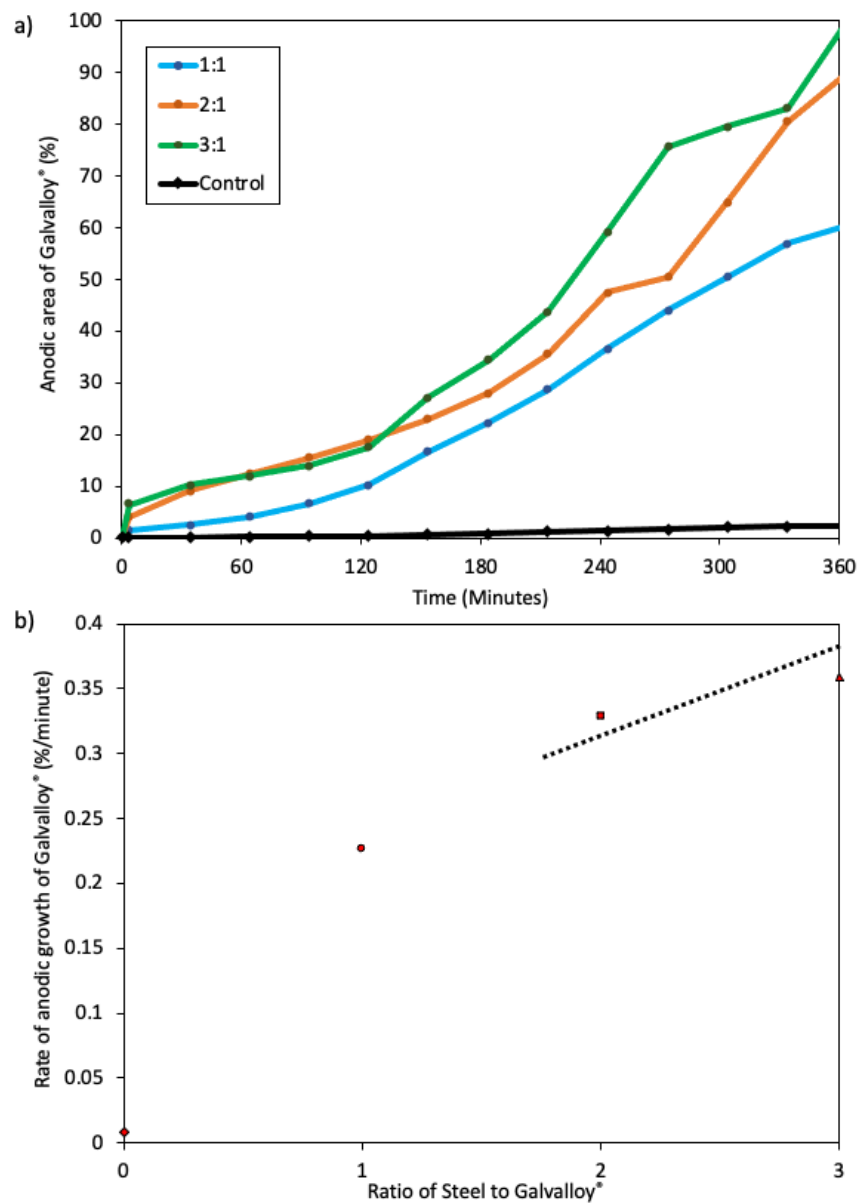
Fig. 6.4 The graphs show the anodic areas as a percentage of the area of Galvalloy® measured using imageJ. a) shows the anodic area over a 6-hour time period, and b) shows the rate of anodic growth as a function of the ratio of steel to Galvalloy®.

6.3.5 Zero Resistance Ammetery

The ZRA experiments were carried out using Galvalloy® samples that has the same surface preparation as the TLM experiments, described in the methods chapter. The samples were immersed in 1 wt.% NaCl solution adjusted to pH 7. The working electrode was the Galvalloy® with a fixed area of 1 cm², and the counter electrode was steel with areas of 1, 2, 3, 5 and 10 cm² to produce the ratio 1:1, 2:1, 3:1, 5:1 and 10:1, respectively.

The ZRA and TLM experiments are not performed in identical conditions. The two electrodes (steel and Galvalloy®) are held separately in a beaker of solution. They are then connected to, via crocodile clips and wires, the potentiostat, where the current passing from the electrodes is measured. A positive value of current represents the net flow of electrons from the Galvalloy® surface to the steel surface. This is different from the TLM, where the electrons flowing from the anode to the cathode will pass through the microstructure of the Galvalloy® and steel.

Another difference is that the electrodes are held vertically in the solution, facing one another, and separated by around 1 – 2cm. Whereas in the TLM tests, they are orientated horizontally and are in contact, which means they can an influence of the local surface chemistry of the other electrodes, influencing their corrosion mechanisms, whether it be by passivation (reduction in rate) or re-activation (increase in rate).

Also, as the area of Galvalloy® and steel combined is constant during the TLM tests, this means that in the 3:1 test the area of Galvalloy® is less than the 1:1 test, and vice versa for the area of the steel. This leads to an increase in the current density on the 3:1 ratio compared to the 1:1 as the area of the Galvalloy® is decreased by 3, increasing the current density by the same factor, as well as increasing the cathodic area, which will also increase the total current. These differences will give rise to different rates of corrosion seen, but, in general, the rates will be similar and representative.

The 'as-received', raw ZRA graph, is shown in Fig. 6.5, and displays the current densities of the samples (A.cm⁻²) from the initial corrosion period (from 1.0 to 1.9 hours). The reason this time period is being analysed is because it allows time for the surface oxides, present on the samples, to be removed, in order for more representative results of the TLM to be captured. It is very clear from inspecting this hour window at the initial stage of corrosion that there is a clear, linear correlation, where increasing the ratio of steel exposed, increases the rate of anodic dissolution of the Galvalloy®.
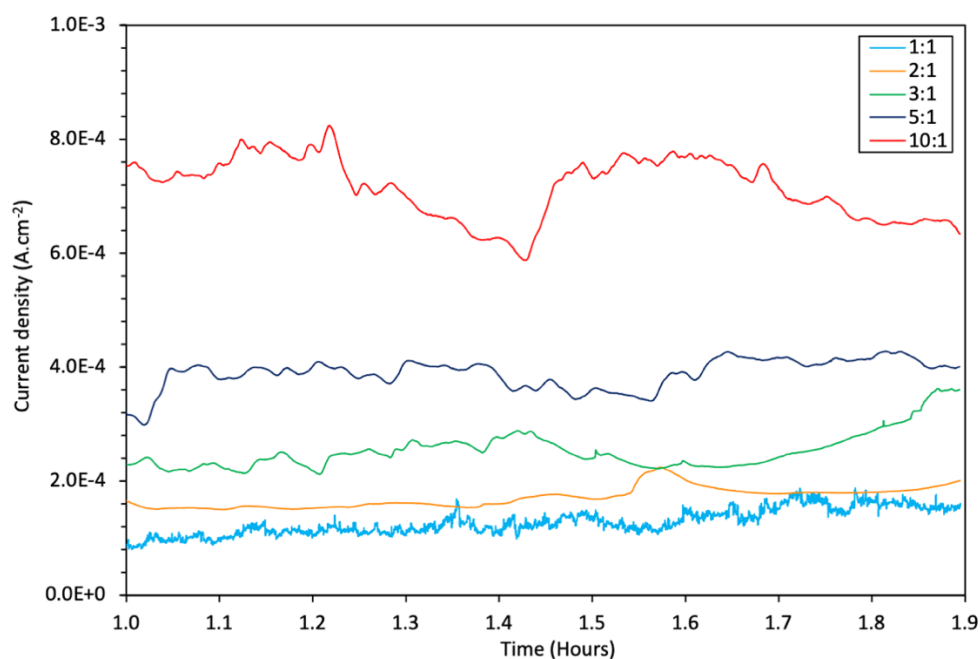
Fig. 6.5 ZRA data of Galvalloy® coupled with the steel substrate in pH neutral 1 wt.% NaCl with varying ratios of increasing steel to Galvalloy® (1, 2, 3, 5 and 10:1). The graph shows the current density between the first and second hour of the experiment.

The cumulative charge dissipated for this time period is shown in Fig. 6.6. The value represents the number of net electrons that have passed from the Galvalloy® to the steel, which is directly proportional to the amount of Zn^{2+} and Al^{3+} ions that undergone anodic dissolution from the surface of the Galvalloy® electrode. It is seen from this time period (Fig. 6.6), that there is a clear linear relationship between the anodic dissolution rate and the area of steel exposed.
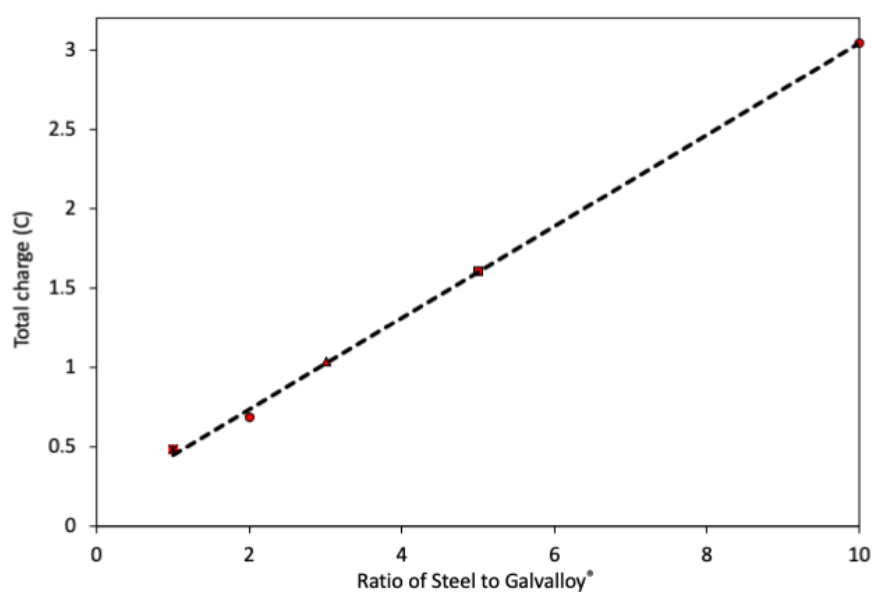
Fig. 6.6 The total charge (C) dissipated (proportional to metal loss) from the Galvalloy® (anode) to the steel (cathode) versus the ratio of steel to Galvalloy® (1, 2, 3, 5, and 10:1), between 0.7 and 1.9 hours for the representative data show in Fig. 6.5.

6.4   Discussion

The ZRA and TLM results reported in this chapter show that with an increase in the ratio of steel to Galvalloy®, during galvanic corrosion, results in a corresponding increase in rate of corrosion of the coating. The reason for this, is that the corrosion of Galvalloy® at pH 7, is cathodically controlled, something that has been established in the potentiodynamic polarisation curves in chapter 4. As the area of the steel, shown to act as a net cathode in the ZRA experiments, increases, as does the rate of anodic dissolution of the Galvalloy® coating. This is due to the oxygen reduction reaction (ORR), occurring on the surface of the steel, being the rate determining step of the corrosion of the electrochemical, galvanic cell that has been set-up. As the cathodic area is increased, the area allowing the ORR to take place is increased, increasing the cathodic current, which in turn increases the anodic current on the Galvalloy® to balance the charge.

The ZRA results in this chapter clearly show this trend, with a linear increase in anodic rate with respect to the increasing cathode area. The visual information and quantitative data from the TLM experiments supports this trend further. However, the correlation seen in the TLM results is not a linear one, when comparing the 2-dimensional anodic growth. The results demonstrate a diminishing anodic rate increase with increasing cathode/steel area. This, non-linearity can be attributed to a number of factors. Firstly, $Zn(OH)_2$ formation on the steel surface, seen in all of the TLM experiments, prevents the transport of oxygen to the surface of the steel, decreasing the cathodic current, therefore decreasing the anodic dissolution rate. Thébault et al. (115) demonstrated there is an area between the steel and the coating where the pH is low and past this distance the pH increases as a result of an increase in OH⁻ ions . As the area of the steel during the 3:1 TLM experiment was larger, the area of increased pH was also increased. Increasing the concentration of OH⁻ ions allows for more precipitation of $Zn(OH)_2$, leading to a decrease in the cathodic area and therefore the overall corrosion rate. When this is put into the context of the cut edge of the manufactured coated sheet steel, the area for precipitation of $Zn(OH)_2$ and therefore reduction in corrosion is also increased. Secondly, Zn^{2+} ions that release over the anode alter the surface chemistry changes that occur at the cut-edge, reducing the pH due to hydrolysis, further activating the Zn and Al, increasing the anodic dissolution rate. Another point to consider when comparing the TLM image analysis data with the ZRA results is that the Galvalloy® area is not constant, so the current density for the smaller areas is greater. This is demonstrated by comparing the ratios of corrosion product and anodic areas are compared, it is found that at 3:1 there is far more corrosion product (2.4) compared to 1:1 and 2:1 which are the same (1.4).

Another question arises as to why the ZRA results show a linear relationship, rather than a parabolic relationship, that was seen in previous studies on the same alloy (13). This can be attributed to the changes in microstructure caused by the increase in gauge thickness, specifically the increase in the size of the dendrites, which was deemed the cause of the parabolic trend. As

the microstructure of the Galvalloy® tested in this report was that found on the surface of the coating which has the same cooling rate, a more consistent microstructure was measured for its corrosion behaviour in the ZRA tests and seen in the TLM results. Therefore, the microstructure was a controlled variable, and the linear increase in corrosion rate can be attributed to the increase in cathode size.

6.5   Conclusions

- ZRA electrochemical experiments and time-lapse microscopy (TLM) methods were employed to elucidate the effect of increasing steel area at the cut-edge on the corrosion rate of the sacrificial Galvalloy® coating.

- ZRA showed a linear trend between initial corrosion rate and ratio of steel to Galvalloy® exposed. This is attributed to the cathodic control of Galvalloy® at pH 7, thus increasing the steel area, which acts as the cathode, increases the kinetics of the oxygen reduction reaction due to an increase in area available for the reduction of oxygen, driving the anodic dissolution of the Galvalloy® surface.

- TLM supported the results found in ZRA visually and with image analysis data. However, the trend was non-linear, which is attributed to the precipitation of corrosion product ($Zn(OH)_2$) on the steel, reducing the rate of the oxygen reduction reaction and therefore the anode growth rate.

- The comparison of the results from the two techniques is a reminder that when researching a deducing corrosion rates, care must be taken to assess variables that could be give results that do not fully represent the real-world product-life conditions.

Chapter Seven

Accelerated testing: filiform corrosion of Galvalloy®

7 Accelerated testing: filiform corrosion of Galvalloy®

7.1 Introduction

The Active Classroom at Swansea University's Bay Campus is a demonstration building blah. It has chromate-free, 255 gsm Galvalloy®-coated, steel cladding with a Colorcoat Prisma® organic coating as its exterior wall, which, after two years, experienced substantial cut edge and filiform corrosion (FFC), shown in Fig. 7.1. This building experiences a harsh service environment, subjected to strong wind, heavy rain and high exposure to corrosive substances, chloride and sulphate ions, due to the proximity to the sea and neighbouring steel factory. The building is also located near a site of specific scientific interest (SSSI), which has many trees which produce acetic acid, which is also a corrosive media. As such, this coating system provides a real-world case study of the Galvalloy® coating that has been investigated in the previous chapters.

Fig. 7.1 Corrosion found on the Active Classroom at Swansea University at corner of an exterior window frame.

Sacrificial alloy coatings have previously been coated with model organic coatings, such as PVB, to assess their corrosion performance. PVB coated HDG fails according to a cathodic disbondment mechanism, yet zinc-magnesium-aluminium alloys (116,117) and aluminium alloys (118,119) fail via a filiform corrosion (anodic) disbondment mechanism.

In this chapter, attempts were made to reproduce the corrosion seen on the Active Classroom with different salts to establish any similarities in the visual mechanisms seen and thus develop an understanding as to why these materials have failed so rapidly. This is in order to determine the prevailing mechanism on Galvalloy® using different corrodent salts. So, four electrolytes of CH_3OOH (acetic acid), NaCl, HCl and $FeCl_2$ were individually administered to penetrative defects in 255 gsm, line produced, polyvinyl butyral coated, Galvalloy® samples, as shown in (120), and subsequently placed in an environment of >90 % relative humidity for a 21-day period.

7.2   Experimental

The Filiform Preparation (2.3) section in the methods chapter details the experimental procedure carried out for this chapter.

7.3   Results

7.3.1   Imaging

Fig. 7.2 shows the surface of the scribed (10 mm), PVB coated, Galvalloy® samples after a 21-day exposure period in a >90 % relative humidity (RH %) environment after administration of 2 µL of evenly distributed, 2M electrolyte. The humidity was controlled by a shallow pool of 5 wt.% NaCl at the bottom of the sealed chamber. The surface of the Galvalloy® was polished with 1 µm alumina paste to aid the adhesion of the PVB, to reduce the delamination caused by effects other than FFC.

Images A and B in Fig. 7.2, show the scribed areas of the samples exposed to CH_3OOH and HCl, respectively. The samples show slight lightening under the surface of the PVB near the scribe, indicating disbondment between the Galvalloy® substrate and the PVB. The CH_3OOH and HCl samples both have white, radial fronts on the major disbonded areas, and the HCl sample also shows dark fronts on some minor disbonded areas.

Images C and D in in Fig. 7.2, show the scribed areas of the samples exposed to $FeCl_2$. The corrosion product in these tests is an orange-red colour. The area of delamination is greater than that seen in the CH_3OOH and HCl samples. As well as red corrosion product, white, radial corrosion product areas are seen, which are likely to be $Zn(OH)_2$.

Images C and D in in Fig. 7.2, show the scribed areas of the samples exposed to NaCl. The delamination in these tests were the largest of all of the salts tested. The corrosion under the film has formed dark blistering. White rust is also seen in the NaCl samples. These two characteristics indicate filiform corrosion.
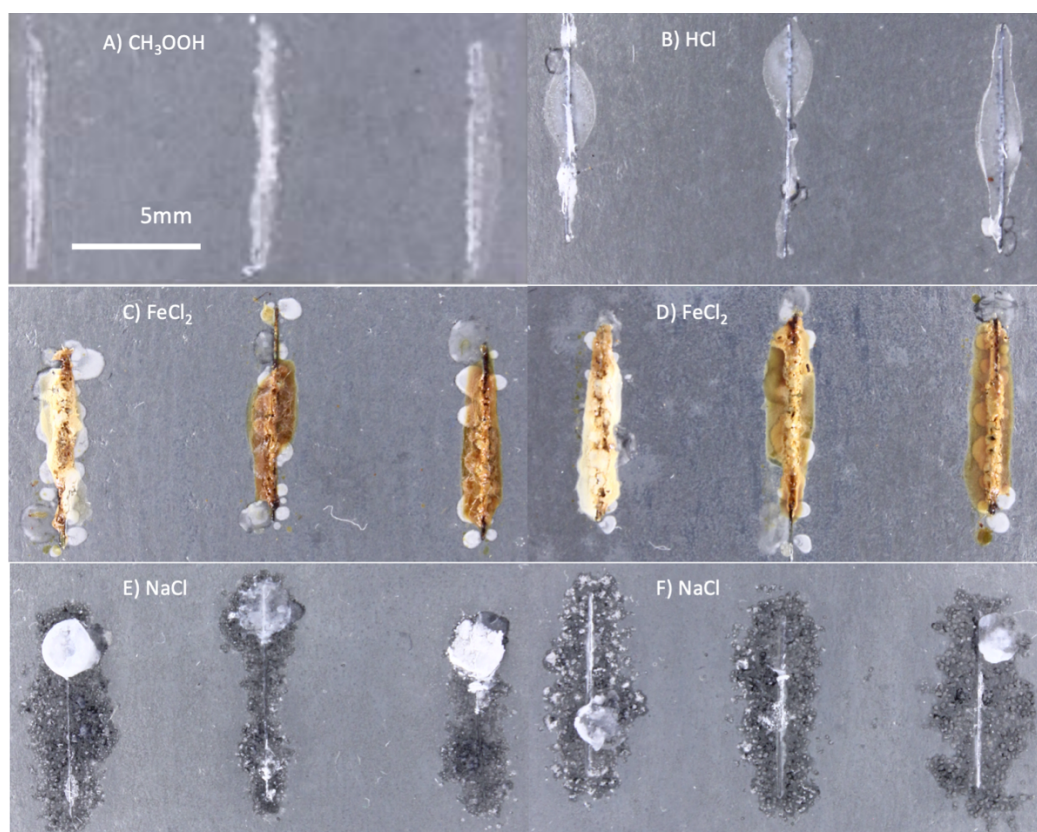
Fig. 7.2 D-SLR images of the scribed samples after 21-day exposure at 95 % RH to 2 M electrolytes of A) CH₃OOH (acetic acid), B) HCl, C and D) FeCl₂, and E and F) NaCl.

7.3.2   Environmental measurements (EasyLog)

The graph in Fig. 7.3 shows the data collected from an EasyLog humidity and temperature sensor placed in the chamber for 7 days to obtain the climatic conditions during the test. The temperature (°C), dew point (°C) and RH % were recorded every minute and plotted against time. The data in Fig. 7.3 shows these conditions in the initial 96 hours of the experiment, and thereafter the conditions had stabilized and remained constant. The key data from this graph is shown in Table 7.1. The minimum values recorded of all three variables were recorded at the initial stages of the experiment when the conditions within the chamber were identical to those outside of the chamber. It is seen that the temperature within the chamber stabilised quickly, while the dew point and RH % took a period of 12 and 24 hours, respectively, to stabilise.
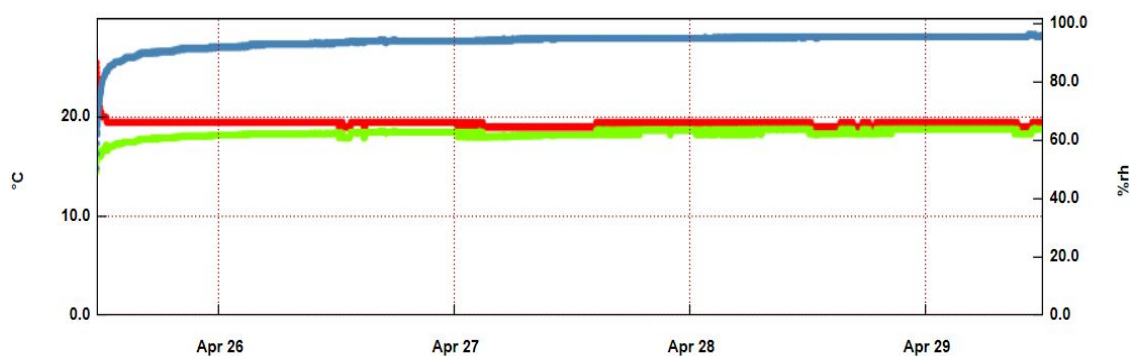
Fig. 7.3 Graph showing the change in temperature (red), dew point (green) and RH% (blue) over a the initial 4-day period. After this point the values remained constant.

Table 7.1 Data readings of the temperature, dew point and RH % within the incubation environment over a 7-day period.

Measurement	Maximum	Minimum	Mean
Temperature (°C)	28.5	19.0	19.5
Dew Point (°C)	23.5	14.5	18.6
RH (%)	96.5	49.5	94.6

7.4 Discussion

CH_3OOH, HCl and $FeCl_2$

The samples exposed to CH_3OOH, HCl and $FeCl_2$ salt electrolytes demonstrated varying degrees of anodic undermining. This is a class of corrosion reaction that occurs underneath the organic coating and the resultant loss of adhesion observed is due to anodic dissolution of the substrate or its oxide (22). It occurred due to the low pH formed under the film, which is the anodic site. Whereas, the cathodic activity occurs at the scribe defect site, and has a high pH. When the products from the cathodic and anodic reactions meet due to diffusion, they undergo a reaction to form corrosion products. The mechanisms of anodic undermining as similar to those in FFC, however there is a lack of filament propagation from the defect. Instead, the delamination occurs more uniformly.

The orange discolouration exhibited by the specimens exposed to the $FeCl_2$ electrolyte is predominantly due to the colour of the electrolyte. The increased delamination seen due to the $FeCl_2$ compared to the CH_3OOH and HCl could be due to an increase in the oxidation state of iron from Fe^{+2} to Fe^{+3} at the anodic site, creating a local environment of extreme acidity due to hydrolysis and resulting in the increased rate of delamination.

NaCl

The NaCl tests demonstrated signs of FFC. Van Loo et al. (32) showed relative humidities > 93 % results in a blister morphology on the surface of the substrate instead of the characteristic thin branch like filaments observed at lower humidities. The data collected from the EasyLog sensor (Fig. 7.3 and Table 7.1), supports this hypothesis, as the average RH measured during operation was 94.6 %. This is greater than the lower boundary referenced for inducing the blistering type of FFC (32).

The FFC mechanism cannot be entirely attributed to the corrosion seen in the NaCl samples. Cathodic disbondment may also be responsible for the observations. This is due to the influence of the NaCl electrolyte, which, when presented with OH^- ions, undergo a redox reaction to form sodium hydroxide (NaOH). This is a very alkali chemical and is known to produce cathodic disbondment behaviour, shown in Fig. 7.4. This mechanism sees cathodic activity occurring at the delamination front and anodic activity at the scribe defect. Demonstrating a change in mechanism from the presence of a different electrolyte.
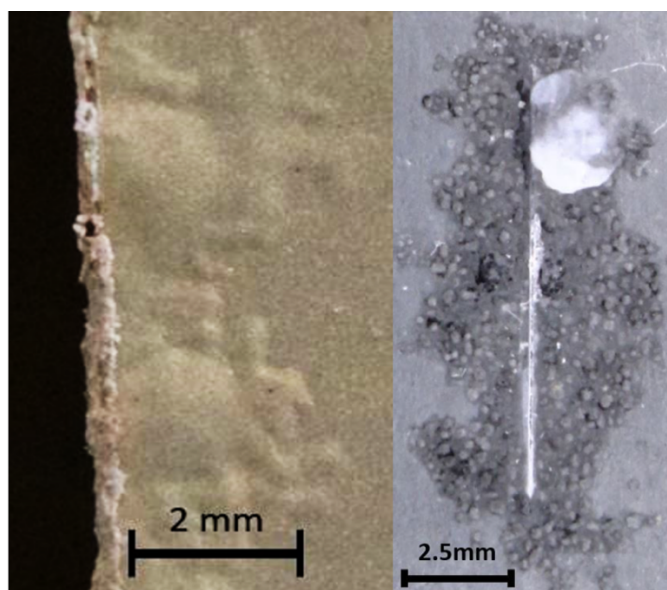
Fig. 7.4 Comparison of corrosion seen on the Active Classroom (left) with that see during the scribed samples exposed to 2 M NaCl (right).

Fig. 7.4 shows the corrosion that occurred on the outside of the Active Classroom over a 2-year period compared with the under-film degradation seen during the controlled, laboratory experiment. When comparing the two it is important to remember that the cut-edge of the Active Classroom site is mimicked by the scribe on sample tested during the laboratory experiment. This is supported by the white deposits found at both the cut-edge and the scribe, demonstrating similarities in morphology.

An initial area of more uniform corrosion occurs, extending approximately 1.5 and 3 mm on the Active Classroom and from the scribe, respectively, at its furthest point. After this, the more characteristic filaments begin to propagate outwards, more so in the case of the classroom, but initial signs suggest that a similar event is occurring around the scribe.

It is of significant interest that the NaCl electrolyte test has shown the closest resemblance to the corrosion observed on the Active Classroom. The classroom, as previously mentioned, is exposed to a relatively high concentration of chloride ions due to close proximity to the sea. It can be deduced that the NaCl electrolyte is a substantial contributor in this example of real-life, in-service corrosion.

7.5 Conclusion

Cut-edge corrosion was seen on the Active Classroom, at the Swansea University Bay Campus. Filiform corrosion experiments were performed on organically coated Galvalloy® with a range of salt electrolytes to determine which electrolytes were most prevalent in the corrosion seen on the Active Classroom. CH_3OOH, HCl, and $FeCl_2$ electrolytes produced anodic undermining under the PVB film. During the corrosion of the NaCl samples, it is very likely cathodic disbondment is seen, and the NaCl tests produced similar morphology to that seen on the Active Classroom, suggesting that the marine environment that the building is in close proximity to, is a substantially contributing the corrosion mechanism.

This study could be continued further to better understand the kinetics and mechanism of the under-film corrosion. Periodic imaging of the defects would allow a better understanding of the growth of the corrosion over time. A scanning Kelvin probe (SKP) can also be employed to better understand the kinetics if scans are taken periodically. As well as kinetics, the SKP can determine the potential at the head of the propagating corrosion filiform. If the potential of the head is positive the corrosion mechanism is cathodic disbondment, whereas if the head is negative, the mechanism is anodic disbondment.

Chapter Eight

Conclusions and Future Work

8 Conclusions and Future Work

8.1 Conclusions

Time-lapse microscopy (TLM), married with electrochemical techniques, have been used to study the corrosion mechanisms and rates of TATA Steel's premium galvanised coating, Galvalloy® (Zn-4.8wt.%Al). In chapter 3, microscopy showed that the microstructure was made up of pro-eutectoid primary zinc dendrites, Zn (η), as well as a eutectic lamellae of alternating layers of Zn (η) and Zn68Al (α), which are produced from room temperature degradation of Zn22Al (β). When the surface of the coating was immersed in a pH neutral saline electrolyte, the eutectic phases was preferentially attacked. However, when the coating was coupled with the steel substrate at the cut-edge, the zinc dendrites were preferentially attacked. This change in mechanism was postulated to be due to the zinc dendrites greater ability to reduce oxygen compared to the Zn68Al phase during surface corrosion, shown by rotating disk electrode. Potentiodynamic polarization (PD) showed that with increasing aluminium content, the phases became more noble, explaining the susceptibility of anodic attack of the dendrites during cut-edge corrosion.

In chapter 4, TLM and PD were used in unison, again, to demonstrate the surface corrosion rates of Galvalloy® at pHs 3, 7, 10 and 13. A $y=x^2$ trend was shown to exist, with high rates at pHs 3 and 13 and low rates at pH 7 and 10, with pH 10 having the lowest rate. TLM showed preferential eutectic attack at all pHs bar pH 3, where generalized corrosion occurred. It also showed that the corrosion product would readily form at pH 10, due to greater concentration of OH^- ions. PD showed that the corrosion at pH 3, 7 and 10 are anodically controlled, whereas, at pH 13, it is cathodically controlled. In chapter 5, Cut-edge corrosion of Galvalloy® was investigated using TLM and zero resistance ammetery (ZRA) across the same pH range. The same $y=x^2$ trend of the corrosion rates was seen with respect to pH, and preferential attack was seen to occur at the eutectic phase at pHs 7, 10 and 13, and generalized corrosion at pH 3.

In chapter 6, TLM and ZRA were used together once more to elucidate the relationship between effect of the ratio of steel to Galvalloy® on the rate of corrosion. A linear relationship was found, with both techniques supporting one another's findings. In chapter 7, scribed samples of Galvalloy® coated steel that had been coated with PVB were left in laboratory-controlled humid conditions exposed to various salts. Anodic undermining occurred in HCl, CH_3OOH and $FeCl_2$, whereas cathodic delamination occurred from exposure to NaCl. This supported the blistering that had occurred at the Swansea University Active Classroom, which is exposed to extreme marine conditions.

8.2   Future work

To further understand the corrosion mechanisms of Galvalloy® and other iterations of galvanic coating systems, such as MagiZinc®, elemental dissolution rates are key to measure. For instance, pairing TLM and PD and atomic emission spectroelectrochemistry (AESEC) would be a promising next step. This involves observing the microstructure of these alloys whilst they are being polarized. As the alloy is corroding, the electrolyte can be pumped away, at a known rate, to an AES machine which can detect elements and the time at which they have gone into dissolution. This can then be used across the same pHs as the ones in this study to ascertain which elements are going into dissolution, and therefore responsible for the anodic currents seen in the PD test. It can also be used to add further scientific backing to the visual evidence seen from the TLM experiments. This will be especially important when testing other alloys, with a variety of different alloying elements, to deduce which are going into dissolution when to gather a fundamental grounding into the corrosion mechanisms.

Another suggestion is to adapt the chemistry of the inhibitor systems to take into consideration the location at which the corrosion is likely to take place. For instance, if the inhibitor is near the cut-edge and the product has an intended lifetime around neutral pH, inhibiting the corrosion of the zinc due to the preferential initial dissolution of zinc phases. Also, if the inhibitor is working where surface corrosion of Galvalloy® is likely and the product has an intended lifetime around neutral pH, an inhibitor that reduces the corrosion of aluminium, due to the preferential attack of Al containing phases at this location. Having a dynamic approach to the inhibitor systems used whether it be location of the strip steel or a response to the environment the product will work in has the potential to greatly improve the product lifetime.

9 References

1. World Steel Association. Steel Facts [Internet]. 2015. Available from: https://www.worldsteel.org/Steel-facts.html

2. Lang J. Roman iron and steel: A review. Mater Manuf Process. 2017;32(7–8):857–66.

3. Simmons MR. Oil And Gas "Rust": An Evil Worse Than Depletion. Offshore Technol Conf. 2008;

4. Scully J. Editorial CORROSION Assigns " Editor ' s Choice " Open Access to Key Papers Related to the Water Crisis in Flint , Michigan. 2014;72(4):451–3.

5. Scholz F. Electroanalytical Methods. 2nd ed. Vol. 53, Journal of Chemical Information and Modeling. Springer; 2010.

6. Evans C. An Anecdotal History or the Galvanizing Industry [Internet]. 1992. Available from: http://www.galvanizing.org.uk/hot-dip-galvanizing/history-of-galvanizing/

7. Thomas JM, Edwards PP, Kuznetsov VL. Sir Humphry Davy: Boundless chemist, physicist, poet and man of action. ChemPhysChem. 2008;9(1):59–66.

8. G82 A. ASTM G82 - 98(2021)e1 - Standard Guide for Development and Use of a Galvanic Series for Predicting Galvanic Corrosion Performance. 2021.

9. Vanysek P. "Electrochemical series", in Handbook of chemistry and physics. 2000;1–13.

10. Marder AR. Metallurgy of zinc-coated steel. Progr Mater Sci. 2000;45(3):191–271.

11. Goodwin F. Galfan: Galvanising Alloy Technology. 1984;

12. Penney DJ, Sullivan JH, Worsley D a. Investigation into the effects of metallic coating thickness on the corrosion properties of Zn-Al alloy galvanising coatings. Corros Sci. 2007;49:1321–39.

13. Sullivan J, Weirman C, Kennedy J, Penney D. Influence of steel gauge on the microstructure and corrosion performance of zinc alloy coated steels. Corros Sci. 2010;52(5):1853–62.

14. Elvins J, Spittle J a., Worsley D a. Microstructural changes in zinc aluminium alloy galvanising as a function of processing parameters and their influence on corrosion. Corros Sci. 2005 Nov;47(11):2740–59.

15. Howard RL, Zin IM, Scantlebury JD, Lyon SB. Accelerated tests for prediction of cut edge corrosion of coil-coated architectural cladding. Part II: cyclic immersion. Prog Org Coatings. 1999;37(1):83–90.

16. Li S, Hihara LH. In situ Raman spectroscopic identification of rust formation in Evans'

droplet experiments. Electrochem commun. 2012;18(1):48–50.

17.   Tafel J. Über die Polarisation bei kathodischer Wasserstoffentwicklung. Zeitschrift für Phys Chemie. 1905;50A:641.

18.   Pourbaix M. Lectures on Electrochemical Corrosion. Power. 1973.

19.   Fontana MG. Corrosion Engineering. Third. McGraw Hill; 1987. 576 p.

20.   Sastri VS, Ghali E, Elboujdaini M. Corrosion Prevention and Protection. Chichester, UK: John Wiley & Sons, Ltd; 2007. 574 p.

21.   Schweitzer PA. Corrosion-Resistant Linings and Coatings. 2001. 434 p.

22.   Schweitzer PA. Corrosion-Resistant Linings and Coatings. New York: Marcel Dekker, Inc.; 2001.

23.   Trethewey KR, Chamberlain J. Corrosion for Science and Engineering. 2nd ed. Longman; 1995. 466 p.

24.   Eurofer. European Steel in Figures 2008-2017. 2018;

25.   BEIS. Future capacities and capabilities of the UK steel industry. BEIS Research Paper Number 26. Executive Summary. 2017;(26).

26.   Howard RL, Lyon SB, Scantlebury JD. Accelerated tests for the prediction of cut-edge corrosion of coil-coated architectural cladding. Part I: Cyclic cabinet salt spray. Prog Org Coatings. 1999;37(1):91–8.

27.   Dafydd H, Worsley DA, McMurray HN. The kinetics and mechanism of cathodic oxygen reduction on zinc and zinc–aluminium alloy galvanized coatings. Corros Sci. 2005;47(12):3006–18.

28.   Leng A, Streckel H, Hofmann K, Stratmann M. The delamination of polymeric coatings from steel Part 3: Effect of the oxygen partial pressure on the delamination reaction and current distribution at the metal/polymer interface. Corros Sci. 1998;41(3):599–620.

29.   Fürbeth W, Stratmann M. Scanning Kelvin Probe investigations on the delamination of polymeric coatings from metallic surfaces. Prog Org Coatings. 2000;39(1):23–9.

30.   Slabaguh WH, Dejager W, Hoover SE, Hutchinson LL. Filiform Corrosion of Aluminium. J Paint Technol. 1972;44:76.

31.   Bautista A. Filiform corrosion in polymer-coated metals. Prog Org Coatings. 1996;28(1):49–58.

32.   Loo M Van, Laiderman D, Bruhn R. Filiform Corrosion. Vol. 9, Corrosion. 1953. p. 277–83.

33. Williams G, McMurray HN. The mechanism of group (I) chloride initiated filiform corrosion on iron. Electrochem commun. 2003;5(10):871–7.

34. Kaesche H. Untersuchungen über die Filigrankorrosion lackierter Stahlbleche. Mater Corros und Korrosion. 1959 Nov;10(11):668–81.

35. Ruggeri RT, Beck TR. Analysis of Mass Transfer in Filiform Corrosion. Corrosion. 1983;39(11):452–65.

36. Leidheiser H. Corrosion of Painted Metals - a Review. Corrosion. 1982;38(7):374–83.

37. Funke W. Blistering of paint films and filiform corrosion. Prog Org Coatings. 1981;9(1):29–46.

38. Lenderink HJW. Filiform corrossion of coated aluminium alloys. Techniche University Delft; 1995.

39. Holness RJ, Williams G, Worsley DA, McMurray HN. Polyaniline inhibition of corrosion-driven organic coating cathodic delamination on iron. J Electrochem Soc. 2005;152(2).

40. Zhang X, Leygraf C, Odnevall Wallinder I. Atmospheric corrosion of Galfan coatings on steel in chloride-rich environments. Corros Sci. 2013;73:62–71.

41. Organisation IS. Corrosion tests in artificial atmospheres — Salt spray tests (ISO 9227:2017). 2017;

42. ASTM. Standard Practice for Operating Salt Spray (Fog) Apparatus (ASTM B117 - 19). 2019;

43. Wong C, Chen AA, Behr B, Shen S. Time-lapse microscopy and image analysis in basic and clinical embryo development research. Reprod Biomed Online. 2013;26(2):120–9.

44. Behr B, Suraj V, Tan L, Atypical SS. Evaluation of early cytokinetic timepoints by timelapse microscopy. Fertil Steril. 2016;106(3):e354.

45. Watson TM, Coleman AJ, Williams G, McMurray HN. The effect of oxygen partial pressure on the filiform corrosion of organic coated iron. Corros Sci. 2014;89(C):46–58.

46. Sullivan J, Mehraban S, Elvins J. In situ monitoring of the microstructural corrosion mechanisms of zinc-magnesium-aluminium alloys using time lapse microscopy. Corros Sci. 2011;53(6):2208–15.

47. Sullivan J, Cooze N, Gallagher C, Lewis T, Prosek T, Thierry D. In-situ monitoring of corrosion mechanisms and phosphate inhibitor surface deposition during corrosion of Zinc Magnesium Aluminium (ZMA) alloys using novel time-lapse microscopy. Faraday Discuss. 2015;1–19.

48. Prosek T, Goodwin F, Thierry D. Alloying of Zn-Al-Mg coatings for corrosion stability

improvement. 2015;813–21.

49.   Bellezze T, Giuliani G, Roventi G. Study of stainless steels corrosion in a strong acid
        mixture. Part 1: Cyclic potentiodynamic polarization curves examined by means of an
        analytical method. Eval Program Plann. 2017;

50.   Thomas S, Birbilis N, Venkatraman MS, Cole IS. Corrosion of zinc as a function of pH.
        Corrosion. 2012;68(1):1–9.

51.   Pletcher D. A first course in electrode processes. Royal Society of Chemistry; 1991. 301
        p.

52.   Levich V. Physicochemical Hydrodynamics. Englewood Cliffs, NJ: Prentice Hall; 1962.

53.   Pourbaix M. Atlas of electrochemical equilibria in aqueous solutions,. [1st Engli.
        Oxford ;New York: Pergamon Press; 1966.

54.   Zembura Z, Burzynska L. The corrosion of zinc in de-aerated 0.1 M NaCl in the pH range
        from 1.6 to 13.3. Corros Sci. 1977;17(10):871–8.

55.   Suzuki I. Corrosion-Resistant Coatings Technology. New York: Marcel Dekker, Inc.;
        1989.

56.   Porter FC. Corrosion Resistance of Zinc and Zinc Alloys. New York: CRC Press; 1994.
        536 p.

57.   Zhang XG. Corrosion and Electrochemistry of Zinc. Vol. 1, Statewide Agricultural Land
        Use Baseline 2015. Springer Science & Business Media; 1996.

58.   Hisamatsu Y, Hirose Y. Corrosion Protection Handbook. 1986. 511 p.

59.   Belin R, Tillard M, Monconduit L. Redetermination of the iron±zinc phase FeZn 13. Acta
        Crystallogr. 2000;C56:267–8.

60.   Kubaschewski O. Iron - Binary phase diagram. 1982. 136–138 p.

61.   Long JM, Haynes DA, Hodgson PD. Characterisation of galvanneal coatings on strip
        steel. Mater Forum. 2004;27:62–7.

62.   Dionne S. The characterization of continuous hot-dip galvanized and galvannealed steels.
        J Miner Met Mater Soc. 2006;58(3):32–40.

63.   Mehraban S. Corrosion Mechanism, Inhibition and Mechanical properties of Zinc
        Magnesium Aluminium Alloy coated Galvanised Steel. Swansea University; 2013.

64.   Sendzimir T. US 2212481 A. US 2212481 A, 1940.

65.   Treatments S. The Spangle on Hot-Dip Galvanized Steel Sheet 2.6. 2011;1–6.

66.   Suarez L, Leysen F, Masquelier C, Warichet D, Houbaert Y. Effects of Mg Additions on

Surface Morphology and Corrosion Resistance of Hot-Dipped Zn Coatings. Defect Diffus Forum. 2008;273–276:300–5.

67.   Porter DA, Easterling KE, Sherif MY. Phase Transformations in Metals and Alloys. Third. Vol. 53, Journal of Chemical Information and Modeling. CRC Press Taylor & Francis Group; 2009. 538 p.

68.   Askeland D, Fulay P, Wright W. What is Materials Science and Engineering? Sci Eng Mater. 2010;650–1.

69.   Jodogn P, Pelini L, van Campenhout C. The Development of Galfan at Cockerill Sambre. Zinc Coat Steel Sheet. 1994;4th.

70.   Sullivan J, Penney D, Elvins J, Khan K. The effect of ultrasonic irradiation on the microstructure and corrosion rate of a Zn–4.8wt.% Al galvanising alloy used in high performance construction coatings. Surf Coatings Technol. 2016;1–10.

71.   Sullivan JH. Metallic Runoff From Coated Steels. Swansea University; 2003.

72.   Elvins J. The relationship between microstructure and corrosion resistance of Galfan coated steels. Corros Eng Sci Technol. 2003;38(3):197–204.

73.   Goodwin F. Galfan. 1985.

74.   Protection SC. Superior Corrosion Protection 5% aluminum, 95% zinc.

75.   Moon S-M, Pyun S-I. The Corrosion of Pure Aluminium during Cathodic Polarization in Aqueous Solutions. Corros Sci. 1997;39(2):399–408.

76.   Miao W, Cole IS, Neufeld AK, Furman S. Pitting Corrosion of Zn and Zn-Al Coated Steels in pH 2 to 12 NaCl Solutions. J Electrochem Soc. 2007;

77.   Yadav AP, Nishikata A, Tsuru T. Degradation mechanism of galvanized steel in wet – dry cyclic environment containing chloride ions. 2004;46:361–76.

78.   Schürz S, Luckeneder GH, Fleischanderl M, Mack P, Gsaller H, Kneissl AC, et al. Chemistry of corrosion products on Zn–Al–Mg alloy coated steel. Corros Sci. 2010;52(10):3271–9.

79.   Hosking NC, Ström MA, Shipway PH, Rudd CD. Corrosion resistance of zinc–magnesium coated steel. Corros Sci. 2007;49(9):3669–95.

80.   Salgueiro Azevedo M, Allély C, Ogle K, Volovitch P. Corrosion mechanisms of Zn(Mg,Al) coated steel: 2. The effect of Mg and Al alloying on the formation and properties of corrosion products in different electrolytes. Corros Sci. 2015;90:482–90.

81.   Stoulil J, Prosek T, Nazarov A, Oswald J, Thierry D. Electrochemical properties of corrosion products formed on Zn-Mg, Zn-Al and Zn-Al-Mg coatings in model

atmospheric conditions. Mater Corros. 2015;66(8):777.

82.   Roetheli BE, Cox GL, Littreal WB. Effect of pH on the Corrosion Products and Corrosion Rate of Zinc in Oxygenated Aqueous Solutions. Met Alloy. 1932;3:73–6.

83.   Vujičić V, Lovreček B. Study of the influence of pH on the corrosion rate of aluminium. Surf Technol. 1985;25:49–57.

84.   Vu TN, Volovitch P, Ogle K. The effect of pH on the selective dissolution of Zn and Al from Zn–Al coatings on steel. Corros Sci. 2013 Feb;67:42–9.

85.   Han J, Ogle K. Dealloying of MgZn 2 Intermetallic in Slightly Alkaline Chloride. J Electrochem Soc. 2017;164(14):952–61.

86.   Elvins J, Spittle JA, Worsley DA. Relationship between microstructure and corrosion resistance in Zn-Al alloy coated galvanised steels. Corros Eng Sci Technol. 2003;38(3):197–204.

87.   Elvins J, Spittle J a., Sullivan JH, Worsley D a. The effect of magnesium additions on the microstructure and cut edge corrosion resistance of zinc aluminium alloy galvanised steel. Corros Sci. 2008;50(6):1650–8.

88.   McMurray HN, Williams G. Under Film/Coating Corrosion. Ref Modul Mater Sci Mater Eng. 2016;(July 2015):1–19.

89.   Wint N, Eaves D, Michailidou E, Bennett A, Searle JR, Williams G, et al. The kinetics and mechanism of filiform corrosion occurring on zinc-aluminium-magnesium coated steel. Corros Sci. 2019;(June):108073.

90.   Jordan CE, Goggins KM, Benscoter AO, Marder AR. Metallographic preparation technique for hot-dip galvanized and galvannealed coatings on steel. Mater Charact. 1993;

91.   Drewien CA, Benscoter AO, Marder AR. Metallographic Preparation Technique for Electrodeposited Iron-Zinc Alloy Coatings on Steel. 1991;51:45–51.

92.   Thormählen I, Straub J, Grigull U. Refractive Index of Water and Its Dependence on Wavelength, Temperature, and Density. Vol. 14, Journal of Physical and Chemical Reference Data. 1985. p. 933–45.

93.   ASTM International. Standard Guide for Conducting and Evaluating Galvanic Corrosion Tests in Electrolytes. ASTM G71-81 (2014). West Conshohocken, PA; 2014.

94.   Macdonald DD, Owen D. The Electrochemistry of Iron in 1M Lithium Hydroxide Solution at 22 ~ and 200~. 1973;120(3):317–24.

95.   Prosek T, Hagström J, Persson D, Fuertes N, Lindberg F, Chocholatý O, et al. Effect of the microstructure of Zn-Al and Zn-Al-Mg model alloys on corrosion stability. Corros

Sci. 2016;110.

96.   Yadav AP, Katayama H, Noda K, Masuda H, Nishikata A, Tsuru T. Effect of Al on the galvanic ability of Zn-Al coating under thin layer of electrolyte. Electrochim Acta. 2007;52(7):2411–22.

97.   Salgueiro Azevedo M, Allély C, Ogle K, Volovitch P. Corrosion mechanisms of Zn (Mg , Al) coated steel in accelerated tests and natural exposure : 1 . The role of electrolyte composition in the nature of corrosion products and relative corrosion rate. Corros Sci. 2014;

98.   Salgueiro Azevedo M, Allély C, Ogle K, Volovitch P. Corrosion mechanisms of Zn(Mg,Al) coated steel: The effect of HCO3− and NH4+ ions on the intrinsic reactivity of the coating. Electrochim Acta. 2014;153:159–69.

99.   Shkirskiy V, Ogle K. Electrochimica Acta A novel coupling of electrochemical impedance spectroscopy with atomic emission spectroelectrochemistry : Application to the open circuit dissolution of zinc. Electrochim Acta. 2015;168:167–72.

100. Han J, Ogle K. Cathodic Dealloying of α -Phase Al-Zn in Slightly Alkaline. J Electrochem Soc. 2018;165(7):334–42.

101. Vu TN, Mokaddem M, Volovitch P, Ogle K. The anodic dissolution of zinc and zinc alloys in alkaline solution. II. Al and Zn partial dissolution from 5% Al-Zn coatings. Electrochim Acta. 2012;74:130–8.

102. Bonnel A, Dabosi F, Deslouis C, Duprat M, Keddam M, Tribollet B. Corrosion Study of a Carbon Steel in Neutral Chloride Solutions by Impedance Techniques. J Electrochem Soc. 1983;130(4):753–61.

103. Delahay P. A Polarographic Method for the Indirect Determination of Polarization Curves for Oxygen Reduction on Various Metals. J Electrochem Soc. 1950;97(6):198.

104. Jovancicevic V, Bockris JO. The Mechanism of Oxygen Reduction on Iron in Neutral Solutions. J Electrochem Soc. 1986;133(9):1797.

105. Zečević S, Dražić DM, Gojković S. Oxygen reduction on iron: Part III. An analysis of the rotating disk-ring electrode measurements in near neutral solutions. J Electroanal Chem Interfacial Electrochem. 1989;265(1–2):179–93.

106. Davis JR. Corrosion: Understanding the Basics. Davis JR, editor. Materials Park, OH: ASM; 2000. 21–48 p.

107. McMurray HN, Parry G, Jeffs BD. Corrosion resistance of Zn-Al alloy coated steels investigated using ... Ironmak Steelmak. 1998;25(3):210–5.

108. Vu AQ, Vuillemin B, Oltra R, Allély C. Cut-edge corrosion of a Zn-55Al-coated steel: A comparison between sulphate and chloride solutions. Corros Sci. 2011;53(9):3016–25.

109. Ogle K, Serdechnova M, Mokaddem M, Volovitch P. The cathodic dissolution of Al, Al2Cu, and Al alloys. Electrochim Acta. 2011;56(4):1711–8.

110. Dafydd H, Worsley DA, McMurray HN. The kinetics and mechanism of cathodic oxygen reduction on zinc and zinc – aluminium alloy galvanized coatings. 2005;47:3006–18.

111. McKubre MCH, Macdonald DD. The Dissolution and Passivation of Zinc in Concentrated Aqueous Hydroxide. J Electrochem Soc. 1981;128(3):524–30.

112. Thébault F, Vuillemin B, Oltra R, Ogle K, Allely C. Investigation of self-healing mechanism on galvanized steels cut edges by coupling SVET and numerical modeling. Electrochim Acta. 2008 Jun 30;53(16):5226–34.

113. St-Pierre J, Piron DL. A Model for the Potential Oscillations of the Zinc Electrode Polarized Cathodically in an Alkaline Medium. J Electrochem Soc. 1987;134(7):1689–95.

114. St-Pierre J, Piron D. Mechanism of cathodic potential oscillations of the zinc electrode in alkaline solutions. J Electrochem Soc. 1990;137(8):2491–8.

115. Thebault F, Vuillemin B, Oltra R, Allely C, Ogle K, Tada E. Investigations of cut-edge corrosion of galvanized steels by coupling local electrochemical methods and computational modeling. ECS Trans. 2008;11(22):91–105.

116. Wint N, Eaves D, Michailidou E, Bennett A, Searle JR, Williams G, et al. The kinetics and mechanism of filiform corrosion occurring on zinc-aluminium-magnesium coated steel. Corros Sci. 2019;158(May):108073.

117. Wint N, Eaves D, Williams G, McMurray HN. The effect of composition and thickness on the mechanism and kinetics of filiform corrosion occurring on zinc-aluminium-magnesium coated steel. Corros Sci. 2021;179(November 2020):109168.

118. Coleman AJ, McMurray HN, Williams G, Afseth A, Scamans GM. Filiform Corrosion on 6000 Series Aluminium: Kinetics and Inhibition Strategies. Mater Sci Forum. 2009;519–521:629–34.

119. McMurray HN, Holder A, Williams G, Scamans GM, Coleman AJ. The kinetics and mechanisms of filiform corrosion on aluminium alloy AA6111. Electrochim Acta. 2010;55(27):7843–52.

120. Williams G, McMurray HN. Anion-exchange inhibition of filiform corrosion on organic coated AA2024-T3 aluminum alloy by hydrotalcite-like pigments. Electrochem Solid-State Lett. 2003;6(3):9–11.